THESIS

GEOCHEMICAL AND MINERALOGICAL INVESTIGATION OF BRECCIAS AT THE EL NIÑO AU-AG DEPOSIT, ELKO COUNTY, NEVADA

Submitted by

Rocky Barker

Department of Geosciences

In partial fulfillment of the requirements

For the Degree of Master of Science

Colorado State University

Fort Collins, Colorado

Summer 2017

Master's Committee:

Advisor: John Ridley

John Singleton
Christopher Bareither

ABSTRACT

GEOCHEMICAL AND MINERALOGICAL INVESTIGATION OF BRECCIAS AT THE EL NIÑO AU-AG DEPOSIT, ELKO COUNTY, NEVADA

The Button Hill deposit is a breccia-hosted Au-Ag deposit at the extreme north end of the Carlin-Trend, Nevada. The current operation at Button Hill is the Arturo mine, owned and operated by Barrick Gold Company. The El Niño underground mine will exploit a higher-grade section of the Button Hill gold deposit to the north. The objective of this study is to determine the mineralogy, petrology, whole-rock geochemistry, relative timing and genesis of breccia types and ore bodies in the El Niño section of the Button Hill deposit for the purpose of refining the geologic model, to predict complications in ore processing, and to identify pathfinders for future near and far exploration.

Representative core samples from 8 drill-holes that intersected the proposed El Niño underground mine, within the Button Hill Au-Ag deposit, were re-described and sampled for hyperspectral analysis, selective geochemical analysis and for thin-sections. 4-acid digest (aqua regia digest for Hg) ICP-MS/OES 48-element whole rock geochemistry was performed for 9,664 drill-core and RC samples from 33 holes and 21 selective hand samples. 23,467 samples were analyzed using fire assay method for Au and Ag and 1,898 samples were analyzed using LECO™ for organic carbon and carbonate. Corescan's hyperspectral core imager, the Mark III (HCI-3) was used to analyze 594.6 ft. from 6 drill-holes and 14 grab sample from 9 drill-holes and the handheld TerraSpec Halo was used for spot analysis on the same samples.

The stratigraphy at the El Niño deposit has four known formations. The stratigraphically highest Tertiary Carlin Formation consists of alternating terrigenous gravels and ash beds. The

Ordovician Vinini Formation primarily consists of deep marine facies chert. The Devonian Rodeo Creek Formation consists of argillites, shales, mudstones, siltstones, sandstones, marls, and minor limestone. It lies directly below the Roberts Mountain thrust and is the stratigraphically highest unit of the "lower-plate" stratigraphy and the major host to mineralization at Arturo and El Niño. The deepest exposed unit at the Arturo and El Niño mines is a massive limestone called the Silurian-Devonian Bootstrap Formation.

The major hosts of Au and Ag at the El Niño mine are tectonic and hydrothermal breccias, and to a lesser degree, dissolution collapse breccias of the Rodeo Creek and Bootstrap Formations. The thickest and most continuous breccia is the Roberts Mountain thrust tectonic breccia (Bx1). Bx1 is a deformed mélange of carbonaceous and metalliferous limey mudstone clasts and matrix primarily derived from the Rodeo Creek Formation. The general high original porosity and presence of diagenetic pyrite in Bx1 makes it a favorable host to Carlin-type Au. Bx4 is the name for all other tectonic breccias. Bx4 is distinguished from Bx1 by the presence of; 1) Bx1 clasts in the breccia, 2) pure limestones clasts from the Bootstrap Formation, 3) vertical or near vertical orientation of faults, and/or 4) presence of any clast that is younger than Antler shortening (i.e. Jurassic diorite, or includes younger styles of alteration, silicification, quartz veining, and pyrite veining).

There are four types of hydrothermal breccias in the Button Hill Au-Ag deposit. They are: 1) Bx1a: the strongly silicified tectonic breccia (Bx1), which consists of two subtypes, a white quartz flooded breccia, and a dark vuggy silica flooded breccia, 2) Bx2: vuggy silica cemented hydrothermal breccia that often rebrecciates Bx1, 3) Bx3: pyrite matrix hydrothermal breccia. Of the Bx3 breccias, there appears to be at least two subtypes. The first is a crackle to chaotic breccia associated with thin bleached selvages (Bx3a) around the pyrite veinlets. Bx3b contains pyrite

veining with no bleached selvage. 4) Bx6: the youngest of the hydrothermal breccias, a late calcite ± barite matrix crackle to chaotic breccia.

The second most prevalent breccia type in the Button Hill deposit are the collapse breccias (Bx5), of which there are two major subtypes characterized by the presence of silicification (Bx5b), or lack of silicification (Bx5a).

Timing of mineralization, alteration and brecciation was determined by a combination of thin-section petrography, geochemical analysis and infrared spectroscopy and is as follows.

- The first brecciation event was associated with movement on the Roberts Mountain thrust (Bx1).
- Early calcite and barite veins appear to be after and coincident with Roberts Mountain thrust-related deformation.
- A relatively small portion of Bx1 was intensely silicified (Bx1a) at the lower contact with the Bootstrap limestone.
- The diorite intrusion (Russet Dike) in the North wall of the Arturo pit intruded into the Russet fault and cross-cuts Bx1 and Bx1a.
- Bx2 hydrothermal breccia and pre-ore weak silicification occurred after the intense silicification of Bx1a but before some local fault brecciation (Bx4).
- Bx3b pyrite vein breccia likely occurred during or just before Carlin-type Au mineralization. Bx3a quartz-sericite-pyrite alteration was after Bx3b and is likely associated with Miocene low-sulfidation epithermal Ag mineralization
- Bx5 dissolution collapse brecciation occurred at different stages throughout the development of the Button Hill system, starting before Bx1a and continuing until after the development of Bx2.

- The coarse-grained calcite ± barite veins and breccia matrix (Bx6) cross-cuts all other features at the Button Hill deposit and thus is the youngest. This event is not related to Au-Ag mineralization and is likely from circulating groundwater precipitating calcite and barite in void space created by dissolution and faulting.

A principal component analysis (PCA) of whole-rock geochemical data showed that there are four distinct chemical suites within the Button Hill Au-Ag deposit. The four suites of elements were substantiated and refined by examination of bivariant scatter plots, down-hole geochemical variation plots, Grant isocon plots, enrichment factor scores, and 2-dimensional geochemical distribution contours. Suite 1 consists of Al, Ce, Fe, La, Nb, Th, Ti, and Zr and is interpreted to represent the clay component of pre-alteration lithogeochemistry. Suite 2 is the mineralization suite and includes Au, Ag, As, Cu, Fe, Hg, (Re?), S, Se, Sb, Te, Tl and W. Suite 2 is further subdivided into 1) Au, As, Cu, Fe, Hg, S, Te, Tl, and W and 2) Ag, Hg, Sb, Se, and Te. Suite 3 includes C, CO3, Ca, Mg, Mn, S, and Sr. This suite consists of many of the elements lost or added during the most common alteration styles associated with Carlin-Type gold deposits (decarbonatization/decalcification, carbon replacement, and sulfidation). Suite 4 consists of Cr, Mg, Mn, Mo, P, Pb, Th, U, V, W, Y, and Zn, which is interpreted to be associated with organic-rich deposition in an anoxic to euxinic environment.

The spatial distributions and geometries of concentrations of ore-related elements in cross-section are very similar; however, Au mineralization (+As, Tl and Re) and Ag mineralization (+Te, Se, and Hg) differ in that the former tends to have the highest concentrations above the intensely silicified zone (Bx1a), partly in the main breccia zone and partly in the overlying Rodeo Creek Formation. The highest concentrations of Ag are typically below Au, completely within the breccias, especially associated with Bx3a, and are also in the upper plate, NW of the Tara West fault.

Short-wave infrared spectroscopy has been successfully applied to identify phyllosilicates, carbonate, silica, iron oxide and sulfate mineralogy. At the Button Hill Au deposit, SWIR spectroscopy has identified 16 mineral classes and 3 mineral compositions.

Muscovite is the major mica in the altered rocks. This is shown by the mineral maps and histogram of the mica 2200nm absorption feature position. Phengite is a minor mica that appears to be associated with weathering and some unaltered limestone. Ammonium muscovite has a relatively strong signature in the upper silicified breccia zone. It is directly associated with bleached alteration in Bx3a. The illite spectral maturity of ammonium muscovite suggests that they are sourced from a higher temperature fluid of alteration (≥300°C) compared to non-ammonium-bearing micas that had an approximate temperature range of 100-200°C. Montmorillonite, gypsum, goethite, hematite, and jarosite are also associated with weathered zones in faults and porous collapse breccias. Kaolinite is found coating some faults and fractures; however, the majority is within a specific collapse breccia (Bx5b) at the lower contact of the zone of silicification.

Carbonates in the breccia zone are negatively correlated with silica. The carbonate signature is spotty throughout both the intensely silicified and weakly silicified zones and is highest below the silicification zone. The carbonate 2330nm features shows that all carbonate is calcite. The absence of dolomite in the SWIR samples is in contrast to other Carlin-type deposits.

Deposition of Au and Ag is interpreted to have been in two phases. The first was Eocene Carlin-type Au mineralization that involved fluids carrying Au, As, (Cu?), Hg, S, Te, Tl, and (W?) that rose buoyantly along the Hend-Nicks fault zone where it spread out at areas of high permeability such as the Otto fault, Hendrix fault and Nicks fault, as well as bedding contacts, porous lithologies and breccia zones. The largest Au-ore body is hosted in Bx1 and Bx2 at the upper contact of the intensely silicified Bx1a breccia. The fluids appear to have preferentially precipitated Au in the rocks above the Bx1a breccia, likely due to its lack of permeability. Because

of the position of the silica body on the upper contact of the Bootstrap limestone, it is likely that collapse breccias played a role in controlling the precipitation of silica by causing upper units to collapse into the karstic voids, increasing permeability for silica-bearing fluids to flow and precipitate.

The distribution of Carlin-Au-related elements shows that mineralization was minor in the upper plate; however, many of the elements such as As, Sb and Te have a much more extensive footprint than Au, reaching as high as the outcropping surface. Tl and Re appear to have remobilized and precipitated anomalous values where faults breach the Carlin Formation. Anomalous values of these elements at the surface is potentially valuable as pathfinders for future exploration efforts.

The second phase of mineralization is interpreted to be a Miocene low-sulfidation epithermal Ag deposit that enriched the ore-system in Ag, Hg, Sb, Se, and Te. The second phase ore fluids followed the same pathways as Carlin-Au-bearing fluids; however, precipitated ore elements in slightly different areas. The main breccia-hosted Ag-ore body is slightly lower than the Au-ore body. It formed lower in the Bx1a breccia. Ag, Hg, Se, and Te have a much more widespread distribution in the upper plate and appear to have also precipitated along the Tara West fault, suggesting that this Basin and Range normal fault was present and was used as a conduit for fluids of this phase.

ACKNOWLEDGEMENTS

This study has been conducted under the supervision of Dr. John Ridley of Colorado State University Geoscience Department, who has guided and helped to develop this project and who has provided financial, moral and scholastic support. I am eternally grateful to John for his friendship and guidance through this project, as well as through my stay at CSU. Without his support, none of this would have been possible.

Thank you to Jim Byars, Jerry Johnson, and Paul Dobak of Barrick Gold Company for their willingness to take a chance on me and fund this project, and for inviting me back to Barrick every summer for highly fulfilling internships.

To Brigette Martini, Erin Looby and the other folks at Corescan, I thank you for the use of your outstanding hyperspectral core scanning service and for putting up with the incessant questions regarding infrared spectroscopy. A very special thank you to Brigette Martini who was always available for questions, who visited my poster at GSA and who visited CSU to teach me how to use the hyperspectral program ENVI.

Thank you to Gerry Griesel, John Porter, Tyson Hasselquist, Kerry Hart, Dana Holbrook, and Thomas Wright of Barrick Goldstrike for your support of this research.

I would also like to thank my wife and children for putting up with the long hours required for this project, as well as school in general. I am particularly grateful for their support and encouragement.

TABLE OF CONTENTS

LIST OF TABLES

LIST OF FIGURES

CHAPTER 1 - INTRODUCTION

1.1 Introduction

Nevada may be known as the "Silver State" but there is another commodity in which it is much more well-known for. Nevada produced approximately 213.4 M ounces of gold as of 2014, accounting for 3.8% of the world's historic production. Gold production within the United States was valued at $6.26 billion in 2014, of which Nevada is responsible for 73% (4.94 M oz), making it the first largest producer of gold in the US and fifth largest in the world behind China, Australia, Russia, and Canada. Silver production in Nevada was valued at $209 million, considerably less than gold and about half the value of copper ($427 million) and was primarily produced as a byproduct of gold production (Muntean, 2016).

By far the largest gold producing deposit type in Nevada are the sediment-hosted disseminated (SHD) gold deposits. Of the deposits that contain ≥5 M oz Au, SHDs make up 80% (Davis and Tingley, 2005). SHDs are characterized by the presence of gold as submicron-sized particles or solid solution with disseminated arsenian pyrite or marcasite (Cline, 2005; Berger et al., 2014). They are found throughout the world in places like the Great Basin, USA, China, Indonesia, Iran, and Malaysia (Berger et al., 2014; Ashley et al., 1991; Garwin et al., 1995; Mehrabi et al., 1999).

SHD gold deposits were recognized as a distinct deposit type after 1961 when the Carlin Deposit was first discovered. The name given to these deposits was "Carlin-Type" (Cline et al., 2005). It has since been recognized that Carlin-Type deposits are a subclass of SHD deposits, on account of minor differences in alteration and mineralogy, and the size differences, with Carlin-Type deposits typically being much larger, reaching sizes considerably greater than 5 M oz (Berger et al., 2014).

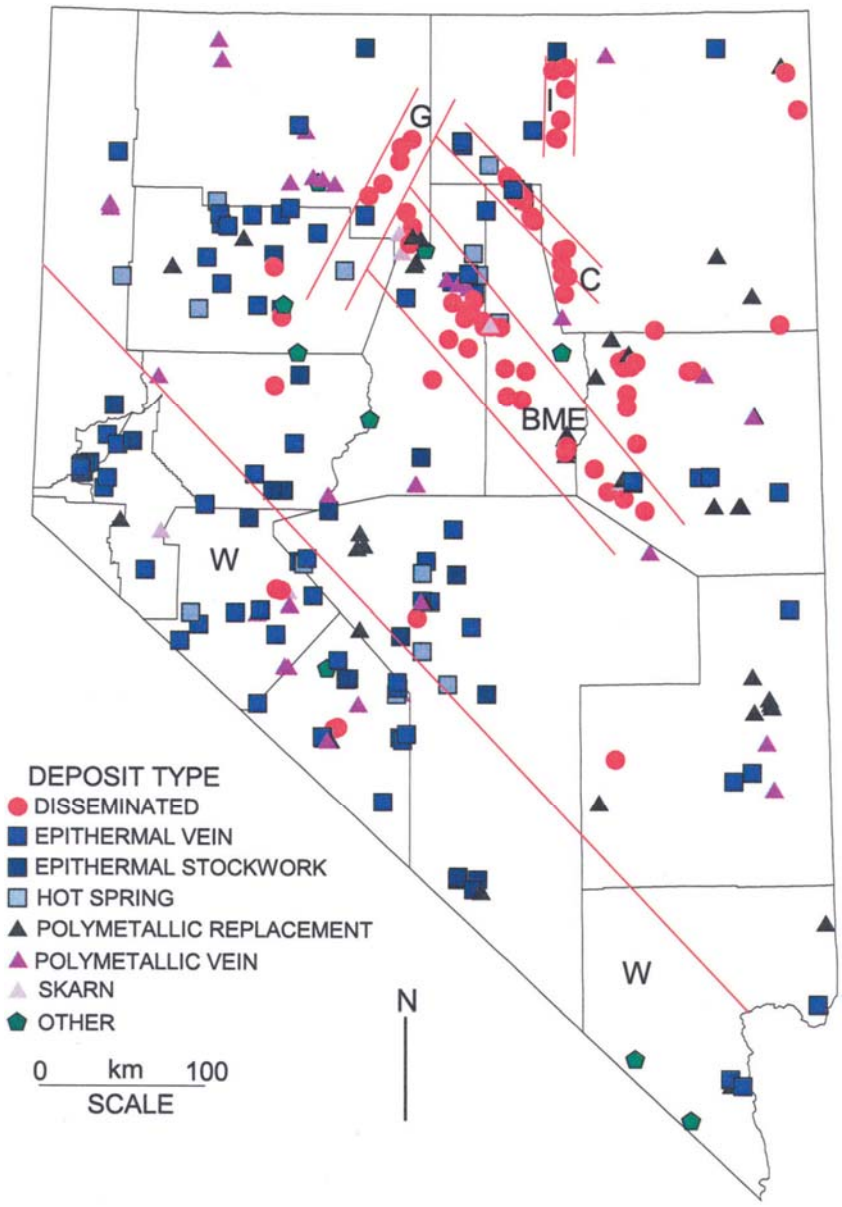

Figure 1. Map showing the location of metal deposits in Nevada. The Carlin-Type Au-deposit trends (red lines) are: BME—Battle Mountain-Eureka trend, C—Carlin trend, G—Getchell trend, I—Independence trend, and W—Walker Lane (Davis and Tingley, 2005).

Carlin-Type gold deposits of Nevada are hosted in passive margin, calcareous, carbonaceous sediments along high-angle normal faults, bedding plains, in breccias and along low angle thrust faults and occur along lineaments, or trends. There are five major trends; the Getchell

trend, the Jerritt Canyon trend, Battle Mountain – Eureka trend, Alligator Ridge and the Carlin trend (Cline et al., 2005). The Carlin-Trend consists of a series of over 40 sediment-hosted gold deposits in a north-northwest alignment (Cline et al., 2005) that stretches approximately 70 km in northeastern Nevada (Figure 2).

Historically, the Carlin trend has been the major producer in Nevada, accounting for 1.5% (84.2 M oz) of historic world production and producing 1.729 M oz in 2014, 35% of Nevada's gold production (Muntean, 2016). Together, the deposits that make up the Carlin-Trend boast an extraordinary gold endowment of approximately 100 M oz. (Cline et al., 2005).

1.2 Arturo Project

The Arturo Project (Figure 3) is a three-phase plan by Barrick Gold Company in partial partnership with Premier Gold Mines. It is located in northeastern Nevada, at the northern end of the Carlin Trend in Elko County, approximately 43.5 km (27 miles) northwest of the town of Carlin (Figure 2) and approximately 3.5 km northwest of the Betze pit. The Arturo Project plan includes a layback in the north of the historic Dee pit (Phase 1), the Arturo pit approximately 400 meters to the east of Dee (Phase 2), and another open pit operation called South Arturo to the South of Dee and Arturo (Phase 3).

The Arturo pit operation, headed by Barrick Goldstrike, began in the spring of 2015, with a projected completion in the spring of 2017, at which time the El Niño portal will be opened. The El Niño is a proposed underground mine that will have a portal near the bottom of the Arturo pit that will follow a higher-grade portion of the Button Hill, breccia-hosted gold deposit to the north. The El Niño underground mine will be controlled by the Barrick Meikle underground operation.

1.3 Objectives of Study

The Button Hill deposit in the northern-most portion of the Carlin-Trend (Figure 2) is a breccia-hosted Au + Ag deposit exposed in the Arturo Pit. The El Niño mine will be an underground mine that follows a higher-grade portion of the Button Hill breccia-hosted gold deposit to the north. The objective of this study is to determine the mineralogy, petrology, geochemistry, relative timing and genesis of known breccia types and ore bodies in the El Niño section of Button Hill deposit for the purpose of creating a mineralogical and geochemical model that will help predict complications in ore processing, to identify pathfinder elements for future exploration, to describe the petrogenesis of the El Niño alteration zone and to understand how mineralization is related to the Button Hill breccias.

1.4 Previous Research at El Niño and Host Sequence

El Niño is a relatively new discovery and so no known research has been completed for this deposit. However, some research has been completed in nearby deposits and stratigraphy that may be relevant to the understanding of this deposit. Trotman (2009) completed a Master's thesis on the general geology and description of the Storm underground high-grade Au-Ag deposit. The Storm mine portal is approximately 1.6 km (1 mile) west of the proposed portal of the Button Hill mine and on the west side of a horst block that separates the two deposits. Dobak et al. (2002) also gave a description of the history, geology and timing of the ore body at the Storm mine. Cook et al. (2002) published a paper in the Mineralogical Record that had the primary goal of describing the world class barite samples that were collected from the Storm mine (Called Dee North in the paper). They included a very cursory explanation of the history and geology of Storm. The technical report from Roscoe Postle Associates Inc. (RPA) (Valliant, et al., 2015) titled, "Technical report on the South Arturo Mine, Elko County, State of Nevada, U.S.A.," provides an excellent

overview of the entire Arturo Project, including Arturo, South Arturo and Dee. The report includes mining and processing specifics, history of mining and exploration, geology, and deposit descriptions.

In 1985, J. D. Greybeck completed a thesis titled, "Geology of the Dee Mine Area, Elko County, Nevada." This research contributed a description of the stratigraphy, structural geology and 24-element ICP-AES whole-rock geochemistry of the Dee mining area. Ellis (1986) also gave a description of the Dee mine with an added contribution of the mining operations in a paper published in Mining Magazine titled, "The Dee Gold Mine."

Cope et al. (2008) gave a thorough description of exploration findings at the South Arturo deposit in a paper titled, "South Arturo: a recent gold discovery on the Carlin Trend," published in Mining Engineering magazine. In their paper, they gave a history of mining and discovery at both the South Arturo deposit and Dee/Storm deposit, as well as Barrick's history on the Carlin Trend. A similar paper titled, "South Arturo, Nevada," (Hipsley et al., 2006) also gives a historic overview and exploration findings of South Arturo.

The Bootstrap window (Figure 2) is an allochthonous window in the Northern Carlin Trend where lower Devonian and Silurian rocks are exposed through a thrust zone that placed deeper water facies Ordovician, Silurian and Devonian sedimentary rocks over shallow water shelf and slope facies sediments, and where several deposits are exposed, including the Bootstrap and Dee mines. Evans and Mullens (1976) provided a general description of lithology, structural geology and alteration of the Bootstrap window. Furley (2001) and Morgan (2007) gave a thorough description in their thesis work of the Bootstrap limestone, a host for gold at the Button Hill deposit.

The importance of breccias as a host to Carlin-Type gold was not truly appreciated until drilling at the Meikle deposit intersected 136 m of 0.47 opt (16.1 g/t) gold hosted in breccias in

1989 (Bettles, 2002). However, most Carlin-Type gold deposits are either hosted in, or spatially associated with, some breccia type, whether it be sedimentary debris flow, dissolution collapse breccias, fault breccias or hydrothermal breccias (Williams, 1992). Research on breccias in the northern Carlin-trend is focused on a wide variety of breccias associated with Carlin mineralization. In 1993, the Geological Survey of Nevada put out a field guide to breccias in northeastern Nevada called, "Handout for the symposium on Northeast Nevada breccia bodies" (Williams, 1993). The field guide includes an overview of breccia types and their formation, as well as specific gold-hosting breccias at various mineral deposits. In 1997, S. G. Peters and others published a paper titled, "Breccia types in the Betze orebody, Goldstrike Mine, Eureka County, Nevada." In their paper, they describe the sedimentary, rip-up, debris-flow, collapse, tectonic and hydrothermal breccias within the Betze deposit. Evans (2000) completed a master's thesis titled "Carbonate-hosted breccias in the Meikle mine, Nevada and their relationship with gold mineralization" that carefully describes mineralized breccias within the Meikle deposit. Emsbo et al. (2003) described the post-ore calcite and barite-bearing breccias that are common in the northern Carlin-trend in a paper titled, "Origin and significance of postore dissolution collapse breccias cemented with calcite and barite at the Meikle gold deposit, Northern Carlin Trend, Nevada."

1.5 Mining History

The gold deposits of the Arturo project, together with the Bootstrap, Tara, Capstone, and Dee make up the Bootstrap mining district (Trotman, 2009). Mining in this district began with the discovery of antimony in 1918 at the Bootstrap mine, approximately 2 km south of the Button Hill deposit (Bettles, 2002; Trotman, 2009). Gold was not discovered at the Bootstrap mine until the 1950's when highly altered porphyry dikes were found to be mineralized (Nuckolls, 1985; Evans, 200; Trotman, 2009).

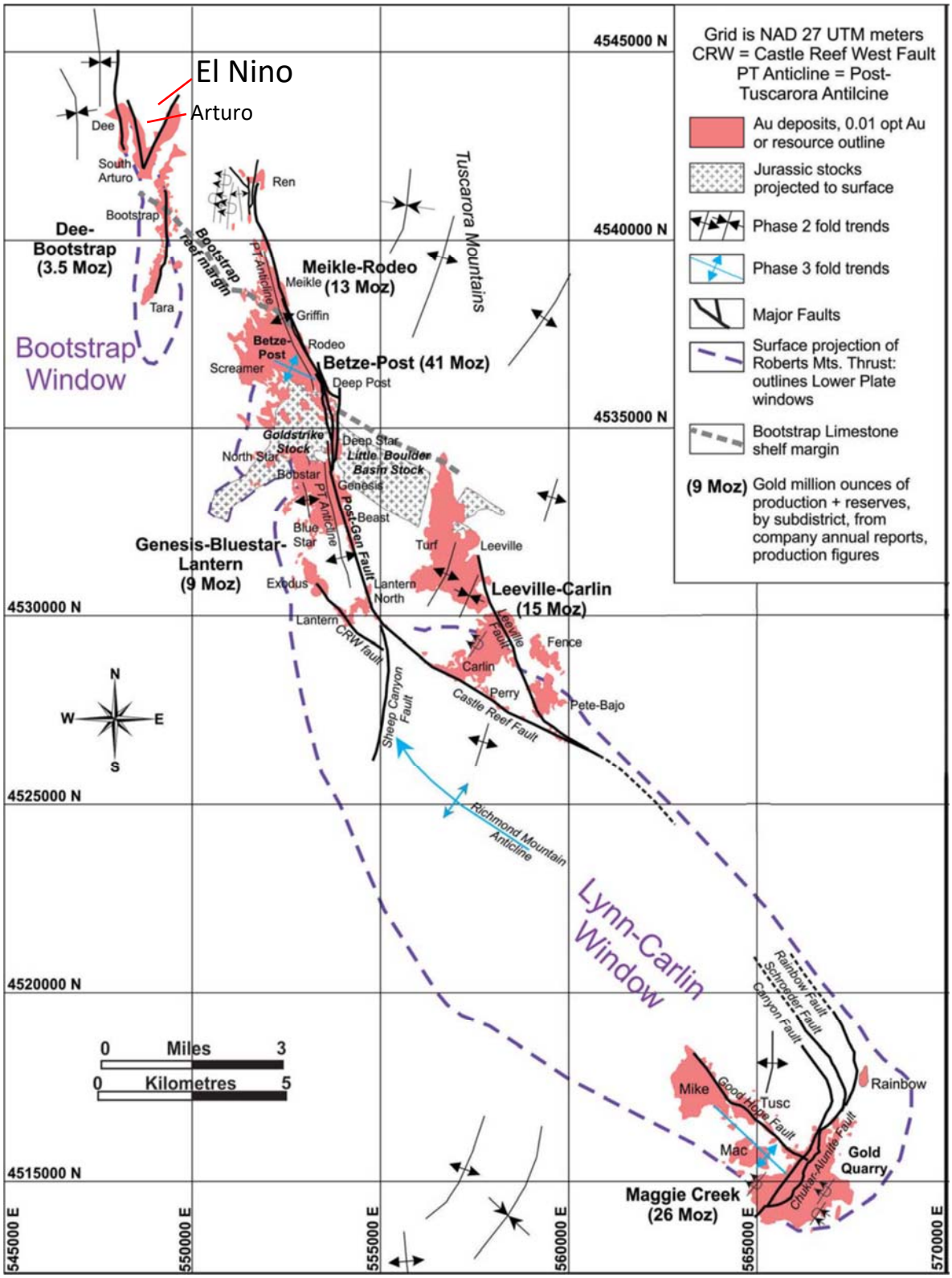

Figure 2. Gold deposits (projected to surface) and major structural features of the Northern Carlin-Trend. It shows the location of the allochthonous windows, major deposits, major structural features and the El Niño and Arturo Mines. Modified from Rhys et al., 2015

In 1961 the Carlin mine was discovered and the Carlin-Type gold deposit was subsequently recognized. It was this finding that eventually led to the discovery of a larger ore body at the Bootstrap mine and the later discovery of the Tara, Capstone and Dee gold deposits (Trotman, 2009).

1.5.1 Dee Mine

The Dee gold deposit was discovered by a Cordex Exploration Company geologist named G.W. (Dee) DeLaMare in 1981. In 1984 the Dee mine was put into production by the Dee Gold Mining Company and Rayrock Mines Incorporated. During the mines 16-year lifespan it produced approximately 682,000 oz Au and 400,000 oz Ag (Dobak et al., 2002; Trotman, 2009). One year before closing the mine in 2000; however, a decline was constructed from the bottom of the Dee pit that accessed the Dee Deep North deposit, an oxide orebody that was not accessible from the current geometry of the pit. This 1,039 m decline also acted as an access point for the later discovered gold resources of the Storm Mine (Dobak et al., 2002).

1.5.2 Storm Mine

Early in the life of the Dee mine, several low tonnage, high grade, breccia hosted Au + Ag ore bodies were discovered north of the Dee deposit. Meridian Gold entered into a joint venture with Rossi to mine the newly discovered Discovery Zone, End Zone, and 49er ore bodies that would eventually make up the Storm underground mine (Dobak et al., 2002; Valliant et al., 2015). In 2007 Meridian Gold Corp. was purchased by Yamana Gold Inc., who swiftly sold their portion of the Rossi exploration joint venture to Barrick Gold Company. Barrick mined the Storm deposits from 2007 to 2012 producing a total of 342,835 oz. Au by 2011 (Valliant et al., 2015).

1.5.3 South Arturo

In 2005, after gold prices were back on the rise, an exploration program aimed at the property surrounding the Dee mine focused its drilling efforts on the reclaimed Dee Waste Rock Disposal Facility. This led to the discovery of the South Arturo oxide ore deposit, or phase 3 of the 3 phase Barrick mining strategy (Valliant et al., 2015). As of spring 2017, plans to mine South Arturo have been put on hold until gold prices rebound, or cheaper ore processing methods developed.

1.5.4 Arturo Mine

In 2009 the Button Hill deposit was discovered (Valliant et al., 2015). The Arturo mine was subsequently started to extract the Button Hill ore in 2015 operated by the Barrick Gold Company in partnership with Premier Gold Mines. This operation began in the spring of 2015 and, at the time of writing, is still in production with a projected completion of spring 2017 when the El Niño mine will be started.

1.6 Regional Geology

Sediment hosted disseminated gold mineralization in Nevada is often controlled by large Paleozoic thrust faults and Cenozoic normal faults within Paleozoic miogeoclinal sediments (Cline et al., 2009). Nevada has a complex geologic history that includes periods of compression, extension, sedimentation and volcanism, all of which have influenced ore deposition.

Rifting during the Neoproterozoic (Dickinson, 2006) initiated deposition of terrigenous, shallow-water and deep-water sediments that continued into the Late Devonian. This period of accumulation produced a wedge of sediments with a thickness of approximately 600 m at the Wasatch hinge, Utah to approximately 10,000 m in central Nevada (Stewart, 1980).

The Antler orogeny initiated during the Late Devonian into the Early Mississippian, during which the area switched from being a passive margin to an active margin, partially temporally overlapping with sedimentation (Stewart, 1980; Dickinson, 2006). The Roberts Mountain Thrust (RMT), which caps the majority of mineralization, initiated during this time (Cline et al., 2005, Rhys et al., 2015). The Roberts Mountain allochthon thrust eastward, approximately 145 km over younger sedimentary units (Stewart, 1980). The stratigraphic column above the RMT is collectively known as "upper plate," and rocks below the RMT are the "lower plate."

The Sonoma orogeny followed the Antler orogeny during the Late Permian to Early Triassic (Dickinson, 2006), causing ocean-floor sediments to be thrust approximately 100 km eastward, along what is called the Golconda thrust (Stewart, 1980). The effects of the Sonoma orogeny are mostly seen in the western portion of Nevada and do not likely reach as far east as the Carlin trend (Rhys et al., 2015).

Sedimentation reinitiated during the Triassic to Cretaceous. Mesozoic sedimentation, included shallow-marine carbonates, ocean floor mudstones, turbidites and volcaniclastic sediments with localized back-arc basin deposits (Stewart, 1980; Stewart, 1997), amplified by backarc extension (Wyld, 2000).

During the Jurassic and Cretaceous, widespread backarc volcanism occurred throughout Nevada (Stewart, 1980), including many of the dikes of the Bootstrap and Goldstrike districts and the Goldstrike stock (158 Ma; Arehart et al., 1992).

During the Cretaceous to Eocene, more folding and thrusting occurred, affecting central Nevada to central north Utah, resulting in the Central and East Nevada fold and thrust belts (Rhys et al., 2015). This compressional regime is associated with retroarc thrusting of the Sevier orogeny (Stewart, 1980; Dickinson, 2006). A later folding event in the Late Cretaceous to early Tertiary,

likely associated with the Laramide orogeny, formed northwest-trending folds that may have influenced mineralizing fluid flow in the Battle Mountain-Eureka and Carlin-Trends (Rhys, 2015).

Basin and Range extension in northern Nevada initiated at approximately 40 Ma (Henry et al., 2011) creating the horst and graben topography that Nevada is so well known for (Dickinson, 2006). This period of extension is responsible for uplifting of core-complexes along low-angle faults (Rhys et al., 2015) and the many high-angle normal faults that segment the thrust faults and folds in the Carlin-trend.

Volcanism in Nevada was contemporaneous with Basin and Range extension. Arc magmatism was voluminous in Nevada during the Eocene. Volcanic activity began around 43 Ma in the northeast and rapidly migrated south-southwest, possibly due to a sinking Farallon plate after low-angle subduction during the Laramide (Humphreys, 1995). Rhyolitic ash-flow tuffs and lavas continued until approximately 17 Ma (Stewart, 1980).

Main-stage Au mineralization in Nevada was concurrent with the onset of Basin and Range extension and volcanism (42-36 Ma). Carlin-Type Au deposits are thought to have formed as a result of moderate temperature fluids (~180°-240°C) carrying Au with H_2S ligands, that decarbonatized, argillized, and silicified the host Proterozoic miogeoclinal sediments and deposited gold as submicron particles and solid solution with arsenian pyrite as a result of iron in the host rock reacting with reduced sulfur in the ore fluids (Cline et al., 2005).

In the Middle Miocene (16-14 Ma) rifting occurred in a narrow, north-northwest-trending alignment in north-central Nevada known as the Northern Nevada Rift (Zoback et al., 1994). The rifting is associated with igneous intrusions and Ag-Au ore deposition. Low sulfidation epithermal Ag-Au deposits are mined in the Ivanhoe district, Midas and Mule Canyon (Wallace and John, 1998) and may be the source of high silver concentration in the Storm mine (Trotman, 2009), approximately 1 km west of the El Niño mine, within the Arturo Project.

1.7 Northern Carlin-Trend Geology

The Carlin-trend is an alignment of gold deposits that extends approximately 70 km from the Rain district in the southeast to the Arturo Project in the northwest (Figure 2). Approximately 95% of the known gold mineralization is concentrated in a 35 km section to the north (Rhys et al., 2015) known as the Northern Carlin-trend (NCT). Known mineralization in the northern Carlin-trend begins approximately 10 km northwest of the town of Carlin, at Gold Quarry. It includes many well-known gold deposits such as the Carlin mine, Goldstrike, Meikle, Rodeo, Leeville, Tara, Bootstrap, Arturo and Dee mines. The linear pattern of gold deposits in the Carlin-trend, and other Carlin-Type gold deposit trends, suggests that the gold-carrying fluids may have migrated at Proterozoic rift margins along early, deep rift-related faults (Tosdal et al., 2000; Wijns et al., 2004).

Rocks of the NCT consist of an "Upper Plate" that contains structurally higher Ordovician limestones, quartzite and dolomites of the Pogonip Group, primarily in the South NCT, and muds, cherts and argillites of the Slaven, Elder and Vinini Formations in the north. The "Lower Plate" is structurally lower and younger, and is the primary host to the Carlin-Type gold in the NCT. It consists of silty limestones, calcareous siltstones, muddy limestones and sandstones of the Devonian Roberts Mountains, Popovich, and Rodeo Creek Formations, and to lesser extent, and principally to the north, the Bootstrap limestone. The Upper and Lower plates are separated by the Roberts Mountain Thrust (RMT).

The RMT is an Antler Orogeny-related low-angle thrust fault that emplaced deep-water Paleozoic sediments on top of contemporaneous continental shelf facies rocks. This deformation event is what Rhys et al. (2015) refer to as "Phase 1 deformation." The thrust contact between the structurally higher deep-water sediments and underlying continental shelf sediments is a common trap for mineralizing fluids in NCT gold deposits. Central to the southern section of the NCT is

the Roberts Mountain allochthonous window called the Lynn-Carlin Window (Figure 2) that exposes Lower Plate rocks. To the north, in the Bootstrap District, is a smaller window exposing Lower Plate rocks of the Rodeo Creek Formation and Bootstrap limestone called the Bootstrap Window.

The second deformation phase, according to Rhys et al. (2015), is a thin-skinned Paleozoic and Jurassic contraction event responsible for east-northeast and southeast trending folds that include the Post-Tuscarora anticline in the south of the NCT. Shallow-dipping, west and west-northwest dipping reverse faults also formed as a result of this phase of contraction.

According to Rhys et al. (2015), phase 3 deformation is a late Mesozoic to early Tertiary Laramide-style, thick-skinned, contractional deformation event. In the NCT, Phase 3 is represented by north- to northwest-trending folds included the Richmond Mountain anticline, exposed in the Lynn-Carlin Window, and the Betze Post anticline in the Betze pit. Phase 3 is also responsible for northwest-trending, moderate to steeply-dipping, reverse faults including Bazza fault at Goldstrike, Good Hope fault at Gold Quarry and other fault and fault zones at Rodeo, Meikle and North Post. Contractional events were followed by extension in the Tertiary. Extensional structures in the NCT are primarily oblique-normal faults that have a general northwest, north, to northeast trend and moderate to steep dips and include structures such as the Chukar-Alunite fault zone at Gold Quarry, and the Post-Gen fault that cuts off the Goldstrike stock on the east side.

Igneous contributions to the NCT include Jurassic stocks and Jurassic and Eocene dikes. The largest exposed intrusion is the Jurassic (158 Ma, Mortensen et al., 2000; Bettles, 2002) Goldstrike diorite-granodiorite stock exposed in the Betze Pit. The stock is associated with lamprophyric, mafic to felsic, north-northwesterly-trending Jurassic dikes that can be seen throughout the NCT.

Small Eocene intrusions and volcanic rocks in the NCT range in age from 40 to 37 Ma. They are primarily felsic to intermediate in composition and can be seen throughout the NCT with dike exposures in most of the mining pits (Rhys, 2015).

Other Eocene magmatism includes the Emigrants Pass volcanics. The Emigrant Pass volcanics are an Eocene (38.3-36.4 Ma) andesite and dacite field in the southern section of the NCT (Henry and Faulds, 1999), approximately 5 km southwest of the Gold Quarry mine to approximately 5 km south of I-80.

Miocene magmatism is mostly restricted to the north of the NCT, just west of the Goldstrike and the Carlin mine. It consists of 15.3 Ma rhyolite laves (Henry and Faulds, 1999) that extend approximately 15 km in a northwest to southeast alignment.

1.8 Characteristics of Carlin-Type Gold Deposits

Carlin-Type deposits of Nevada are characterized by: (1) submicron gold inclusions as particles or solid solution with arsenian pyrite/marcasite rims around diagenetic pyrite, (2) hosted in impure carbonate rocks of a Paleozoic passive margin, (3) alteration consists of decalcification, silicification, argillization, and gold-enriched sulfidation of reactive iron, (4) structural and stratigraphic control of deposits, and (5) high Au/Ag ratio of ore (Cline et al., 2005; Teal and Jackson, 2002).

Alteration of Carlin-Type gold deposits has been studied extensively along the Carlin Trend (Hausen and Kerr, 1968; Radtke, 1985; Kuehn, 1989; Bakken, 1990; Teal and Jackson, 2002; Cline et al., 2005). Structural conduits, porosity and permeability has a significant effect on the level of intensity of alteration and the size of the alteration footprint. Generally, deposits in host strata with high amounts of original porosity and permeability have weaker but broad alteration

patterns, while deposits along discrete high angle faults, as the main pathways for fluid flow, have more localized and intense alteration (Teal and Jackson, 2002).

Decalcification/decarbonatization, while variable in extent and intensity, are typically the most pervasive style of alteration in Carlin-Type deposits. They are characterized by the dissolution of calcite (decalcification) or calcite and dolomite (decarbonatization). This alteration is interpreted as being the result of moderately acidic to acidic fluids flowing through permeable rock, reacting with carbonates and dissolving the calcite or dolomite from the limey mudstones (Teal and Jackson, 2002).

Silicification generally co-occurs with decalcification. Silicification is typically less intense but more pervasive when fluid flow was spread-out along porous and permeable stratigraphy. This is in contrast with structurally controlled deposits that likely experience focused fluid flow along faults. In this case, silicification is typically localized and intense (Teal and Jackson, 2002).

Argillic alteration is the result of moderately acidic fluids reacting with detrital clays and potassium feldspar (Cline et al., 2005). Alteration clay minerals consist of montmorillonite, kaolinite, and illite.

1.9 Geology of the Arturo Project

The Arturo project is a three-phase mining plan in the northern-most Carlin-Trend that includes a layback in the north of the historic Dee pit (Phase 1), the Arturo pit (Phase 2), and the South Arturo pit (Phase 3) (Figure 3).

1.9.1 Structural and Intrusive Geology

The following description of the Arturo Project structural and intrusive geology is based on personal communication with Barrick Goldstrike geologists.

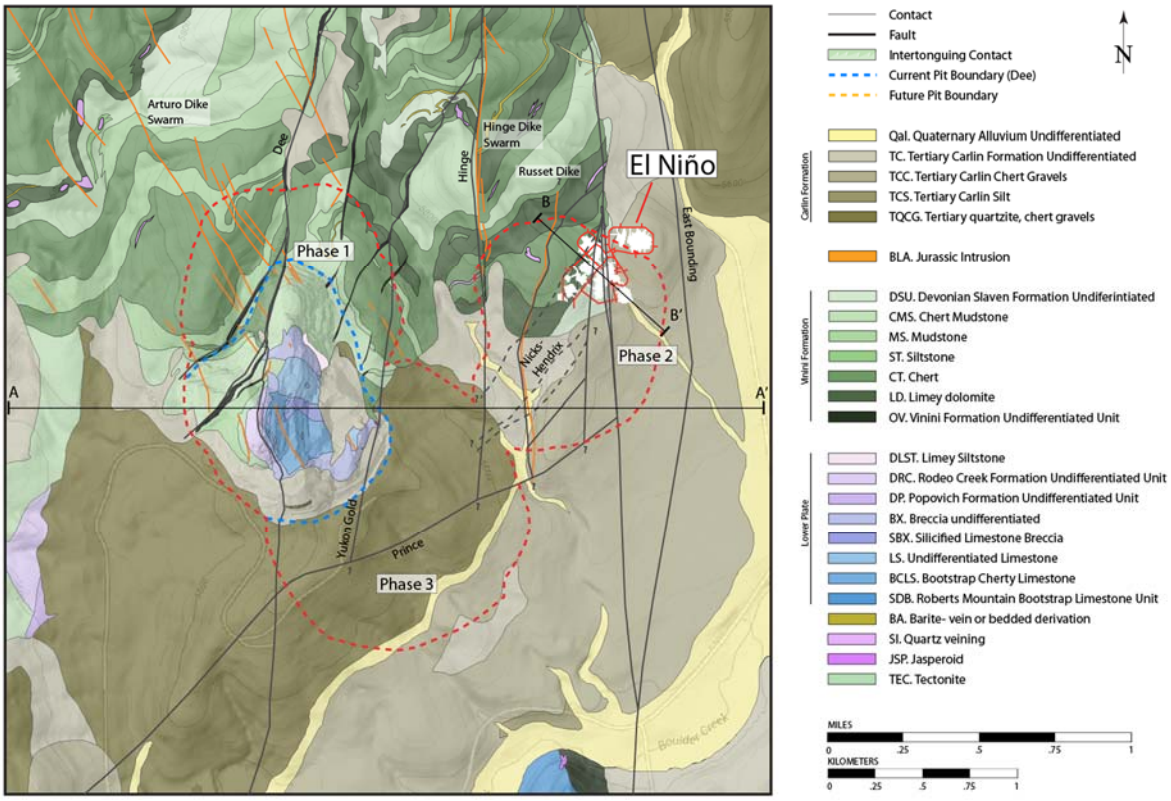

Figure 3. Geologic map of the Arturo mine property. The blue outline shows the historic Dee pit. The yellow dashed line outlines the three phases of the Arturo project that includes; Arturo (Phase 2, east), South Arturo (Phase 3, south) and Dee (Phase 1, west), in relation to the El Niño mine. The Bootstrap Mine is at the southern edge of the map. Purples and blues represent lower plate, greens are upper plate and browns are Tertiary Carlin Formation. Modified from Dobak and Chadwick, Carlin Basemap, 2000.

Phase 1 and 2 of the Arturo Project are separated by a horst block approximately 500 meters wide. The west side of the horst block has several hundreds of meters of offset on a high-angle normal fault running through the Dee mine that dips to the west called the Dee fault. To the east is a series of north-south striking, high-angle normal faults that dip to the east and gradually step down to the east in a sequence of subsequently lower faults (Figure 4). East Bounding fault is the furthest east and marks the end of the known mineralized zone. These north-south striking faults have been interpreted to cut all other faults and folds (in most cases) and are consistent with the geometry of Tertiary-aged normal faults in the NCT (Rhys et al., 2015). While most of these faults cut mineralized faults, and are not mineralized themselves, the Dee fault is mineralized. It is

thus possible that the Dee fault is slightly older than the other extension related faults from the Tertiary.

Within the horst block, between Dee fault and East Bounding fault, is a gentle anticline (Figure 7). Unfolding of this anticline may rotate Dee fault and other north-south faults at appropriate angles to be earlier thrust faults. Figure 4 shows a high-angle thrust fault just east of Dee fault that could be part of this thrust system. It may be that Dee fault has been reactivated as a normal fault after thrust faulting.

The Prince fault is found in the east and southeast of the Arturo Pit. Other faults that are part of the Prince fault system include the Nicks, Hendrix and Hend-Nicks faults, just northwest of Prince (Figure 3). The Prince fault is a normal fault that dips to the southeast, but may also be a reactivated thrust fault. The Prince fault zone, including Nicks, Hendrix, and Hend-Nicks faults (Figure 7), is second only to the Roberts Mountain Thrust shear zone as host to gold at Arturo and El Niño.

All intrusions of the Arturo project discovered so far are Jurassic in age. The Arturo dike swarm trends northwest to southeast from northwest of the Dee pit, through the Dee pit and likely terminates at the Prince fault zone. It is also possible that this series of dikes intruded in a fault zone that was a conjugate to the Prince fault zone. The Hinge dike swarm and Russet dike are north-south trending on the west side of the Arturo Pit and slightly within (Figure 3). The orientation of these dikes is consistent with the proposal that some of the north-south normal faults are older reactivated faults and hence were present during mineralization.

1.9.2 Stratigraphy

The sedimentary stratigraphy at the Arturo Project, in general, consists of a sequence of Lower Paleozoic deep-water siliceous rocks thrust over a sequence of Lower Paleozoic shelf and

slope-facies carbonate rocks, all of which are capped by loosely consolidated Tertiary clastic to volcaniclastic rocks (Figure 5). The following are formations of the Arturo Project deposits with Barrick Goldstrike naming conventions and descriptions.

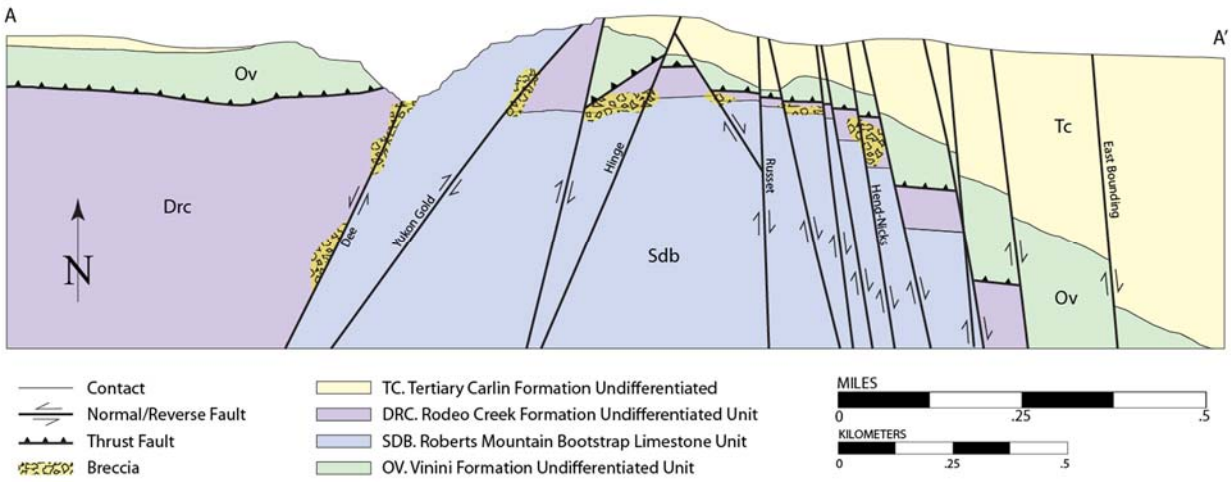

Figure 4. Schematic cross-section through the Arturo property (Figure 3) created from the Barrick Goldstrike 3-dimentional model of Arturo and showing the horst block that separates the Dee mine from the Arturo mine and the high angle faults that host the Dee deposit in the west and step down to the east as each fault offsets the units deeper and deeper. The contact between Tc and Ov is an unconformity.

The stratigraphically highest unit is the Tertiary Carlin Formation. It consists of poorly consolidated tuffaceous lacustrine sediments and gravels that varies in thickness from 0m on the west side of the Arturo pit to >300m east of the pit. The three main units of the Carlin Formation are: 1) upper, unconsolidated lacustrine silt and sands that typically consist of a significant amount of ash and tuff; 2) middle, variably consolidated ash-fall tuffs with $^{40}Ar/^{39}Ar$ ages from 14.3 to 15.3 Ma (Fleck et al., 1998) and; 3) a basal gravel unit that contains clasts of Paleozoic cherts, silicified mudstones/siltstones, jasperoid, and local igneous dike fragments that unconformably overlie Devonian rocks of the Slaven Formation.

The Devonian Slaven Formation is a highly deformed series of thinly bedded brown, black, green, and grey cherts with local beds of barite, limestone and mudstone.

The Silurian Elder Formation consists of three major units. The upper unit consists of an intertonguing series of black, white, and grey siliceous mudstones with cherts. The middle unit is a micaceous, olive to red sandstone and siltstone that may contain lenses of grey to black mudstone and cherts. The basal unit is a green chert named the Cherry Springs Chert.

The Ordovician Vinini Formation is a highly sheared and folded series of mudstones, siltstones, cherts and jasperoid. It is divided into the Upper and Lower Vinini. The Upper Vinini is further divided into three subunits. The upper subunit of the Upper Vinini is a silicified brown limestone and unaltered light-grey limestone that is between 0 and 7m thick. The middle subunit is a 15-20m thick series of black to dark brown thinly bedded cherts and interbedded mudstones. The basal subunit is a sequence of bedded cherts approximately 9-15m thick over a series of black thin bedded siltstones, mudstones, and cherts that is approximately 100-150m thick (Trotman, 2009).

The Lower Vinini sits directly above the Roberts Mountain Thrust and thus is highly sheared and deformed. The upper portion of the Lower Vinini is dominated by mudstones, siltstones with local grey chert lenses. This is stratigraphically above a sequence of light grey mudstones with black chert and local siliceous mudstones. The basal series is a thick section of mudstones and siliceous mudstones with black chert lenses.

The Roberts Mountain Thrust separates the upper and lower plates, between the Vinini and Rodeo Creek Formation, and is the reason that older, deeper marine sedimentary rocks of the Slaven, Elder and Vinini are structurally higher than the shallow marine Rodeo Creek, Popovich, Bootstrap and Roberts Mountain Formations.

The Devonian Rodeo Creek Formation is the uppermost formation of the lower plate. The upper unit is called the upper argillite and consists of thinly bedded silicified black mudstones with interbedded mudstones, siltstones, and cherts. The Bazza Sands lie below the upper argillite

and are comprised of interbedded siltstones, calcareous siltstones, and muddy siltstones. The lowermost unit is the Lower Argillite. This unit is a black, silicified mudstone with minor siltstones, mudstones, and cherts and unconformably overlies the Devonian Popovich Formation.

The Devonian Popovich Formation is a series of calcareous mudstones, muddy limestones, debris flows and turbidite of a slope and toe-of-slope facies sequence (Armstrong et al., 1997).

The Silurian-Devonian Bootstrap Formation consists of massive, oolitic and peloidal limestones that are locally fossiliferous. The thickness of this unit at the Arturo pit is unknown.

The Silurian-Devonian Roberts Mountains Formation is thought to be time equivalent to the Bootstrap Limestone. Within the Arturo Project it is only present to west of the Dee fault. It primarily consists of light to dark gray bedded to laminated limestone with local interbedded debris flows (Trotman, 2009).

The Hanson Creek Formation is the name given to a massive dolomite that was intersected in several drill-holes on the west side of the Dee fault. Little is known about this formation and it has not been seen in drill-core from the east of the Dee fault.

1.9.3 Ore Distribution

Ore distribution at the Arturo Project can be divided into 5 mineralized zones, or ore-body systems, that include Deep North, Southwest Dee, South Arturo, Hinge and Button Hill (Figure 6). The overall shape of ore in the Bootstrap district (Figure 2) is linear from south to north starting at the Tara, through the Bootstrap, Capstone and South Arturo. It then Y's at South Arturo, around the Arturo horst block to Southwest Dee and Deep North in the west, and Hinge and Button Hill in the east (Figure 6).

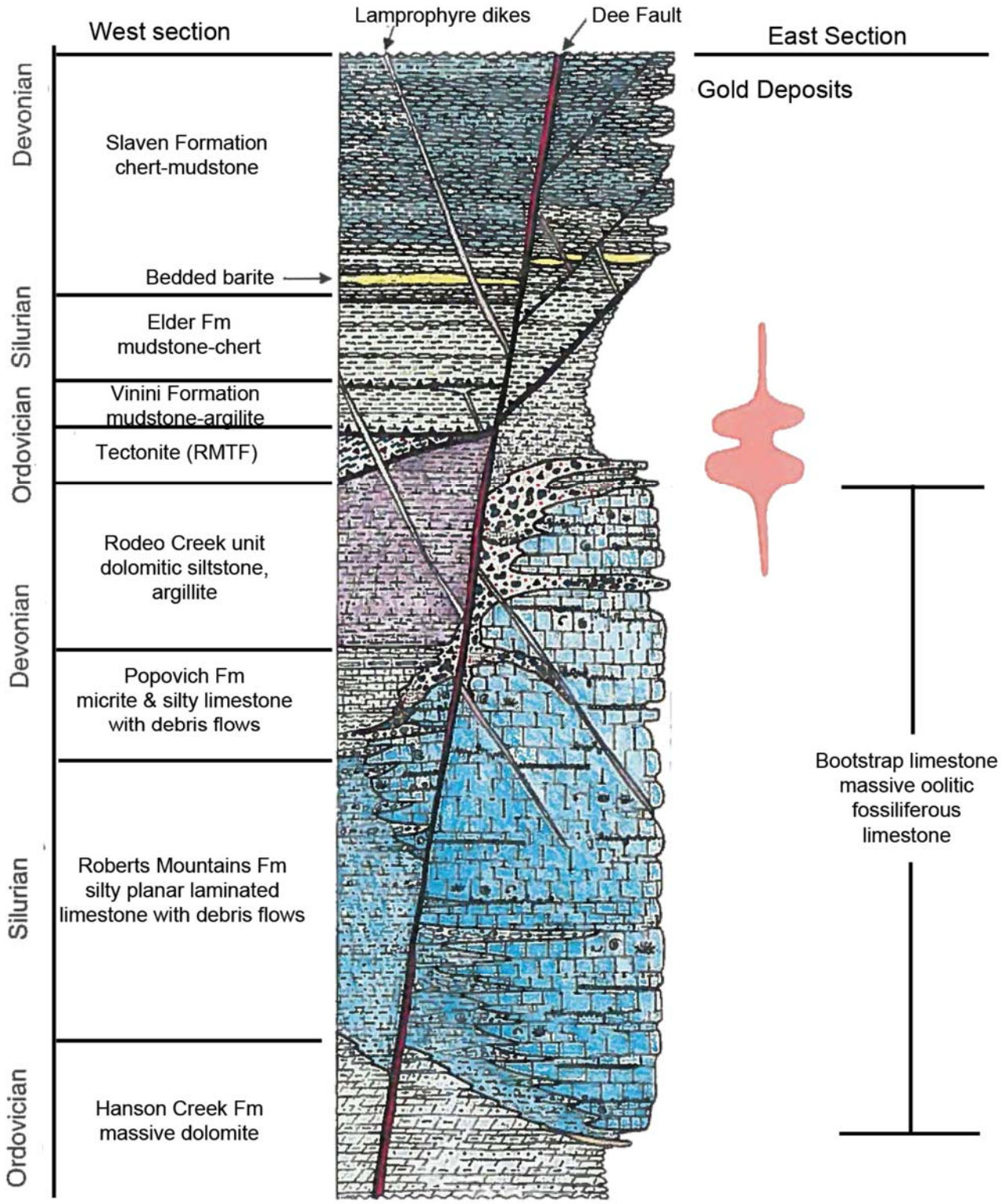

Figure 5. Stratigraphic column from the nearby Storm mine. Arturo and Button Hill mines are east of the Dee Fault and so the relevant portion of this figure to those mines is the column to the right of the Dee Fault. Dobak et al., 2002

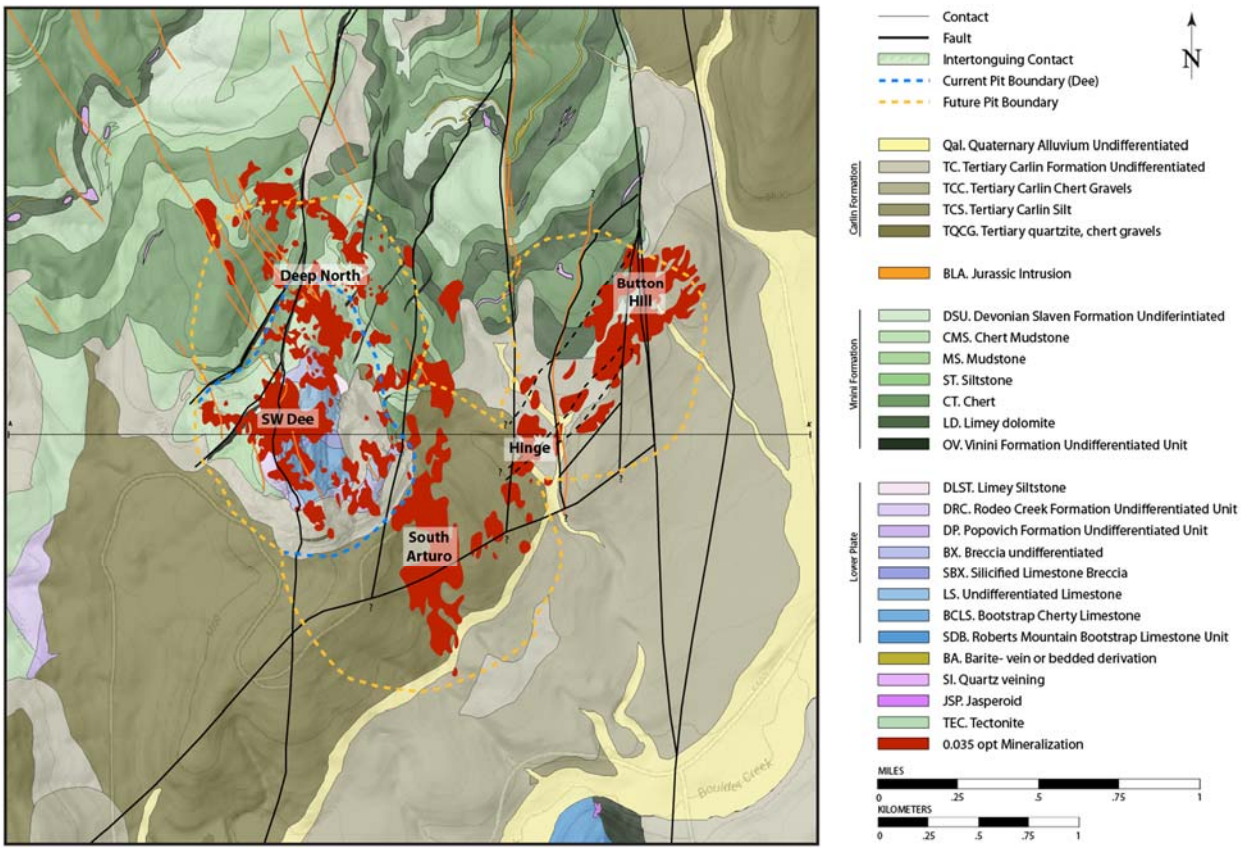

Figure 6. Geologic map of the Arturo mine property that shows the 5 major gold deposits (>0.035 opt, projected to the surface). Modified and digitized from Dobak and Chadwick Carlin Basemap, 2000. Ore deposit outlines from Valliant, 2015.

1.9.3.1 Dee Deep North

The Dee Deep North ore-body system is approximately 180m x 45m x 45m and hosted in a silicified, sulfide rich, polylithic dissolution collapse breccia body at the upper contact of the Bootstrap limestone. The ore is controlled by north-northeast trending high angle normal faults and southwest dipping low angle thrust faults. The Dee layback, or Phase 1, is designed to exploit this ore system (Valliant et al., 2015).

The Storm mine consists of a deep (250-500 m below the north high-wall of Dee), high-grade, low tonnage gold-silver deposit with a production plus proven and probable reserve of approximately 3.2 M oz Au, as of 2002 (Dobak, 2002). The Storm mine was designed to exploit

three ore-bodies that are collectively known as Dee Deep North. Dee Deep North consists of the 49er, End Zone and Discovery Zone ore-bodies. Each of the ore bodies are hosted in tectonic breccias, associated with high angle normal faulting, and dissolution collapse breccias, associated with the Silurian-Devonian Bootstrap limestone. Like all other gold deposits in the Bootstrap district, main-stage mineralization is Carlin-Type. This deposit, however, is also overprinted by a younger low-sulfidation epithermal Ag deposit characterized by silver-bearing quartz-sulfide-selenide veins with an apatite fission track age of 20.8 Ma and a silver to gold ratio of 4:1 (Trotman, 2009). The Storm mine is on the west side of horst block that separates it from the Button Hill deposit. The main structural control for ore forming fluids that created the Storm and Dee deposits was the Dee high-angle normal fault (Trotman, 2009).

1.9.3.2 Southwest Dee

Like other mineralization at the Dee mine, the Southwest Dee ore system is controlled by the high angle, north-northwest trending Dee Fault zone. The ore is hosted within both tectonic and dissolution collapse breccia with a 100m x 30m x 45m geometry. Part of this ore body is exposed in the southwest high wall in the Dee pit (Valliant et al., 2015).

1.9.3.3 South Arturo

Approximately 60 m southeast of the Dee pit is the South Arturo ore body system. It lies beneath approximately 245 m (800 ft) of Tertiary Carlin Formation (Cope et al., 2008) and 180 m (590.5 ft) of waste rock from the historic Dee mine. Ore at South Arturo is mostly oxidized and hosted in silicified, dissolution collapse breccia. The ore zone is approximately 520m x 115m with the long axis trending north-south and dipping gently to the south. Gold values range from 0.2 to 35 g/t and average 2.0 g/t. At grades higher than 2.06 g/t Au the silver to gold ratio is about 1:1;

though, lower grade can be as high as 5:1 (Valliant et al., 2015). Resources at South Arturo were estimated to be 40.4 t (1.3 M oz) Au as of 2008 (Cope et al., 2008).

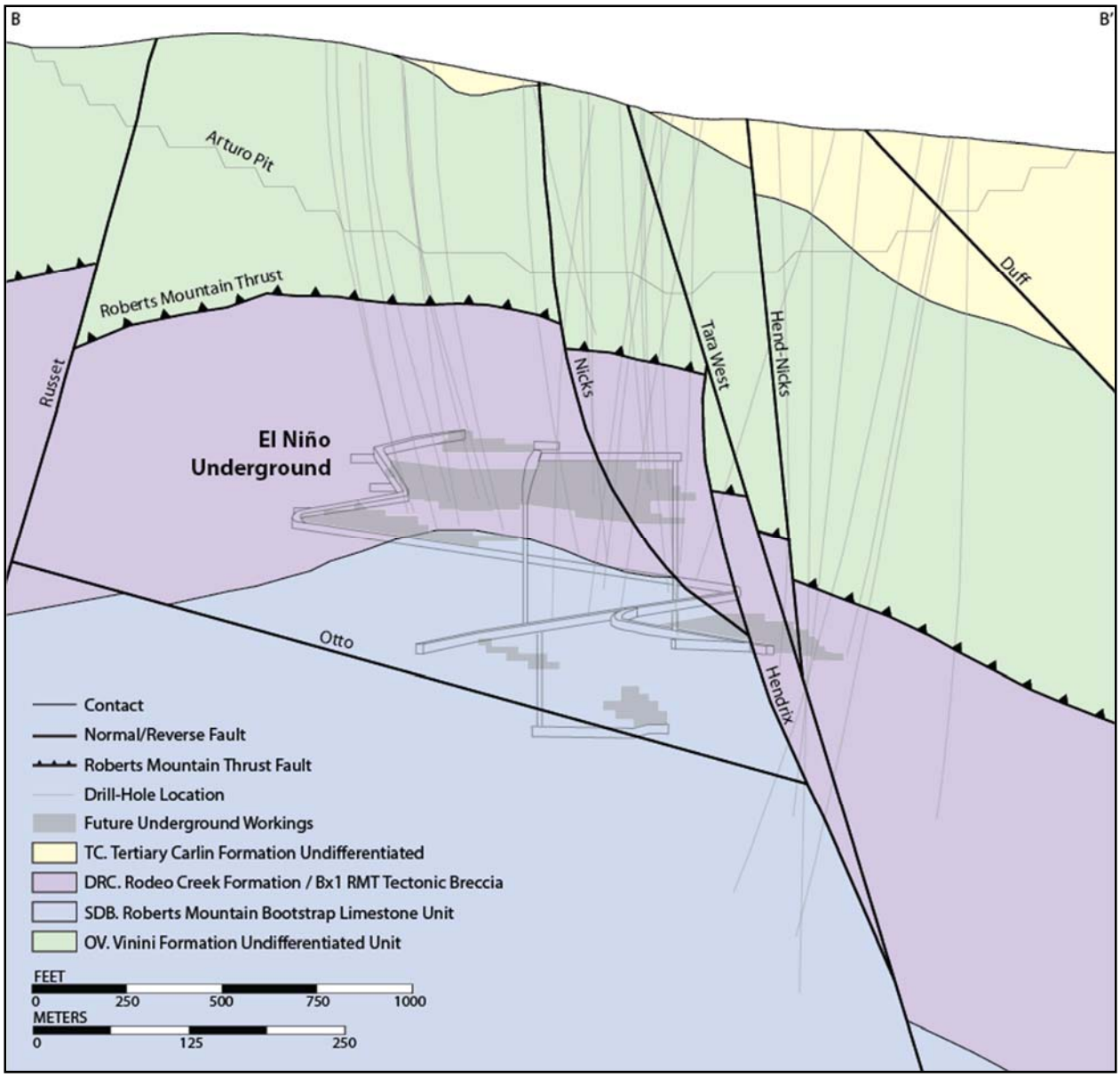

Figure 7. Cross-section through the northeast of the Arturo pit going from NW (B) to SE (B') created from the Barrick Goldstrike 3-dimentional model of Arturo. It illustrates the depth and location of the El Niño underground mine relative to the four major formations. This figure also displays the names of each fault, as well as the location of the drill-holes that were used to make the geochemical contours in Chapter 4. Important to note is that the Rodeo Creek Formation is mostly what I have identified as Bx1 Roberts Mountain thrust tectonic breccia.

1.9.3.4 Hinge

The Hinge zone lies between the Button Hill and South Arturo ore bodies. It is an oxidized ore zone approximately 425 m long and 90 m wide that trends to the north. Mineralization is hosted in dissolution collapse breccias on the upper contact of the Bootstrap limestone and Rodeo Creek and silicified breccias of the Rodeo Creek and Popovich Formations. The major control on fluid flow was the Hinge fault, a normal fault that dips steeply to the east and is thought to be an extension of an ore controlling fault at the Bootstrap pit to the south (Valliant et al., 2015). Mining of the Hinge ore body will be completed during the South Arturo (Phase 3) of the Arturo Project.

1.9.3.5 Button Hill

The Button Hill ore body, also referred to as West Button Hill, is a north-northeast trending ore body that lies mostly within the upper contact of the Bootstrap limestone and lower Rodeo Creek mudstone. Mineralization is hosted within tectonic breccias of the Roberts Mountain thrust, and dissolution collapse breccias at the top of the Bootstrap Formation. However, no mineralization has been discovered below the underlying unaltered limestone. The presence of unaltered and unbrecciated limestone in drill-core usually marks the end of a drill-hole. The zone of mineralization is approximately 600 m long, 120 m wide and 15 m thick. Major controls for mineralizing fluid flow are high-angle normal faults and a north trending anticline. The Arturo pit mines ore from the Button Hill mineralized zone, as will El Niño underground (Valliant et al., 2015).

CHAPTER 2 - METHODS

2.1 Core Logging

Representative core samples from holes that intersected the proposed El Niño underground mine, within the Button Hill Au-Ag deposit, were selected and re-described for the purpose of identifying and delineating breccia-types associated with Au-Ag mineralization. Drill-core from hole BD15-052 was first selected because it was recognized by Barrick Goldstrike to intersect many of the breccia types within the Button Hill ore body. Once a number of breccia "types" were differentiated, the Barrick Drill-Core Photo Library was searched for representative core samples of breccia types and ore zones. A total of 8 holes out of 33 in the El Niño area were selected and retrieved from the Core Laydown Yard, logged, and sampled for hyperspectral analysis, selective geochemical analysis and thin section creation. The remaining cores were logged from images from the 'Core Photo Library.'

2.2 Three-Dimensional Modeling and Data Analysis Software

Vulcan 3D mining software by Maptech was used to model the 3D geometry of major units of the Arturo stratigraphy for visualization, based on drill hole data and models created by Barrick Goldstrike geologists.

A database was created for whole-rock geochemistry results and linked to the drill-hole three-dimensional positioning of 135 drill-holes to create cross-sectional interpretations of geochemical and mineralogical geometry from which to interpret mineralizing fluid flow progression.

IoGAS geochemistry software by Reflex was used for analyzing and visualizing the whole-rock geochemical, LECO™, assay, and quantitative hyperspectral mineralogical data by creating scatter plots, box plots, 3D distribution plots, down-hole plots, and a principal component analysis.

ENVI, Halo Manager and View Spec Pro hyperspectral software packages were used for selecting and displaying spectra from samples analyzed by Corescan hyperspectral company and TerraSpec Halo spectrometer.

Coreshed is a portal created by the company Corescan that allows access to a centralized database for all hyperspectral core data, images, mineral maps and assay logs. Coreshed was used to store and retrieve all hyperspectral data and to visualize mineralogical results with high resolution images of core and assay data from splits of the core.

2.3 Geochemistry

2.3.1 Sample Preparation

Samples from reverse circulation and core were prepared and selected by Barrick Goldstrike and were analyzed prior to this study. Samples from reverse circulation (RC) drill-holes were taken from the chips created during drilling. Diamond drill-core was sampled by splitting the core, preserving half and sending the other half to the Barrick Assay Lab for Au ± Ag Assay and LECO™, and to ALS for whole-rock geochemistry. A total of 9,664 samples from 5, 10 and 20 ft. intervals over 111,003.5 ft., and 21 selective samples over 10.4 ft. were analyzed for whole-rock geochemistry. 23,467 samples over 120,881.2 ft. at mostly 5 ft. intervals were analyzed using fire assay method for Au ± Ag. LECO™ analyses were completed on 1,898 samples over 34,969 ft. at 5 ft. and 20 ft. intervals.

2.3.2 ICP-MS and ICP-AES

ME-MS61m is a 48-element, two-step package from the company ALS involving initial sample (0.250 g prepared) decomposition with a hydrofluoric, nitric, perchloric acid digestion and HCl leach (4-acid digest). The solution is made up to a final volume of 12.5 mL with 11 % hydrochloric acid and homogenized. The sample digest is analyzed by inductively coupled plasma-atomic emission spectrometry (ICP-AES) or inductively coupled plasma-mass spectrometry (ICP-MS) for all 48 elements except mercury (Li, Be, Na, Mg, Al, P, S, K, Ca, Sc, Ti, V, Cr, Mn, Fe, Co, Ni, Cu, Zn, Ga, Ge, As, Se, Rb, Sr, Y, Zr, Nb, Mo, Ag, Cd, In, Sn, Sb, Te, Cs, Ba, La, Ce, Hf, Ta, W, Re, Tl, Pb, Bi, Th and U) (ALS, 2009).

2.3.3 Mercury

Due to the high temperature (185°C) of the four-acid digestion, significant amounts of mercury can be lost by evaporation. Use of the lower temperature aqua regia digestion (115°C) prevents this evaporation allowing for more accurate results (ALS, 2009).

A prepared portion of the same sample as above is digested with aqua regia in a graphite heating block. After cooling, the resulting solution is diluted to 12.5 mL with deionized water and mixed well. A portion of the sample is treated with stannous chloride to reduce the mercury. The resulting mercury is volatilized by purging with an inert gas, such as argon or nitrogen, and measured by Atomic Absorption Spectrometry (ALS, 2009).

2.3.4 Fire Assay and LECO™ Analysis

Fire assay for Au and Ag, and LECO™ analysis for C and CO_3 were performed at Barrick Goldstrike's assay and LECO™ labs by Barrick lab employees. Assay is completed by heating the sample with additives which separates metals from the host rock. LECO™ method uses

proprietary methods of combustion and infrared spectroscopy for identification and quantification of organic carbon and infrared spectroscopy for identification and quantification of carbonate.

2.3.5 Grant Isocon and Enrichment Factor Score

Enrichment Factoring is a variation of the Gresens' (1967) and Grant's (1986; 2005) methods. In hydrothermally altered rock, especially when silicified, changes in the mass of the rock can distort geochemical results by 'diluting' the whole-rock and giving the geochemistry of the rock the appearance of overall depletion. The Grant isocon method resolves this issue by looking at an altered sample (or median of a large sample set) contrasted with the unaltered equivalent. The Enrichment Factoring method is designed to resolve dilution issues and determine changes in mass over a larger dataset by quantifying the deviation from the isocon (see below) of each element in each sample, as well as the overall change in mass of each sample.

The unaltered sample was created by compositing and averaging Rodeo Creek Formation samples that appeared to be unaltered in hand samples and that contained Au + Ag values at or below average crustal abundance in the Earth's crust (≤0.0011 ppm Au, ≤0.070 ppm Ag; Barbalace, 2017). Using these parameters, a total of 347 assay samples were selected for Au and Ag values. Of the depth intervals that correlated with the 347 assay samples, 15 geochemistry samples and were selected to represent the range of unaltered Rodeo Creek Formation. Carbon and CO_3 were not calculated due to insufficient LECO™ analysis from the unaltered samples.

In all samples, Al, Ti and Zr have consistent ratios and are interpreted to be immobile. For each of the three immobile elements, a slope through the point (x=standard, y=altered sample) and the origin (0,0) is determined and a median slope of the three determined to create the isocon (m_i).

$$m_i = \left(\frac{C_A^{Al}}{C_0^{Al}} + \frac{C_A^{Ti}}{C_0^{Ti}} + \frac{C_A^{Zr}}{C_0^{Zr}}\right)\left(\frac{1}{n}\right)$$

Where C_0 = concentration of standard (unaltered rock), C_A = concentration of the altered sample and n = number of immobile elements used.

The deviation of each element from the isocon is quantified by treating each point as a point along another isocon with origin 0,0 and defining the factor (F_0) that describes the difference between that slope and the isocon.

$$F_o = \left(\frac{C_A^x}{C_0^x}\right)\left(\frac{1}{m_i}\right)$$

Where C^x = concentration of the element. The final Enrichment Factor Score is;

$$EFS = \frac{C_A^x(n)}{C_0^x\left(\frac{C_A^{Al}}{C_0^{Al}} + \frac{C_A^{Ti}}{C_0^{Ti}} + \frac{C_A^{Zr}}{C_0^{Zr}}\right)}$$

2.4 Infrared Spectroscopy

Molecules absorb electromagnetic radiation at frequencies that are characteristic of their vibrational modes. Infrared spectroscopy utilizes this fact to identify minerals by introducing infrared radiation to the sample and measuring the wavelength that was absorbed (Clark, 1999). The following two wavelength bands of very-near infrared (VNIR) and short-wave infrared (SWIR) were used to identify iron-oxides, hydroxides, hydrous minerals, carbonates, and hydrous or fluid inclusion-bearing silicate minerals.

2.4.1 Corescan Infrared Spectroscopy and Imaging

Corescan's hyperspectral core imager, the Mark III (HCI-3) was used by a Corescan technician to analyze 594.6 ft. from 6 drill-holes and 14 grab sample from 9 drill-holes at their

mobile facility in Denver, Colorado. All hyperspectral samples were chosen for this study and analyzed for this purpose.

Corescan's HCI-3 operates across the VNIR and SWIR portion of the electromagnetic spectrum with 3 spectrometers (VNIR, SWIR-A, SWIR-B) and a total spectral range of 450nm to 2500nm at a spectral resolution (FWHM) of 3.5nm (Table 1). This wavelength range covers the spectral region where a wide range of fundamental rock-forming and hydrothermal alteration minerals exhibit specific, unique combinations of spectral absorption features. The HCI-3 is combined with a high resolution RGB camera and a 3D laser profiler to obtain a continuous measurement of core infrared reflectance, color variations, surface features, textures and shape.

The data is evaluated by Corescan hyperspectral specialists and algorithms applied using specialized software to identify minerals and create false color mineral maps of the core.

Table 1. HCI-3 system specifications from http://www.corescan.com.au/services/the-corescan-system.

Spectrometers	VNIR, SWIR-A, and SWIR-B
Spectral Range	450-2500 nm
Spectral Resolution	~4nm
Spatial Resolution	0.5mm square pixels
RGB Image Resolution	50 µm
Height Profile Resolution	20 µm

2.4.2 TerraSpec Halo Infrared Spectroscopy

The other infrared spectroscopy was completed using the handheld TerraSpec Halo Mineral Identifier for spot analysis. The Halo has a range of 350-2500 nm and an on-board

spectral library it uses to assist in mineral identification with 11 minerals in the VNIR and 142 minerals in the SWIR with over 700 spectra collected using the Halo.

Scalars are properties of mineral crystallinity or composition that are evaluated by the Halo on-board software based on spectral metrics and corresponding mineral identification. For example; the position of the Al-OH, Mg-OH, and Fe-OH absorption features are recorded for minerals that are known to have those specific bonds. The exact wavelength of these absorption features is used to establish geochemical parameters related to mineral composition or crystallinity.

The following are the system specifications for the TerraSpec Halo (Table 2).

Table 2. TerraSpec Halo Mineral Identifier specifications from https://www.asdi.com/products-and-services/terraspec/terraspec-halo-mineral-identifier#!

Spectral Range	350-2500 nm
Spectral Resolution	3 nm @ 700 nm
	9.8 nm @ 1400 nm
	8.1 nm @ 2100 nm
Spot Size	~9.6mm

CHAPTER 3 – GEOLOGY RESULTS

3.1 Lithologic Descriptions of El Niño

Figure 8. Arturo pit looking north-northwest. The blue line represents the top of the exposed Bootstrap Formation, green is the approximate top of the Rodeo Creek Formation, yellow is the top of the Vinini Formation, above which is the Carlin Formation. The orange line shows where the Russet Dike outcrops in the Arturo pit.

The following results are from outcrop, core and thin section observations from the proposed El Niño underground mine, with emphasis on samples that are representative of variations in breccias. Classification of mudstones, marls, and limestones are based on the classification scheme in Pettijohn (1975), which uses the clay to calcite ratio in the samples (Figure 9). Clay to calcite ratios were determined by estimating modal percentages in thin section. Classification of shale was based on organic content >15%. Organic content of 10-15% were referred to as "carbonaceous," and organic contents 1-10% were referred to as "carbon-bearing." Breccias are named based on the breccia descriptive scheme from Jackson (2008), a modified

naming scheme from Davies (2002). The breccia internal organization classification is based on Davies (2002).

Unlike the stratigraphy at the Dee mine to the west that consists of approximately 7 formations (Figure 5), the stratigraphy of Arturo (Figure 9) and El Niño consists of only four known formations. The following is a description of the four formations that include the Tertiary Carlin Formation, Ordovician Vinini Formation, Devonian Rodeo Creek Formation, and the Silurian-Devonian Bootstrap Formation, as well as the Russet diorite dike at the Arturo and El Niño mines.

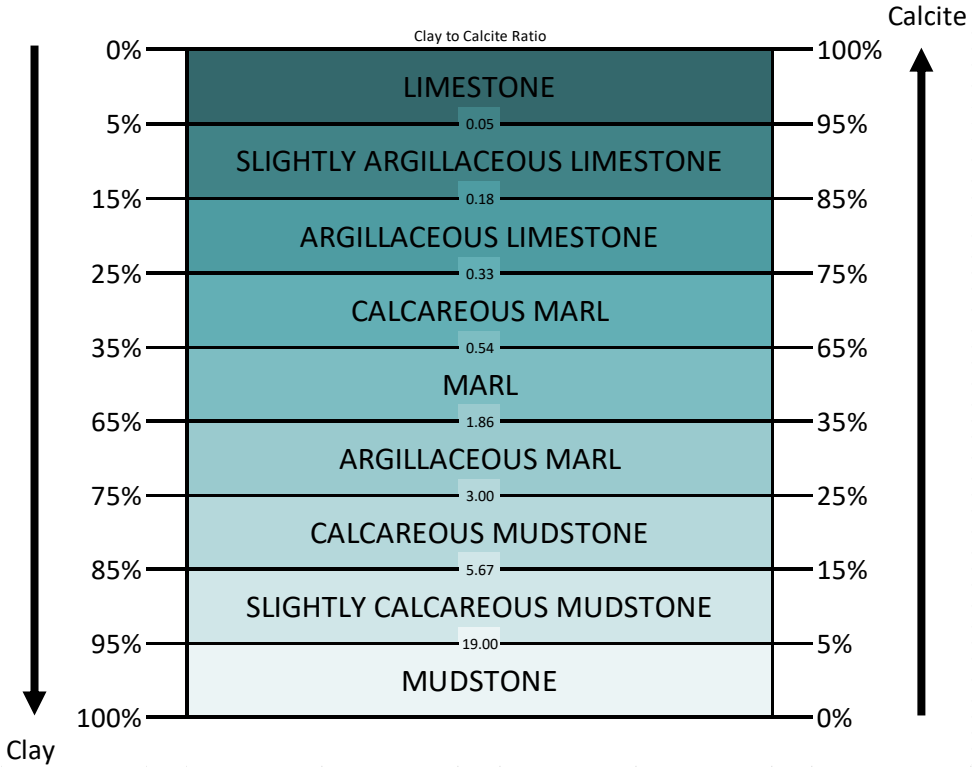

Figure 9. Mudstone, marl, and limestone classification scheme from Pettijohn, 1975.

3.1.1 Tertiary Carlin Formation

The stratigraphically highest unit in the Arturo pit is the Tertiary Carlin Formation. There are two major lithologies of the Carlin Formation; the Tertiary Gravels (TG) and Tertiary Ash

beds. On the east side of the pit, the Carlin Formation is approximately 90 m (300 ft.) thick (Figure 8). It dips to the east and steps down to the east in progressively downdropped segments separated by young high-angle normal faults. The gravels are largely unconsolidated, clast supported, angular to sub-rounded, cobble to sand sized weathering product of the underlying Vinini Formation cherts and mudstones. Colors of the gravels include; white, gray, tan, brown and orange. The gravels are often interbedded with ash lenses and occasionally well laminated lacustrine silts and muds. In core samples, thickness of the gravel unit ranges from 1 to 60 m and reach depths of up to 95 m near El Niño, but much deeper to the east.

Ash beds in the Carlin Formation are white to tan with minor to very minor lithic fragments of chert, silicified mudstone and glass and commonly intensely altered to clay. Ash beds in core range from centimeter scale to approximately 14 m thick and are found at up to 82 m depth.

3.1.2 Diorite Dike

The only dike in the pit, besides the Hinge swarm that contacts the pit in the very top of the west wall, is the Russet diorite dike exposed in the north wall. The Russet dike is approximately 1 m wide and has a general north-south orientation with very steep dip. It cuts through the center of the pit, crossing both Rodeo Creek and Vinini Formations and is offset by multiple high-angle faults.

Barrick Goldstrike geologists suggest that the Russet dike is from the same Jurassic magmatic event that created the diorite dikes in the Goldstrike pit because of the similarities in composition and textures. Diorite from Goldstrike is typically hypidiomorphic granular with plagioclase, biotite, hornblende, and quartz. It is often fine-grained and porphyritic texture at the contact between intrusion and host-rock. The Russet dike in the Arturo pit is strongly altered to

quartz + sericite + pyrite, with very little preserved original texture. Quartz ranges form 10-25% (original quartz unknown) with 55-75% fine-grained, shreddy mica, 3-20% pyrite after mica, and 5-20% pore space (Figure 10).

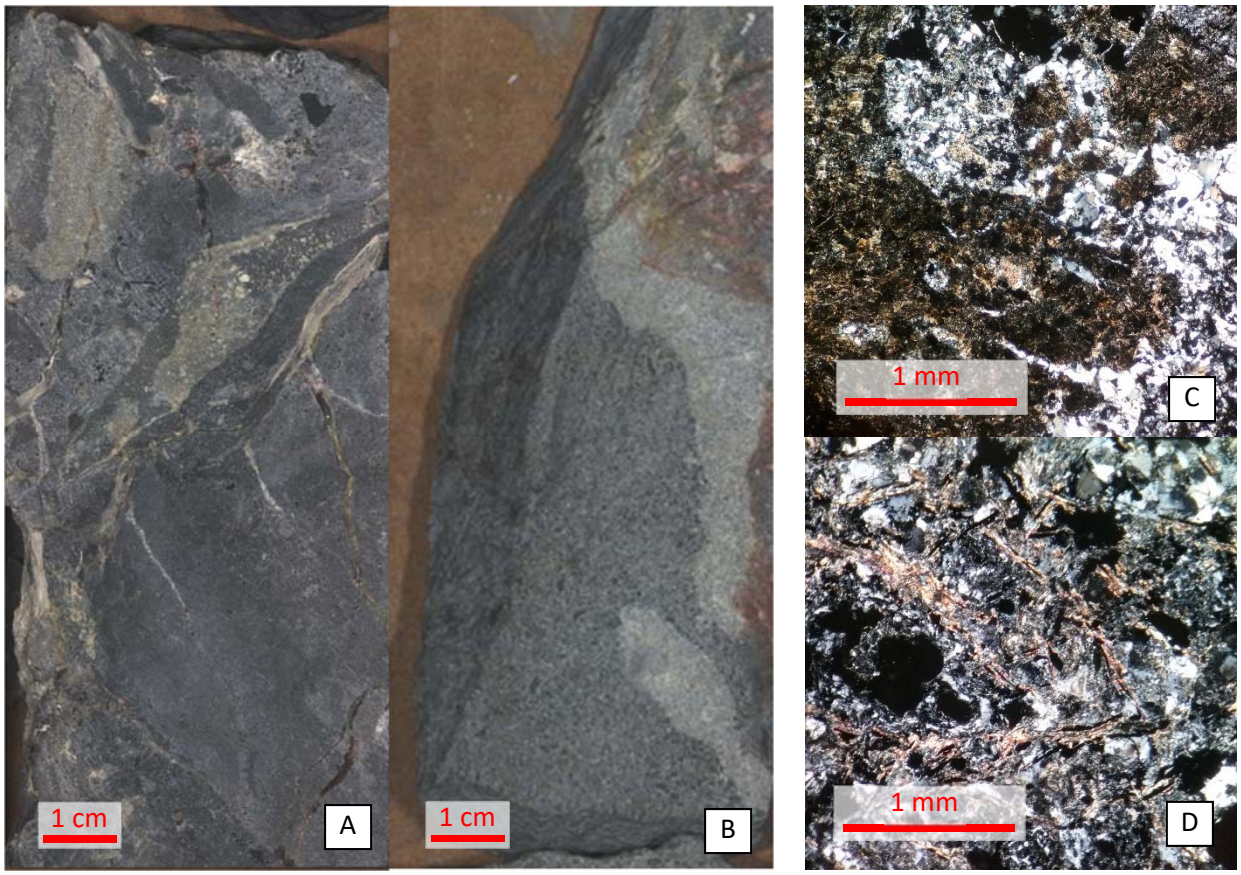

Figure 10. BD14-04C_701.2 (left and upper right) and BD14-04C_706 (center and bottom right) are samples of the Russet diorite dike. Figure A is an example of small clasts (peperite?) of diorite in the upper contact of the silicified zone and unsilicified zone of the Rodeo Creek Formation. The contacts are both igneous and faulted. Figure C is the photomicrograph from that sample. Figure B is the upper contact (intrusive) of the Russet dike into the Rodeo Creek mudstone showing the chilled margin of the dike and the baked contact of the mudstone. Figure D is the photomicrograph from that sample.

3.1.3 Ordovician Vinini Formation

Identification of upper-plate Paleozoic units at El Niño, and the exact location of the Roberts Mountain thrust, is poorly defined. The major lithology of what is mapped as the upper plate is chert. It is interpreted by Barrick Goldstrike geologists that the Slaven and Elder

Formations are absent at Arturo and El Niño. Instead, all upper plate Paleozoic rocks are part of the Vinini Formation. Exposed Vinini Formation in the Arturo pit is approximately 50 m thick in the north and 60 m thick to the east where it downdrops at the Prince fault (Figure 8). It dips gently to the east and has broad overall anticlinal geometry. The Vinini chert (CT) is opaque to translucent, white, gray tan, brown, yellow, orange, red, pink, green and black in color. Laminated to medium bedded chert consists of 1 cm to 40m thick intervals, most of which are between 30 cm and 7m.

3.1.4 Devonian Rodeo Creek Formation

The Devonian Rodeo Creek Formation lies directly below the Roberts Mountain thrust. It is the stratigraphically highest unit of the "lower-plate" stratigraphy and the major host to mineralization at Arturo and El Niño. In the west side of the Arturo pit Rodeo Creek is approximately 85m thick (Figure 8). It is highly sheared and deformed with a poorly defined upper contact with overlying Vinini Formation chert. The top approximately 12m of the Rodeo Creek is oxidized and looks very similar the Vinini. Lithologies of the Rodeo Creek identified by Barrick geologists consist of mudstone (MS), limey mudstone (LM), siltstone (ST), limey siltstone (LS), argillites (AG), sandstone (SS) and minor interfingered limestones and cherts. I used a slightly different naming convention based on Pettijohn (1975) (Figure 9) and identified a variety of argillites, shales, mudstones, siltstones, sandstones, marls, and limestone.

Barrick Goldstrike geologists use term argillite to describe a thinly bedded siliceous mudstone, siltstone, and minor chert, specific to the Rodeo Creek Formation. They have interpreted this rock type, originally identified at the Goldstrike pit, to extend to the Arturo and El Niño mines. In core samples from Goldstrike, it is usually 1.5-7.5m thick laminated and "puck-shaped" light gray to black lenses of lithified siliceous oozes interbedded with mudstone.

Shale has been identified only as breccia clasts within tectonic, hydrothermal and collapse breccias. The identified shale lithology is calcareous muddy shale (Figure 11A). It consists of ~15-25% organic material, 1-1.5% pyrite (1.85-14.8 μm, subhedral diagenetic, disseminated), 1.5-3% quartz gains (14.8-37 μm, angular to subangular), 25-35% fine-grained material (clay±silt), and 10-12% calcite variably replaced by fine-grained, amorphous silica ± illite.

The mudstones of the Rodeo Creek Formation are <1 cm to >75 m thick sections of bedded (finely laminated (<0.5 mm) to thick bedded (>10 cm)) and massive gray to black fine-grained sediments that consists of <50% silt ± calcite ± organic carbon ± diagenetic pyrite. Mudstone lithologies of the Rodeo Creek Formation consist of carbonaceous calcareous silty mudstones, carbon-bearing calcareous mudstones, and sandy carbonaceous calcareous mudstones. The carbonaceous calcareous silty mudstones (Figure 11B) consist of approximately 10-15% organic material, 1-5% diagenetic pyrite (3.7-74 μm, anhedral, disseminated), 7-10% quartz grains (22-37 μm, angular to subangular), 40-50% clay±silt, 5-10% calcite replaced by silica + 5-6% white mica (3.75-5.6 μm, elongate, aligned). The carbon-bearing calcareous mudstone (Figure 11C) has 5-10% organic material, 0.25-0.5% pyrite, no original quartz, 65-70% clay±silt 10-15% calcite (variably replaced by quartz) and 5-6% illite. The sandy carbonaceous calcareous mudstone (Figure 11D) has a higher content of quartz grains (15-20%, 8.75-70 μm, angular), 40-45% clay±silt, 20-25% carbonaceous material, and 5-10% calcite variably replaced with silica ± illite.

Siltstone and limey siltstone are similar to mudstones except the presence of >50% silt. The siltson and limey siltsonte lithologies are silt and clay rich ± calcite ± organic carbon ± synsedimentary pyrite, gray to black (orange and red in oxidized zone) laminated to thinly bedded and massive, mm to 44 m-thick packages.

Sandstones in the Rodeo Creek Formation at El Niño are interpreted to be the northern expression of the Bazza sands unit found at Goldstrike. They are laminated to massive, 4.5-16.5

m-thick units of fine-grained, red, yellow, gray, black tan and brown, well-sorted sandstones with >80% quartz, clay altered feldspar, biotite and lithic clasts.

The marl lithologies, observed as clasts within breccias, are divided into carbonaceous (>10% organic material) and carbon-bearing (<10%->1% organic material) marl (Figure 12A and B). They consist of 0-1% quartz grains, 0.25-1% disseminated diagenetic pyrite, 35-57% clay±silt, and 30-40% calcite replaced by silica ± illite. The carbon-bearing calcareous marl (Figure 12C) and carbonaceous calcareous marl (Figure 12D) are like the carbon-bearing marl and carbonaceous marl (respectively) except that the clay to calcite ratio is approximately 0.38-0.47 in the calcareous marl, compared to 0.47-1.9 in the marl (Figure 9). The carbonaceous argillaceous marl (Figure 13A) has >10% organic material and a clay to carbonate ratio of 1.9-3.

Limestone intervals within the Rodeo Creek are relatively thin, cm to m scale. Usually the limestones are marls, but can contain less than 25% clays. The argillaceous limestone (Figure 13B) contains approximately 10-15% clay±silt, 78-80% calcite variably silicified, 1-1.5% diagenetic pyrite (1.85-7.4 μm, anhedral, disseminated), 3-5% organic material, and 3-5% illite (5.5-11.25 μm).

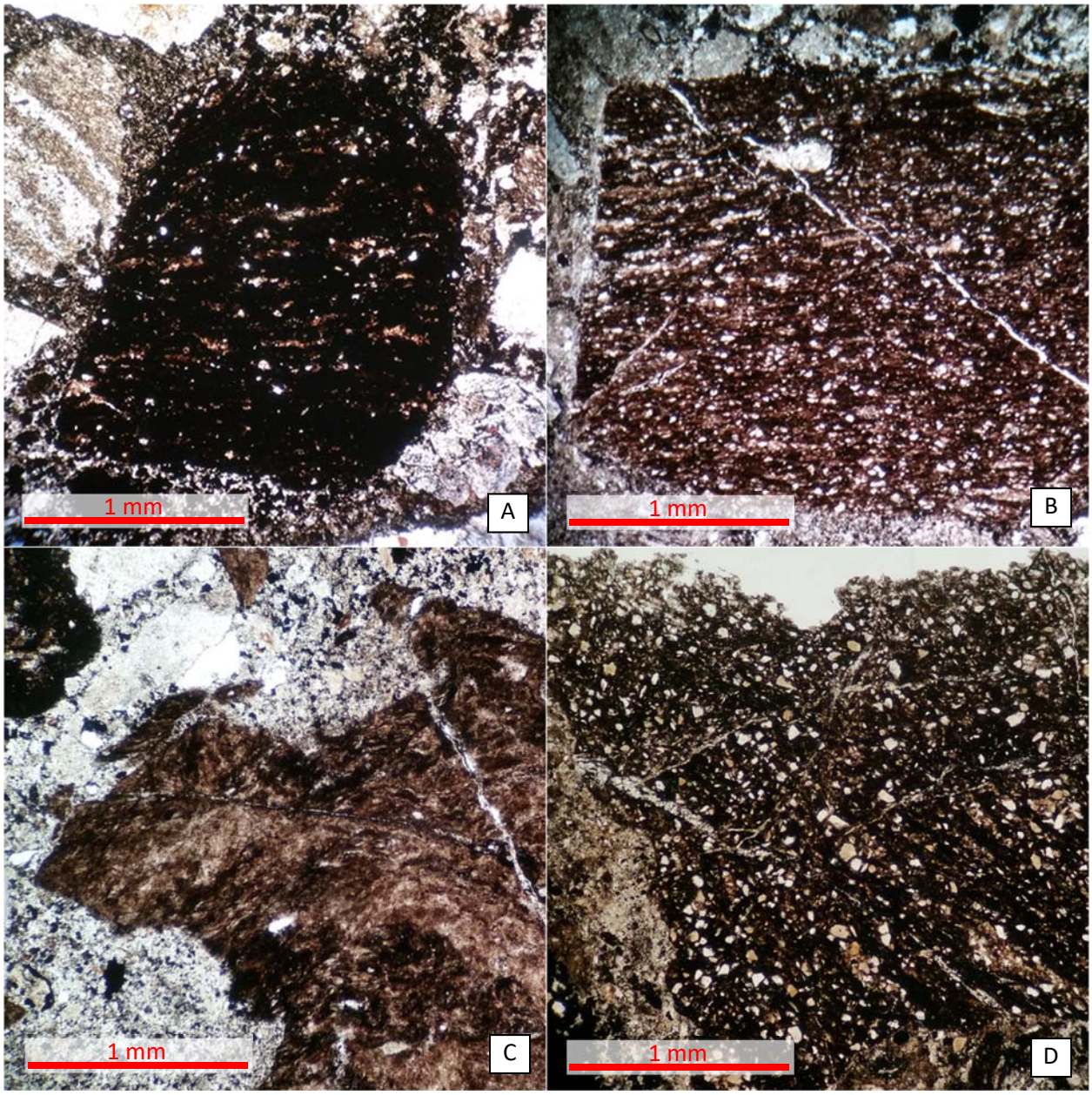

Figure 11. Photomicrographs of tectonic breccia clasts representing difference in lithologies of the Rodeo Creek Formation at the El Niño mine. A: Calcareous muddy shale from sample BD15-023A_1363.8-1364.5, an approximately 10cm thick fault breccia. B: Silicified carbonaceous calcareous silty mudstone from sample BD15-023A_1363.8-1364.5. C: Carbon-bearing calcareous mudstone from sample BD15-023A_1377-1377.8, D: Sandy carbonaceous calcareous mudstone from sample BD15-023A_1377-1377.8

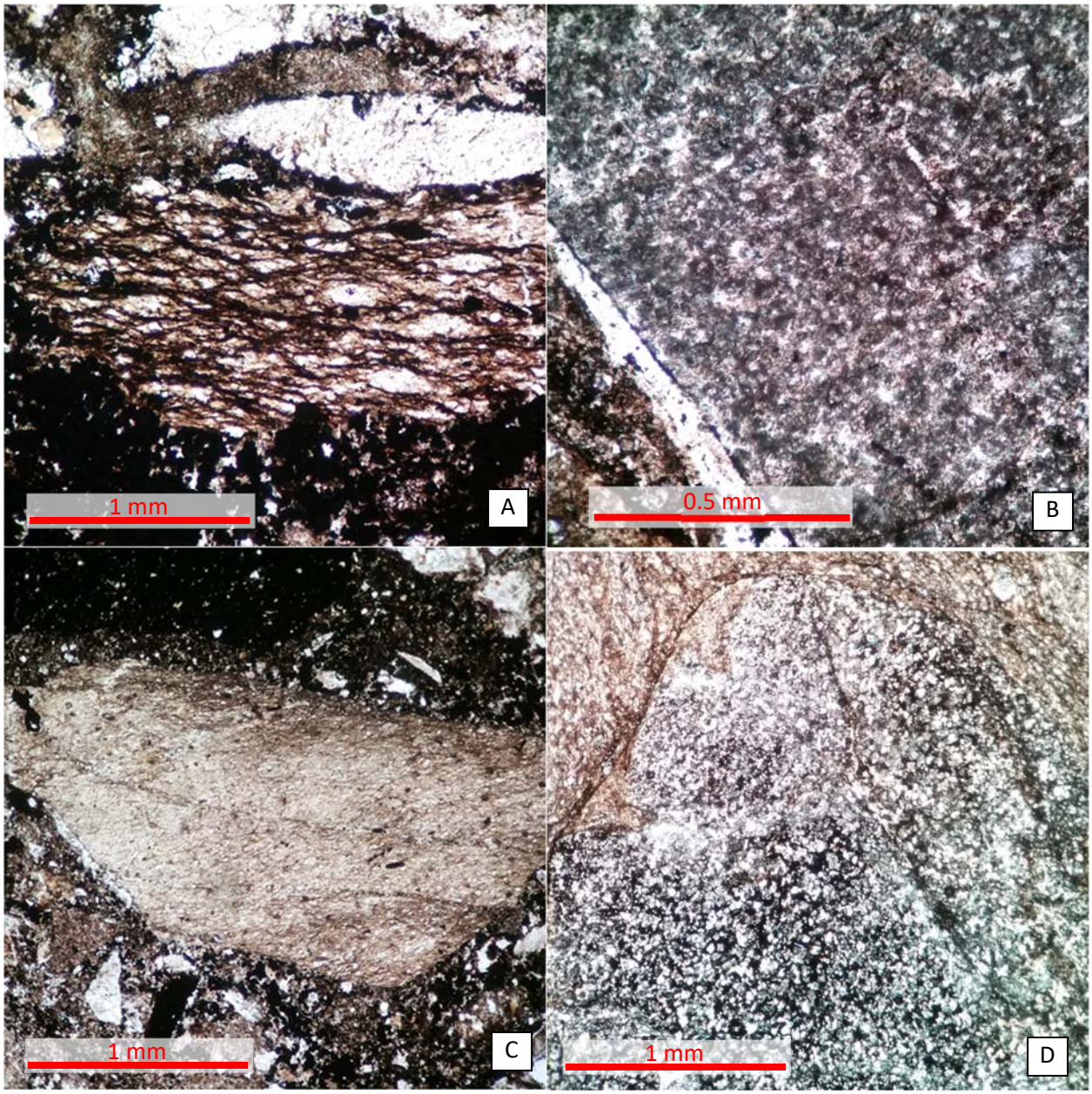

Figure 12. Photomicrographs of tectonic breccia clasts representing lithologies of the Rodeo Creek Formation. A: Undulating laminated carbonaceous marl of unknown origin from sample BD15-023A_1363.8-1364.5, a localized tectonic breccia (Bx4). B: Carbon-bearing marl from sample BD15-052_746.2, Roberts Mountain Thrust fault zone tectonic breccia (Bx1). C: Silicified carbon-bearing calcareous marl from sample BD15-023A_1363.8-1364.5 (Bx4). D: Carbonaceous calcareous marl from sample BD15-052_746.2 (Bx1).

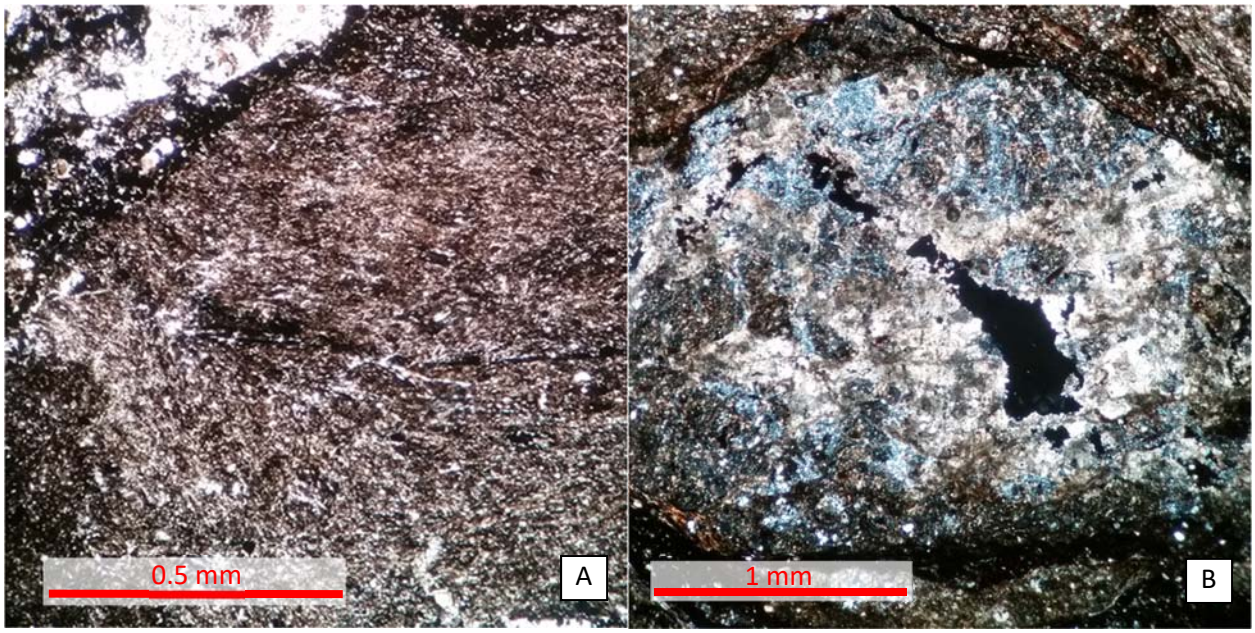

Figure 13. Photomicrographs of tectonic breccia clasts representing lithologies of the Rodeo Creek Formation. A: (BD15-023A_1363.8-1364.5) silicified carbonaceous argillaceous marl. B: (BD15-052_746.2) porous, incipiently silicified argillaceous limestone.

3.1.5 Silurian-Devonian Bootstrap Formation

The deepest exposed unit at the Arturo and El Niño mines is the Bootstrap Formation. Total thickness of the Bootstrap limestone is unknown. In most cases the upper contact of the limestone is intersected at 277-306 m depth, but has been intersected at depths of 512 m in the El Niño area. The limestone is generally massive but can be laminated and bedded, especially in the sedimentary fill of karstic voids. It is gray, white, and tan and largely unaltered below the zone of dissolution collapse brecciation with approximately 95% calcite ± quartz and clay ± bioclasts (Figure 14A and B), ooids (Figure 14C and B) and peloids (Figure 14D and Figure 15A). Limestone clasts from collapse breccias of the Bootstrap Formation are fine-grained, often silica-replaced (jasperoidal) limestone/marl (Figure 15B), course-grained silica-replaced pure to argillaceous limestones (Figure 15C), tectonically deformed pure to argillaceous limestones (Figure 15D), oomicrite, biomicrite, and pelmicrite.

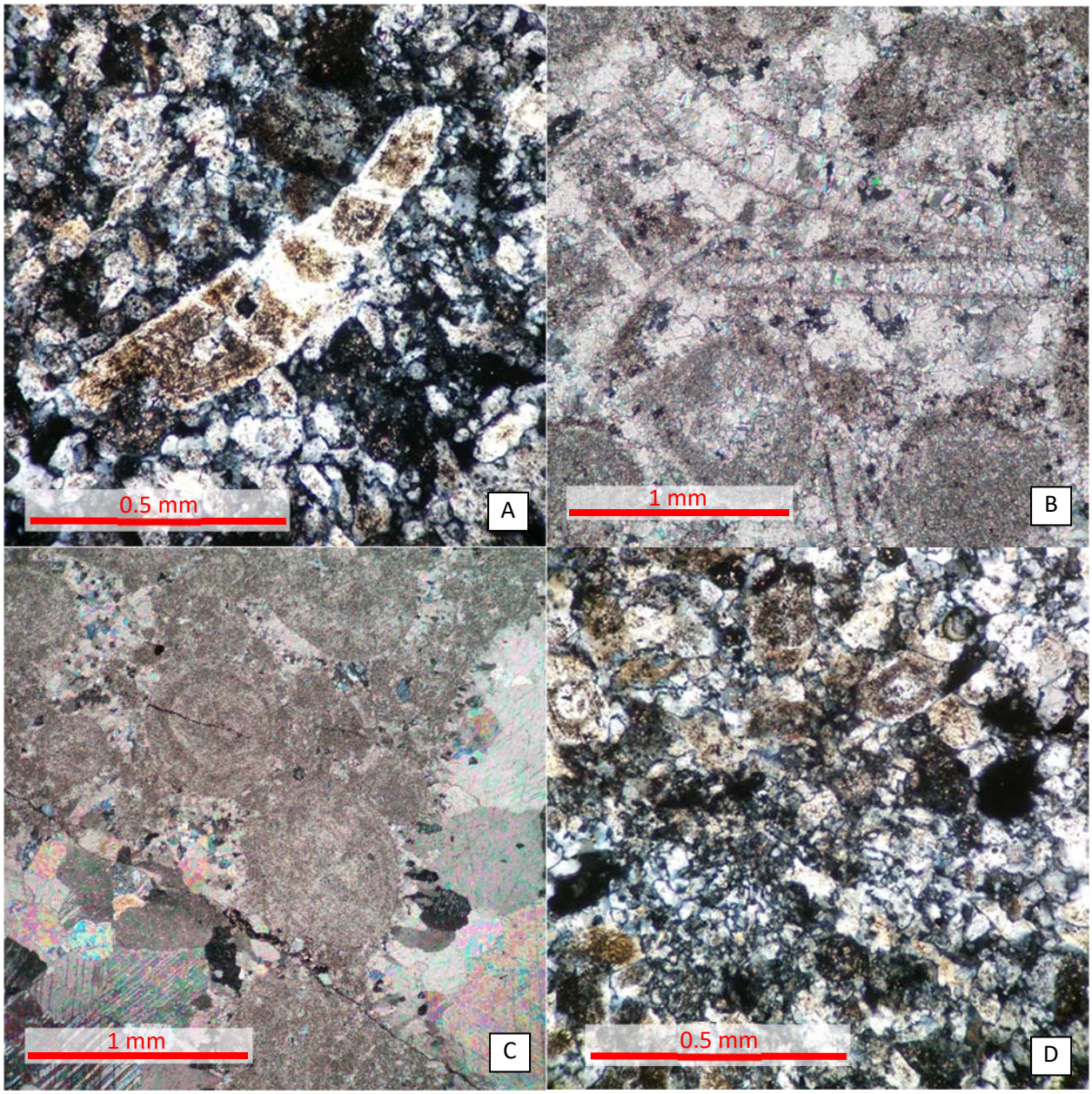

Figure 14. Photomicrographs of clasts from dissolution collapse breccias representing lithologies of the Bootstrap Formation. A: Weakly silicified fossil-bearing pelmicrite from sample BD15-052_861.3-861.8. B: Fossil-bearing oomicrite from sample BD15-053_984.2-954.8. C: Oosparite to oomicrite with interstitial sparite BD15-023A_1531.1-1531.9). D: Moderately silicified peloidal marl (BD15-051_861.3-861.8).

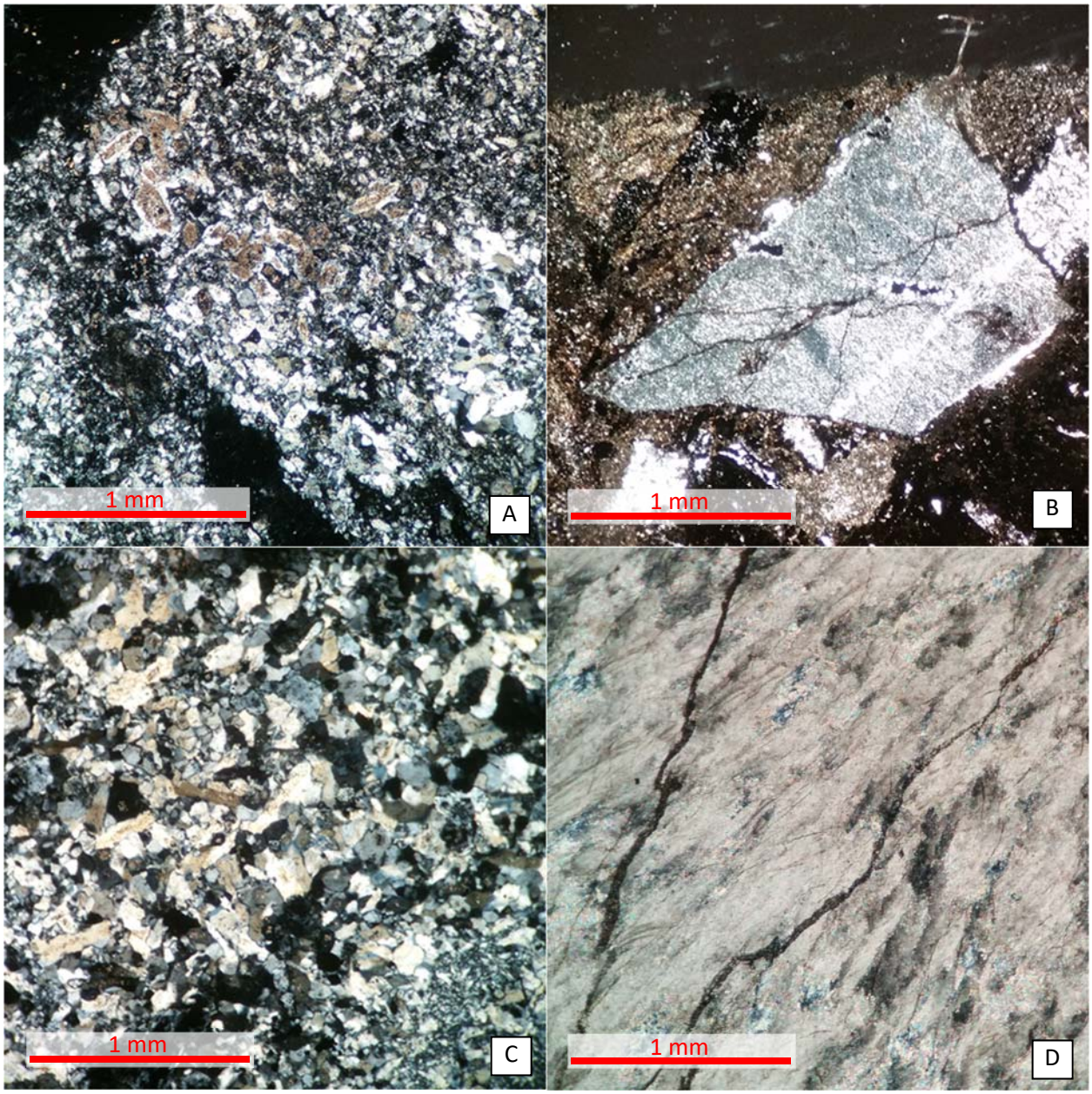

Figure 15. Photomicrographs of clasts and matrix from dissolution collapse breccias representing lithologies of the Bootstrap Formation. A: Moderately silicified peloidal marl from sample BD15-052_861.3-861.8. B: Silicified ultra-fine grained limestone/marl (jasperoid) (BD15-023A_1363.8-1364.5). C: Moderately to intensely silicified slightly argillaceous limestone (BD15-023A_1363.8-1364.5). D: Deformed (sheared) calcite (BD15-053_984.2-954.8).

3.2 Breccias

The El Niño Au-Ag deposit is hosted in tectonic, hydrothermal and, to a lesser extent, dissolution collapse breccias of the Rodeo Creek and Bootstrap Formations. The following are descriptions and naming abbreviations for breccias identified in core samples from the Button Hill gold deposit.

Identification of Bx1, Roberts Mountain Thrust (RMT) tectonic breccia, is primarily based on the thickness of brecciated shear zone, the location of the breccia in relation to the major formations, the presence and nature of shear fabrics and clasts, and the general composition as described by Barrick Goldstrike and stratigraphic descriptions in papers such as Trotman (2009) and Hall (2006). The RMT breccias zone is much thicker than any of the other identified fault breccia zones in the Arturo/El Niño deposit area.

The RMT shear zone is as thin as 1 m to the west of the Dee Fault (Hall, 2006), but up to 50-65m thick on the east side, in the Arturo pit. Samples taken from this zone are all presumed to be from the RMT zone and thus are Bx1. However, not all of the Rodeo Creek Formation is brecciated, and core samples must also contain shear fabrics such as mineral alignment, micro faults, and local flaser textures (Trotman, 2009) to be considered Bx1. Finally, the general composition of the breccia was also used to identify Bx1. RMT related tectonic breccias are typically chaotic and clast supported with a matrix that consists of sand to silt sized fragments of the same or similar composition as the clasts.

Post RMT are identified as Bx4. Bx4 tectonic breccias are distinguished from Bx1 by their location within the stratigraphy, location in relation to other lithologies, and the thinner breccia zone. Similarly, if a fault breccia is surrounded by lithologies known to cross-cut or overprint Bx1, such as pervasively silicified breccias or limestones (Bx1a), it is interpreted to be a fault breccia not associated with the RMT.

Hydrothermal breccias are identified by the obvious hydrothermal alteration of clasts or mineral precipitation in breccia matrix that, in most cases, appears to be associated with fluids that have had an effect on the formation of the breccia. For example, Bx2 contains clast-coating vuggy quartz veins and breccia cement that appears to have been partially responsible for the brecciation of the host rock; yet, could have also post-dated brecciation. All of the hydrothermal breccias are associated with silicification of clasts, quartz veining, and/or pyrite veining.

Qualifying characteristics for a dissolution collapse breccia (Bx5a and Bx5b) include a spatial relationship to limestone, typically on the upper contact of the Bootstrap limestone, poorly sorted and angular clasts, sedimentary matrix and dissolution fronts in the limestone host and clasts. Bx5b is distinguished from Bx5a by the presence of carbonate replacement by silica; whereas, Bx5a has not been silicified.

Following is a description of the know breccia types within the Arturo and El Niño mines.

3.2.1 Tectonic Breccias

The thickest and most continuous tectonic breccia in the Arturo pit/ El Niño area is the Roberts Mountain thrust tectonic breccia. Localized, high-angle fault-related breccias are also common.

3.2.1.1 Bx1: Roberts Mountain Thrust Tectonic Breccia

The Roberts Mountain thrust (RMT) is a thick (up to 65 m in the Arturo pit) tectonic breccia zone that largely consist of mudstone clasts and deformed mudstone matrix derived from the Rodeo Creek Formation, plus minor contributions from the overlying Vinini Formation. Within the Rodeo Creek Formation, the RMT tectonic breccia will be referred to as Bx1.

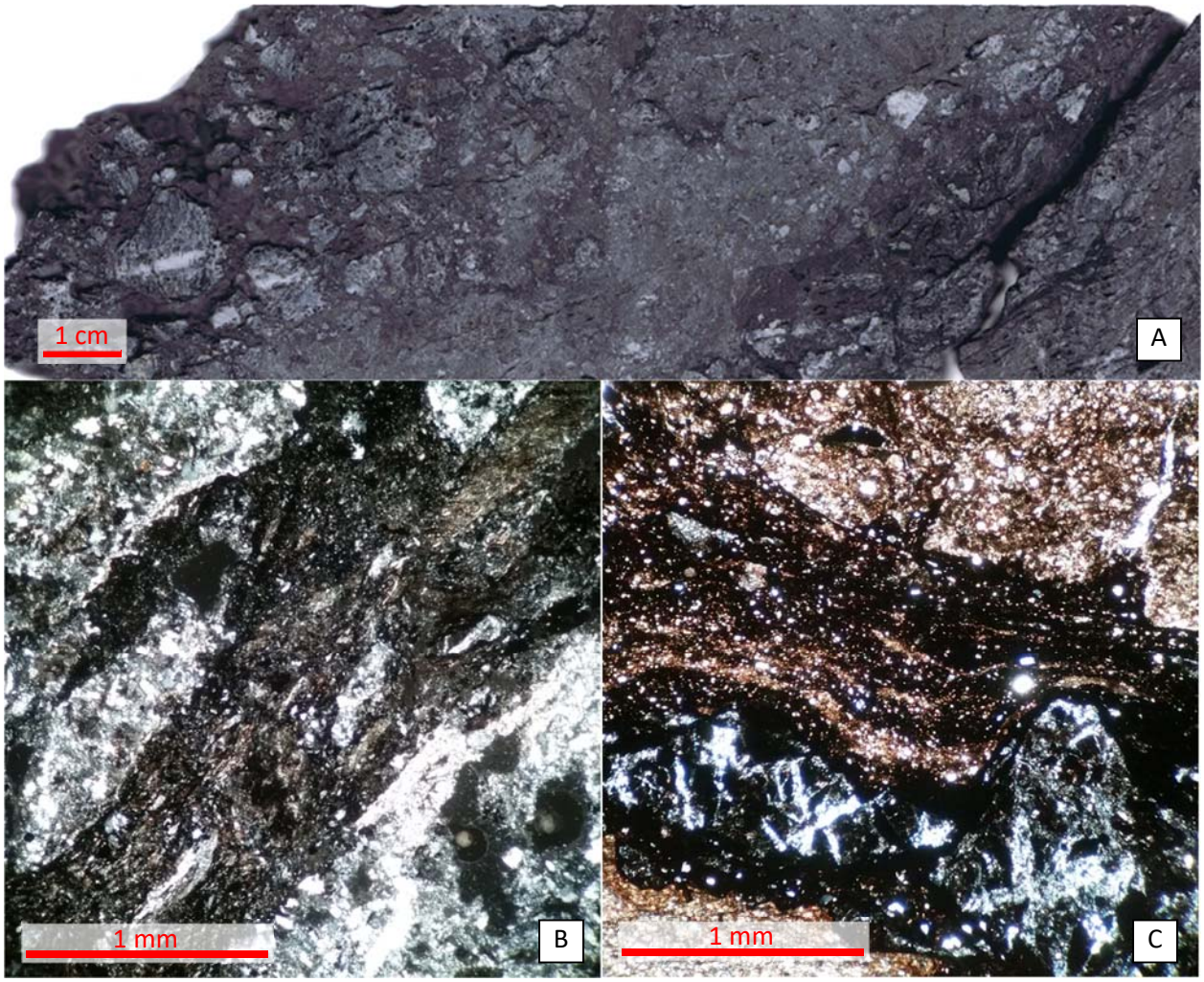

Figure 16. Sample BD15-023A_1312.4-1312.6 is a weakly silicified and decalcified, carbonaceous mudstone, clast supported tectonic breccia (Bx1). A is a scan of the core showing early calcite veins in rounded to subrounded clasts. B is a photomicrograph of the matrix which is a carbonaceous slightly calcareous mudstone. C (BD15-052_746.1) is a photomicrograph of a muddy calcareous shale clast with minor silicification and approximately 3-5% pyrite. The truncated quartz veins in a clast in the lower portion of figure C may indicate reactivation along the RMT or a later fault through the RMT.

Sample BD15-023A_1312.4-1312.6 (Figure 16a and b) is an example of the Bx1 breccia. Bx1 typically contains less than 5% matrix; however, this is approximate due to the similarity between matrix and clasts. It is a weakly silicified, decalcified, clast supported, calcareous mudstone tectonic breccia. It consists of approximately 5% carbonaceous, slightly calcareous mudstone matrix (Figure 16b) with a high degree of grain alignment. The matrix has approximately 1.5-2% diagenetic pyrite (0.5-18.75 μm, anhedral blobs, disseminated) 20-25% organic material, 60-

70% clay±silt and 5-10% calcite approximately 60% replaced by silica + illite. The clasts are primarily of a single lithology, a silicified carbonaceous calcareous silty mudstone with a clay/carbonate ratio of ~2.8 and 1-5% pyrite, 7-10% subangular quartz and 5-6% white mica.

There are 3 types of veins within the BD15-023A sample of Bx1. There are vuggy quartz veins (15-90 μm wide), pyrite veins that fill the vug space and cut the quartz veins, and calcite veins (~50-100 μm wide). The quartz and pyrite veins cut some deformation structures in the clasts and matrix, but are themselves cut by fractures (with minor, if any, offset). There are two generations of calcite veins. There are calcite veins that are cut by clast boundaries and are partially silicified, and there are coarse grained calcite + barite veins that cut all other features, including the quartz and pyrite veins.

Figure 16C is a photomicrograph of the matrix within another Bx1 sample from hole BD15-052. This matrix is composed of smaller fragments of the rock that formed it and has a similar shear fabric as in the BD15-023A sample. The matrix is identified as a muddy, calcareous shale due to the much higher organic content (45-50%). The BD15-052 Bx1 sample contains approximately 4 distinctively different lithologies that include weakly silicified argillaceous limestone, calcareous mudstone, carbon-bearing marl, and carbonaceous calcareous marl.

3.2.1.2 Bx4: Other Fault Breccias

Bx4 is the designation used for fault breccias that are not within the Roberts Mountain thrust zone (Bx1). Bx4 is characterized by polylithic, angular clasts and rock-flour matrix with slip-surface contacts between the clasts and between the clasts and matrix. Bx4 is distinguised from Bx1 by the presence of; 1) Bx1 clasts in the breccia, 2) pure limestones clasts from the Bootstrap Formation, 3) vertical or near vertical orientation of faults, and/or 4) presence of any clast of a unit

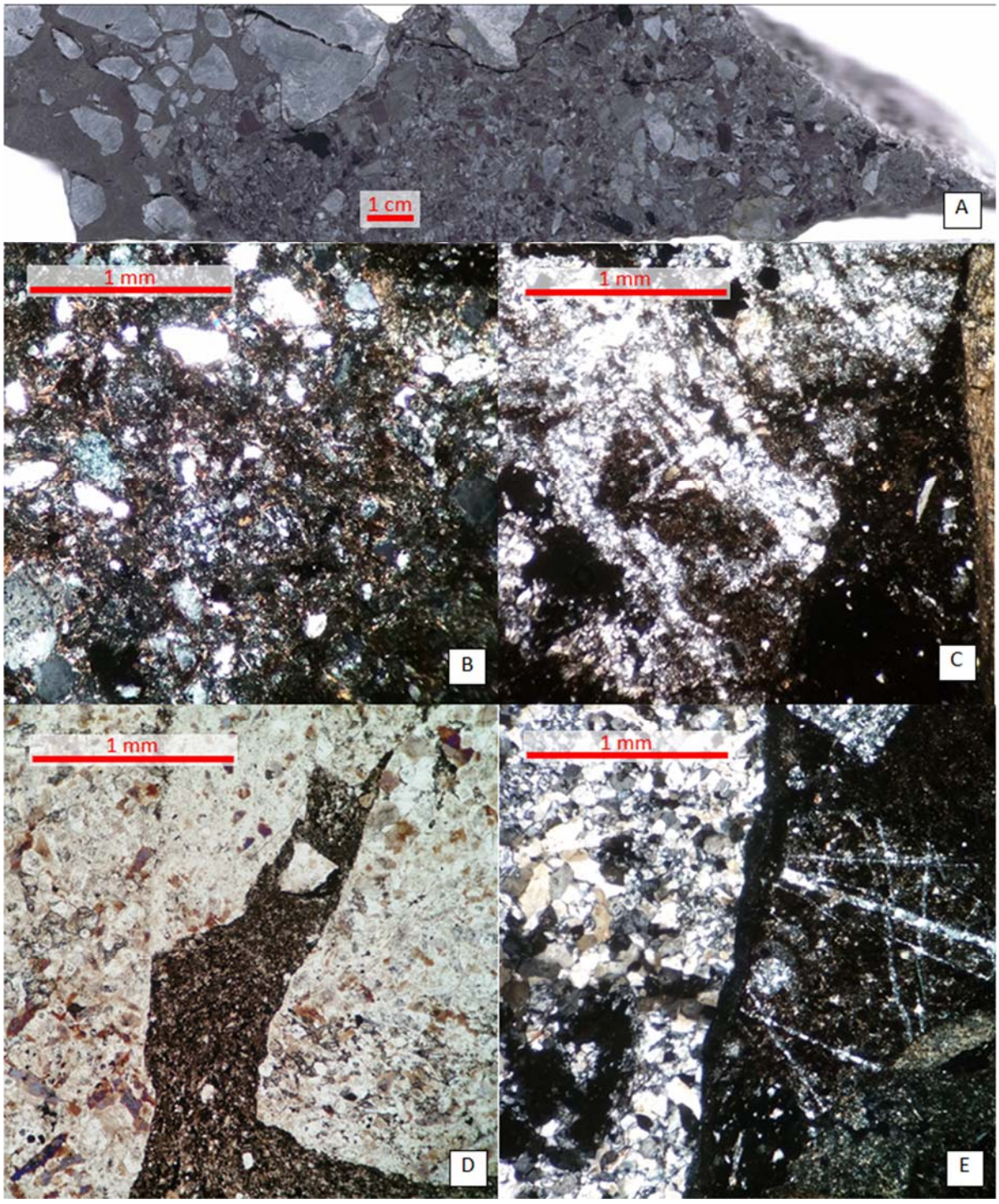

Figure 17. Sample BD15-023A_1363.8-1364.5 (Bx4) is a silicified, decalcified and sulfidized, clast supported, polylithic, clastic matrix fault breccia that contains a variety of clasts including polylithic dissolution collapse breccia clasts (B) and pervasively silicified hydrothermal breccia clasts (C). D and E show faulted contacts between silicified limestone clasts and matrix. There are two types of matrix in the core sample. A fine-grained, pulverized mixture of lithic fragments and single-grain clasts, and a coarse-grained matrix with larger lithic fragments and very few single-grain clasts.

or of an alteration type that is younger than Antler shortening (ie. Jurassic diorite, silicification, quartz veining, and pyrite veining).

Sample BD15-023A_1363.8-1364.5 (Figure 17) is an example of Bx4 fault-related breccia. It is a silicified, decalcified, and sulfidized, clast supported, polylithic, clastic matrix fault breccia. It contains clasts of two types of breccias that total approximately 40% matrix with fine-grained and coarse-grained clastic matrix that have a sharp contact visible in hand sample (Figure 17A). The breccia with fine-grained matrix and courser clasts has a matrix that is fairly uniform black and uniform grain size in hand sample. It consists of 36-47% clay±silt, 10-12% calcite, 35-40% organic material, 5-8% quartz (40-55 μm), 1-1.5% pyrite (1.5-2.8 μm), and 2-3% white mica. The breccia with course-grained matrix but lacks large, centimeter scale clasts, has a matrix that contains a large abundance of pebble to sand sized clasts and 47-55% clay±silt, 10-15% calcite (~95% silca altered) 20-25% organic material, 1-5% diagenetic pyrite, 5-8% quartz and minor white mica. Clasts within the coarse-grained matrix are angular, <0.25-2mm and are of at least eight different lithologies including bedded carbonaceous marl, calcareous muddy shale, jasperoidal limestone, carbonaceous calcareous marl, carbonaceous argillaceous marl, carbonaceous calcareous silty mudstone and two types of breccia clasts. There are two types of clasts that are themselves breccias. They are a polylithic dissolution collapse breccia (Figure 17b) and a quartz vein hydrothermal breccia (Bx2), which itself contains Bx1 clasts (Figure 17c). The largest clasts are a moderately silicifed slightly argillaceous limestone ± barite (Figure 15C) with 75-80% calcite (~75% silicifed). This specific clast type is also present in many other silicifed limestone-related breccias and is identified by its lack of organic material and clays and the elongate, anhedral to subhedral quartz grains in random orientation. Due to the apparent purity of the silicified limestone and the association with collapse breccias, this clast type likely comes from the Bootstrap Formation. The

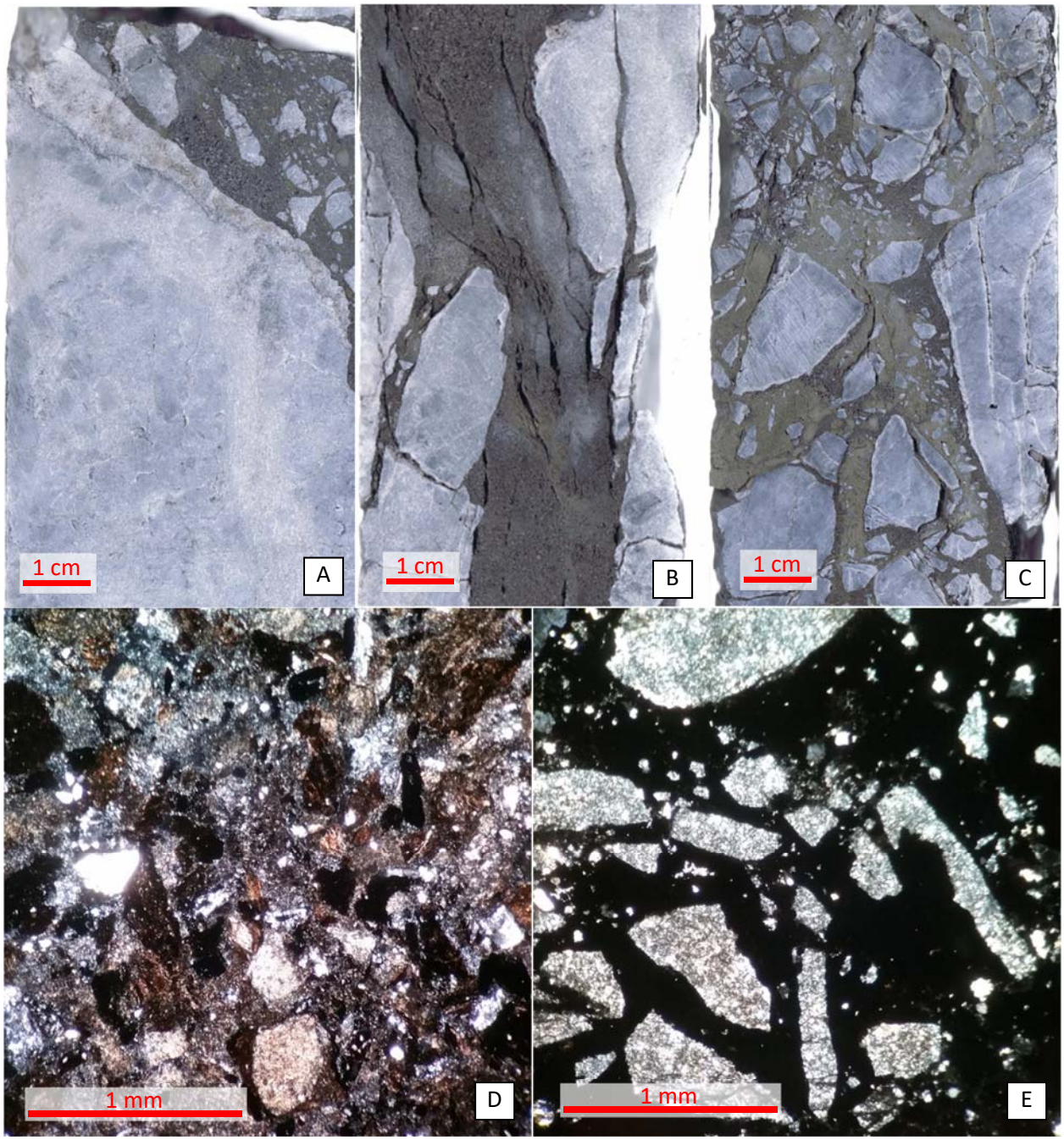

Figure 18. Bx4. Sample BD15-023A_1347.1-1347.5 (A and D). BD15-023A_1351.9-1352.3 (B). BD15-023A_1360-1360.5 (C and E). All samples are from the same fault zone with depth increasing from left to right in the core samples. They represent a silicified, decalcified, sulfidized, clast supported, polylithic, sedimentary matrix fault breccia. Samples A and C were silicified after brecciation (silicified matrix), sample C is sulfidized after brecciation (sulfidized matrix) with almost 100% pyrite in some areas of the matrix (E). D and E are photomicrographs from A and C respectively, that show the matrix before sulfidation (D) and after (E).

contacts of the silicified slightly argillaceous limestone clasts, and between the clasts and much of the matrix, are microfaults.

Figure 18 shows another example of Bx4. Figure 18A and D are taken from a depth of 1347.1-1347.5 ft (410.6-410.7 m), approximately 16 ft (4.9 m) above the sample in Figure 17, within the same fault zone. In hand-sample the matrix appears to be very similar to the fine-grained matrix in sample BD15-023A_1363.8-1364.5; however, in thin-section, this is most similar to the polylithic fault breccia clast seen deeper in the hole shown in Figure 17B, suggesting that the lower portion was re-brecciated by continued or reactivated faulting. Figure 18B has a similar matrix with strong alignment of grains. Figure 18C and E show Bx4 with strong silicification and sulfidation within the matrix. The matrix in this case contains up to 90-95% pyrite (17.5-262.5 μm anhedral) and 5-10% remnant material including clay ± silt. This grades into a matrix that is similar to that of samples BD15-023A_1347.1-1347.5 and BD15-023A_1351.9-1352.3 except that it has much higher concentration of silica. The most abundant clasts in all of these samples are strongly silicified limestone, in some cases with barite.

Figure 10A shows the only identified sample of a breccia with igneous clasts. It is a tectonic breccia (Bx4) near the upper intrusive contact of the Russet diorite dike. The light patches in the figure are fragments of the Russet diorite dike, with both faulted and intrusive contacts.

3.2.2 Hydrothermal Breccias

Hydrothermal breccias that are spatially associated with the Button Hill deposit are of 4 major varieties. 1) Bx1a: the strongly silicified tectonic breccia, which consists of two subtypes, a white quartz flooded breccia (Figure 19a) and a dark vuggy silica flooded breccia and interpreted to be the result of strong silicification of Bx1, and 2) Bx2: vuggy silica cemented hydrothermal breccia that is often rebrecciated Bx1 (Figure 19B), 3) Bx3: pyrite matrix breccia. Of the Bx3 breccias,

there appears to be at least two subtypes. The first is a crackle to chaotic breccia associated with thin bleached selvages (Bx3a) (Figure 19C) around the pyrite veinlets. Bx3b contains pyrite veining with no bleached selvage. 4) Bx6: the youngest of the hydrothermal breccias is a late calcite ± barite matrix crackle to chaotic breccia (Figure 23).

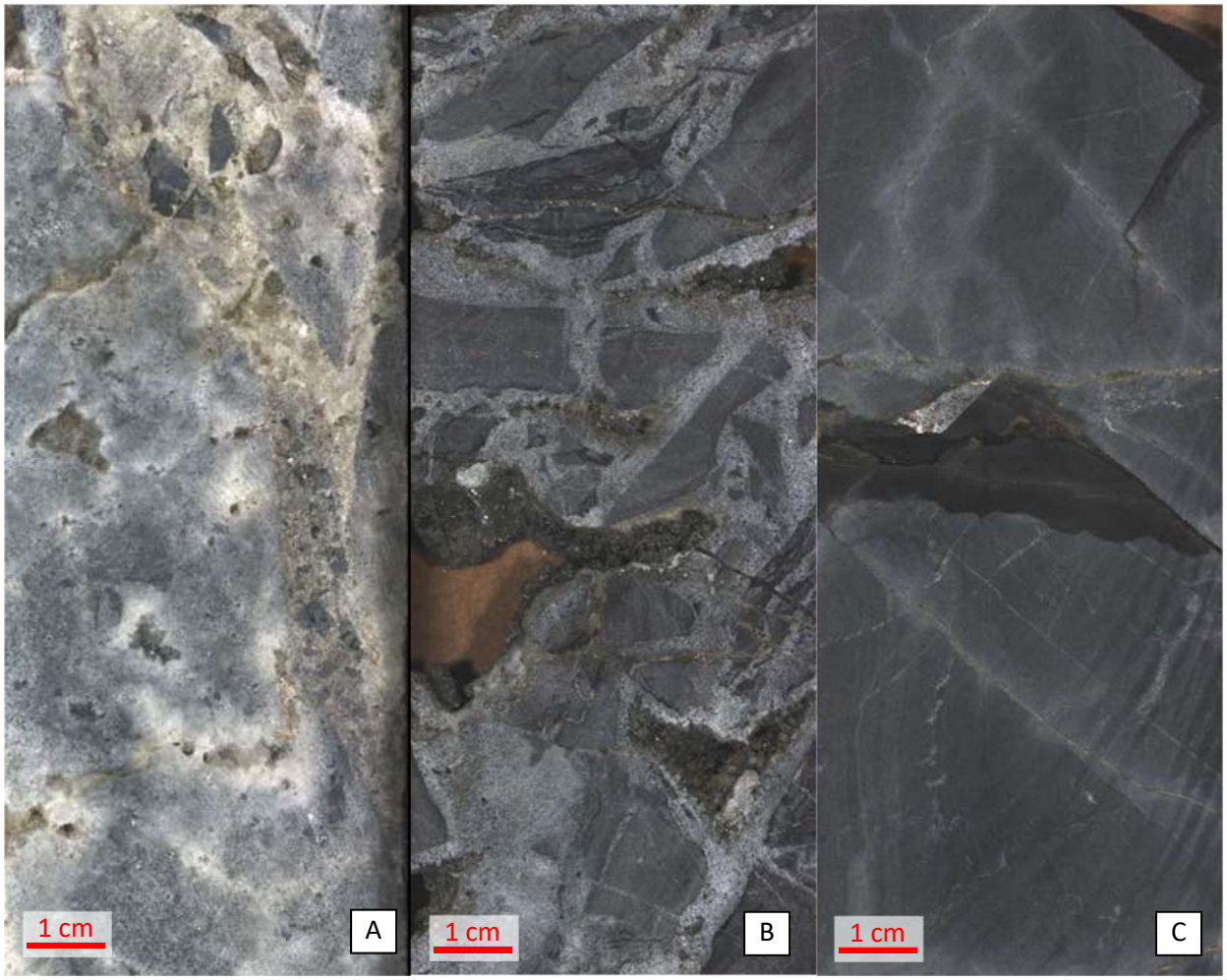

Figure 19. A: (BD15-052_814.6-815.1) is a Bx1a, intensely silicified (clast and matrix) mudstone/limestone hydrothermal breccia which rebrecciated Bx1. This sample also contains an approximately 1 cm wide Bx6, calcite+barite cemented hydrothermal breccia through the right side of the figure. B: (BD15-053_781.5-781.8) is Bx2, a vuggy silica cemented hydrothermal breccia that rebrecciated Bx1 tectonic breccia. This sample also contains post-brecciation pyrite veining. C: is an example of Bx3a. Sample BD15-052_769.2-769.5 is a quartz-(ammonium) sericite-pyrite altered mudstone crackle breccia.

3.2.2.1 Bx1a: Intensely Silicified Mudstone/Limestone

Bx1a is an intensely silicified (white quartz) mudstone/limestone hydrothermal breccia. It is often found within the Bx1 breccia body and in the upper contact of the Bootstrap limestone. The silicification alteration is often texturally destructive. The preexisting Bx1 breccia, in some cases, can only be identified by its location within the larger Bx1 body, and gradational contact with Bx1. Sample BD15-052_814.6-815.1 (Figure 19A) contains 95-97% quartz (μm-mm grain size, anhedral to euhedral), minor pyrite+mica and almost no original texture is preserved. This sample also contains a late calcite + barite matrix chaotic breccia and minor pyrite fill in void space.

3.2.2.2 Bx2: Vuggy Silica Cemented/Veined Hydrothermal Breccia

BD15-053_781.5-781.8 (Figure 19B) is an example of Bx2. This is the most widespread hydrothermal breccia in the Arturo pit. It is a vuggy silica cemented chaotic hydrothermal breccia with a larger tectonic breccia body (Bx1). It is distinguished from Bx1a by the lack of textural destructive alteration in the clasts and the occasional presence of Bx1a clasts in the Bx2 breccia. The matrix is almost entirely composed of euhedral, vuggy quartz that ranges in grain size from <20 μm to >2 mm.

3.2.2.3 Bx3: Pyrite Veined Hydrothermal Breccias

Bx3a is a quartz-(ammonium) mica- pyrite altered mudstone crackle breccia (Figure 19C and Figure 20A and B). It is characterized by pyrite veinlets and bleached selvages that cross-cut Bx1, Bx1a, and Bx2. The pyrite veins of Bx3a appear to have passively filled preexisting fractures and vugs, as opposed to Bx3b pyrite veins that appear to have both passively filled void space, as well as actively fractured and filled void space in the host rock (Figure 21D and E). The bleaching is due to the removal of organic material and replacement of organic material and calcite with

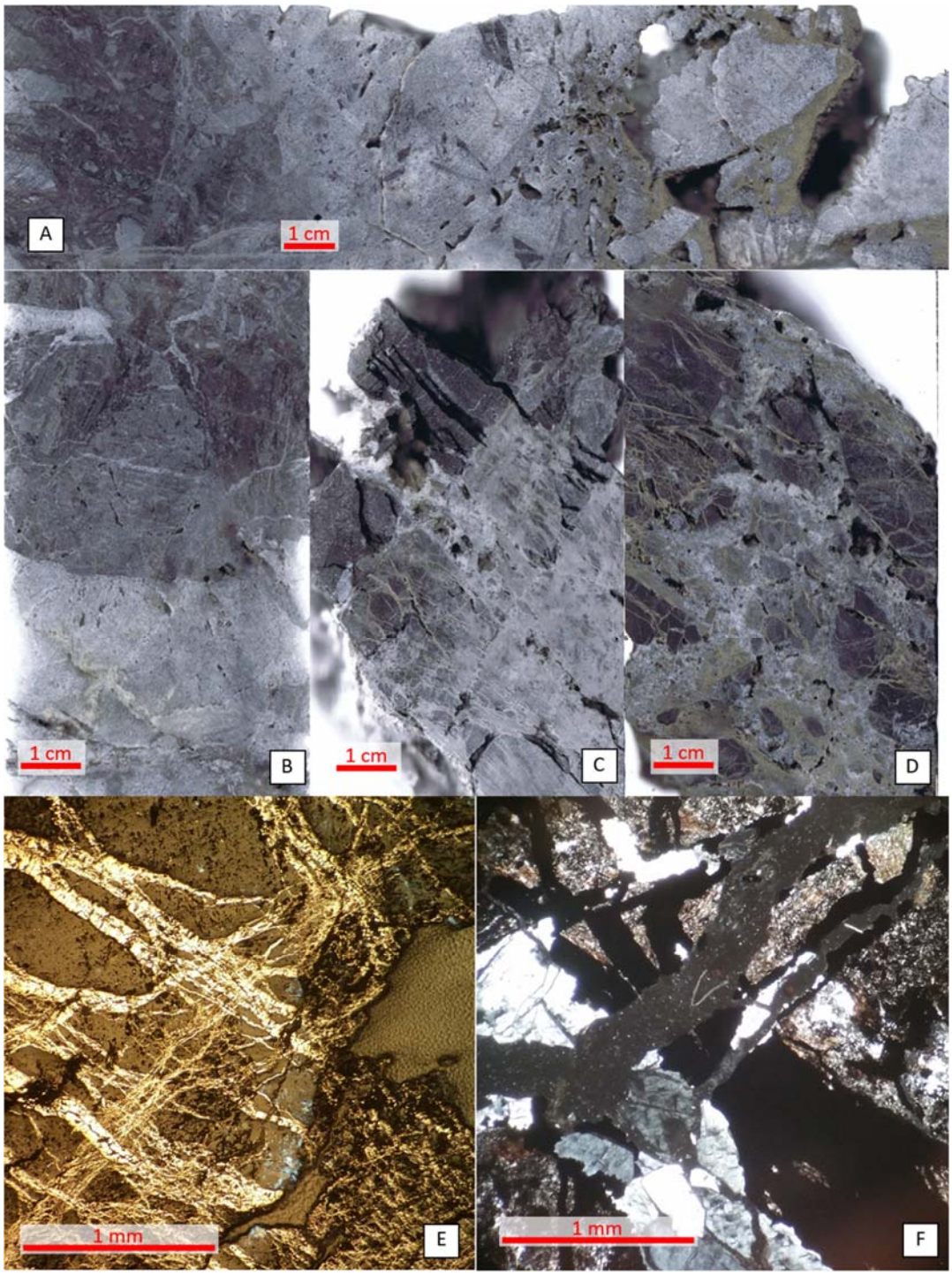

Figure 20. A: Bx3a, (BD15-050A_723.8-724.5) shows a bleached zone (4-5 cm) associated with pyrite, wider than that shown in Figure 19C. B: Sample BD15-050A_722.7-723.5 is similar to A from the same drill-hole. Sample BD15-053_783-783.3 (C) and BD15-053_786.2-786.6 (D) are examples of pyrite stringers that are not associated with bleached selvage (Bx3b). The white coloration in C and D are from Bx2 quartz veins (which the pyrite veins cross-cut) and oxidation of arsenian pyrite (scorodite?). E (reflected light) and F (cross-polarized transmitted): (BD15-053_783-783.3) are photomicrographs of pyrite veins of Bx3b and some fractures (faults?) that cross-cut (offset?) the Bx3b pyrite veins. The cross-cutting fractures is not observed in Bx3a pyrite veins.

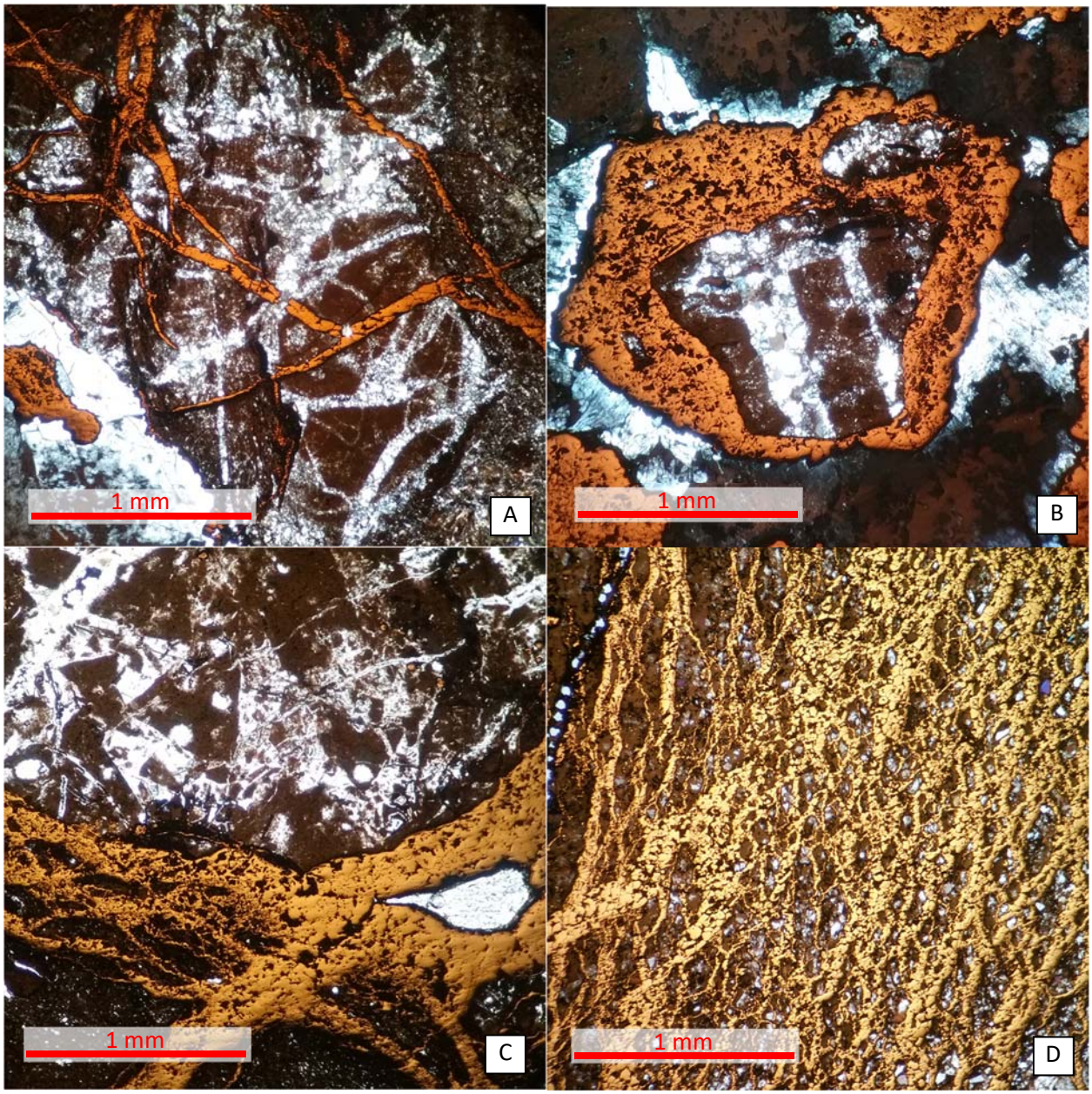

Figure 21. BD15-053_783-783.3 (A), BD15-053_786.2-786.6 (B), and BD15-053_789.4-789.6 (C) (reflected+transmitted light photomicrographs) show Bx3b pyrite veins and their cross-cutting relationship to Bx2 quartz veins. Figure 21A shows both veining, which cross-cuts a rebrecciated Bx2 breccia, and pyrite filling a vug in the bottom left. BD15-053_790.9-791-1 (D) is an example of a higher density of pyrite veinlets within a porous host, similar to that seen in the sulfidized Bx4 samples from BD15-023A (Figure 18C and E).

silica. In sample BD15-052_769.2-769.5 (Figure 19C) the organic material in the unbleached zone is 5-10%, reduced to ~2.5% in the bleached selvage (2-4mm on either side of the pyrite vein).

Conversely, silica from silicification is 10-20% + 0.5-1% mica in the unbleached zone and 30-40% silica + ~10% mica in the bleached selvage.

Figure 20C-F and Figure 21 show core photos and photomicrographs of Bx3b breccia. Bx3b is a pyrite matrix crackle to chaotic hydrothermal breccia. It is distinguished from Bx3a by the lack of apparent relationship to silicification, white mica alteration and leaching/replacement of organic material. The pyrite of Bx3b is primarly in clusters of high density veinlets that criss-cross and fill open void space in Bx1 and Bx2 breccias.

Figure 20E and F show that the pyrite veinlets cross-cut most clasts and matrix but are themselves cut by some fracturing with minor to no offset. Figure 21 are photomicrographs of Bx3b that show the different relationships of pyrite veinlets to the veins and breccias of Bx1 and Bx2. Figure 21A, B and C show that the pyrite veinlets cross-cut and surround clasts of Bx2. Figure 21D is an example of a sample that has been almost completely overwhelmed by the pyrite veinlets, preserving very little original rock texture.

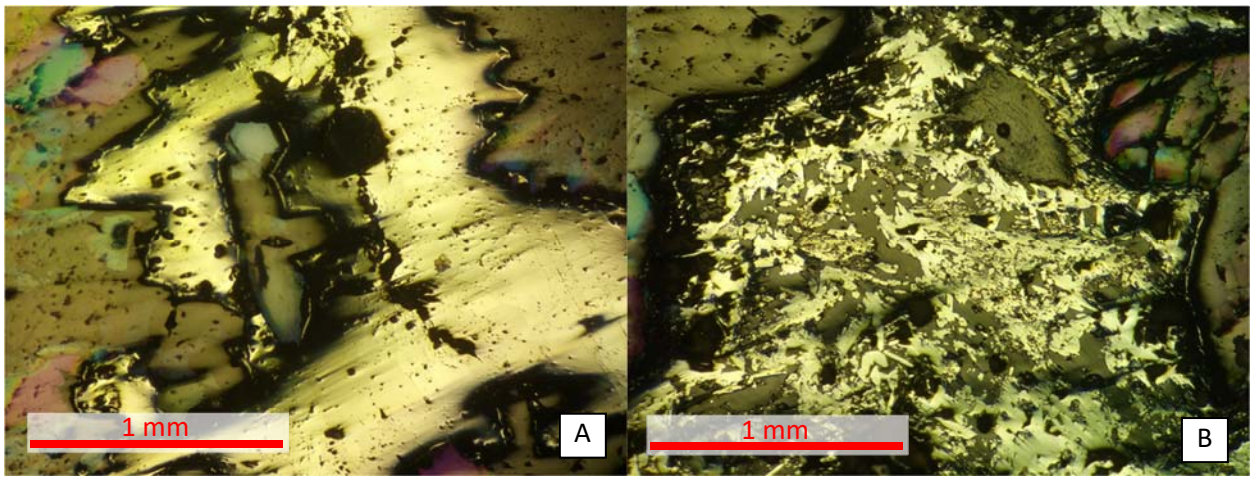

Figure 22. A and B: (BD14-01C_692_1) photomicrographs of stibnite coating Bx2 quartz vein vugs.

The nature of stibnite mineralization, present in sample BD14-01C_692_1 (Figure 22), is similar to that of the pyrite in Bx3. While no relationship between the stibnite and pyrite has been observed, the stibnite appears to have passively filled void space, primarily within Bx2, along open fractures that cross-cutting quartz veins and silicification.

3.2.2.4 Bx6: Calcite ± Barite Matrix Crackle to Chaotic Hydrothermal Breccia

Figure 23. Bx6. BD15-052_841.2-842, 839-839.5, 871.3-872. Late calcite + barite matrix crackle-chaotic breccia overprinting Bx1a. Varying intensity of brecciation and calcite + barite fill from mild (A) to moderate (B) and intense (C).

The youngest observed hydrothermal breccia is Bx6, a calcite ± barite matrix crackle to chaotic breccia. Bx6 is localized, having formed along fractures, faults and void space that ranges from sub-millimeter to 10's of centimeters thick. It occurs throughout the entire mineralized system, cross-cutting all other breccias. It is characterized by coarse-grained calcite and barite that cross-cuts all other alteration and breccia. Figure 23 demonstrates the varying intensity of brecciation and calcite + barite fill from mild (A) to moderate (B) and intense (C).

3.2.3 Dissolution Collapse Breccias

The second most expansive breccia spatially associated with Arturo mineralization is the dissolution collapse breccias (Bx5). There are several varieties of Bx5 breccias and they all form from the dissolution of Bootstrap limestone and collapse of stratigraphically higher material, either on the upper contact of the Bootstrap Formation, or along faults and fractures that cut the Bootstrap limestone. Of the collapse breccias, there are two major subgroups characterized by the presence of silicification (Bx5b), or lack of silicification (Bx5a).

3.2.3.1 Bx5a: Unsilicified Dissolution Collapse Breccia

Figure 24 and Figure 25 are examples of the varieties of Bx5a, or unsilicified dissolution collapse breccias. Sample BD15-023A_1531.1-1531.9 (Figure 24) is a carbonate cemented polylithic dissolution collapse breccia that contains clasts of Bx4 (Figure 24B) fault breccia in its matrix. In the down-hole profile, the breccia grades from Bx4 to Bx5a, with a very similar matrix, and thus faulting may have resulted in increased dissolution collapse brecciation by increasing surface area of clasts and increasing permeability for dissolving fluids to flow. The clasts are a relatively pure mixture of coarse-grained calcite and oomicrite, with minor amounts of barite (Figure 24C).

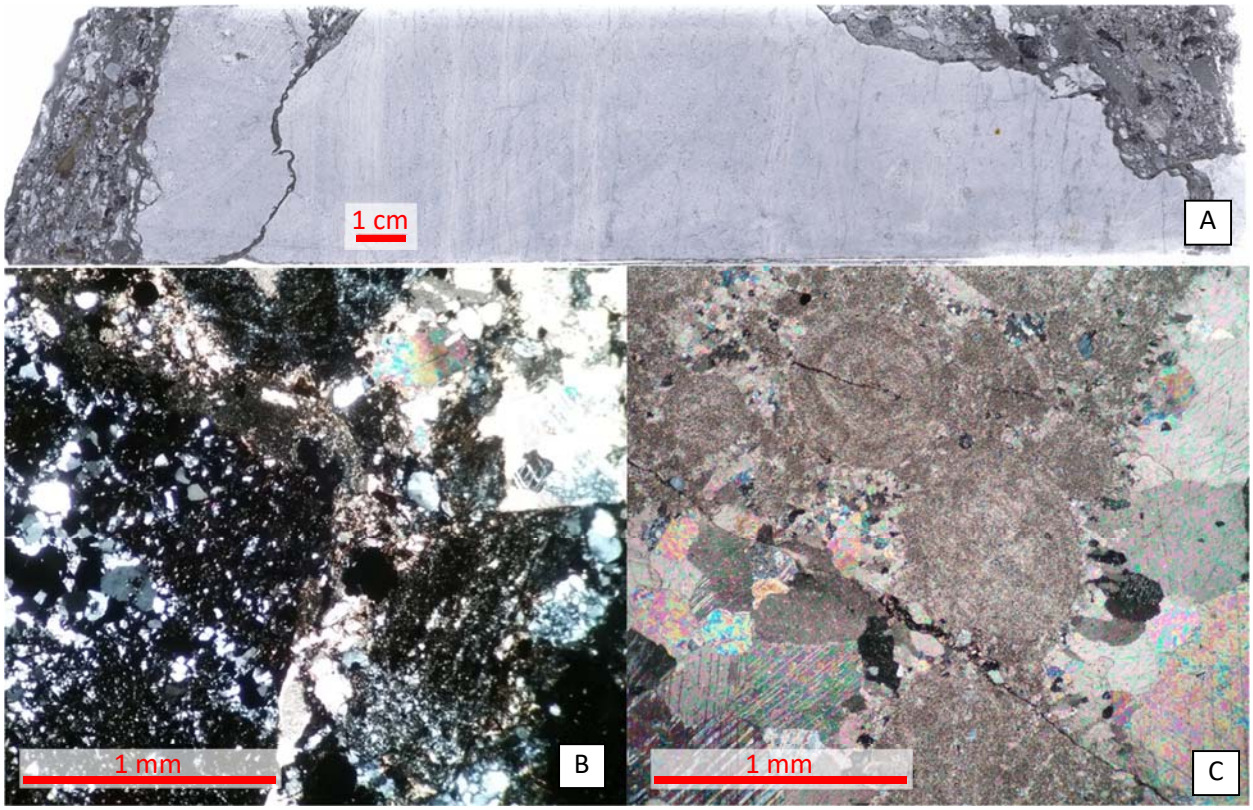

Figure 24. BD15-023A_1531.1-1531.9, Bx5, carbonate cemented dissolution collapse breccia with clasts of Bx4 that is likely closely associated with fault brecciation due to the close proximity to Bx4, the similarities between matrix content and the presence of faulted contacts in the core sample (A). B is a photomicrograph of the matrix, and C is of the ooid-bearing limestone + calcite and minor barite cement.

Figure 25A is also a fault-related dissolution collapse breccia that has both a dissolution front contact and faulted contact. The matrix is mixture of calcareous clasts and precipitated calcite, with a marl to calcareous marl composition. The limestone host is a mixture of biomicrite and oomicrite (Figure 14b) and deformed (sheared) coarse-grained limestone (Figure 15d). Figure 25B is a polylithic collapse breccia with large mudstone and marl clasts with a coarse-grained calcite matrix and cross-cutting calcite veins. Figure 25C and D are polylithic gypsum and barite-bearing carbonate cemented cavity fill breccias. Figure 27C and D are likely examples of a cavity-fill breccia in which gypsum and barite crystals grew through precipitation in a void space saturated by groundwater.

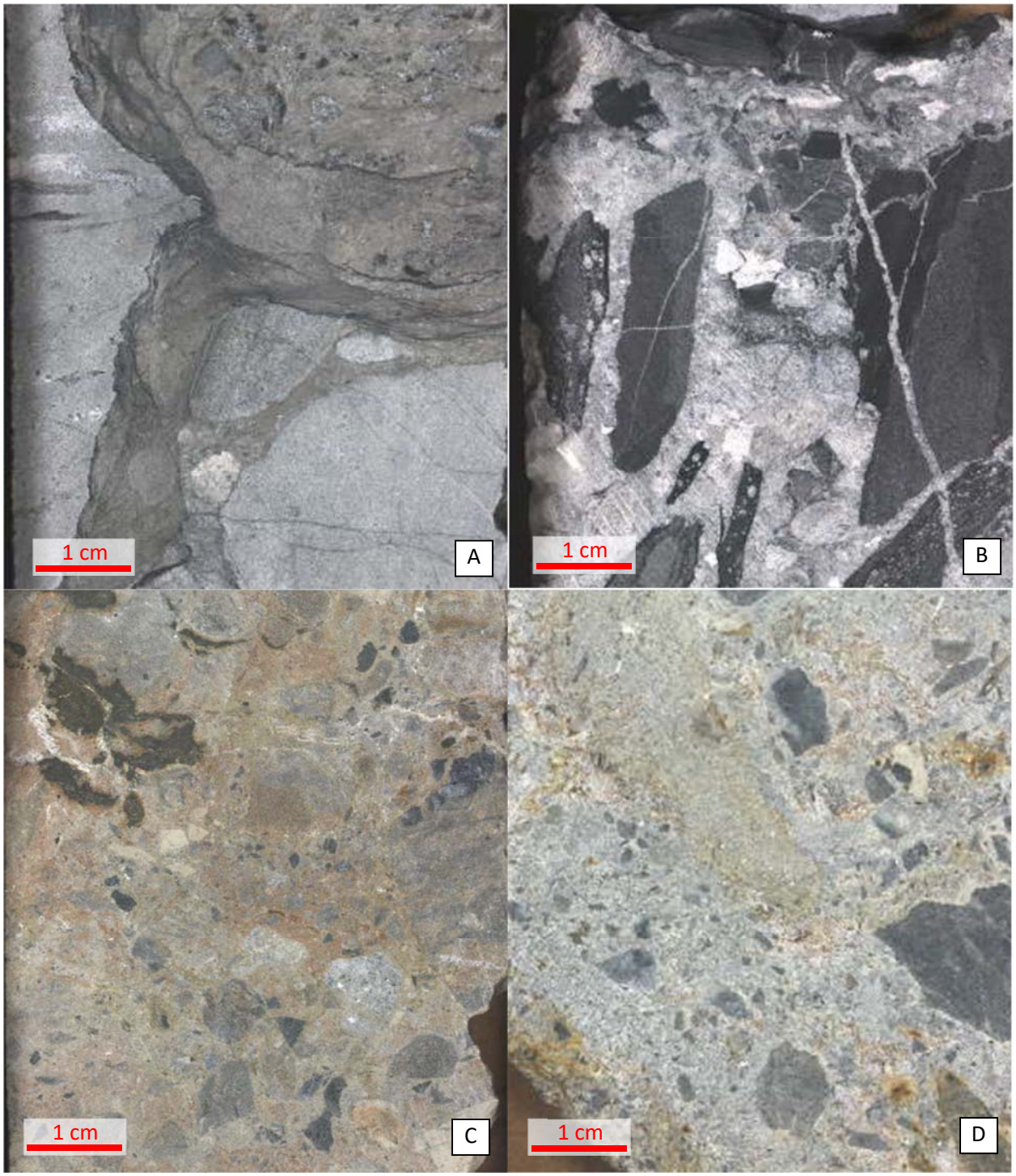

Figure 25. Bx5, unsilicified dissolution collapse breccia types observed in core samples from El Niño. BD15-053_954.2-954.8 (A) polylithic carbonate cemented dissolution collapse breccia spatially associated with tectonic breccia that contains dissolution fronts and slip-surface contacts. This example has an obvious concave contact of the matrix and clast in the upper left of the image, a common feature in dissolution. BD15-052_948.4-948.8 (B) polylithic collapse breccia with calcite cement and veins, and mudstone clasts. BD15-053_881.8-882.1 (C) polylithic carbonate cemented dissolution collapse breccia + pyrite. BD14-04C_745.3-746 (D) polylithic gypsum-bearing matrix carbonate cemented collapse breccia (cavity fill?).

3.2.3.2 Bx5b: Silicified Dissolution Collapse Breccias

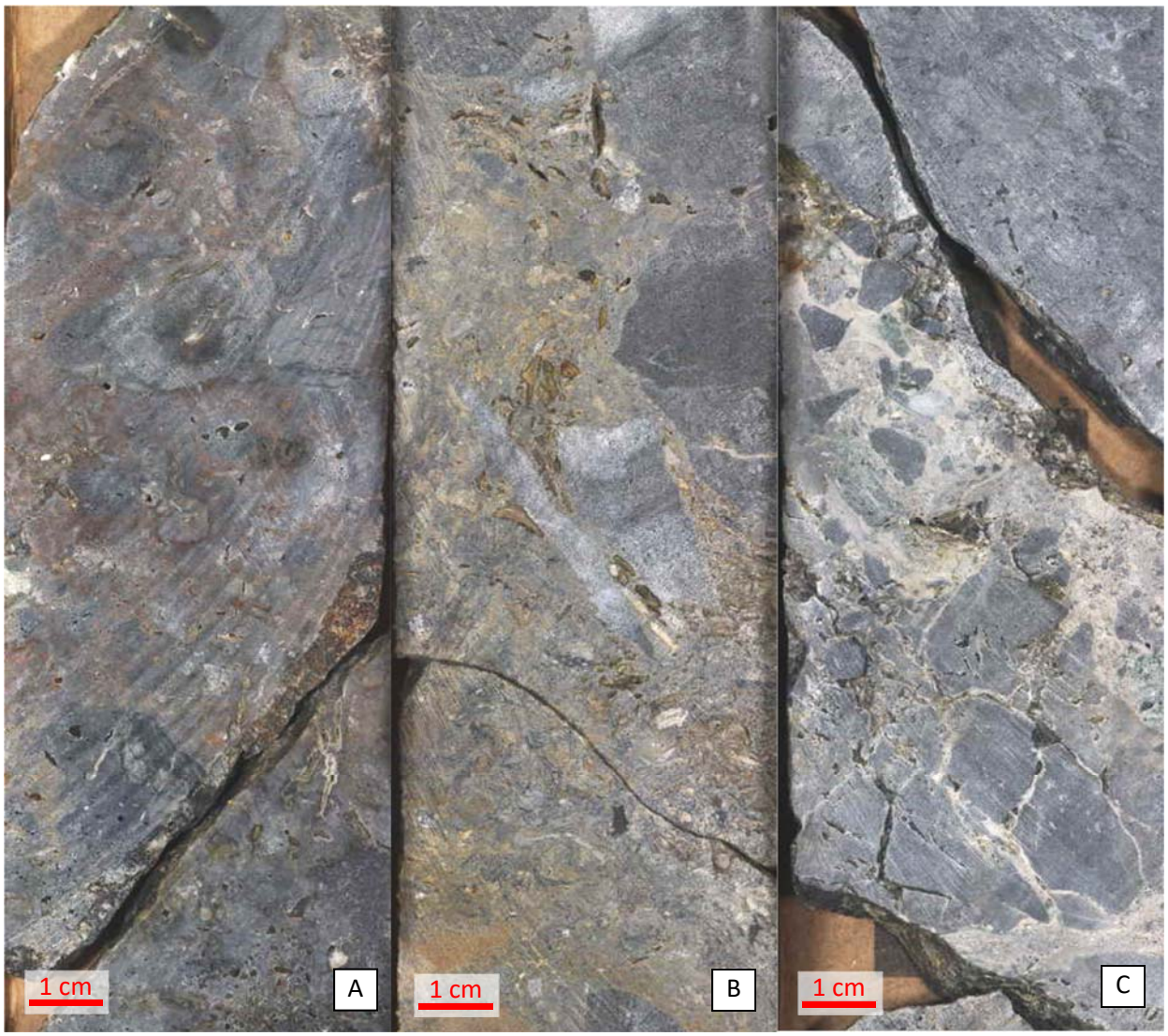

Figure 26. Bx5b, silicified dissolution collapse breccia types observed in core samples from El Niño. A: (BD15-051_860.8-861.3), decalcified, silicified, chaotic limestone clasts, matrix supported, iron oxide stained calcite (replaced by silica) cemented collapse breccia. B: (BD15-052_874.5-875), decalcified, silicified, chaotic limestone clasts, matrix supported, calcite cemented collapse breccia with ~10-15% void space. C: (BD15-052_893.2-893.5), decalcified, silicified, chaotic limestone clasts, matrix supported, peloidal marl cemented collapse breccia. Note the unknown green mineral in the upper left corner of the lighter colored matrix.

Figure 26 shows three examples of decalcified, silicified, chaotic limestone clast, matrix supported, iron oxide stained, calcite (replaced by silica) cemented collapse breccia (Bx5b).

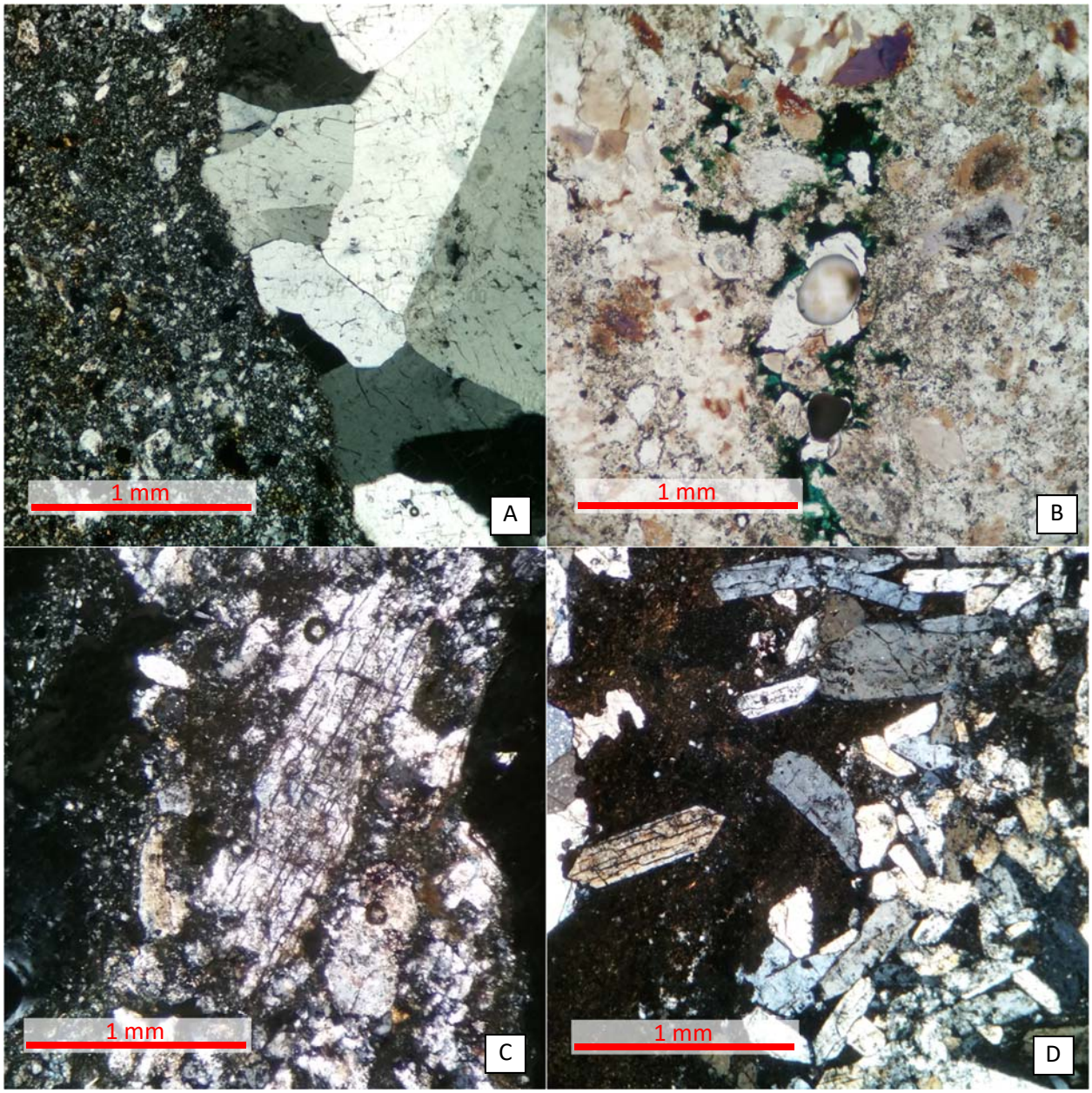

Figure 27. A: Bx5b. (BD15-052_874.5-875) Decalcified, silicified, chaotic limestone clasts, matrix supported, iron oxide stained calcite cemented collapse breccia. Bx5b-Bx1a contact in photomicrograph. BandC: BD15-052_893.2-893.5, unknown green mineral that coats vugs (B) and gypsum (C). D: BD14-04C_745.3-746, bipyramidal barite and gypsum crystals freely precipitated in an open void.

BD15-051_860.8-861.3 (Figure 26A) consists of approximately 55% matrix of 70-80% calcite (~95% silicified), 5-6% clay±silt, 1-5% organic material, 8-10% mica, 0.5-1% pyrite, and 0.5-1% quartz grains. Approximately 40% of the pyrite is weathered out, which likely accounts for the

iron-oxide staining that gives the matrix a red hue. Sample BD15-052_874.5-875 (Figure 26B) is an example of the same breccia type in a different drill-hole.

Sample BD15-052_893.2-893.5 (Figure 26C) has a higher clay content than the previous two samples. It is a decalcified, silicified, chaotic limestone clasts, matrix supported, peloidal marl cemented collapse breccia. It contains 45-50% calcite (~50% silicified), 25-30% clays, 10-12% organic material, 5-6% quartz, 5-6% gypsum, and an unknown dark green mineral (Figure 27B). The unknown green mineral coats vuggy surfaces and gives the hand sample a patchy, light green coloration and is moderately opaque in thin-section with no visible crystalline structure or cleavage (Figure 27).

3.3 Discussion and Interpretations

The Button Hill deposit is a Au-Ag deposit hosted in rocks that have been affected by a complicated series of tectonic breccias, hydrothermal breccias, and to lesser extent, dissolution collapse breccias. Understanding the series of geological events that led to the formation of the Button Hill deposit requires unravelling re-brecciated breccias and hydrothermal alteration from at least three hydrothermal events.

3.3.1 Relative Timing of Events

Figure 28 shows the relative timing of brecciation and related events in the Button Hill deposit, suggested by cross-cutting relationships in thin section and core and previous work on the nearby Au-Ag deposits and breccias (Williams, 1992; Emsbo, 2003; Trotman, 2009). Bx1 tectonic brecciation was the first brecciation event, demonstrated by the presence of Bx1 clasts in all other breccia types.

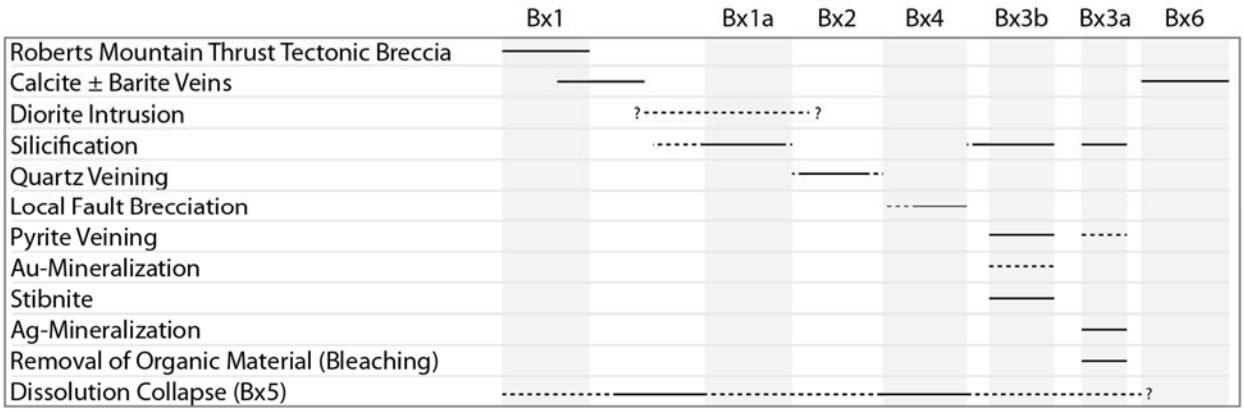

Figure 28. Sequence of brecciation and alteration events in the El Niño mine. Figure shows deformation and alteration events on the left compared to the timing of identified breccias along the top, with the exception of Bx5, which has occurred several times throughout the formation of the Button Hill mineralization and breccia zone.

Calcite and barite veins occur in many of the Bx1 samples. Often they are late and cross-cut all clasts and deformation fabric; though, there are calcite + barite veins within clasts suggesting that there was an early calcite ± barite veining event that was coincident and after the Bx1 tectonic brecciation event.

Bx1a intensely silicified breccia contains Bx1 clasts. It is not appear to be cut by any early calcite veins and has only been observed to be cut by the vuggy quartz veins of Bx2.

The diorite intrusion (Russet Dike) in the North wall of the Arturo pit intruded into the Russet fault and has subsequently been faulted and displaced. The diorite is only slightly silicified but is also spatially associated with intense silicification of Bx1a. This may suggest that it is genetically related to the Bx1a silicification event. It could also be that it cut through previously silicified rock. In the Meikle mine, Teal and Jackson (2002) suggest that Jurassic intrusions were associated with vuggy silica veining, like that of Bx2.

Bx2 occurred after the intense silicification of Bx1a but before the local fault brecciation of BD15-023A (Bx4), indicated by the presence of Bx2 clasts in the fault breccia. However, this is just

one example of a Bx4 (tectonic) breccia and may not be representative of other fault breccias in the El Niño area.

Bx4 local fault brecciation developed after Bx2 but before Bx3b pyrite, shown by the later sulfidation of Bx2, but lack of bleaching and mica alteration associated with Bx3a. There was likely silicification associated with Bx3. Most the rock surrounding Bx3b pyrite is weakly to moderately silicified. The exact timing of silicification and pyritization is unknown but is likely closely linked. Main-stage mineralization (Carlin-type Au) is interpreted to have occurred concurrently with Bx3b, based on the presence of sulfidation, silicification and stibnite combined with the relatively undeformed state of the pyrite veins is consistent with age, alteration and minerals within other observed Carlin-type deposits (Teal and Jackson, 2002; Cline et al., 2005).

The rarity of stibnite in thin section samples makes it difficult to determine timing. In sample BD14-01C_692_1, the stibnite filled void space from Bx2 quartz veins. BD14-01C_692_3 is only a few centimeters away and contains pyrite filled void space, similar to the stibnite, suggesting that they are very close in timing, if not contemporaneous.

Bx3a quartz-sericite-pyrite alteration may have happened after Bx3b. Pyrite of Bx3b, in almost all cases, has been broken by small fractures (shear fractures?). This is not the case for Bx3a. Bx3a pyrite has always been observed completely intact. If this breccia is indeed younger than main-stage mineralization, it may be associated with Miocene low-sulfidation epithermal Au-Ag mineralization, like that seen in the neighboring Storm mine (Trotman, 2009).

Bx5 dissolution collapse brecciation likely occurred at different stages throughout the development of the Button Hill system. Some Bx5 breccias developed before silicification and were subsequently intensely silicified in the Bx1a silicification event. The BD15-023A Bx5 breccias were coincident with (or after) Bx4 faulting and likely developed due to fluid flow along the fault.

Other Bx5 brecciation occurred after Bx3, but before Bx6, demonstrated by the presence of Bx2 clasts in the matrix and the cross-cutting relationship of Bx6.

The youngest brecciation event (Bx6) was the coarse-grained calcite ± barite veins and breccia matrix that cross-cut all other features at the Button Hill deposit. This event is not related to Au-Ag mineralization and is likely from circulating groundwater precipitating calcite and barite in void space created by dissolution and faulting.

CHAPTER 4 – WHOLE-ROCK GEOCHEMISTRY RESULTS

4.1 Introduction

Whole-rock geochemistry data was selected from a vast database from approximately 9,664 48-element ICP-MS samples from 5, 10 and 20 ft. intervals over 111,003.5 ft. of core and RC chips, 23,467 samples over 120,881.2 ft. at mostly 5 ft. intervals for fire assay method (Au ± Ag), and 1,898 samples over 34,969 ft. at 5 ft. and 20 ft. intervals for LECO™ analysis. Whole-rock geochemistry data was used to understand and track changes in chemistry due to hydrothermal alteration and mineralization by identifying the associated suite of elements and tracking them spatially in the Button Hill gold deposit. Several techniques are employed to gain these results, some of which called upon the entire dataset and others required a modified sampling method of the database mentioned above.

The principle component analysis was performed for all geochemistry, assay and LECO™ data. The Grant isocon plot for Rodeo Creek Formation utilized all available 48-element geochemical data and all assay data. This was not completed for LECO™ data due to the lack of LECO™ data from unaltered samples. The geochemical contours of suite 2 elements utilized all available 48-element geochemical data and all assay data for the chosen elements. Scatter plots for the 4 identified geochemical suites and geochemical markers of clay and sulfide mineral plots used all available geochemistry data and all assay data for corresponding elements. All geochemistry of the breccias was from selective sampling and, in the case of the Grant isocon plots and enrichment factor scores, compositions were compared to the whole-rock geochemistry of unaltered Rodeo Creek Formation. The term "trend" is used to describe parts of geochemical data within a scatter plot that aligns but is not necessarily a best-fit line.

4.2 Principal Component Analysis

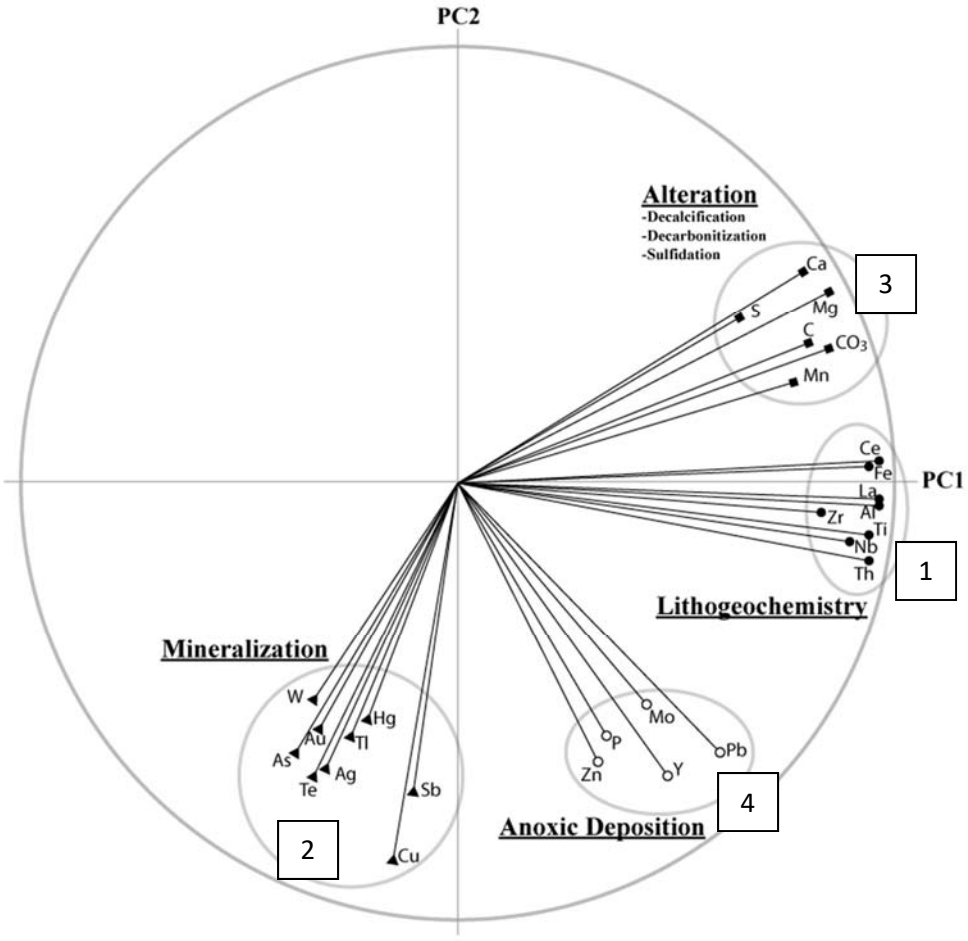

Figure 29. Log10 two-component robust principal component analysis with high outlier rejection of major, immobile, REE and hydrothermal elements completed on the geochemistry software ioGas. Four suites of elements were found and interpreted as elements associated with; 1) lithogeochemistry, 2) mineralization, 3) alteration and 4) anoxic deposition.

A Principal Component Analysis (PCA) was performed on the geochemical, assay and LECO™ data-set (Figure 1) to identify geochemical suites associated with mineralization. The elements were chosen as element groups for major (Ti, Al, Fe, Mn, Mg, Ca, P, C, and S), immobile (Ti, Zr, Y, Nd, Al, Th, and Nb), and epithermal Au-Ag (Au, Ag, As, Cu, Pb, Zn, Sb, Hg, W, Te, and Tl) suites provided by the program ioGas, in addition to CO_3. The first two

components (PC1 and PC2) accounted for 70.8% of the total data variance among the elements chosen.

The PCA shows four distinct chemical suites, indicated by their placement within PCA space. Suite 1 aligns with PC1 and includes the elements Al, Ce, Fe, La, Nb, Th, Ti, and Zr. Many of the elements in this suite are generally considered immobile, especially Al, La, Ti, and Zr and so likely represent lithogeochemistry, or elements from the original rock that were not affected during alteration. Suite 1 is also referred to as the lithogeochemistry suite.

Suite 2 includes Au, Ag, As, Cu, Sb, Te, Tl and W, and aligns with -PC2. The presence of precious metals, and ore elements similar to those identified at the nearby Storm mine (Trotman, 2009) suggests that this group of elements is enriched during mineralization and so is referred to as the mineralization suite.

Suite 3 plots between PC1 and PC2 and includes C, CO_3, Ca, Mg, Mn, and S. This suite consists of many of the elements lost or added during the most common alteration styles associated with Carlin-Type gold deposits (decarbonatization/decalcification, carbon replacement, and sulfidation) (Teal and Jackson, 2002; Cline et al., 2009). Suite 3 is also termed the alteration suite.

Suite 4 consists of Mo, P, Pb, Y, and Zn, and aligns between PC1 and –PC2. Elements in this suite are commonly associated with organic-rich deposition in an anoxic to euxinic environment (P, Zn, Y, and Mo) with possible input from early hydrothermal activity such as seeps (Zn and Pb) (Tribovillard et al., 2006).

4.3 Bivariant and Trivariant Scatter Plots

All elements of the lithogeochemistry suite (suite 1) (Fe, Ce, La, Ti, Nb, Zr and Th) show a positive correlation when plotted against aluminum (Figure 30). Ce, La, Nb, Th and Zr all

demonstrate a scattering effect of data points that moves away from the trend-line at high concentrations (circled in Figure 31). A large majority of the scattered data points (circled in Figure 30) are from the Tertiary Carlin Formation. Iron has a second trend-line that branches from the origin (0,0), near vertical along the y-axis, indicating that iron was locally added, was not immobile, or is within more than one mineral. Thorium may have a similar trend but is much less obvious and may be from scattering data.

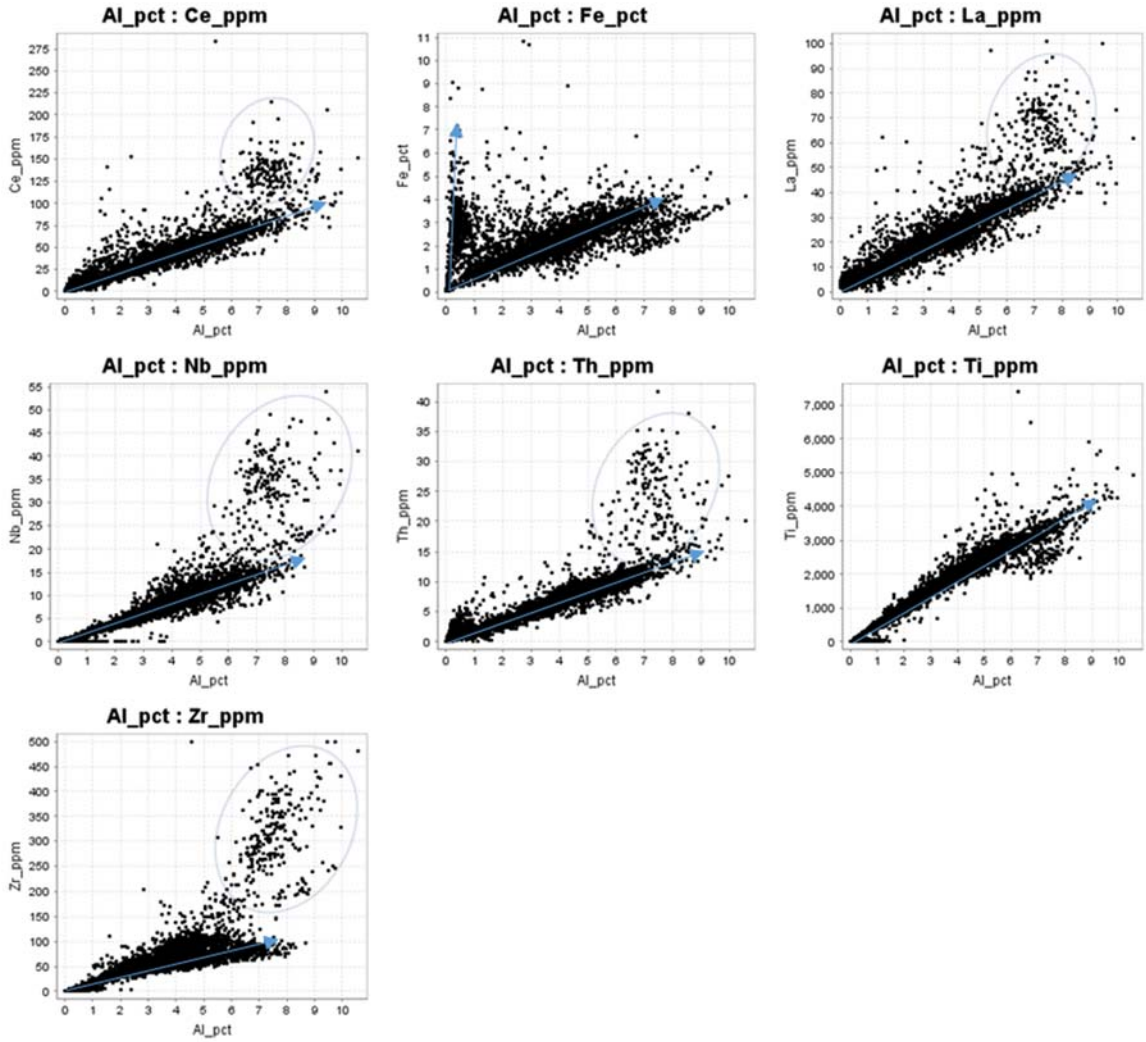

Figure 30. Scatter plots of lithogeochemical suite of elements (suite 1). Blue arrows show trends, blue circles show Tertiary Carlin formation data points.

Ag, As, Cu, Fe, Hg, Re, S, Sb, Se, Te, Tl, and W (mineralization suite) were plotted against Au (Figure 31) and Au, As, Cu, Fe, Hg, Re, S, Sb, Se, Te, Tl, and W versus Ag (Figure 31). Fe,

Hg, Re, and S were included after trial plots demonstrated similar patterns as that seen in the PCA identified suite. In Figure 31, Au appears to have a weak positive trend when plotted with Ag, As, Cu, Fe, Hg, S, Te, and Tl and a steep trend with Sb and Te. Ag, As, Cu, Fe, Hg, Re, S, Se, Tl, and W all have scatter at low Au concentration (circled in blue). Re, Se, and W appear to have no correlation with Au.

The association of Ag with other elements of suite 2 is slightly more complex than Au (Figure 32). Au, As, (Cu?), Fe, Hg, Re, Sb, Se, Tl, and W all have horizontal trends (high Ag values associated with no significant suite 2 elements, circled in orange). All the same elements, baring Sb, also have a vertical trend (high mineralization suite elements with no significant Ag, circled in blue). However, many of the Ag plots (As, Cu, Fe, Hg, Re, Sb, Se, Te, and Tl) also have a third trend (circled in green) that is moderate to steep and apparent correlation of enrichment.

Correlation matrixes for the same elements were created for samples containing Au > 0.05 opt (1.72 ppm) (Table 3) and for samples containing Ag > 0.05 opt (1.72 ppm) (Table 4). The Au and Ag cut-off values were chosen after I trialed various cut-offs and found the strongest correlations.

The correlation matrix for samples containing Au >1.72 ppm show that Au in mineralized zones is correlated with Cu, Fe, S, Te, and W and strongly with As, Hg, and Tl. Interestingly, Ag is not correlated with Au at these higher grades, nor is Re or Se, and Sb has a strong negative correlation. Ag in these samples is correlated with Hg, Sb, Se, and Te, and negatively correlated with Fe.

The correlation matrix for samples containing Ag >1.72 ppm is similar to that of Au. Ag is associated with Hg, Sb, Se, and Te, and negatively with Cu. Au has a correlation with As, Fe, Hg, S, Te, and Tl. It doesn't have the same negative correlation to Sb and is not correlated with Cu or W.

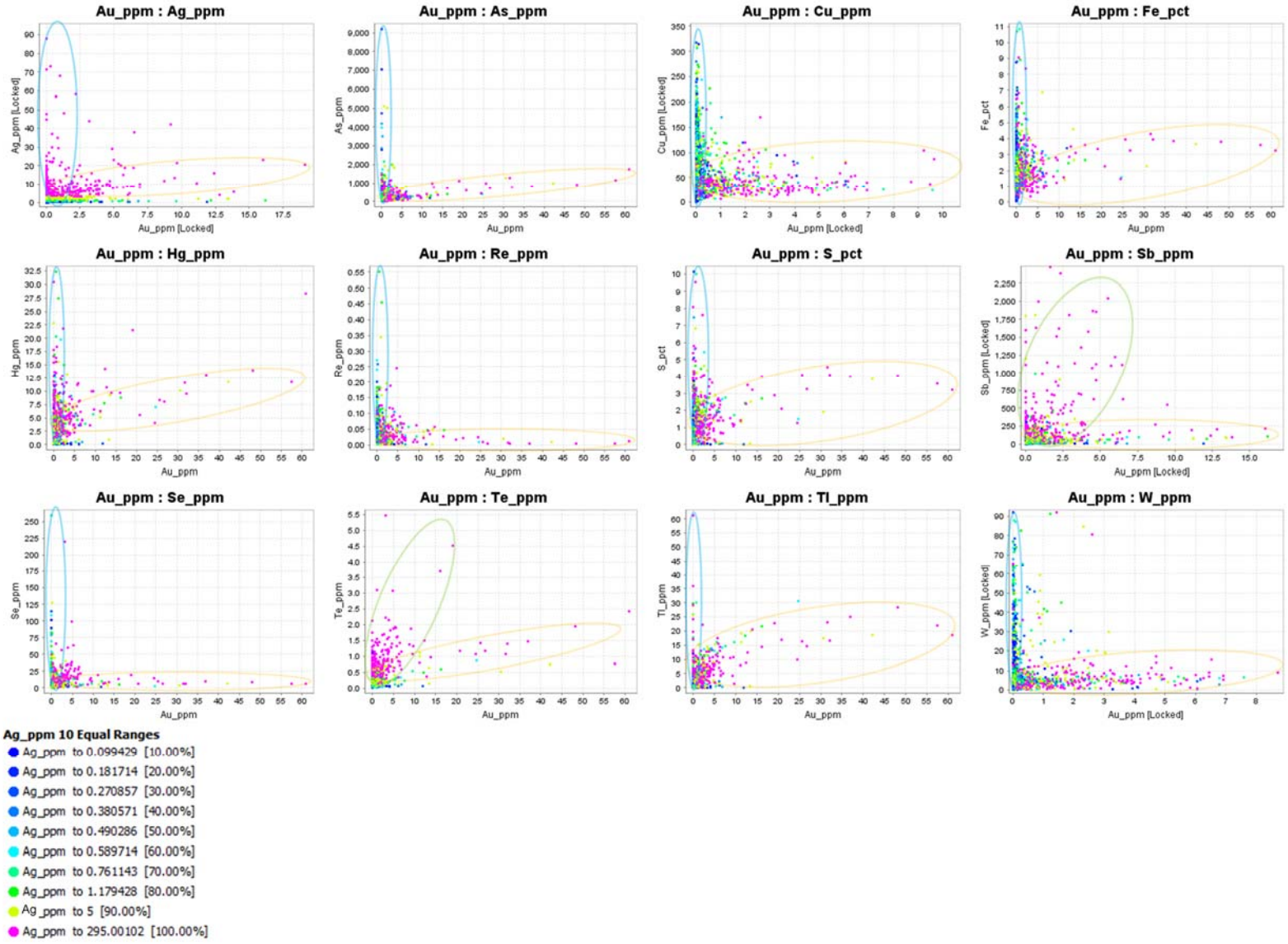

Figure 31. Trivariant scatter plots of Au and other elements of the mineralization suite. The dot colors represent Ag values.

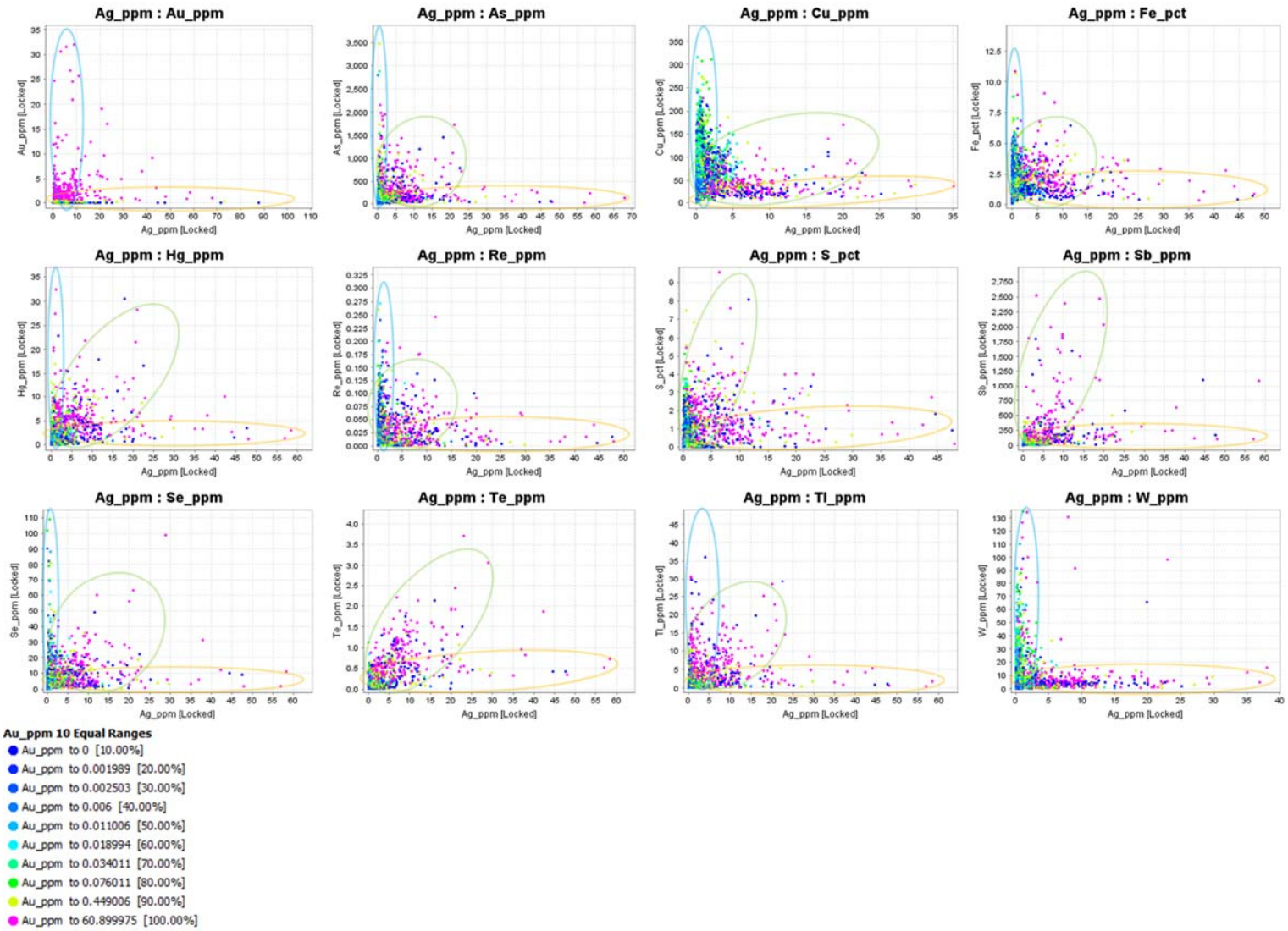

Figure 32. Trivariant scatter plots of Ag and other elements of the mineralization suite. Color of the dots represent Au values.

Table 3. Correlation matrix for data from 201 samples with Au >0.05 opt (1.72 ppm). Blue represents 1 to 1 correlation, dark green represents 0.50-0.99 correlation, light green represents 0.10-0.49 correlation. Orange represents negative correlation (light orange: -0.10 to -0.49, dark orange: -0.50 to -0.99).

Correlation	Au	Ag	As	Cu	Fe	Hg	Re	S	Sb	Se	Te	Tl	W
Au	1.00	0.03	0.46	0.30	0.24	0.51	-0.16	0.34	-0.81	-0.07	0.30	0.62	0.15
Ag	0.03	1.00	-0.04	0.01	-0.11	0.10	-0.02	-0.01	0.16	0.21	0.25	-0.01	0.00
As	0.46	-0.04	1.00	0.15	0.58	0.64	-0.11	0.61	-0.12	-0.07	0.14	0.45	0.14
Cu	0.30	0.01	0.15	1.00	0.35	0.05	-0.20	0.04	-0.06	-0.06	0.04	-0.03	0.15
Fe	0.24	-0.11	0.58	0.35	1.00	0.49	-0.01	0.69	-0.18	-0.13	-0.03	0.35	0.17
Hg	0.51	0.10	0.64	0.05	0.49	1.00	0.20	0.75	-0.07	0.04	0.41	0.74	0.03
Re	-0.16	-0.02	-0.11	-0.20	-0.01	0.20	1.00	0.24	0.16	0.22	0.20	0.20	-0.09
S	0.34	-0.01	0.61	0.04	0.69	0.75	0.24	1.00	0.00	0.11	0.27	0.69	0.11
Sb	-0.81	0.16	-0.12	-0.06	-0.18	-0.07	0.16	0.00	1.00	0.78	0.52	-0.01	-0.03
Se	-0.07	0.21	-0.07	-0.06	-0.13	0.04	0.22	0.11	0.78	1.00	0.66	0.03	-0.02
Te	0.30	0.25	0.14	0.04	-0.03	0.41	0.20	0.27	0.52	0.66	1.00	0.37	0.06
Tl	0.62	-0.01	0.45	-0.03	0.35	0.74	0.20	0.69	-0.01	0.03	0.37	1.00	0.08
W	0.15	0.00	0.14	0.15	0.17	0.03	-0.09	0.11	-0.03	-0.02	0.06	0.08	1.00

Table 4. Correlation matrix for data from 607 samples with Ag >0.05 opt (1.72 ppm). Blue represents 1 to 1 correlation, dark green represents 0.50-0.99 correlation, light green represents 0.10-0.49 correlation. Orange represents negative correlation (light orange: -0.10 to -0.49, dark orange: -0.50 to -0.99).

Correlation	Ag	Au	As	Cu	Fe	Hg	Re	S	Sb	Se	Te	Tl	W
Ag	1.00	0.08	0.00	-0.12	-0.09	0.13	0.06	0.07	0.16	0.21	0.32	0.07	0.00
Au	0.08	1.00	0.33	0.02	0.21	0.42	0.03	0.31	0.07	0.06	0.42	0.51	0.09
As	0.00	0.33	1.00	-0.09	0.53	0.59	0.14	0.59	0.04	0.09	0.27	0.54	0.05
Cu	-0.12	0.02	-0.09	1.00	0.11	-0.23	-0.25	-0.29	-0.12	0.04	-0.21	-0.16	-0.01
Fe	-0.09	0.21	0.53	0.11	1.00	0.53	0.15	0.70	-0.02	0.09	0.15	0.39	0.02
Hg	0.13	0.42	0.59	-0.23	0.53	1.00	0.43	0.78	0.10	0.24	0.55	0.83	0.04
Re	0.06	0.03	0.14	-0.25	0.15	0.43	1.00	0.43	0.18	0.30	0.35	0.36	-0.01
S	0.07	0.31	0.59	-0.29	0.70	0.78	0.43	1.00	0.14	0.28	0.42	0.64	0.05
Sb	0.16	0.07	0.04	-0.12	-0.02	0.10	0.18	0.14	1.00	0.67	0.51	0.15	0.00
Se	0.21	0.06	0.09	0.04	0.09	0.24	0.30	0.28	0.67	1.00	0.58	0.20	-0.01
Te	0.32	0.42	0.27	-0.21	0.15	0.55	0.35	0.42	0.51	0.58	1.00	0.54	0.04
Tl	0.07	0.51	0.54	-0.16	0.39	0.83	0.36	0.64	0.15	0.20	0.54	1.00	0.08
W	0.00	0.09	0.05	-0.01	0.02	0.04	-0.01	0.05	0.00	-0.01	0.04	0.08	1.00

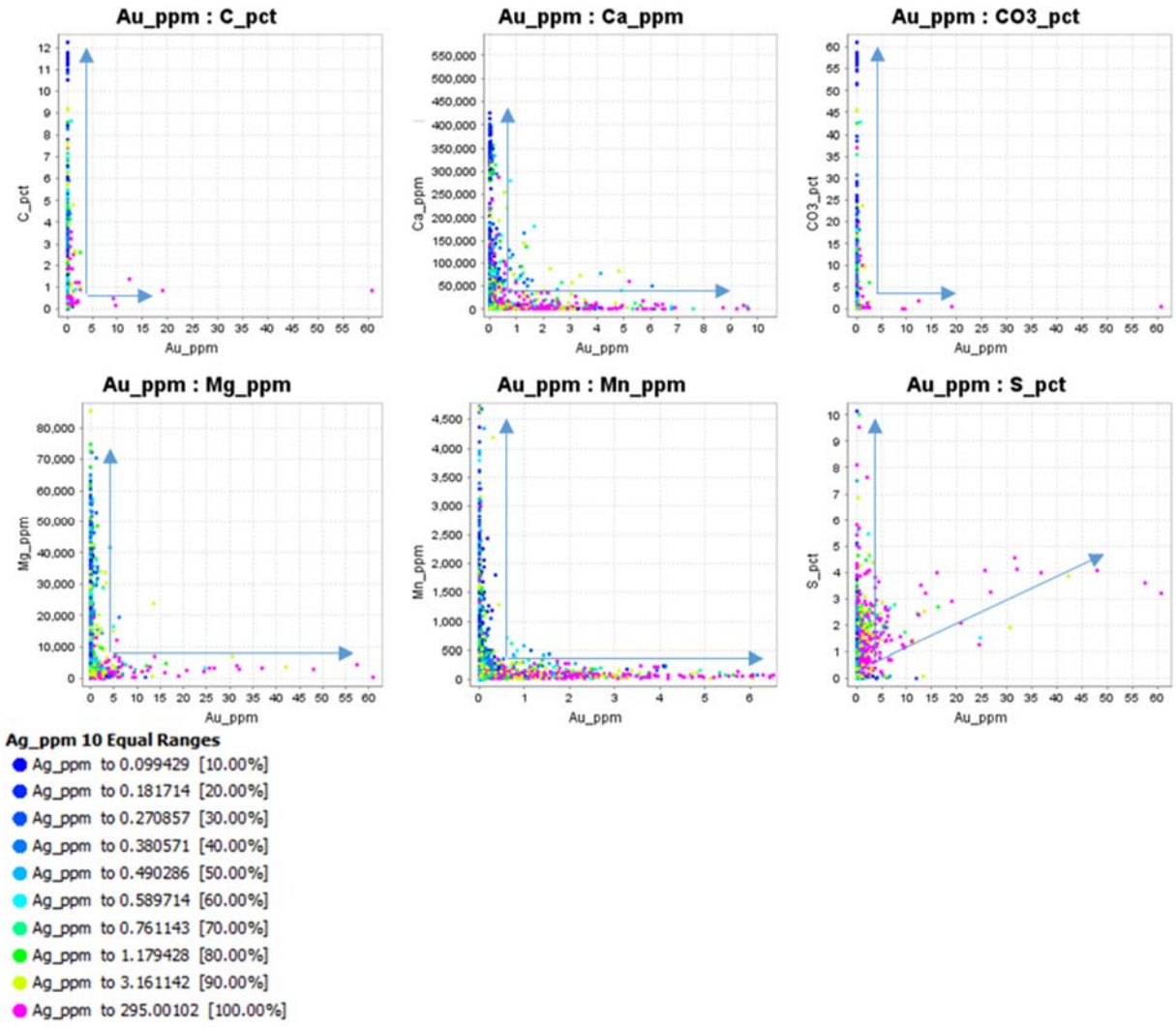

Figure 33. Scatter plots of Au vs. suite 3, the alteration suite, showing no correlation between each element, except S, to gold. S has a positive correlation to gold. Dot colors represent Ag values.

Suite 3 was plotted against Au to examine its relationship with mineralization. C, Ca, CO_3, Mg, and Mn have vertical and horizontal trends with no correlation (Figure 33). Sulfur has a vertical trend and a positive inclined trend, indicating that some sulfur is positively correlated with mineralization, and some S is not associated with Au. This is consistent with the presence of diagenetic pyrite and the later input of sulfur associated with mineralization (Teal and Jackson, 2002).

Table 5. Codes for unit-lithologies identified by Barrick Goldstrike, with short description of the units and corresponding lithologies.

Code	Unit	Lith
TGU-TG	Tertiary Carlin Formation Gravels Unit	Carlin Gravels
TGU-QT	Tertiary Carlin Formation Gravels Unit	Quartzite
TFU-TF	Tertiary Carlin Formation Ashfall Tuff Unit	Carlin Ashfall Tuff
OVU-SHF	Vinini Formation Undifferentiated Unit	Shear/Cataclastic Fabric
OVU-MS	Vinini Formation Undifferentiated Unit	Mudstone
OVU-CT	Vinini Formation Undifferentiated Unit	Clay
OVU-BX	Vinini Formation Undifferentiated Unit	Breccia
AA-SHF	Rodeo Creek Upper Argillite Unit	Shear/Cataclastic Fabric
AA-MS	Rodeo Creek Upper Argillite Unit	Mudstone
AA-LSL	Rodeo Creek Upper Argillite Unit	Laminated Limey Siltstone
AA-LM	Rodeo Creek Upper Argillite Unit	Limey Mudstone
BS-ST	Rodeo Creek Bazza Sandstone Unit	Siltstone
BS-SS	Rodeo Creek Bazza Sandstone Unit	Sandstone
BS-MS	Rodeo Creek Bazza Sandstone Unit	Mudstone
BS-LST	Rodeo Creek Bazza Sandstone Unit	Limey Siltstone
BS-LM	Rodeo Creek Bazza Sandstone Unit	Limey Mudstone
BS-BX	Rodeo Creek Bazza Sandstone Unit	Breccia
AM-MS	Rodeo Creek Lower Argillite-Mudstone Unit	Mudstone
AM-BX	Rodeo Creek Lower Argillite-Mudstone Unit	Breccia
DRCU-ST	Rodeo Creek Formation Undifferentiated Unit	Siltstone
DRCU-MS	Rodeo Creek Formation Undifferentiated Unit	Mudstone
DRCU-LST	Rodeo Creek Formation Undifferentiated Unit	Limey Siltstone
DRCU-LM	Rodeo Creek Formation Undifferentiated Unit	Limey Mudstone
DRCU-BX	Rodeo Creek Formation Undifferentiated Unit	Breccia
DRCBX-BX	Rodeo Creek Undifferentiated Mixed Unit Breccia	Breccia
BXU-SSBX	Mixed Formation Breccia Unit	Silica sulfide breccia
BXU-SBX	Mixed Formation Breccia Unit	Silicified Limestone Breccia
BXU-CT	Mixed Formation Breccia Unit	Chert
SDB-LS	Roberts Mountain Bootstrap Limestone Unit	Undiff. Limestone
SDB-BX	Roberts Mountain Bootstrap Limestone Unit	Breccia
FG (All Units)		Fault Gouge

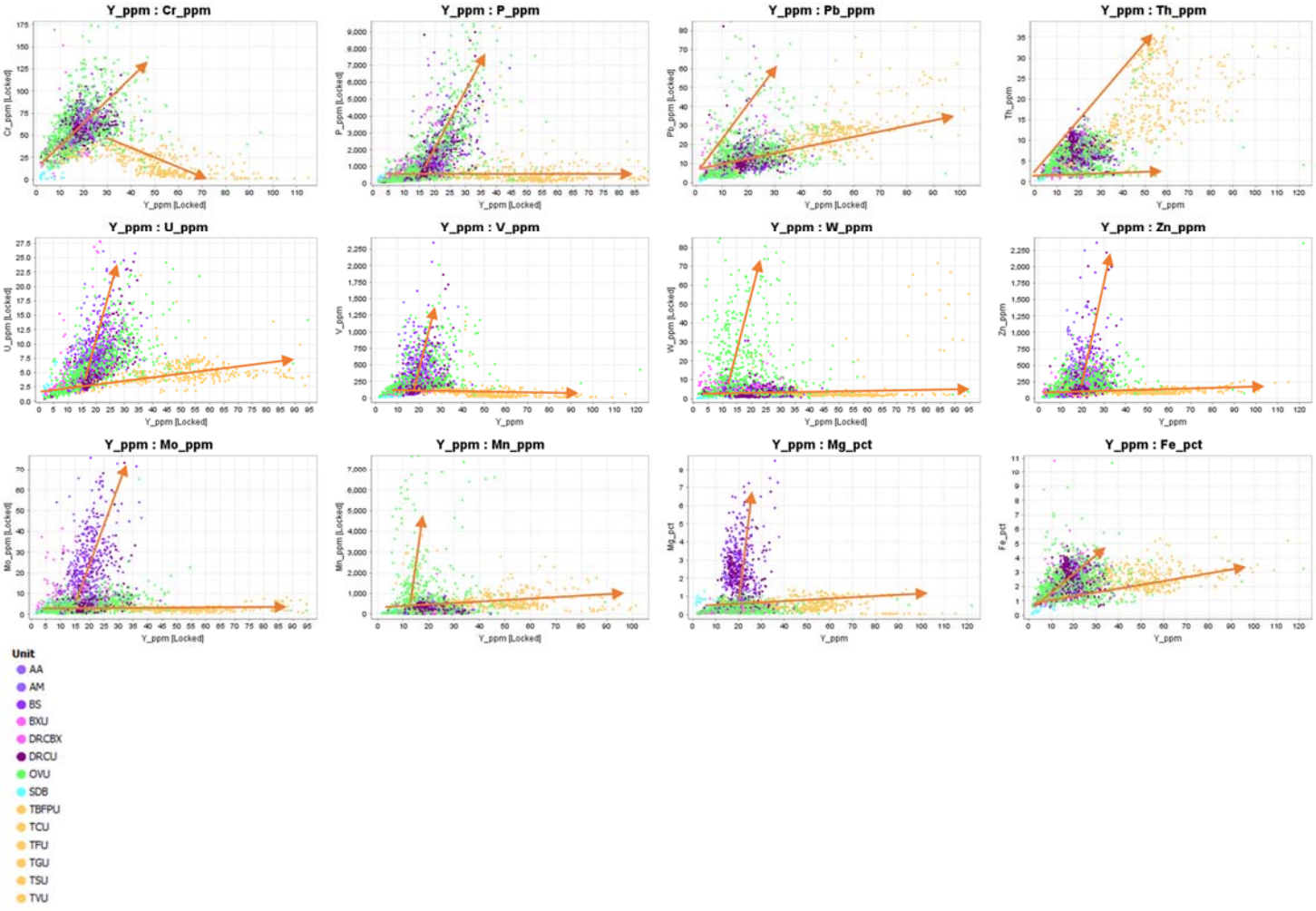

Figure 34. Scatter plots of suite 4 and Cr, Th, U, V, W, Mn, Mg, and Fe with color representing lithological units (see Table 5 for abbreviations), showing 2 positive trendlines in Y vs. Pb, U, Mn, Mg and Fe and 1 positive trendline and one horizontal trendline in Y vs. P, Th?, V, W, Zn, and Mo. Y vs. Cr appears to be the only plot with a negative trendline in the data. The positive trendlines for U, V, W, Zn, Mo, Mn, and Mg appears to begin at around 15 ppm Y, as opposed to the origin (0,0) in the rest.

Scatter plots of suite 4 (Mo, P, Pb, Y and Zn) and Cr, Th, U, V, W, Mn, Mg, and Fe (Figure 34) (chosen after trial plots demonstrated correlations) demonstrate two positive trendlines in Y vs. Pb-U-Mn-Mg-Fe and 1 positive trendline and one horizontal trendline in Y vs. P-(Th?)-V-W-Zn-Mo. Y was chosen after trial plots demonstrated the clearest correlations. In all cases except thorium, the lower slope trendline and the highest Y values represents data from Tertiary samples, while the steeper slope is a mix of Vinini and Rodeo Creek samples. Y vs. Cr appears to be the only plot with a negative trendline and that is only in data from Tertiary samples. The positive trendlines for U, V, W, Zn, Mo, Mn, and Mg appears to begin at around 15 ppm Y, as opposed to the origin (0,0) in Cr, P, Pb, Th, and Fe. Zn, Mo, and Mg have steep slopes in the Lower Plate rocks and a shallow slope in the Upper Plate, whereas W has a steep slope in the Upper Plate and a shallow slope in the Lower Plate.

4.4 Geochemical Markers of Clay and Sulfide Mineralogy

Figure 35 shows that most samples from the Button Hill mining area, regardless of grade, have a K_2O/Al_2O_3 ratio that is consistent with a clay mineralogy dominated by sericite. There are exceptions that fall low of the sericite line close to the K-smectite line, but nothing falls above or below these two lines. This is contrasted with samples from the Screamer Zone of the Betze Pit (Hofstra, et al., 2010), just 7 km south of the Button Hill deposit. These zones have much more variation in K_2O/Al_2O_3 ratio, with many of the high-grade samples falling along the kaolinite line.

Fe/Ti : Si/Ti ratios from the Button Hill deposit (Figure 36) show that sulfide mineralogy falls between pyrite and Fe-silicate/iron-oxide with much of the samples falling along the pyrite line when from the lower plate, and along the iron line if from the upper plate, possibly suggesting that sulfur from sulfides has been weathered out in the upper plate oxide zone. High grade samples

(shown in pink) do not appear to discriminate between pyrite, pyrrhotite/arsenopyrite and iron oxides/silicates at the Button Hill.

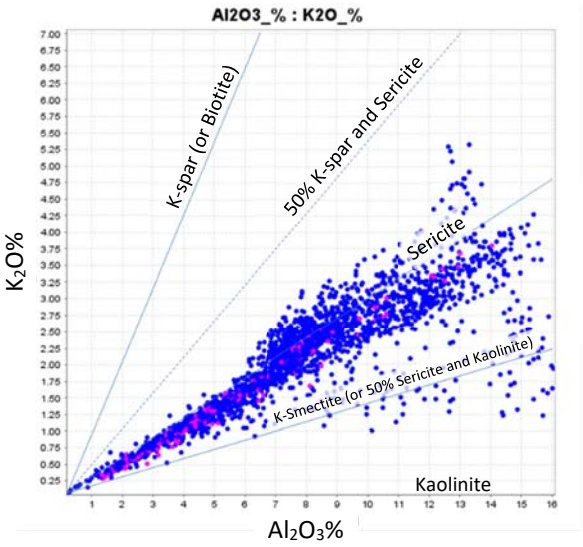

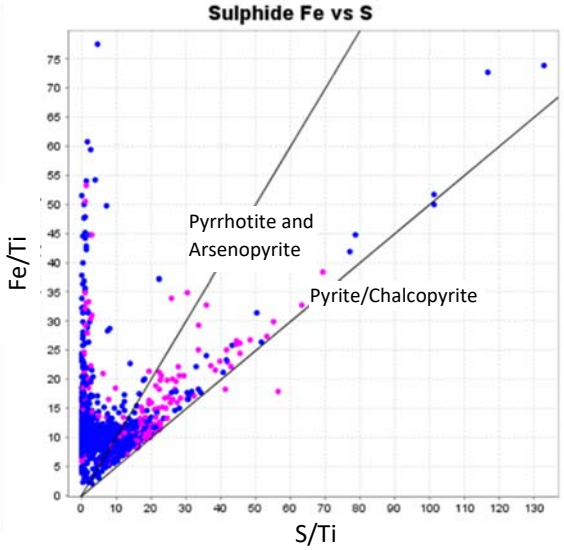

Figure 35 (left). K2O wt% versus Al2O3 wt% from Button Hill shows that a large majority of all samples, regardless of grade, falls along the sericite line. Some samples plot low on the K-smectite line; however, none of these are associated with significant gold grade. Pink dots show 98 percentile concentration Au. Blue dots represent <98 percentile Au.

Figure 36 (right). S/Ti wt% versus Fe/Ti wt% to show sulfide mineralogy (Fe vs. S) of Button Hill samples. High grade samples are not limited to one ratio, falling along the pyrite line, the pyrrhotite/arsenopyrite line and plotting in the purely Fe field. Pink dots show 98 percentile concentration Au. Blue dots represent <98 percentile Au.

4.5 Down-Hole Geochemical Variation Plots

Down-hole geochemical variation plots for two drill-holes (BD13-01 and BD13-15) that intersect the Button Hill ore body are compared to units and lithologies identified by Barrick Goldstrike from reverse circulation rock chips.

A down-hole plot of suite 1 (lithogeochemistry), including Al, Fe, Th, Ti, Zr, Nb, Ce, and La (Figure 37a), shows that variation in chemistry is somewhat predictable with changing lithologies; however, contains some variability within each lithology.

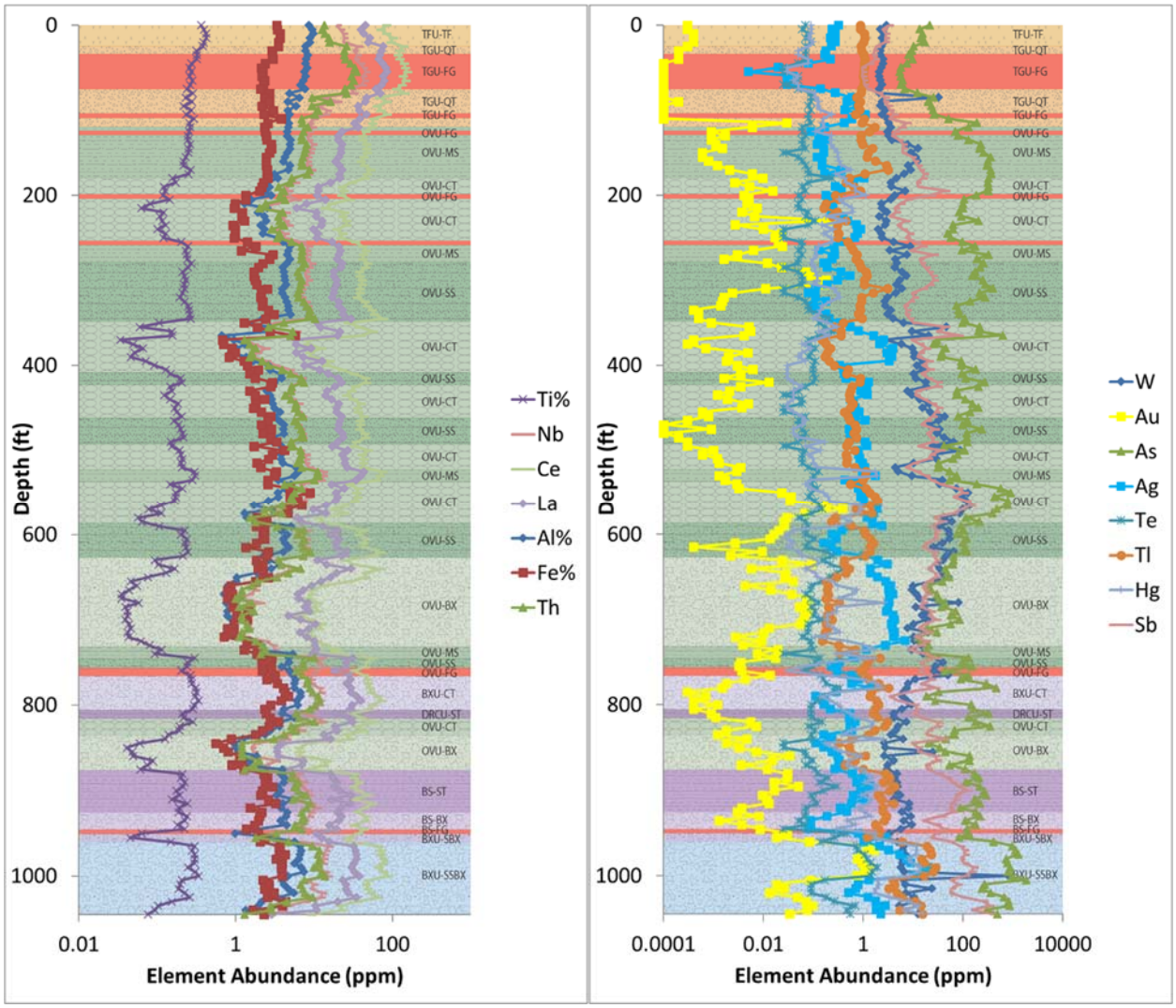

Figure 37. Hole number BD13-15. Down-hole plot of lithogeochemical variation (left) and mineralization suite (right) plotted against unit-lithology in the Button Hill deposit. In the background stratigraphic column, orange represents Tertiary units, green for Vinini Formation, purple for Rodeo Creek Formation, blue represents Bootstrap Formation and red is for faults. See Table 5 for unit-lithology abbreviations.

The mineralization suite (Figure 37b) is also somewhat controlled by lithology; however, has much greater variability within each unit. On average, in a mineralized drill-hole, Au increases gradually with depth in the Rodeo Creek Formation, increases to a maximum just above the silicified breccias, and decreases gradually as it approaches the Bootstrap limestone, creating a broad "hump" in Au abundance over 200' to 300' of section (Figure 38). Ag generally increases with Au; however, rarely has the exact shape as Au. In Figure 38, highest Ag is below the level of

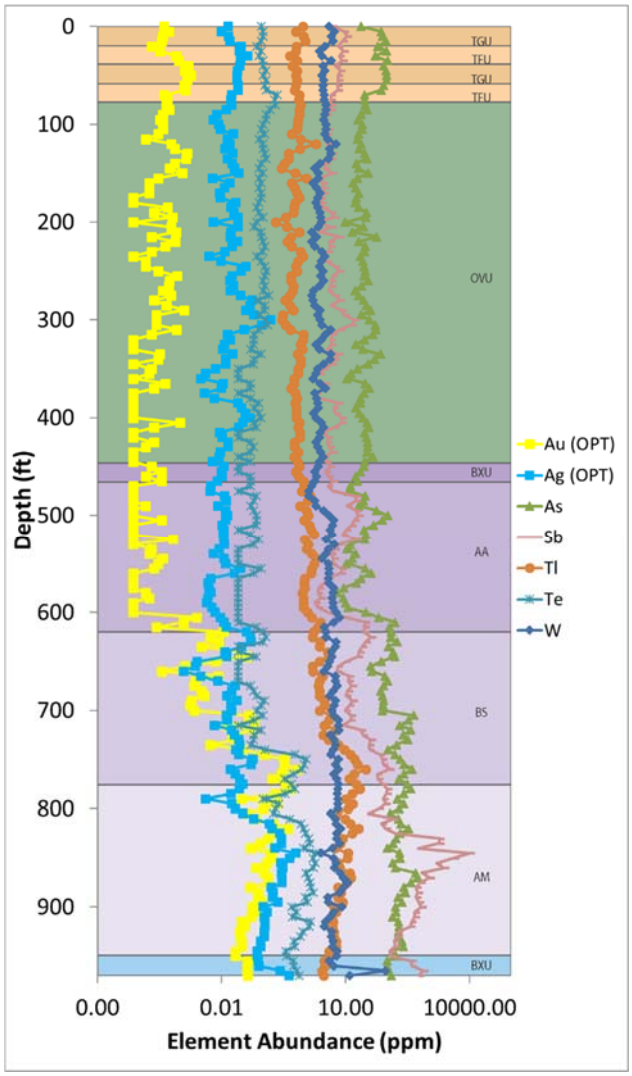

Figure 38. Down-hole plot for hole BD13-01 with element abundance on the y-axis and depth on the x-axis for the mineralization suite (suite 2). Gray stripes represent breaks in lithologies. In the background stratigraphic column, orange represents Tertiary units, green for Vinini Formation, purple for Rodeo Creek Formation and blue represents Bootstrap Formation. See Table 5 for unit abbreviations.

peak Au. Te is typically associated with both Au and Ag. This can best be seen in Figure 38 where Te increases with Au at a depth of ~700-750 ft. and increases again when Ag starts to increase at approximately 800 ft. Arsenic very often closely mimics gold in down-hole plots. The broad "hump" shape of As is either exactly in-line with Au (Figure 38) or slightly wider than gold. Tl also mimics Au; however, doesn't usually appear to increase until Au values reach approximately 0.5-1 ppm or greater (Figure 37b and Figure 38). The association of W to Au or Ag is much less

obvious. There appears to be a very minor increase in W with higher Au values; however, W values do not always increase with Au and are often high at depth intervals with minor Au values. Hg appears to mimic Ag value patterns in most down-hole plots; however, also appears to have areas of increased abundance where Ag is minor. Sb appears to have a general pattern of increase abundance where Au and Ag are enriched; however, it often peaks at the margin of the Au zone. In Figure 38, Sb has a minor spike above anomalous Au and a larger peak at the lower margin of the Au zone. This pattern is recurring in many of the drill-holes analyzed.

4.6 Box Plots

The mean, median, standard deviation, Q1 and Q3 were calculated for each of the immobile and mineralization suite elements to examine whether there is a systematic difference in element concentrations associated with changing lithologies for the entire data-set. Each of the naming conventions is from, and unit-lithology identification was completed by, Barrick Goldstrike (Table 5).

The following box plots show how each element changes with unit-lithology (Figure 39). Variation in lithogeochemistry is visually apparent in the box-plots; however, only a few unit-lithologies show a significant difference. Typically, the Bootstrap Formation (SDB) demonstrate lower concentrations of suite 1, especially in the limestone lithology. Rodeo Creek Lower argillite-mudstone breccia (AM-BX) and Ordovician Vinini breccia (OVU-BX) also have lower concentrations. The other OVU lithologies also appear to have slightly lower concentrations of suite 1, while the Tertiary Carlin lithologies are slightly higher. The remaining unit-lithologies show very little to no variation and a large amount of overlap within the spread of the data-set.

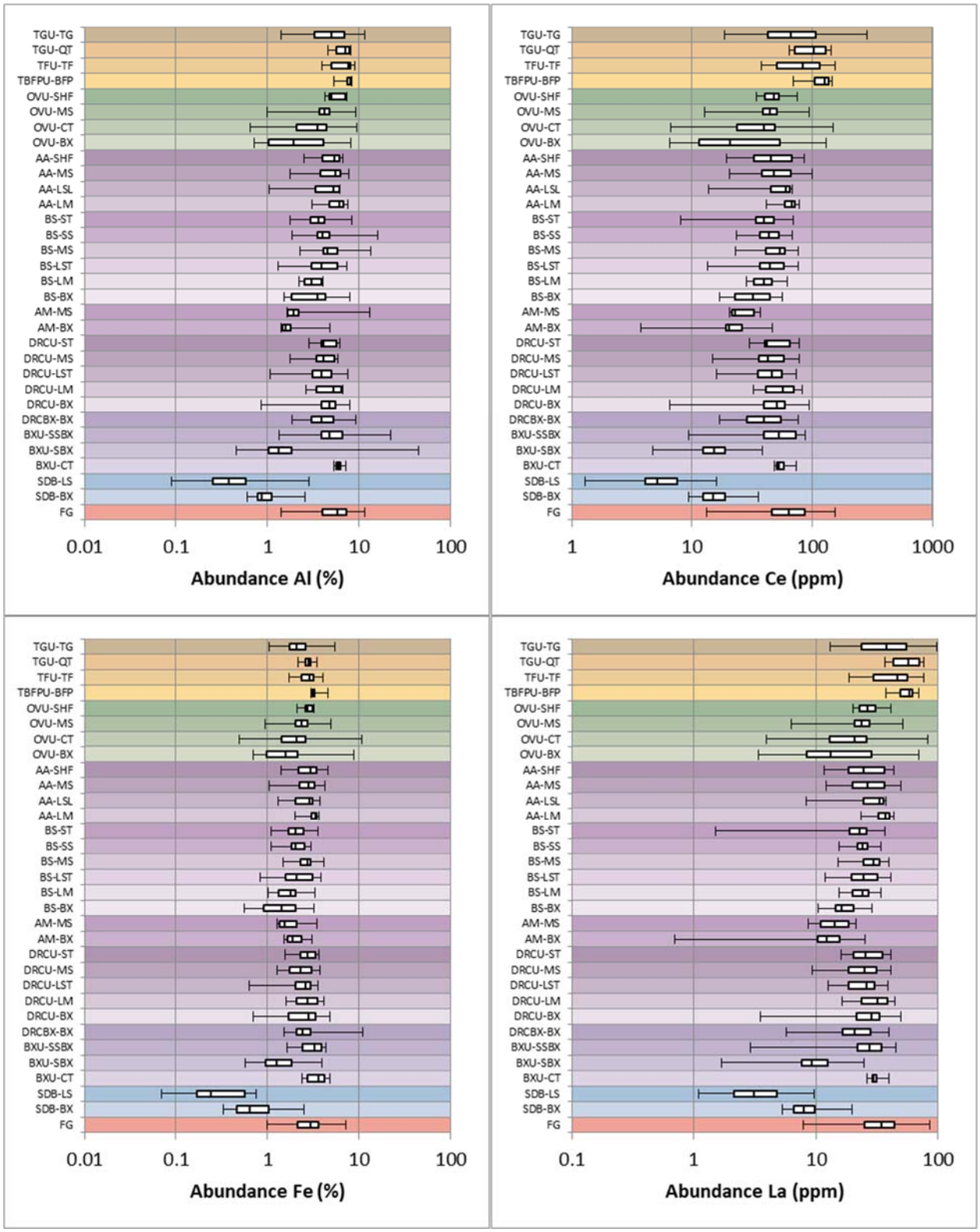

Figure 39. Box-plots of lithogeochemistry elements for each unit-lithology identified by Barrick Goldstrike.

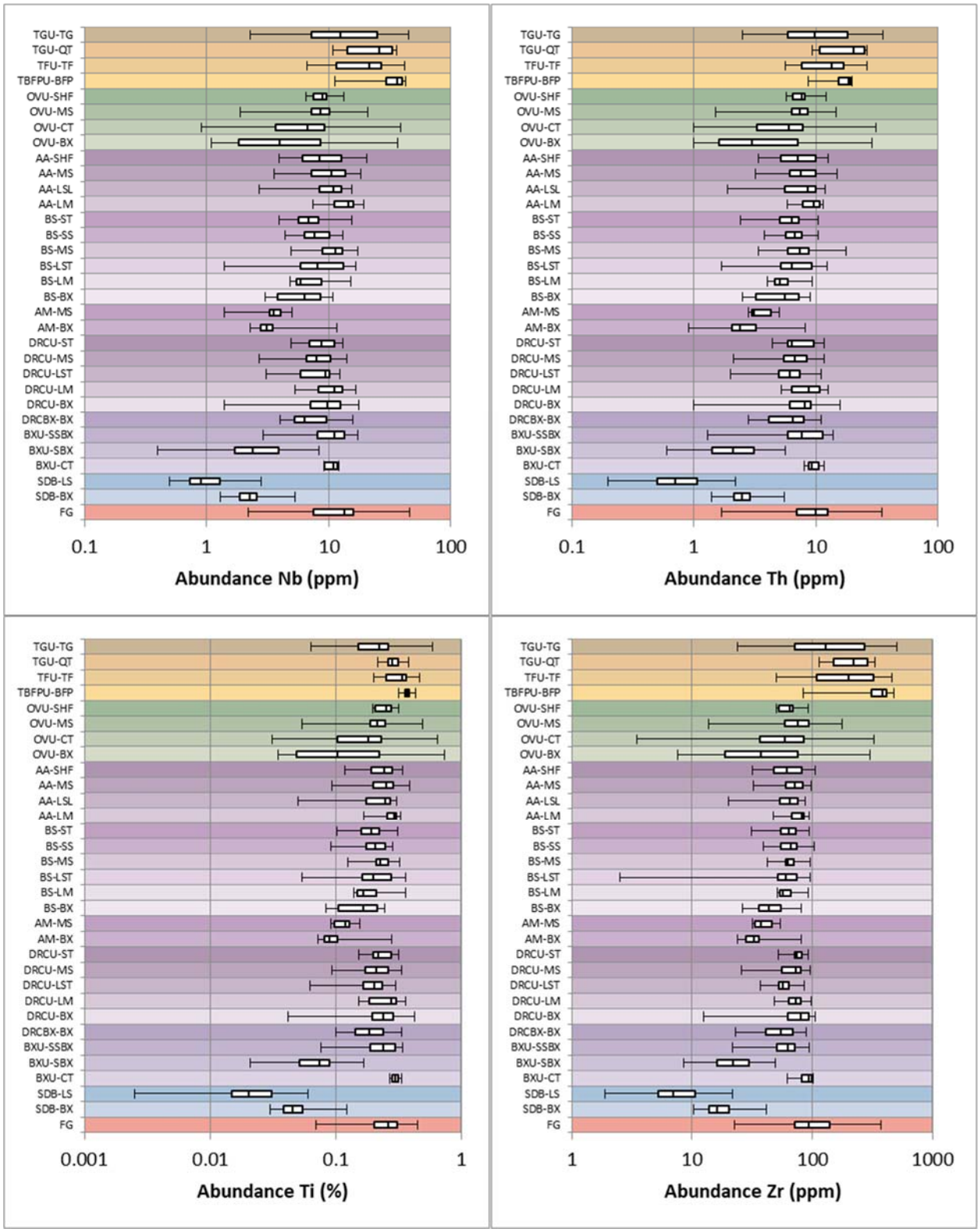

Figure 40. Box-plots of lithogeochemistry elements for each unit-lithology identified by Barrick Goldstrike.

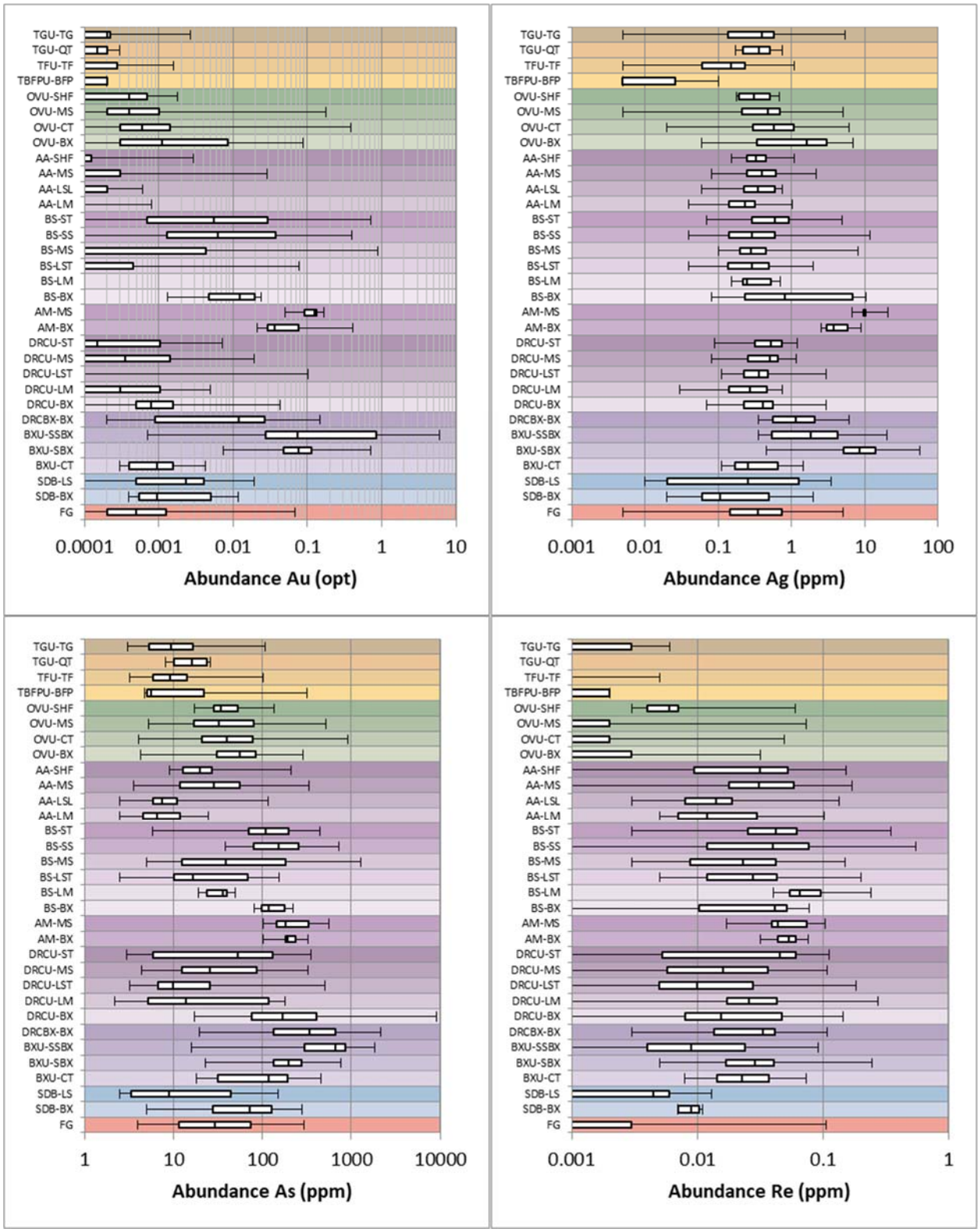

Figure 41. Box-plots of mineralization suite elements (suite 2) for each unit-lithology identified by Barrick Goldstrike.

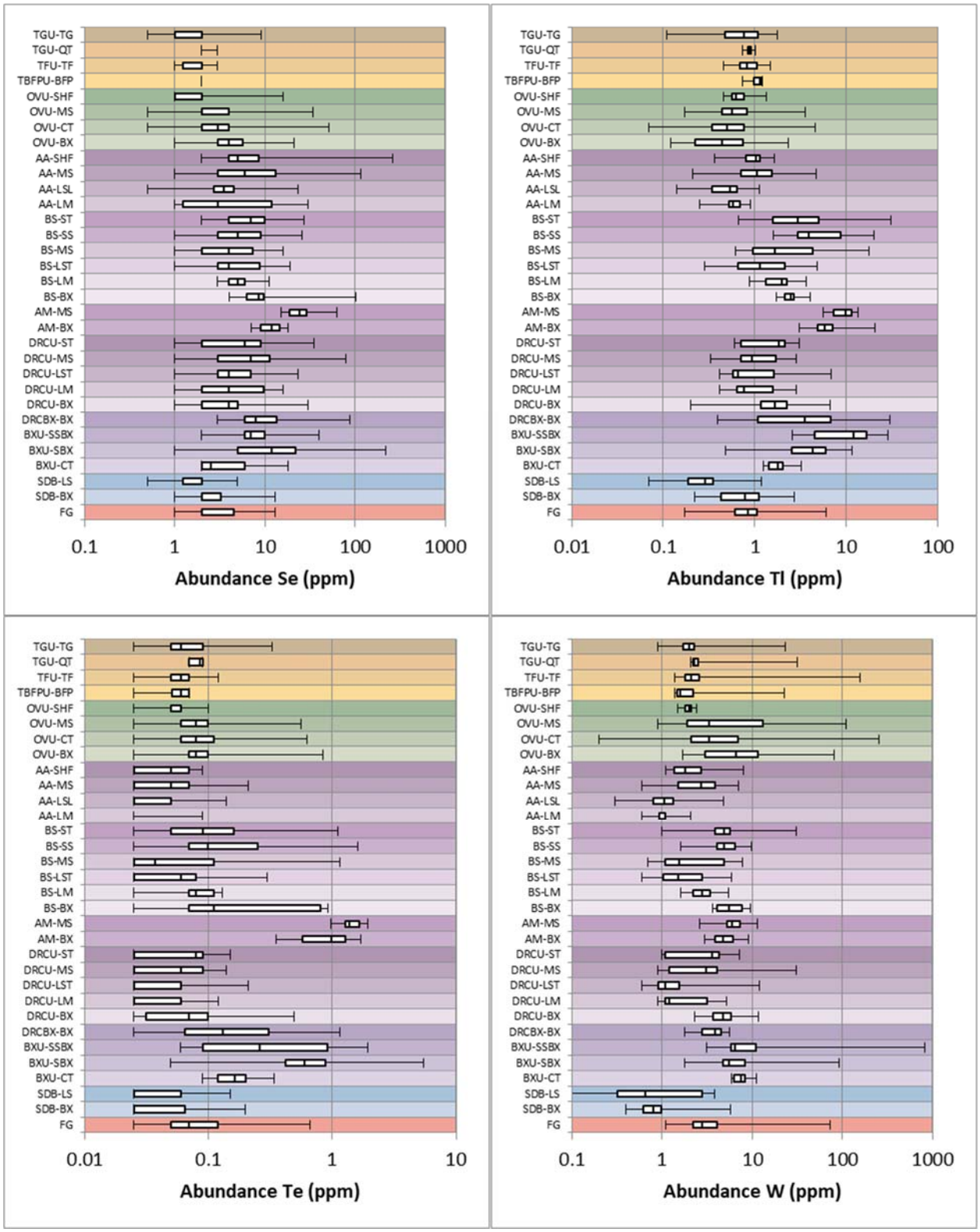

Figure 42. Box-plots of mineralization suite elements (suite 2) for each unit-lithology identified by Barrick Goldstrike.

Mineralization suite element box-plots (Figure 41 and Figure 42) demonstrate the major hosts for Au and Ag. The primary host for Au is the silica sulfide breccia (BXU-SSBX) but is also hosted in silicified limestone breccia (BXU-SBX), Rodeo Creek (RC) lower argillite-mudstone (AM-MS), RC lower argillite-mudstone breccia (AM-BX), with minor contributions from the RC Bazza sandstone and even the upper-plate Ordovician Vinini muds, cherts and breccias. As and Tl mimic this pattern closely.

The major host to Ag (Figure 41) and Se (Figure 42) is the BXU-SBX, AM-MS, RC Bazza sandstone breccia (AM-BX) with minor contributions from many other units that include upper-plate Vinini, and lower-plate Bazza sandstone units, and DRCU units.

Tungsten (Figure 42) has high values in the SSBX, SBX, and AM units; however, the highest values are in the upper plate. Rhenium (Figure 41) also has high values in SBX and AM but has very low values in SSBX and the upper plate with the highest values in the RC Bazza Sands Limey Mudstone (BS-LM). Tellurium (Figure 42) has the highest values in AM-MS, AM-BX, SSBX, and SBX, again, appearing to mimic both silver and gold.

4.7 Grant Isocon and Enrichment Factor Score

The following Grant Isocon plots for the geochemical data is created using the Gresens' (1967) and Grant's (1986; 2005) methods. Samples are compared to averaged unaltered samples of the Rodeo Creek Formation (see Ch. 2.3.5 for method).

Grant isocon mass balance plots of unaltered Rodeo Creek Formation versus median brecciated (Bx1, Bx1a, Bx2) Rodeo Creek Formation values (Figure 43) are consistent with the results of the PCA and show which suites of elements are enriched and which are depleted. Suite 2 (Ag, Au, Cu, As, Sb, Te, Se, Tl, W, together with S) shows on average enrichment in the breccias whereas suite 3 (Ca, Mg, and Mn) (less S) and suite 4 (P, Zn, Y, and Mo (less Pb)), plus U, V, and

Sr, show depletion. Suite 1 (Fe, Ce, Al, La, Ti, Nb, Zr and Th) lies on the isocon and thus are immobile in these hydrothermal systems (Grant, 1986; Grant, 2005). Other apparently enriched elements include Li, Bi, Ga, and Be. K, Th, and Pb; however, are within error of the isocon. Other apparently depleted elements include Sr, Cd, V, U, Ni, Ba, and In. Ge, and In are also within error of the isocon.

The slope of m_i=0.8846 of the isocon (best fit line between Al-Ti-Zr), assuming constant Al, Ti and Zr ratios, equates to a 13% average increase of mass due to alteration in the breccias $(((1/m_i)-1)*100)$.

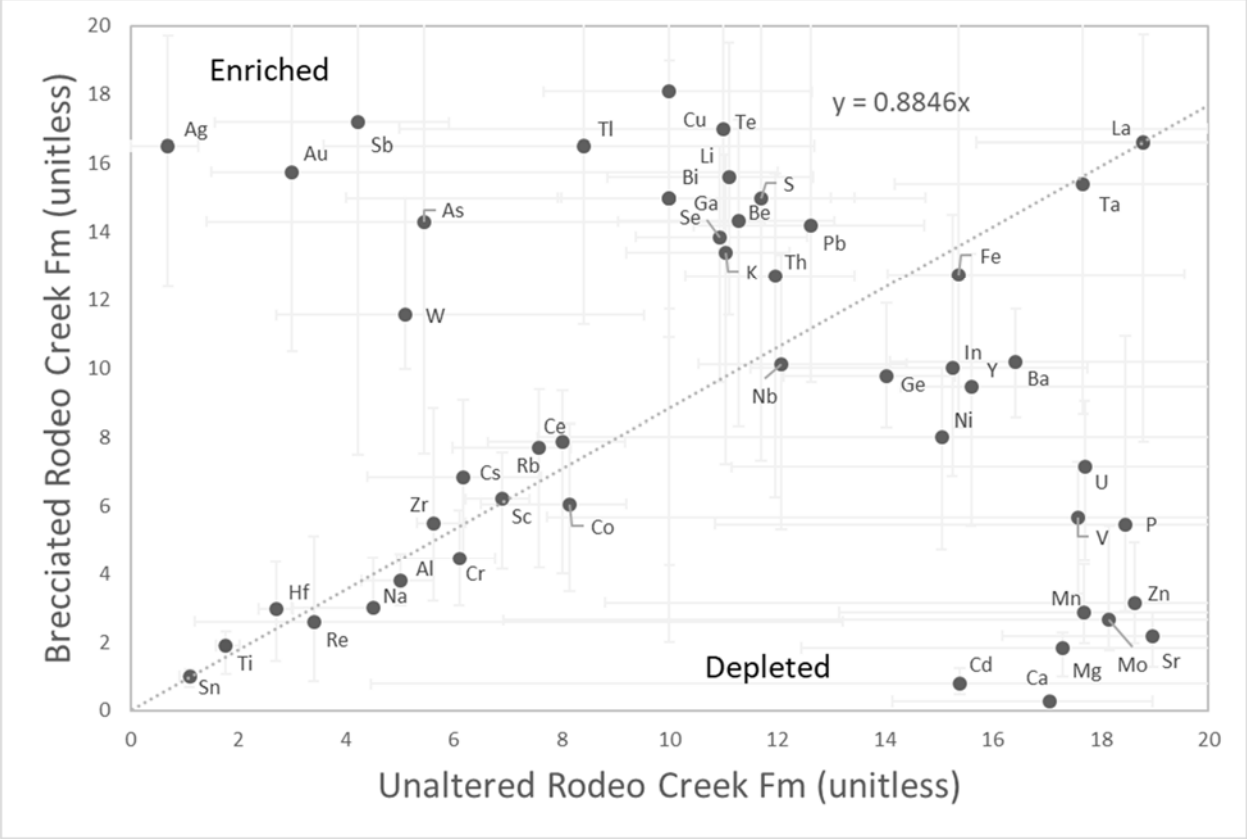

Figure 43. Grant Isocon mass balance plots of whole-rock geochemistry of core from unaltered Rodeo Creek Formation versus brecciated (breccia undifferentiated) Rodeo Creek Formation shows enrichment in mineralization suite, depletion in anoxic elements and elements associated with carbonates (Ca, Mg, Mn, and Sr), and no change in lithogeochemistry (immobile) elements. Error bars shown are calculated from the 1st and 3d quartiles of the dataset. Values on the x- and y-axes are ratios and so are unitless. The slope of m=0.8846 equates to approximately 13% increase of mass of the rock.

The following enrichment factor scores for the geochemical data is a quantified variation of the Gresens' (1967) and Grant's (1986; 2005) methods (see Ch. 2.3.5 for method). Because the unaltered sample in which all the altered samples are compared to is from the Rodeo Creek, only samples from the Rodeo Creek are considered to be enriched or depleted based on the EFS. All samples from other units are normalized to the same standard; however, are not assumed to have been enriched or depleted.

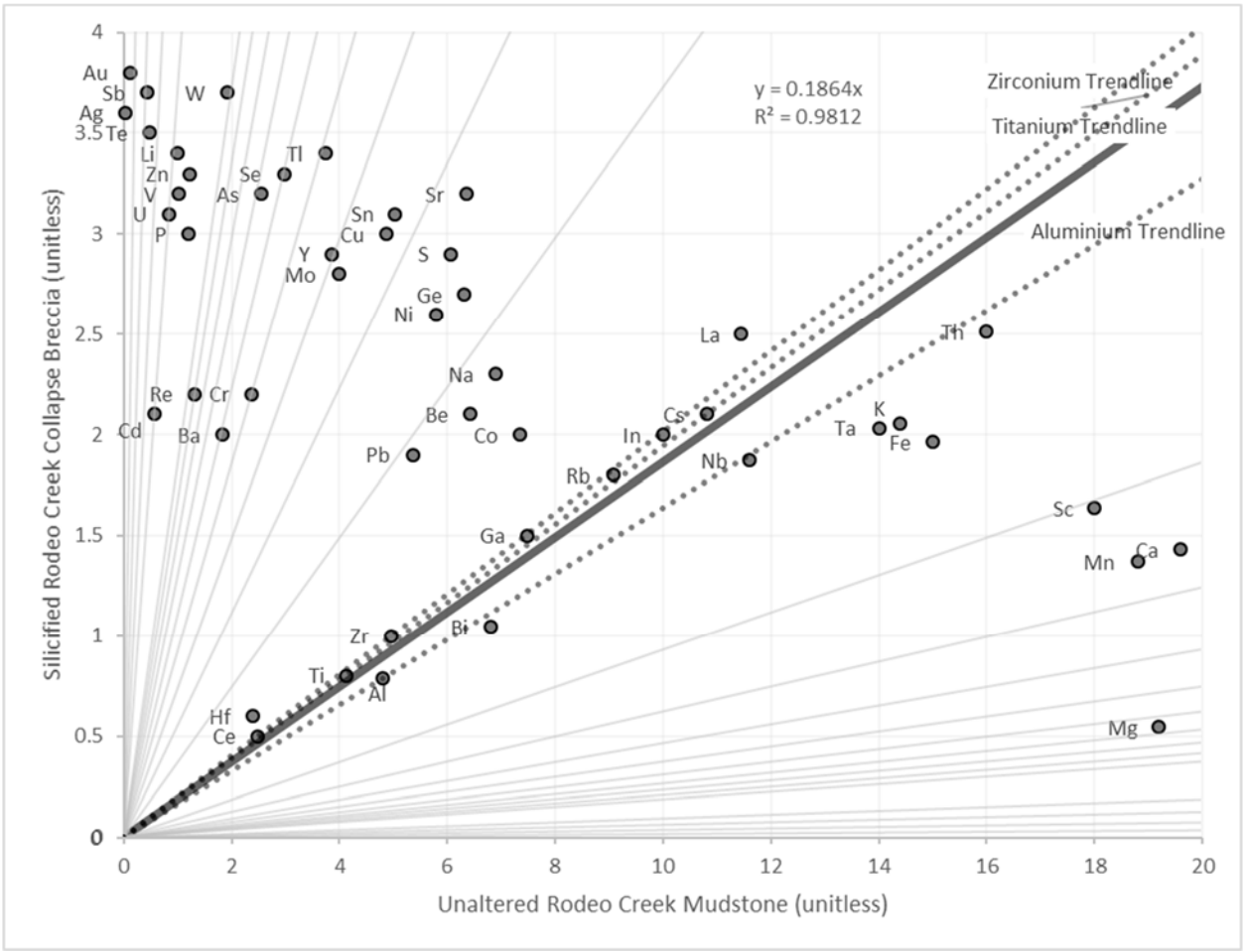

Figure 44. Grant isocon plot of sample BD15-053_875.4-876, a Bx3a breccia, establishing enrichment in Au, Ag, Sb, Te, W, Li, Tl, Se, and As (mineralization), and Zn, V, U, P, Mo, Y, and Pb (anoxic deposition). Ca, Mg, and Mn have been depleted, likely due to decalcificaiton. This figure is to demonstrate the way in which the following EFS diagrams are created. The dark line represents the isocon, a best fit trend-line for Al, Ti, and Zr, and light gray lines show factors of enrichment (above isocon) and depletion (below isocon). The EFS is based on the slope of the line in which the element lies compared to the slope of the isocon.

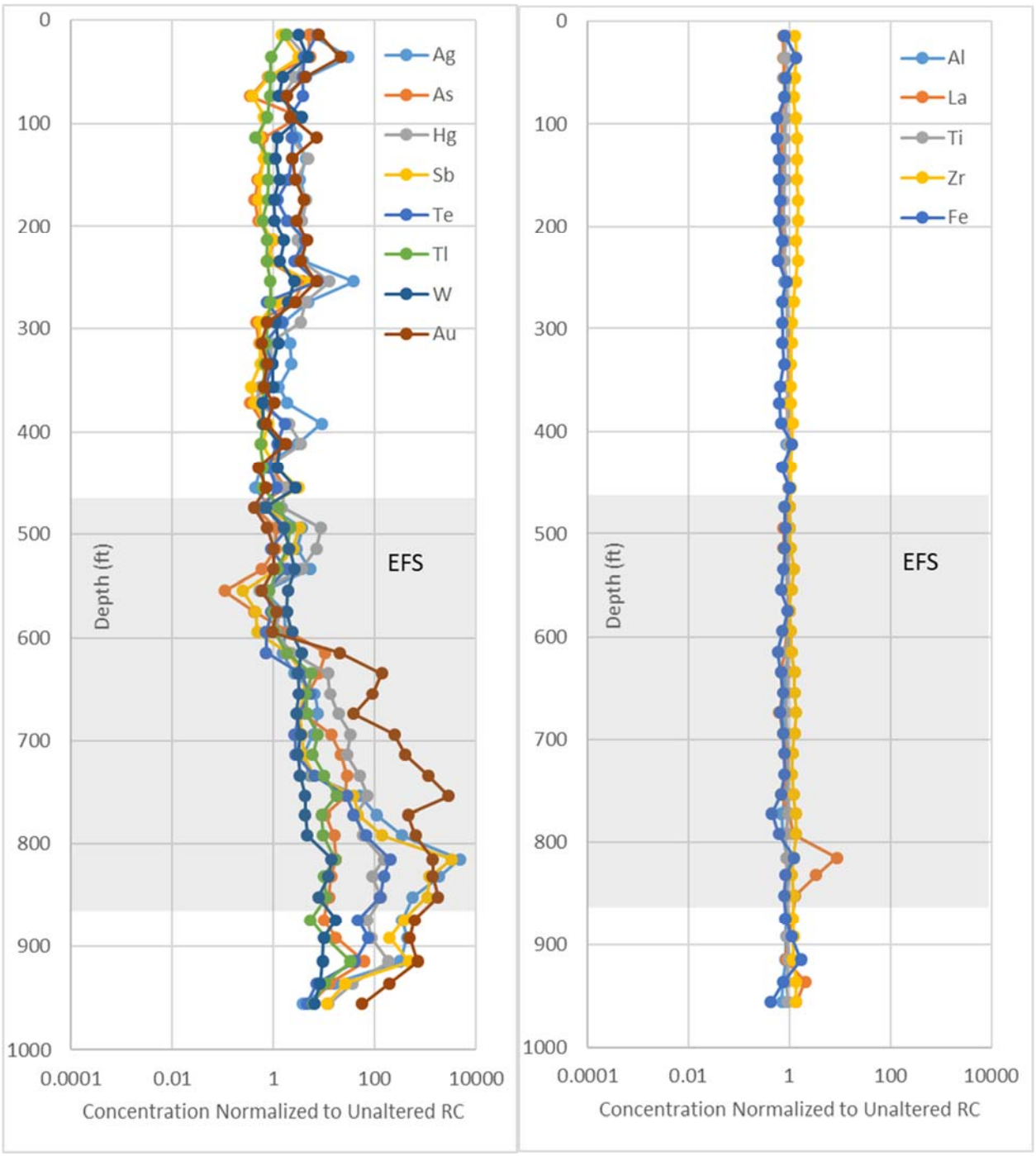

Figure 45. Down-hole plots of concentrations normalized to unaltered Rodeo Creek Formation for hole BD15-052. A (left) shows the mineralization suite (suite 2). B (right) shows the lithogeochemistry suite (suite 1). The gray box shows the depths of the Rodeo Creek Formation and thus these values represent enrichment factor scores (EFS).

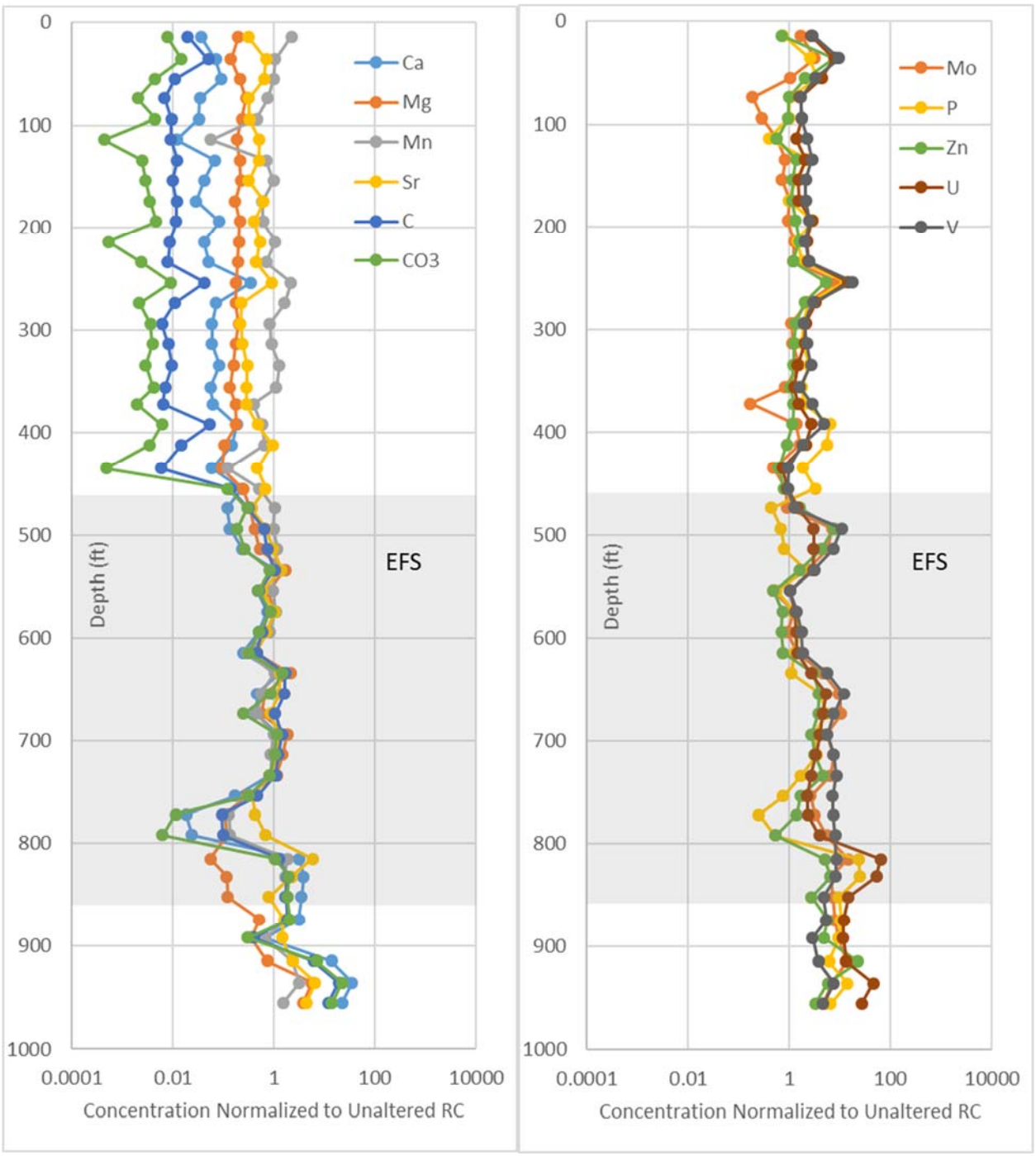

Figure 46. Down-hole plots of concentrations normalized to unaltered Rodeo Creek Formation for hole BD15-052. A (left) shows the alteration suite (suite 3). B (right) shows the anoxic deposition suite (suite 4). The gray box shows the depths of the Rodeo Creek Formation and thus these values represent enrichment factor scores (EFS).

Figure 44 is an example of a Grant Isocon plot showing enrichment of the mineralization suite (suite 2) and anoxic deposition suite (suite 4) with depletion in suite 3 (except S) due to decalcification. Immobile elements lie along the isocon, with no enrichment or depletion. The light gray lines in Figure 44 represent factors of enrichment (above the isocon) and depletion (below the isocon). The following figures show the quantified values of enrichment and depletion for each breccia type plotted relative to a now vertical isocon. Enrichment is to the right and depletion to the left.

The down-hole plot of the enrichment factor scores (EFS) of the mineralization suite in hole BD15-052 (Figure 45a) shows a similar trend as that of the raw geochemistry (Figure 37 and Figure 38). The suite is relatively un-enriched, except anomalous values at various depths throughout the hole, until a depth of about 600 ft. (~183 m) where the EFSs increase in a broad hump, until they return to background levels in the Bootstrap limestone, approximately 960 ft (~293 m) depth. Like that seen in BD13-01 (Figure 38), silver spikes after gold, when gold values begin to decrease, at a depth of 815 ft. (~248 m), which corresponds to an identified fault zone and the Bx3a hydrothermal breccia. W, Te, Sb, Hg and Ag all spike at this depth, and have a similar pattern. As and Tl have a pattern that more closely mimics Au, with no spike in this fault zone.

Al, La, Ti, Zr, and Fe (suite 1) show a surprisingly consistent EFS value of near 1 (neither enriched or depleted) in the down-hole plot (Figure 45b). La and Fe have minor exceptions with La being slightly enriched in the Ag mineralized fault and Fe deviating slightly at similar depth as that of the mineralization suite.

Suite 3 elements (C, CO_3, Ca, Mg, Mn, and Sr) have a very similar pattern in the EFS down-hole plot (Figure 46a). At approximately 450 ft. (~137 m) depth, the normalized values go from being scattered to values that are close to 1. This is the approximate depth of the Vinini-

Rodeo Creek contact. From this depth to approximately 750 ft. (~229 m), the EFS values remain close to 1 with minor spikes of depletion and enrichment that correspond to changes in lithologies within the Rodeo Creek Formation. At approximately 750-810 ft. (~229-247 m) suite 3 becomes depleted. This corresponds to the beginning of Bx1a, or the silicified zone and is likely a result of decalcification. From ~810-880 ft (~247-268 m) Ca, C, and CO_3 increase, with Sr spiking followed by a return to an EFS value of 1, and Mg remaining depleted. This zone corresponds to a high density of late calcite ± barite veining. The entire suite increases in the normalized value at the end of the hole (915-981 ft, 279-299 m), near the transition from brecciated Bootstrap limestone to unaltered Bootstrap limestone.

Mo, P, Zn, U, and V remain at normalized value near 1 for most of the down-hole plot (Figure 46b). The variations seen correspond mostly to changes in lithologies; however, the suite is slightly enriched in the mineralized zone and P and Zn are depleted in the decalcified zone (750-810 ft., 229-247 m). Interesting to note is the lack of variation in the downhole plot across unit boundaries.

Figure 47 shows the quantified change in mass along BD15-052. Proportional change in mass is estimated by the inverse of the slope of the isocon (Grant, 2005). The value remains near 0 (no change in mass), with minor spikes that may represent a difference in lithology outside of the Rodeo Creek Formation, until approximately 750 ft. (229 m) when there is an increase in mass until the end of the hole. This corresponds with silicification, visible in the core samples shown on the right of the figure. The spike at ~810 ft. (247 m) corresponds with the spike in Ag at a fault zone, and an increase in quartz vein and calcite vein density.

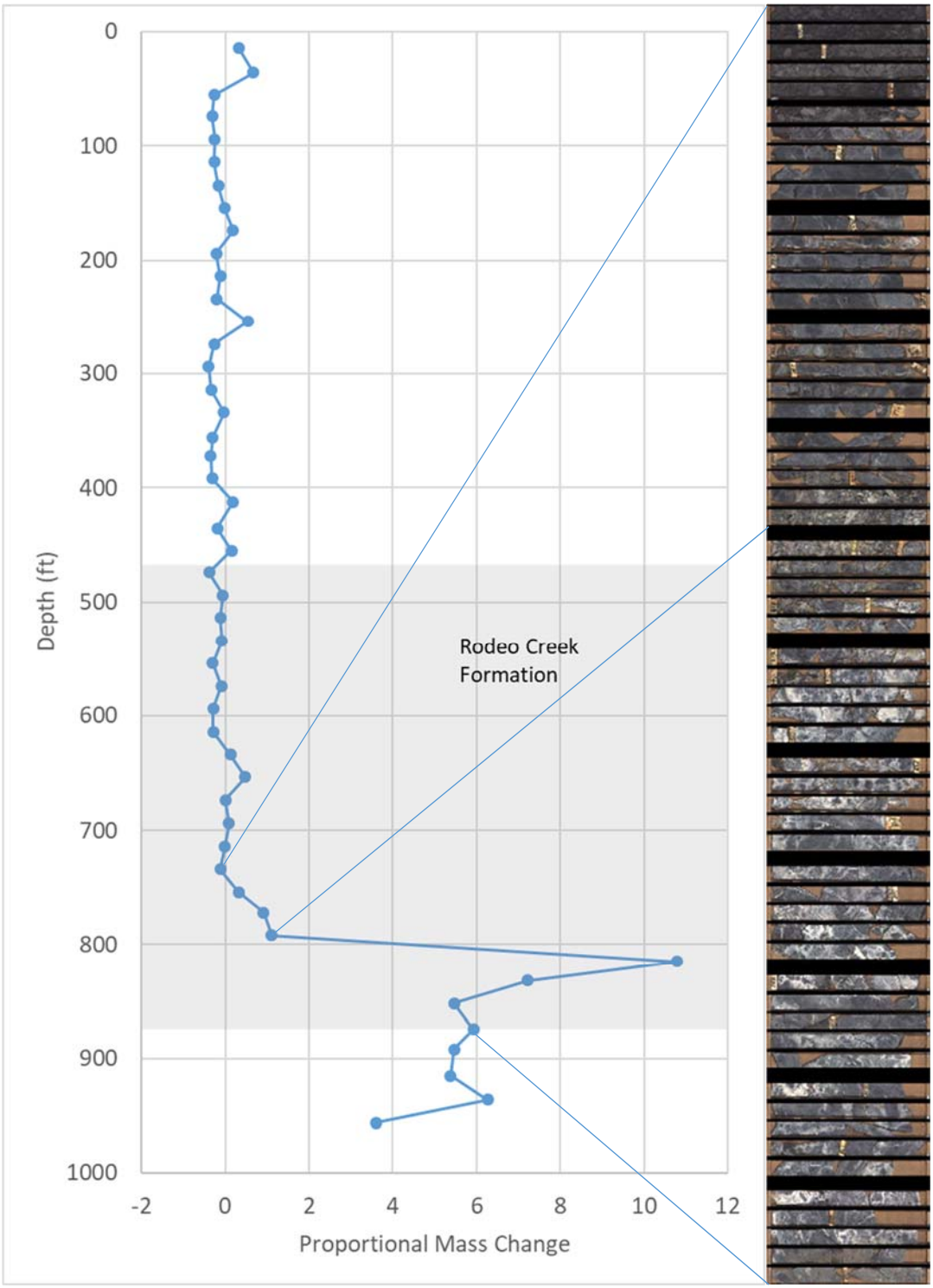

Figure 47. Down-hole plot of the proportional change in mass of hole BD15-052 based on normalization to unaltered Rodeo Creek. The gray box shows the depths of the Rodeo Creek Formation. The silicified zone is shown in the core photos to the right and the depths of the weakly silicified zone shown by the first two lines and the intensely silicified zone (in the Rodeo Creek) by the second and third lines.

4.8 Geochemistry of Breccias

In order to evaluate the geochemical changes associated with brecciation, 21 hand samples of varying breccia types were selected for 48-element ICP-MS whole-rock geochemistry. The data was evaluated using the enrichment factor scoring system for each sample (Figure 48-Figure 54). The raw data (Table 6) was evaluated for silver and other mineralization elements and Barrick Goldstrike assay was used for corresponding gold values.

4.8.1 Tectonic Breccias

Figure 48 shows the EFSs of three separate samples of Bx1 (Roberts Mountain Thrust tectonic breccia) from three separate drill-holes with corresponding drill-core photos. In each example, Au has a higher factor score than Ag and each sample is enriched in suite 2 (mineralization suite plus S), depleted in suite 3 (alteration suite, less S) and a log EFS score of zero or near zero for suites 1 and 4.

BD15-052_761.5-762 has 14.65 ppm Ag and 0.88 ppm Au with a Ag/Au ratio of 16.69 (Table 6). This is a considerably higher Ag/Au ratio than BD14-04C 701-701.2 and BD15-023A 1311.9-1312.4 with 0.93 and 3.85 respectively. BD15-023A 1311.9-1312.4 has low grade Ag and Au values (0.37 and 0.10 ppm) and so may not be a good representation of Ag/Au ratio or values for mineralized zones. BD14-04C 701-701.2 has relatively high Ag and Au values (15.25 and 16.40 ppm respectively).

Figure 49A and B show the enrichment factor score of Bx4 (other fault breccias), the second of which has been silicified and sulfidized. The highest EFS values for each of the Bx4 samples is for Sb and As. Au-Ag and the remaining mineralization suite (W, Cu, Re, Se and Te) and suite 4 plus U are enriched in these samples. In both cases, Au EFS is higher than silver; however, values for Ag and Au are all under 2 ppm. As and Sb values are very high for both

BD15-023A 1352.3-1353 (Figure 49A) and BD15-023A 1361.6-1362.1 (Figure 49B) (1525 and 1780 ppm As, 569 and 601 ppm Sb respectively) (Table 6).

BD14-04C 701.5-701.9 (Figure 49C) is the only example of an igneous clast-bearing breccia in the El Niño drill-core. It is a tectonic breccia (Bx4) near the upper intrusive contact of the Russet diorite dike. The light patches in Figure 49F are fragments of the Russet diorite dike, with both faulted and intrusive contacts. Au has the highest EFS value in this sample, followed by Ag and the rest of the mineralization suite. Ag-Au values are relatively high (17.60 and 10.45 ppm) with a Ag/Au ratio of 1.68. The rest of suite 2 is enriched, and Se has a relatively high value of 53 ppm (Table 6).

There appears to be no significant difference in the enriched and depleted suites between these Bx1 and Bx4 samples.

4.8.2 Hydrothermal Breccias

Sample BD15-052 815.1-815.3 (Figure 50A and D) is an example of Bx1a, a vuggy white silica flooded Bx1. This sample is enriched in the mineralization suite (Ag, Au, Sb, Te, Li, Re, Se, Tl, As, W, and Cu) and depleted in Ca and Mg (suite 3, decalcified). Ag has a higher EFS than Au, and has a concentration of 14.8 ppm Ag, 0.59 ppm Au and a Ag/Au ratio of 25.09. This sample differs from tectonic breccias in that it is enriched in Ce and La and enriched in all suite 4 elements.

Figure 50B and E are examples of Bx2, a vuggy silica cemented hydrothermal breccia within a Bx1 breccia. This sample is enriched in the mineralization suite and depleted in Ca, Sr and Mg. Ag/Au ratio for this sample is 7.57 (53.60 ppm Ag, 7.08 ppm Au) and contains relatively high values of As (115.5 ppm), Re (0.04 ppm), Sb (226 ppm), Se (32 ppm), and Te (1.25 ppm). This sample is very similar in EFS as the tectonic breccias Bx1 and Bx4.

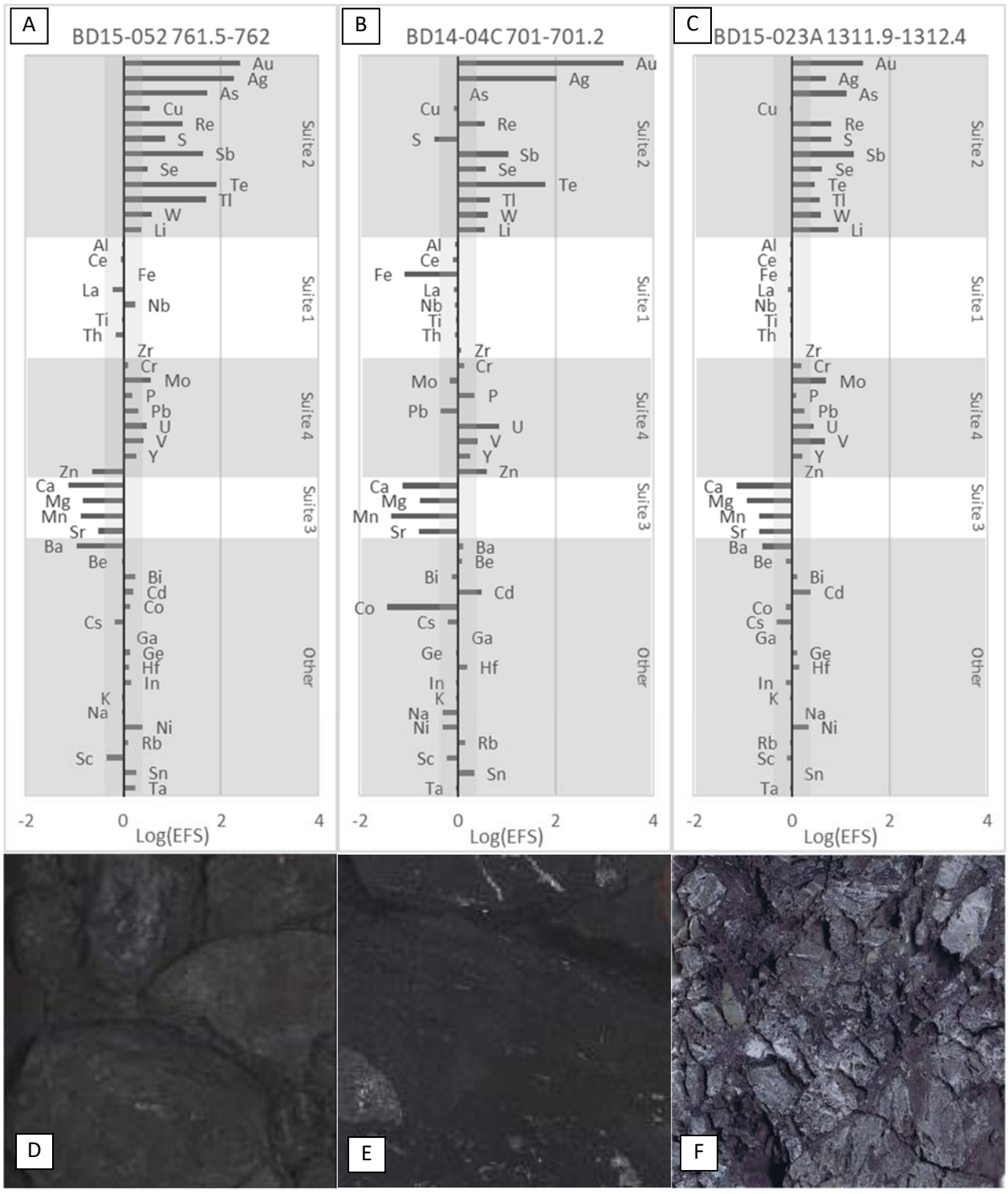

Figure 48. Enrichment factor score plots (A-C) and corresponding core photograph (D-F) of Bx1 samples (Roberts Mountain thrust tectonic breccia). Values greater than zero (right of the black line) are enriched and values less than zero (left of black line) are depleted. Gray boxes outline the various element suites.

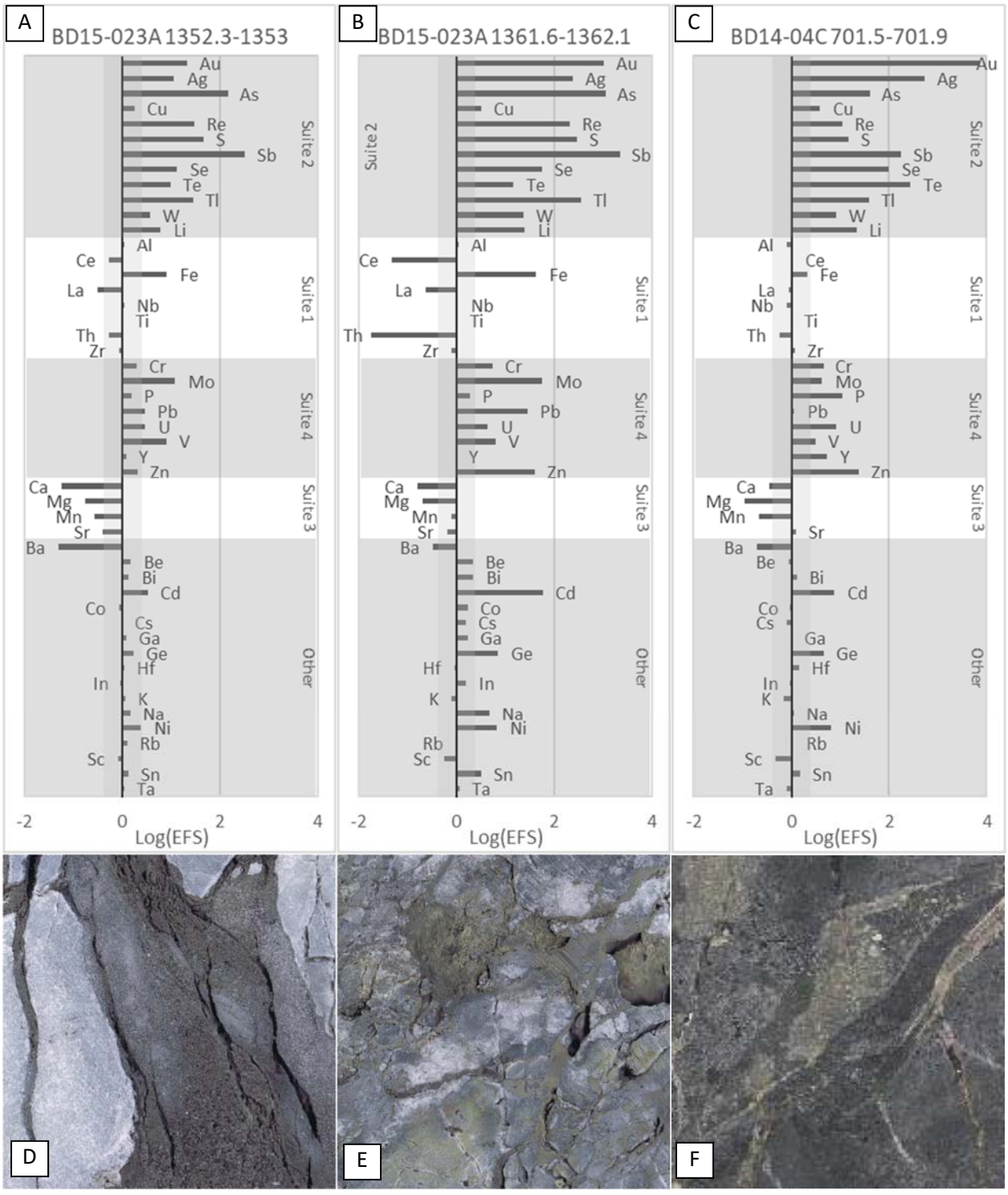

Figure 49. Enrichment factor score plots (A-C) and corresponding core photograph (D-F) of Bx4 (other fault breccias) (A, B, D, and E) and the only example of an igneous clast-hosting breccia in the El Niño drill-core samples (C and F). Values greater than zero (right of the black line) are enriched and values less than zero (left of black line) are depleted. Gray boxes outline the various element suites.

Bx2 is also found within Bx1a, as in sample BD15-023A 1331.4-1332 (Figure 50C and F). This sample, however, has a much different geochemical signature. The EFS for suite 2 is enriched but the concentrations are low. Calcium is not depleted and all suite 4 elements are enriched.

BD15-053_791.1-791.4 (Figure 51A and D) is a pyrite matrix crackle to chaotic hydrothermal breccia (Bx3b). It is enriched in Au, Sb, As, Tl, Re, Ag, S, Se, Te, Fe, Mo, Ni, V, Ge, Li, Na, U, and W and depleted in P, La, Sr, Mg, Mn, and Ca. Ag/Au ratio is 0.81 (3.21 ppm Ag, 3.96 ppm Au) and exceptionally high As (6390 ppm), Sb (1555 ppm), Se (30 ppm), and Tl (33.3 ppm).

Figure 51B, C, E, and F, Figure 52A-F, and Figure 53A, B, D, and E are examples of Bx3a, a quartz-(ammonium) mica- pyrite altered mudstone crackle to chaotic breccia. They are sometimes associated with pyrite veinlets and are distinguished from Bx3b by the bleached selvage of the pyrite veins, and general bleaching of the rock. In all examples the mineralization suite is enriched with Ag greater than Au, and depleted in Mg and Ca. Ag ranges from 5.45 ppm to 17.85 ppm, Au values of 0.05-3.42 ppm and Ag/Au ratios from 2.22 to 120.83, with the majority having a ratio of over 37.98. As, Sb, Se, Te, and Tl values are relatively high in all samples but are the highest in BD15-050A 723.5-723.8, the sample with the most visible pyrite (Figure 51F).

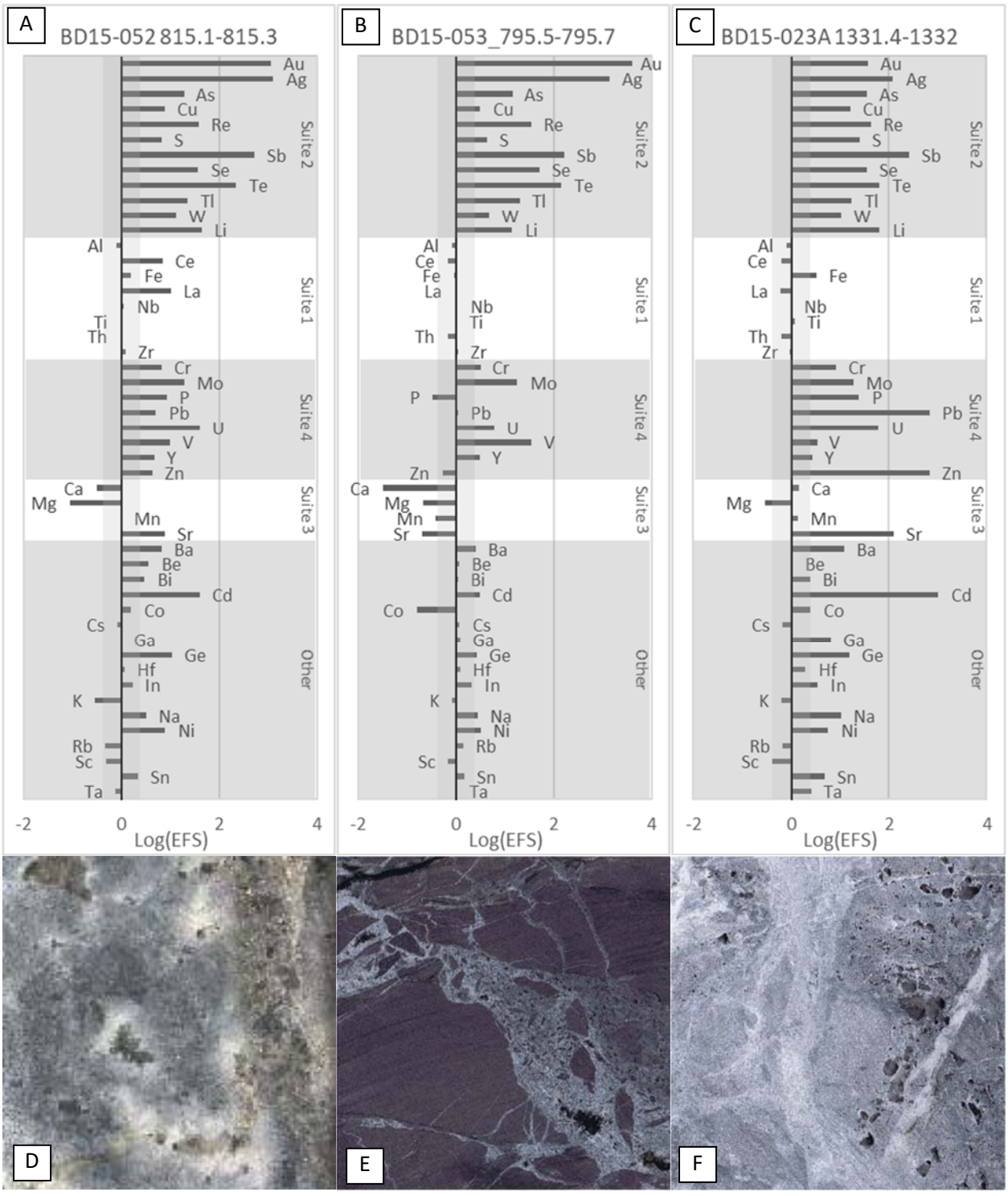

Figure 50. Enrichment factor score plots (A-C) and corresponding core photograph (D-F) of Bx1a (silicified Bx1) (A and D), and Bx2 (vuggy quartz cemented and veined Bx1 (B and E) and Bx1a (C and F). Values greater than zero (right of the black line) are enriched and values less than zero (left of black line) are depleted. Gray boxes outline the various element suites.

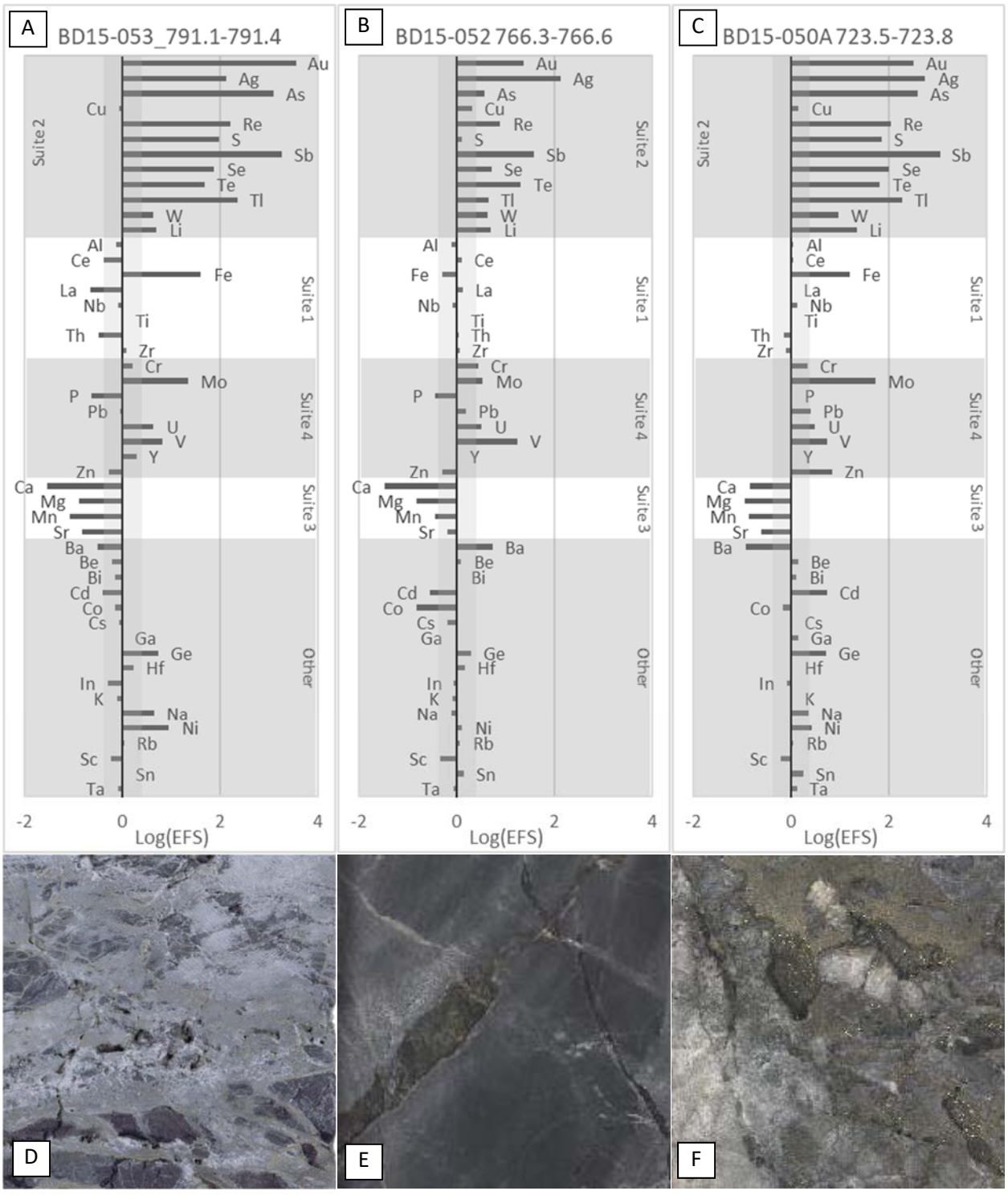

Figure 51. Enrichment factor score plots (A-C) and corresponding core photograph (D-F) of Bx3b (A and D) and Bx3a (B, C, E, and F). Values greater than zero (right of the black line) are enriched and values less than zero (left of black line) are depleted. Gray boxes outline the various element suites.

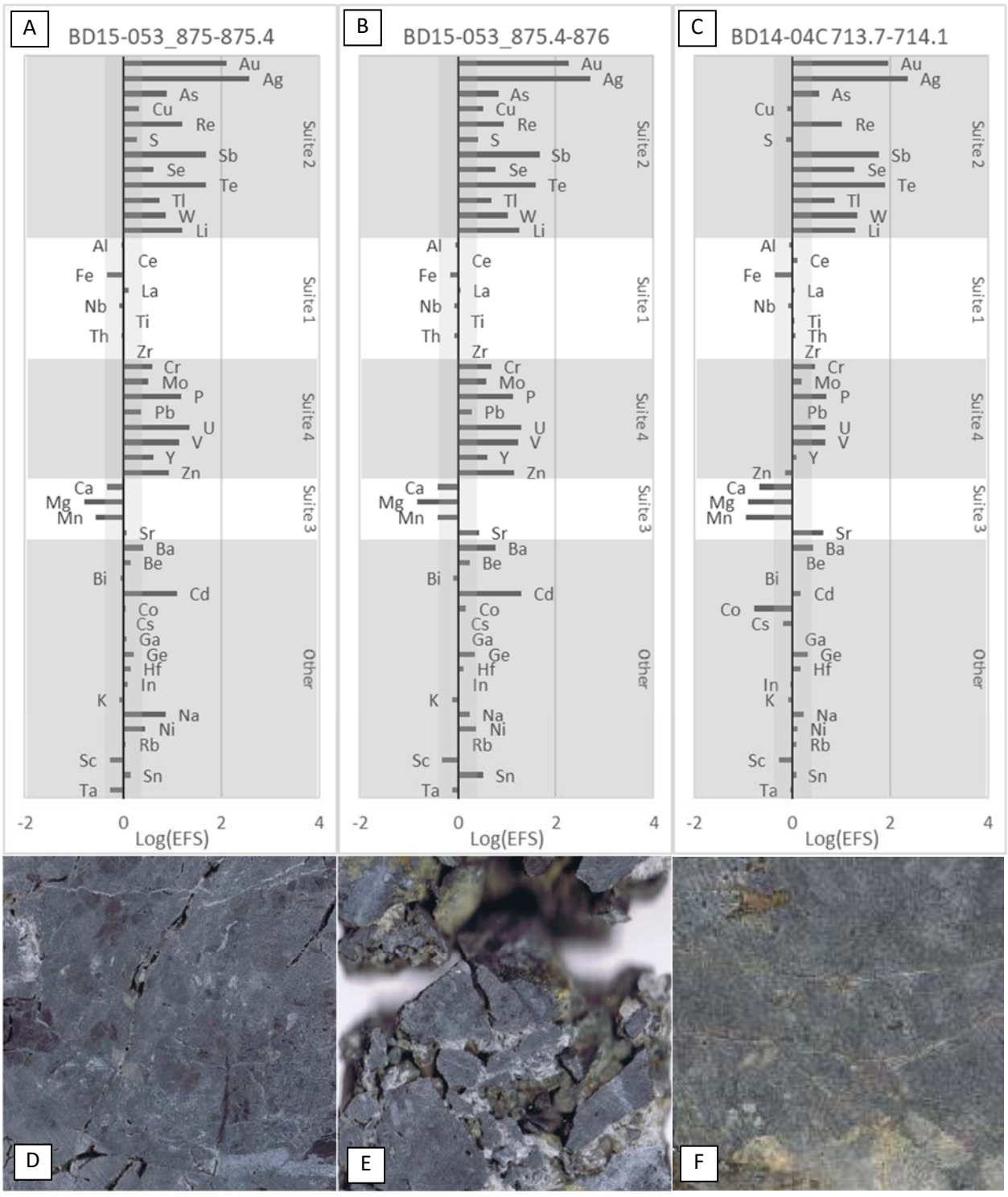

Figure 52. Enrichment factor score plots (A-C) and corresponding core photograph (D-F) of Bx3a breccias. Values greater than zero (right of the black line) are enriched and values less than zero (left of black line) are depleted. Gray boxes outline the various element suites.

4.8.3 Dissolution Collapse Breccias

Figure 53C and F and Figure 54A-F are all examples of Bx5b, silicified dissolution collapse breccias. Sample BD15-052 874.1-874.5 is a Bx6 with late calcite veining (Figure 53C and F). The sample is enriched in mineralization elements and has a Ag/Au ratio of 1.54 (2.25 ppm Ag, 1.46 ppm Au).

BD15-052 875.2-875.3 (Figure 54A and D) is a decalcified, silicified, chaotic limestone clasts, matrix supported, calcite-cemented collapse breccia. While the EFS shows enrichment in suite 2 it has relatively low raw geochemical values of Ag (1.52 ppm), Au (0.77 ppm), As (49.2 ppm), Cu (6.4 ppm), Re (0.00 ppm), Se (1 ppm), Te (0.08 ppm), and Tl (0.14 ppm), with a moderate Sb value (200 ppm) and relatively high W value (11.6 ppm).

BD15-052 892.7-892.9 is a decalcified, silicified, chaotic limestone clasts, matrix supported, peloidal marl cemented collapse breccia + unknown green mineral + gypsum (Figure 54B and E). It is enriched in Au, Ag, Sb, Li, P, Te, U, Tl, As, Re, W, Y, V, Cr, Ge, Mo, Cd, S, and Se. It has a Ag/Au ratio of 12.34 (6.32 ppm Ag, 0.51 ppm Au).

BD15-052 923.4-923.6 (Figure 54C and F) is enriched in many of the same elements as BD15-052 892.7-892.9; however, has much higher concentrations of As (665 ppm) and Sb (411 ppm) and no depletion of suite 3 elements.

In general, these samples show very similar EFS signatures to the hydrothermal breccias; however, with much lower concentrations of the mineralization suite.

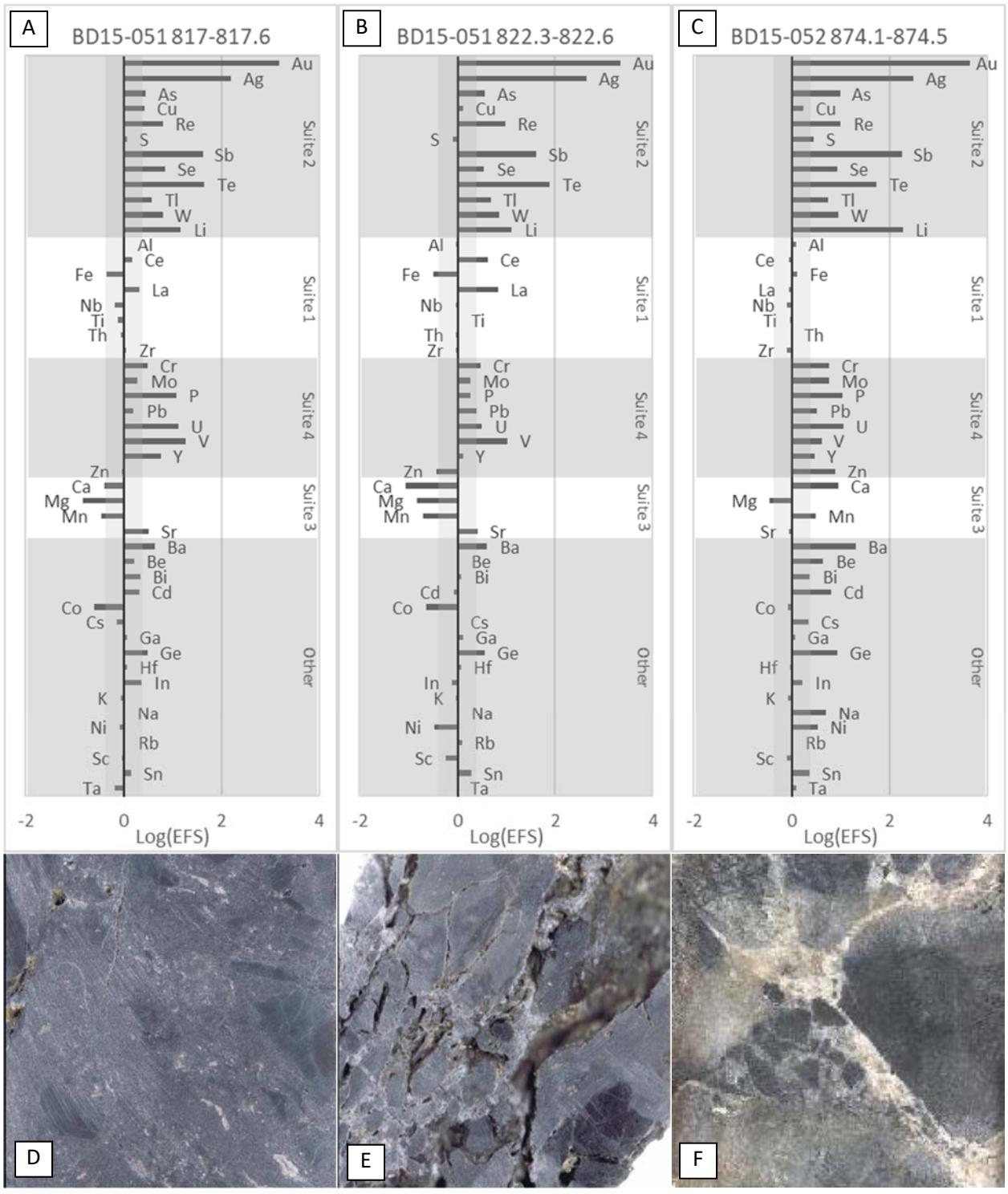

Figure 53. Enrichment factor score plots (A-C) and corresponding core photograph (D-F) of Bx3a (A, B, D, and E) and collapse breccia with calcite veins (C and F).

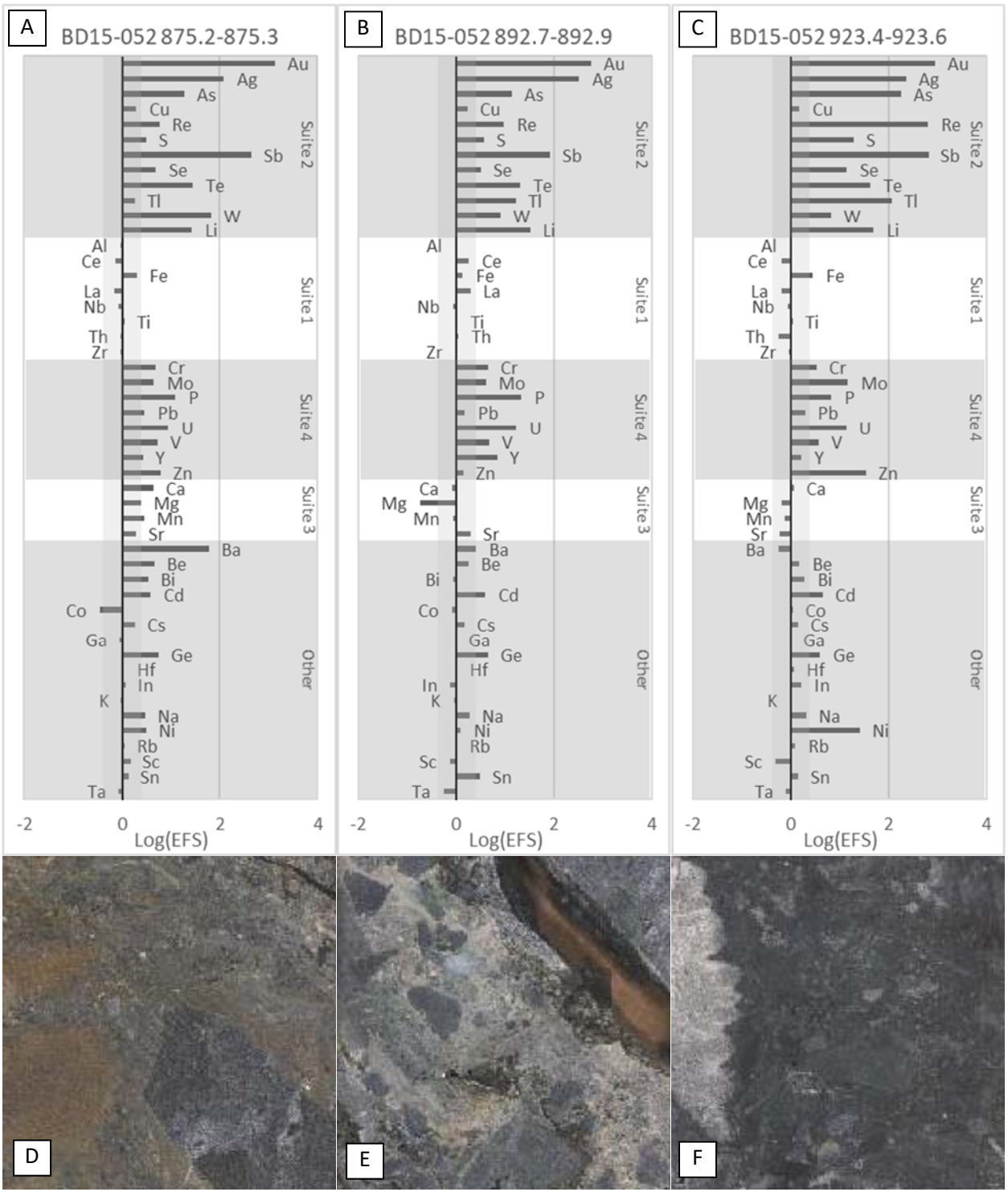

Figure 54. Enrichment factor score plots (A-C) and corresponding core photograph (D-F) of silicified dissolution collapse breccias (Bx6).

Table 6. Mineralization suite element concentrations for samples selected from breccia types with Ag/Au ratios

SAMPLE	Breccia Type	Ag_ppm	Au_ppm	As_ppm	Cu_ppm	Re_ppm	Sb_ppm	Se_ppm	Te_ppm	Tl_ppm	W_ppm	Ag:Au
BD15-052 761.5-762	Bx1	14.65	0.88	865.00	73.10	0.04	122.00	4.00	1.45	23.80	4.20	16.69
BD14-04C 701-701.2	Bx1	15.25	16.40	30.50	32.00	0.01	55.60	9.00	2.07	4.08	8.30	0.93
BD15-023A 1311.9-1312.4	Bx1	0.37	0.10	208.00	18.50	0.01	48.40	5.00	0.05	1.68	4.00	3.85
BD15-023A 1352.3-1353	Bx4	0.58	0.05	1525.00	23.60	0.04	569.00	11.00	0.11	8.63	2.50	12.08
BD15-023A 1361.6-1362.1	Bx4	1.85	0.35	1780.00	6.40	0.04	601.00	7.00	<0.05	16.35	2.50	5.21
BD14-04C 701.5-701.9	Bx4	17.60	10.45	279.00	33.60	0.01	208.00	53.00	2.05	7.79	3.80	1.68
BD15-052 815.1-815.3	Bx1a	14.80	0.59	46.70	23.40	0.01	214.00	7.00	0.59	1.61	2.10	25.09
BD15-053_795.5-795.7	Bx2	53.60	7.08	115.50	32.20	0.04	226.00	32.00	1.25	4.83	2.50	7.57
BD15-023A 1331.4-1332	Bx1a	0.42	0.01	26.40	14.60	0.00	32.40	2.00	<0.05	0.37	0.50	70.00
BD15-053_791.1-791.4	Bx3b	3.21	3.96	6390.00	5.50	0.11	1555.00	30.00	0.26	33.30	1.40	0.81
BD15-052 766.3-766.6	Bx3a	6.22	0.05	36.60	25.40	0.01	63.10	4.00	0.22	1.30	2.80	120.83
BD15-050A 723.5-723.8	Bx3a	17.85	0.47	2630.00	12.20	0.10	1275.00	54.00	0.48	37.00	4.10	37.98
BD15-053_875-875.4	Bx3a	11.05	0.17	47.20	16.30	0.01	50.50	2.00	0.33	0.99	2.90	63.14
BD15-053_875.4-876	Bx3a	10.30	0.17	28.90	17.80	0.01	34.00	2.00	0.18	0.61	2.90	58.86
BD14-04C 713.7-714.1	Bx3a	9.64	0.17	31.90	8.80	0.01	89.00	13.00	0.74	1.88	12.30	55.09
BD15-052 874.1-874.5	Bx5b	2.25	1.46	14.70	3.30	0.00	46.00	1.00	0.09	0.25	0.90	1.54
BD15-052 875.2-875.3	Bx5b	1.52	0.77	49.20	6.40	0.00	200.00	1.00	0.08	0.14	11.60	1.98
BD15-052 892.7-892.9	Bx5b	6.32	0.51	55.70	8.70	0.01	57.90	1.00	0.09	1.94	2.10	12.34
BD15-051 817-817.6	Bx5b	5.45	2.45	20.70	24.40	0.01	51.70	4.00	0.36	0.82	3.00	2.22
BD15-051 822.3-822.6	Bx5b	15.00	3.42	26.60	11.80	0.01	51.70	2.00	0.60	1.01	3.40	4.39
BD15-052 923.4-923.6	Bx5b	4.04	0.73	665.00	7.00	0.31	411.00	4.00	0.17	12.45	1.60	5.53

4.9 Distribution of Mineralization Suite in Cross-Section

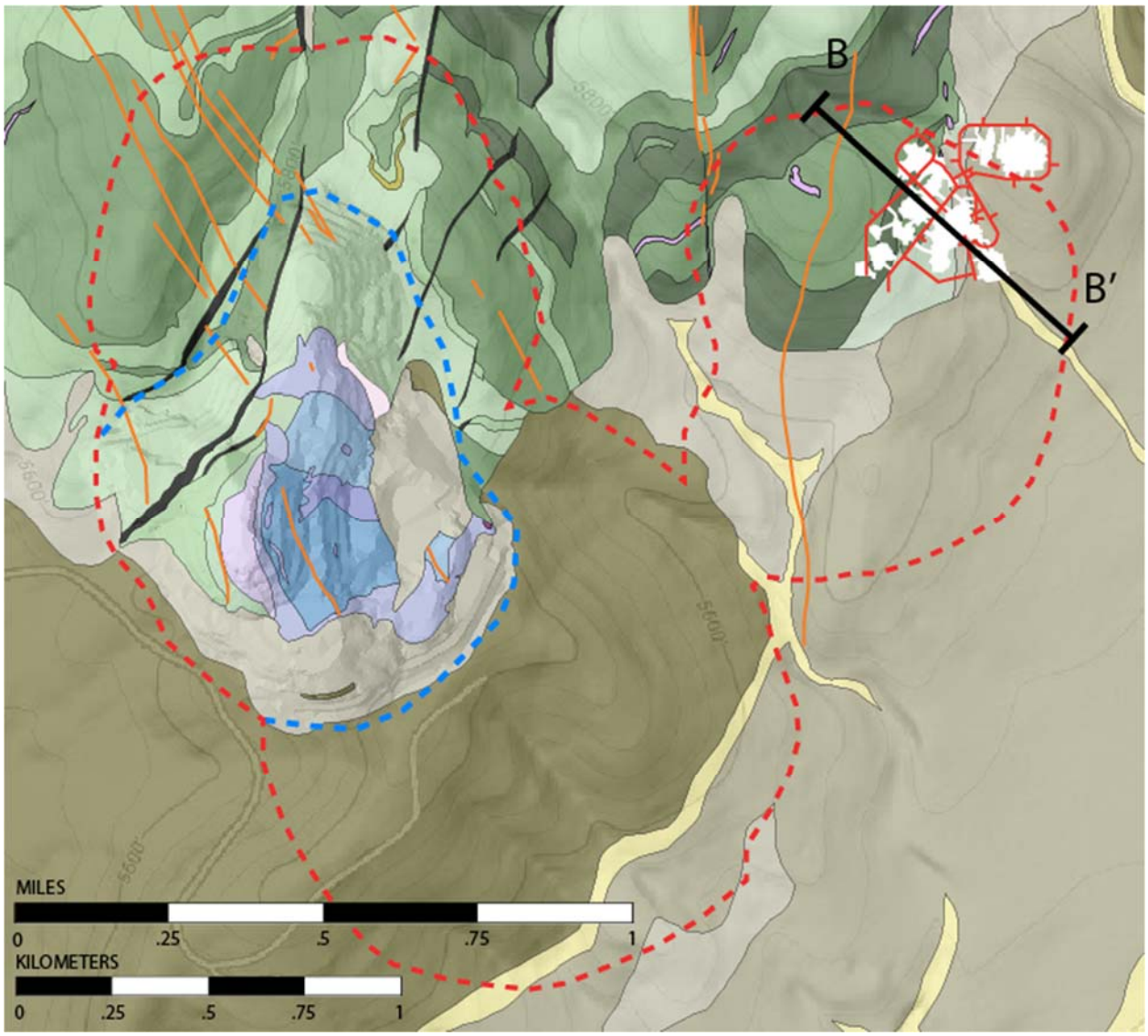

Figure 55. Geologic map of the Arturo Project with Dee (NW corner), South Arturo (south central) and Arturo (NE corner) outlined in red dashed lines. The site of the proposed El Niño mine is in the NE projected to the surface, with the location of the following cross-sections marked as B to B'. See Figure 3 for legend.

Contours of the mineralization suite in cross-section give an idea as to the fluid flow paths and illustrate the spatial association of suite 2 elements to each other in two-dimensions. The following figures show contours of 50, 60, 70, 80, 90, and 98 percentiles for As, Sb, Tl, Re, Te, Se, Hg, W, Cu, and Li, drawn from drill-hole values and 0.050->0.500 opt Au, and 0.250->1.750 opt

Ag, drawn from Barrick Goldstrike block model, overlaying the geologic formations, faults and breccias as modeled by Barrick Goldstrike at the proposed El Niño mine. Enrichment factor score >2 contours for Au, Ag, As, Te, Hg, and Cu are drawn from drill-hole samples.

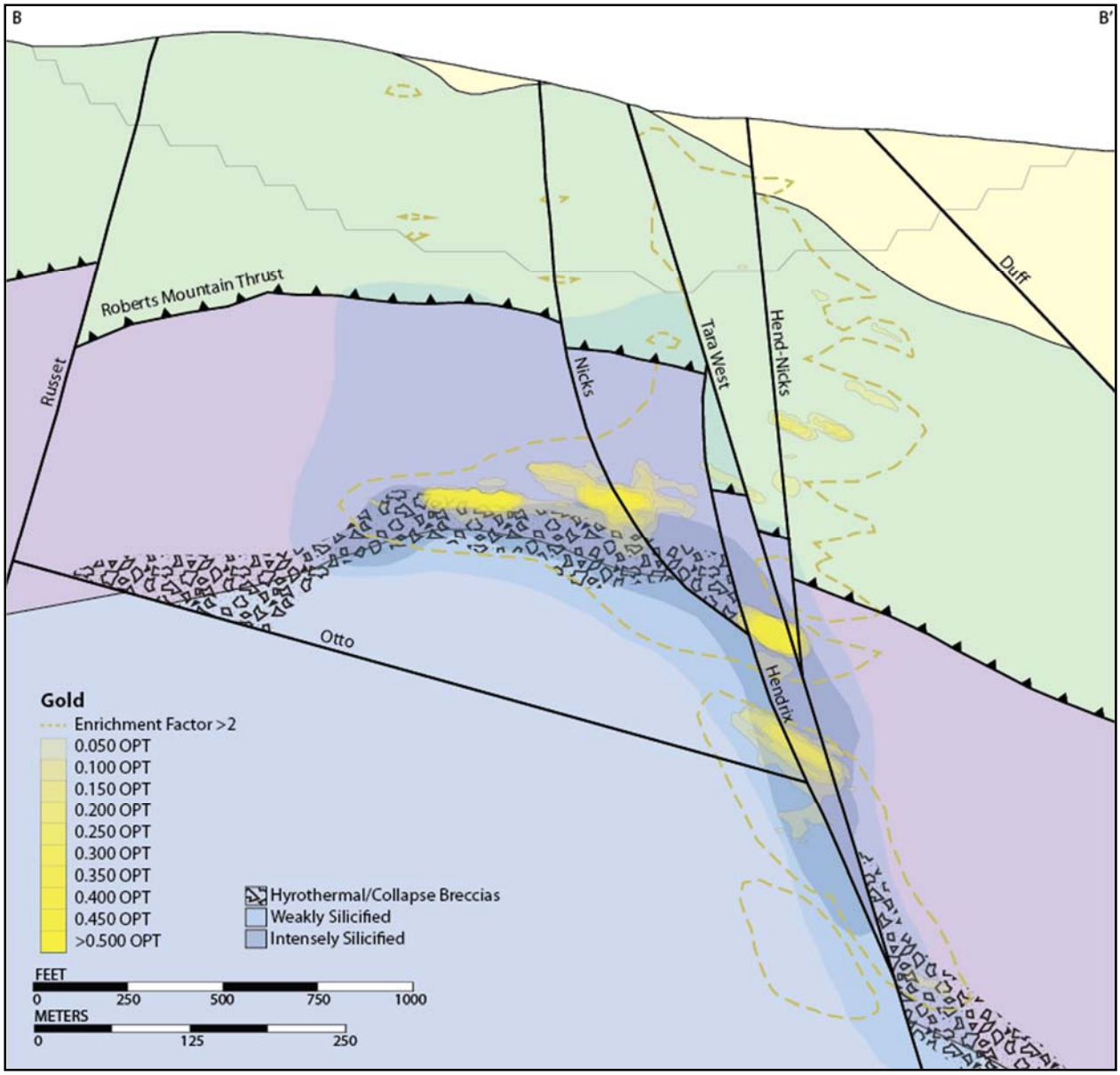

Figure 56. Cross-section through the El Niño mine with contours of gold (0.050->0.500 opt) based on the Barrick Goldstrike block model, and the enrichment factor score >2 relative to the major faults, four major formations, breccias, and silicification zones. See Figure 7 for unit legend and drill-hole locations.

Figure 55 shows the outline of the Arturo project and the location of the cross-section and its relationship to the proposed El Niño underground mine, on the northeast side of the Arturo pit.

Figure 7 in the introduction chapter illustrates the depth and location of the El Niño underground mine relative to the four major formations. It also displays the names of each fault that will be seen in the following figures, as well as the drill-holes that were used to construct the geochemical contours.

Each figure shows the location of the lower breccia zone that caps the upper contact of the Bootstrap limestone. It consists of Bx2, Bx3a, Bx3b, Bx5, and Bx6, and two silicification zones, distinguished by the intensity of alteration, "intensely silicified" being textural destructive and the "weakly silicified" have textures preserved. Bx1 is not shown; however, may be assumed to be the purple unit identified as Rodeo Creek Formation. Bx1 clasts are not distinguishable from unbrecciated Rodeo Creek Formation in core samples; however, observations in the Arturo pit show that the entire thickness of the Rodeo Creek Formation has been affected by the Roberts Mountain Thrust.

Gold contours from 0.050 opt to >0.500 opt are shown in Figure 56 with a contour of the enrichment factor score >2. The shape of the gold ore bodies appear to be controlled by bedding, often being elongate in the direction of dip. Most of the gold pods are either adjacent to a major fault or within a breccia. On the top of the main breccia zone, at the upper contact of the Bootstrap Formation, the gold is above, and slightly overlapping, both the breccia zone and intensely silicified zone. Deeper gold mineralization is mostly adjacent to fault intersections. Upper-plate gold is spatially associated with the Hend-Nicks fault, and elongate in the direction of bedding dip of the Vinini Formation. Most of the upper plate gold is lower grade; however, there is a small pod with gold values of ~0.300 opt directly in contact with the Hend-Nicks fault.

The enrichment factor score (EFS) >2 contour shows where gold is enriched compared to the unaltered Rodeo Creek standard and is taken as the shape of the mineralized body. The deepest portion of the body straddles the Hend-Nicks fault. The contour follows Hend-Nicks, getting slightly wider at the Otto fault, and then spreads out into the breccia zone. The EFS contour remains spatially associated with the Hend-Nicks fault into the upper plate, where it widens into the Vinini to the SE and to the NW stops at the Terra-West fault.

Figure 57 illustrates contours of silver mineralization from 0.250 opt to >1.75 opt and Ag EFS >2 contour in cross-section. Highest silver values are in small pods within the breccia zone, within intensely silicified rock. Smaller, lower grade pods are deeper, along the Otto Fault, and stratigraphically controlled within the upper plate, on the SE side of the Tara West fault within the Vinini Formation. The EFS >2 contour for silver shows enrichment deep along the convergence of the Tera West and Hendrix faults within the silicified Bootstrap Formation. The zone follows the Hendrix up and out to the NW, around the intensely silicified zone of the breccias. There are two zones in the Vinini on the SE side of Hend-Nicks that appear to be associated with the Hend-Nicks and/or the Tara West faults. On the NW side of Hend-Nicks are several pods of enrichment in the Vinini with the only zone of enrichment ≥0.250 opt between Hend-Nicks and Tara West, very close to the Tertiary Carlin Formation contact.

Au and Ag have a close spatial relationship (Figure 58); however, there are areas in which Au and Ag differ. The highest-grade Ag pods tend to be below the highest-grade Au pods in the breccia zone. Au is mostly located within the weakly silicified zone, while the highest grades of Ag are found within the intensely silicified zone. The deeper mineralization region near the Otto fault is similar, with Au being stratigraphically higher than Ag. Within the Vinini Formation, Au and Ag pods are close but do not align; however, the volumes outlined by EFS >2 have a tremendous amount of overlap in most areas.

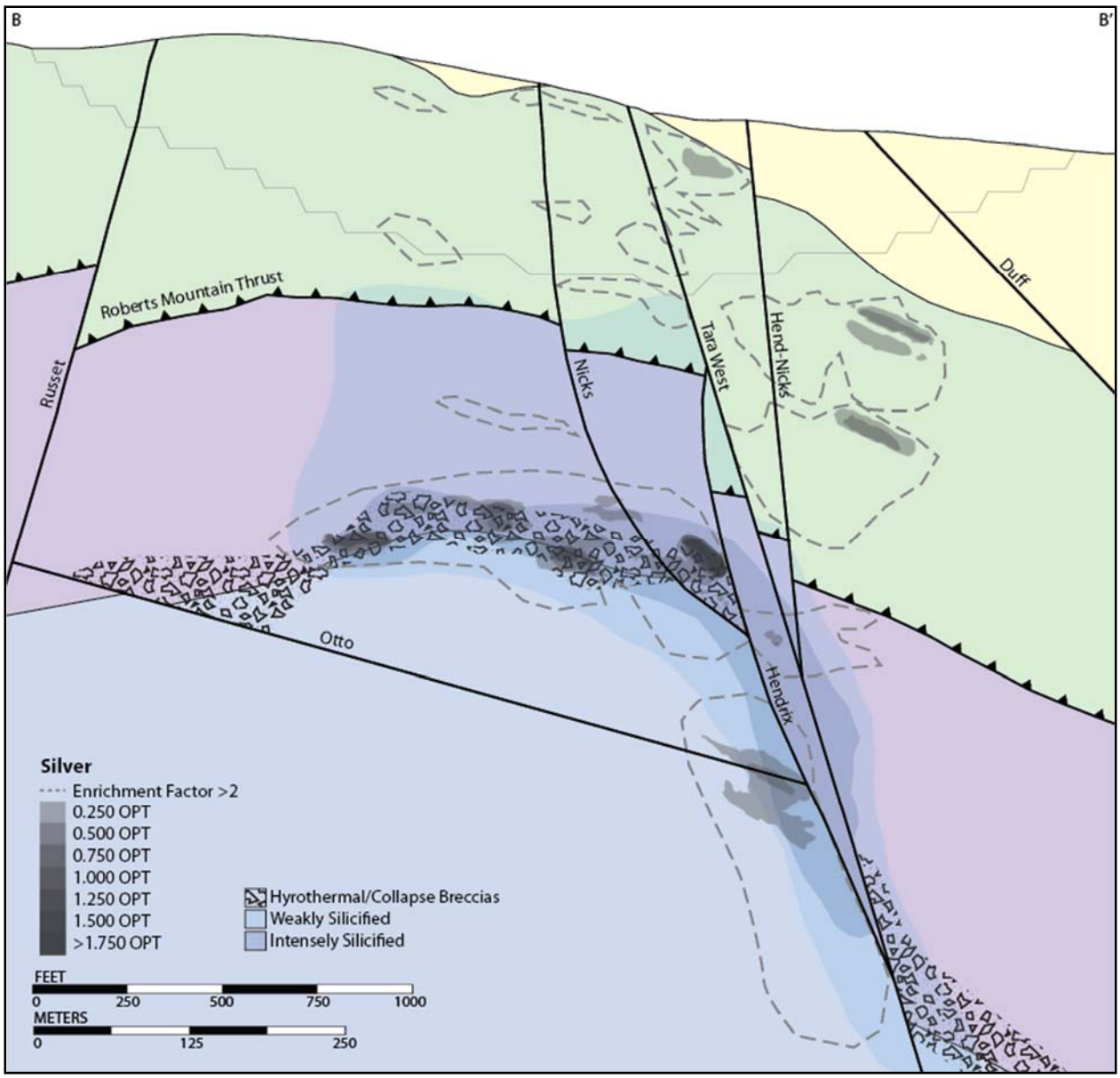

Figure 57. Cross-section through the El Niño mine with contours of silver enrichment (0.250->1.750 opt) and the enrichment factor score >2 relative to the major faults, four major formations, breccias, and silicification zones. See Figure 7 for unit legend and drill-hole locations.

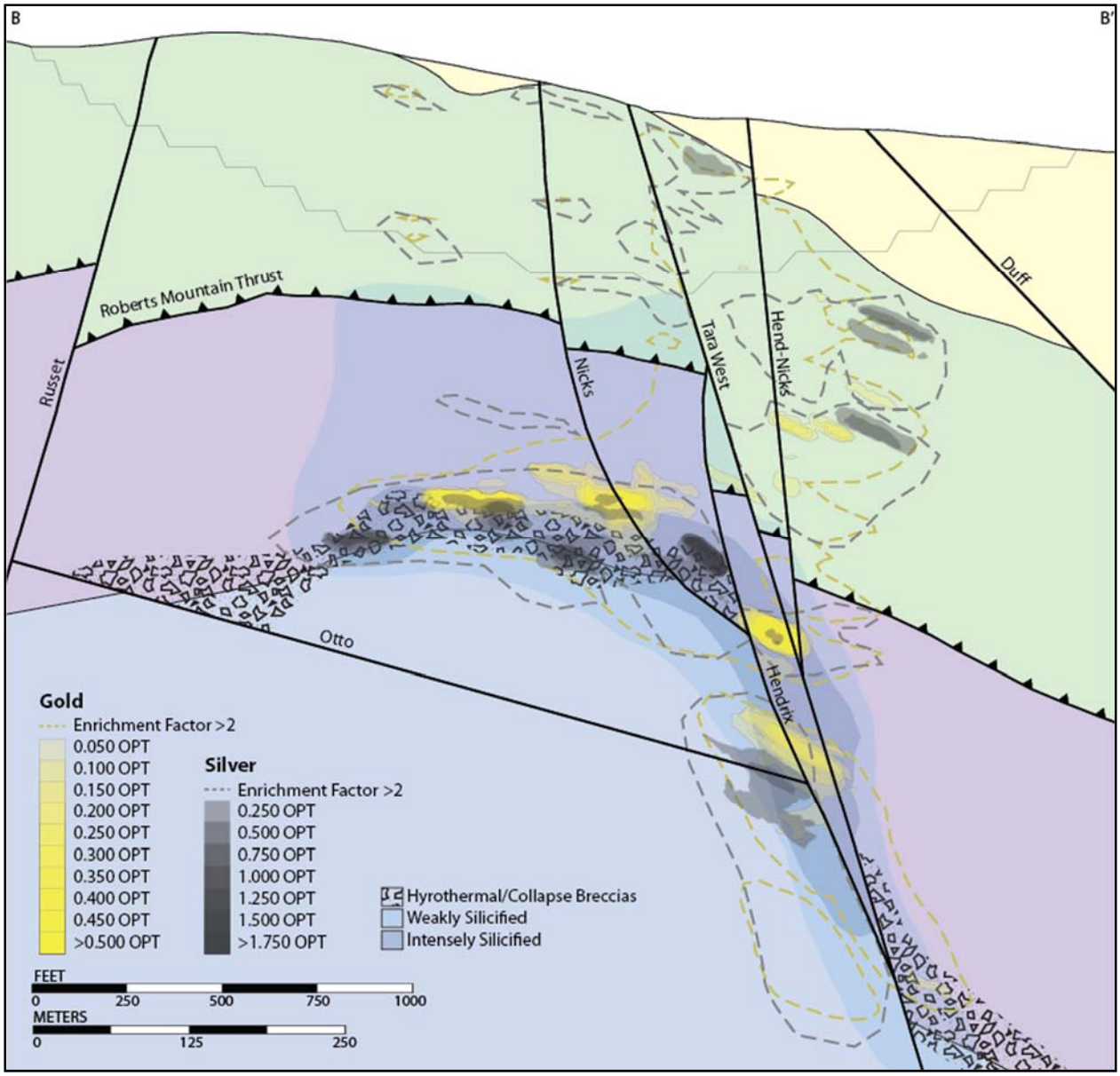

Figure 58. Cross-section through the El Niño mine with contours of gold enrichment (0.050->0.500 opt) and Au EFS >2 compared to silver enrichment (0.250->1.750 opt) and Ag EFS >2 relative to the major faults, four major formations, breccias, and silicification zones. See Figure 7 for unit legend and drill-hole locations.

Of the other mineralization-related elements there appears to be two groups of elements that have similar distribution of concentration in the cross-sections. While all the suite 2 elements have similar distributions overall, including high concentrations in the breccia and high concentrations adjacent to the Hendrix and Hend-Nicks faults, there are enough differences to warrant describing them separately. The first group consists of As, Sb, Tl, and Re and the second group consists of Te, Se, and Hg. W, Cu, and Li.

The first group is distinguished by highest concentrations slightly above and within central parts of the lower breccia body, high concentrations near the convergence of the Otto and Hendrix faults, and the lack of any significant concentrations NW of the Tara West fault in the Vinini Formation. The highest concentrations of As (Figure 59), Tl (Figure 61), and Re (Figure 62) are restricted to the upper portion of the breccia/upper portion of the intensely silicified zone, along the Nicks fault where it intersects with the breccia, the Hendrix fault where it intersects with the breccia, Hendrix-Roberts Mountain Thrust intersection, Hendrix-Otto fault intersection, and the Hend-Nicks fault where it joins with the Tara West fault. Antimony (Figure 60) has a similar distribution; however, extends lower into the Bootstrap limestone beneath the breccia. Arsenic and antimony extend down to the join between Hendrix and Tara West faults and spread out to the NW into the breccia and up the Nicks fault, and to the NE of the Tara West fault in the Vinini Formation, with only small pods to the NW. Thallium and Rhenium have a similar geometry to As and Sb in the lower plate (below the Roberts Mountain Thrust) but have very low concentrations in the Vinini. Rhenium is a little more spread out in the Rodeo Creek Formation than the other three elements. Rhenium concentration geometry most closely mimics the geometry of the weakly silicified zone. EFS >2 contour for As is similar to the 42.55 ppm contour.

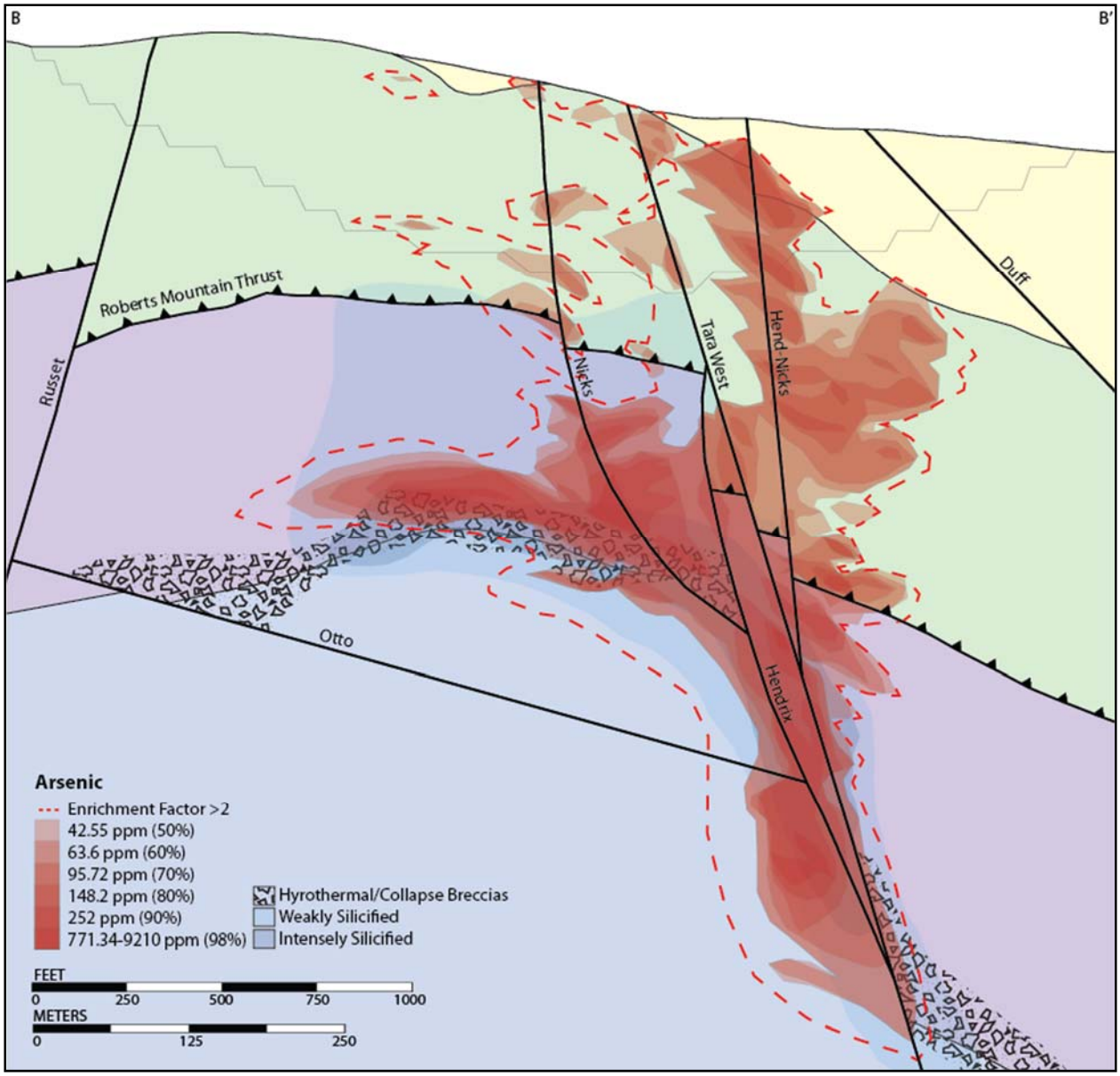

Figure 59. Cross-section through the El Niño mine with contours of arsenic enrichment (42.55-9210 ppm) and the enrichment factor score >2 relative to the major faults, four major formations, breccias, and silicification zones. See Figure 7 for unit legend and drill-hole locations.

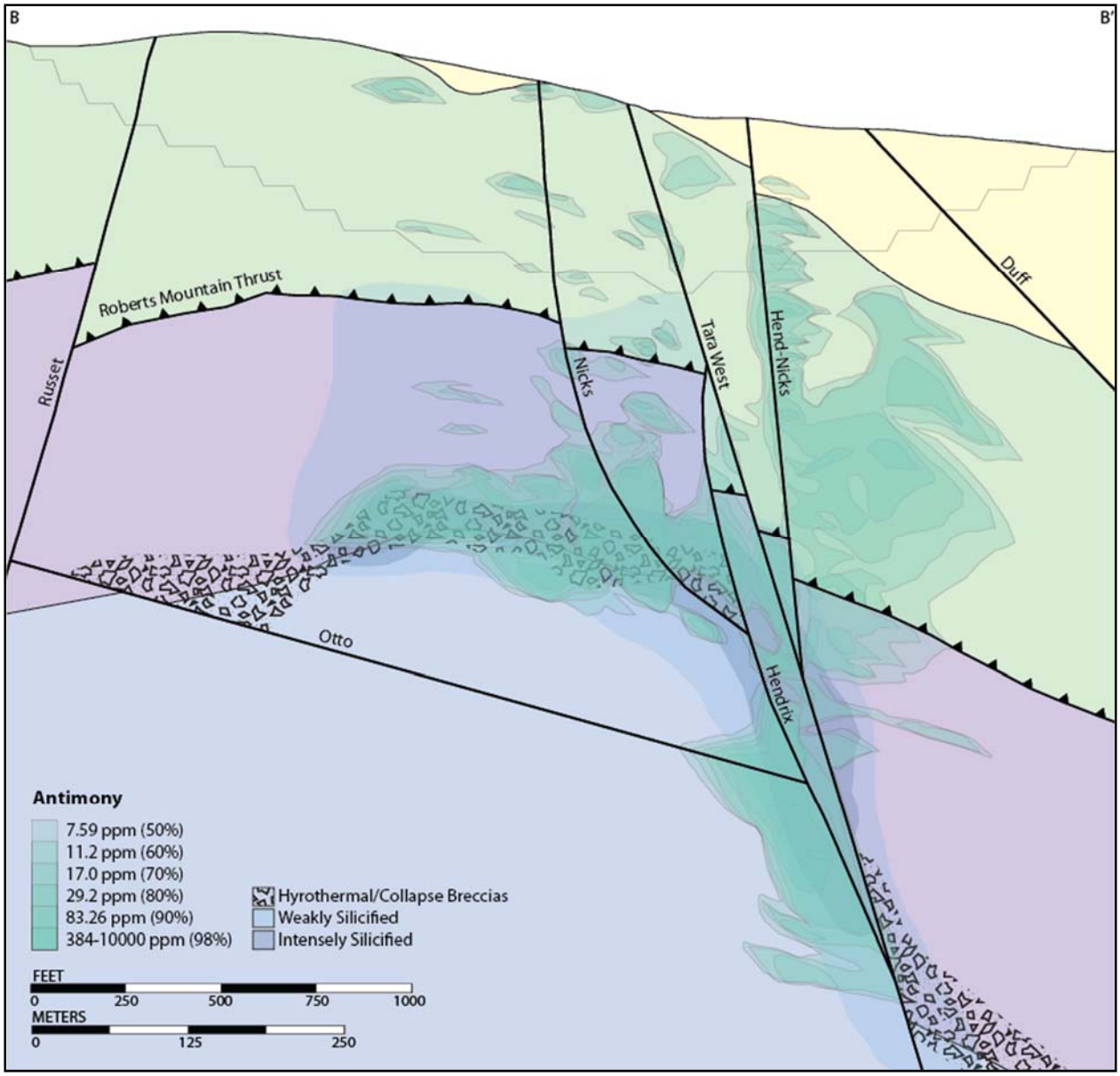

Figure 60. Cross-section through the El Niño mine with contours of antimony enrichment (7.59-10000 ppm) relative to the major faults, four major formations, breccias, and silicification zones. See Figure 7 for unit legend and drill-hole locations.

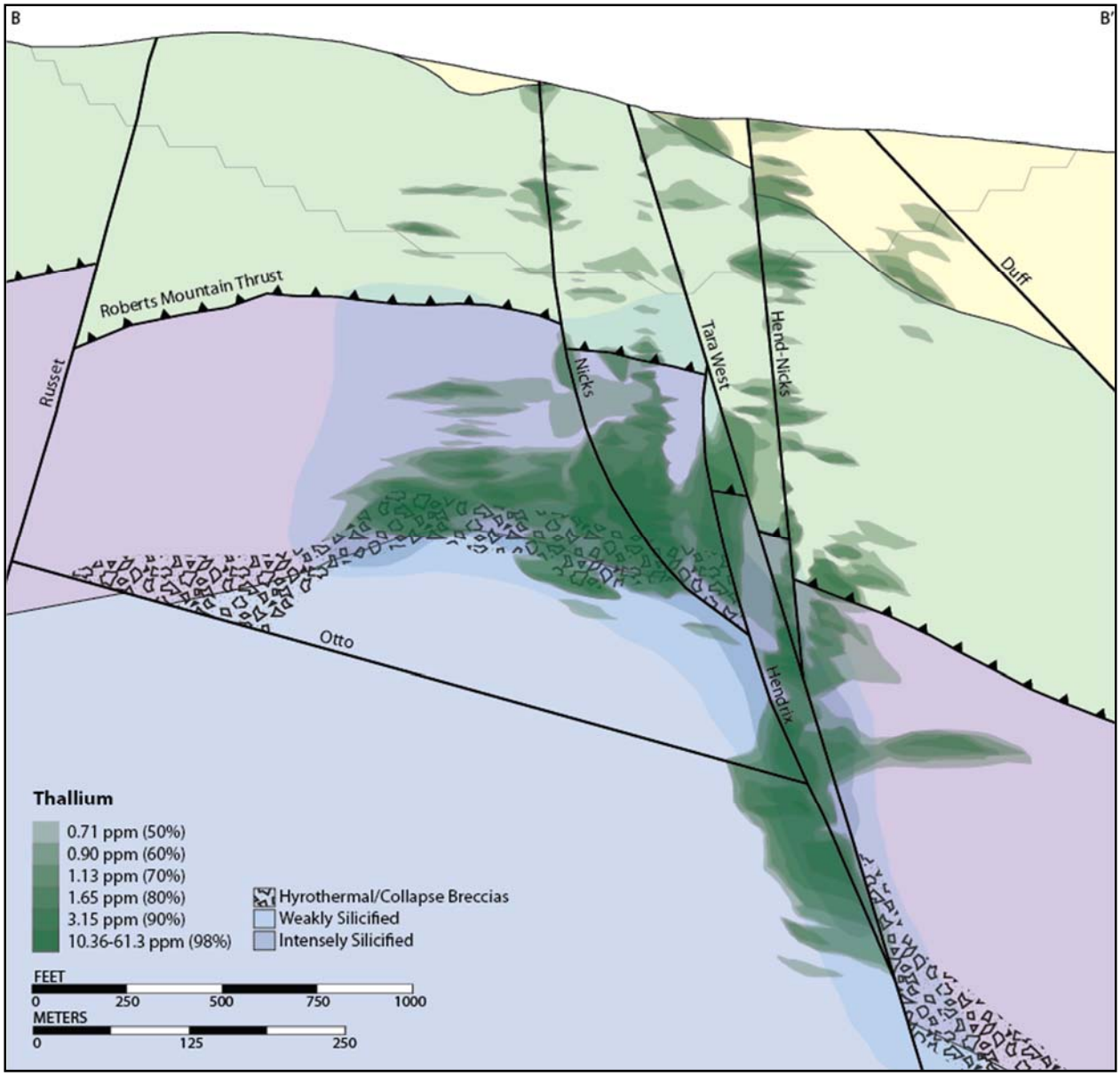

Figure 61. Cross-section through the El Niño mine with contours of thallium enrichment (0.71-61.3 ppm) relative to the major faults, four major formations, breccias, and silicification zones. See Figure 7 for unit legend and drill-hole locations.

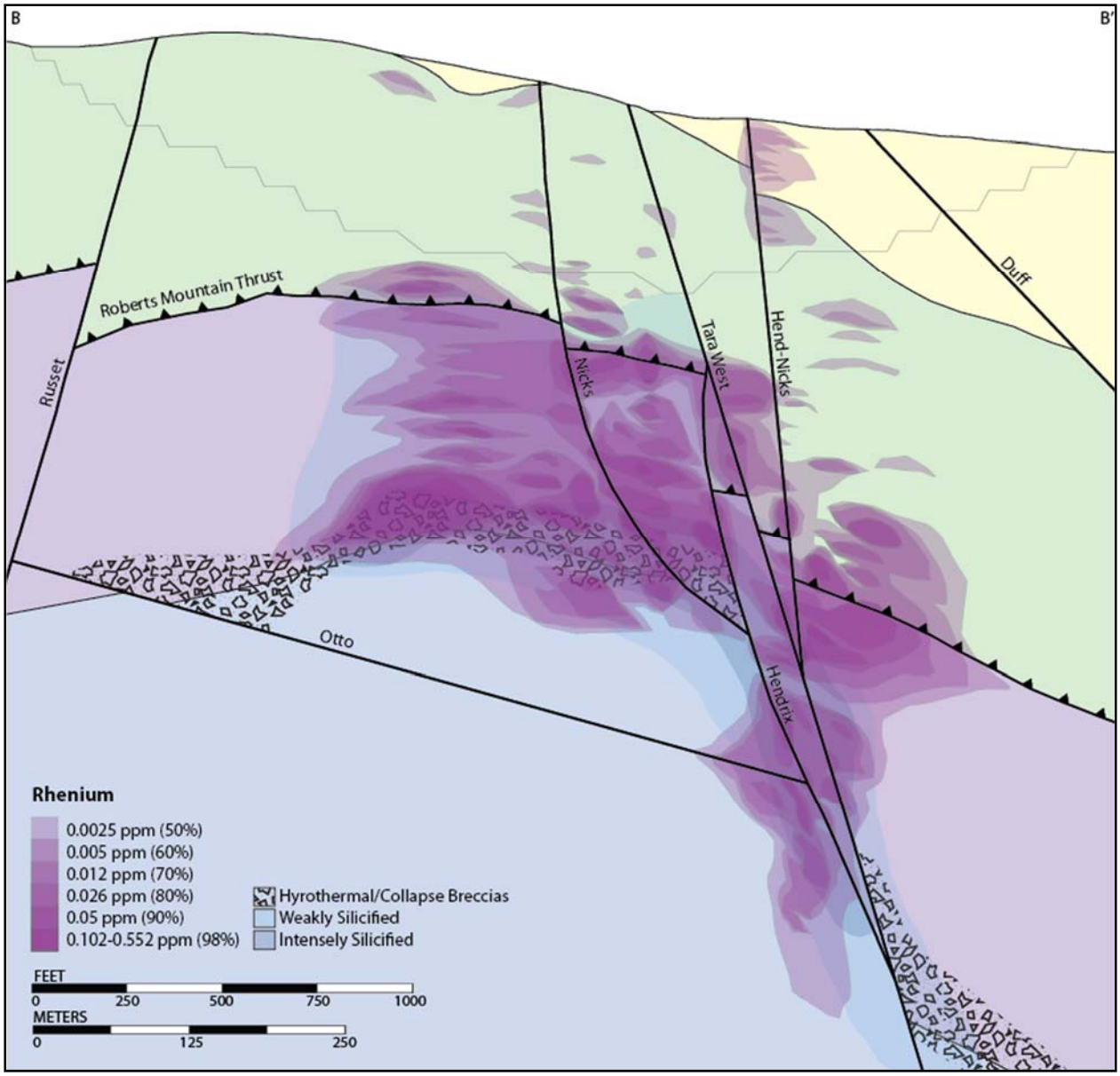

Figure 62. Cross-section through the El Niño mine with contours of rhenium enrichment (0.0025-0.552 ppm) relative to the major faults, four major formations, breccias, and silicification zones. See Figure 7 for unit legend and drill-hole locations.

In contrast, the highest concentrations (90 and 98%) of Te (Figure 63), Se (Figure 64), and Hg (Figure 65) are centralized around the intersection of the Nicks fault and the breccia zone, the convergence of the Otto and Hendrix faults, within the breccia zone and the intensely silicified zone, and small pods spread out in the Rodeo Creek Formation and, to lesser extent, Vinini Formation. Lower concentrations for each of these elements are present throughout the silicified breccias and around the Otto-Hendrix intersection. Where this set of elements differs from the first is the distribution of this suite in both the upper plate and lower plate, while the first set is confined to the lower plate. This set also has highest concentrations at the Nicks-Breccia intersection and a larger footprint in the upper plate, on both the SE and NW side of the Tara West fault. These elements also have a larger footprint in the Rodeo Creek Formation detached from concentrations along the Hend-Nicks faults and appear have used the Tara West fault as a fluid conduit because high concentrations are scattered along the fault. This is in contrast with elements associated with Au that appear to be cut off by the Tara West fault.

Tungsten (Figure 66), while similar in geometry to other mineralization-related elements, has highest concentrations along the Hend-Nicks fault and within the Vinini Formation. Lower concentrations are within the intersection of Otto and Hendrix, Nicks and the Breccia, Hend-Nicks and Tara West and in the upper portion of the intensely silicified breccias.

Highest concentrations of Cu (Figure 67) are in the upper plate, along the Hend-Nicks fault and spatially associated with the Nicks fault. The footprint is largest in the upper plate and enrichments are minor in the breccias and Otto-Hendrix intersection. The EFS >2 contour shows that Cu is enriched in the intensely silicified breccia; however, concentrations are less-than 60th percentile (<57.6 ppm), just slightly above average crustal abundance (Barbalace, 2017).

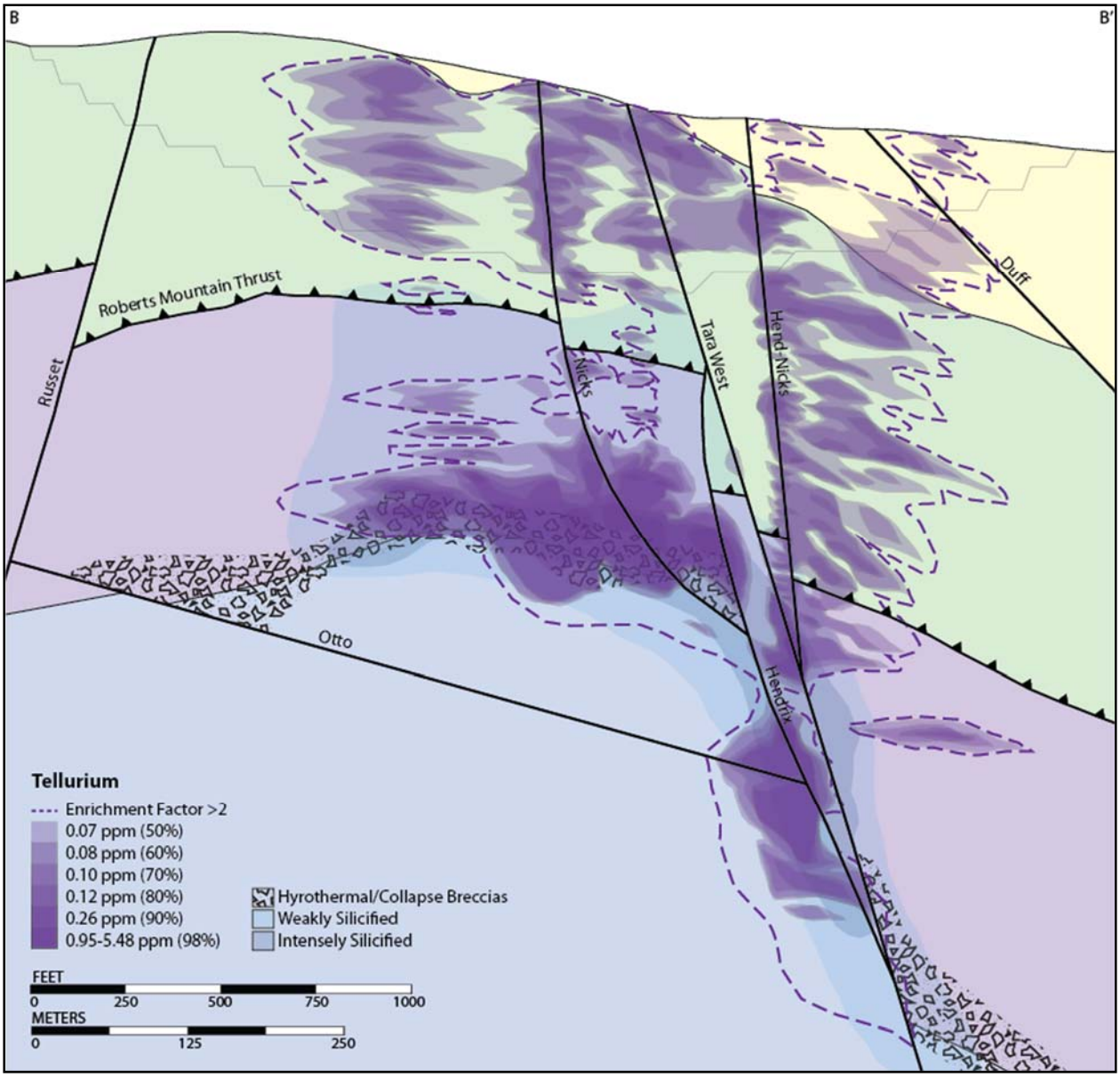

Figure 63. Cross-section through the El Niño mine with contours of tellurium enrichment (0.07-5.48 ppm) and EFS >2 relative to the major faults, four major formations, breccias, and silicification zones. See Figure 7 for unit legend and drill-hole locations.

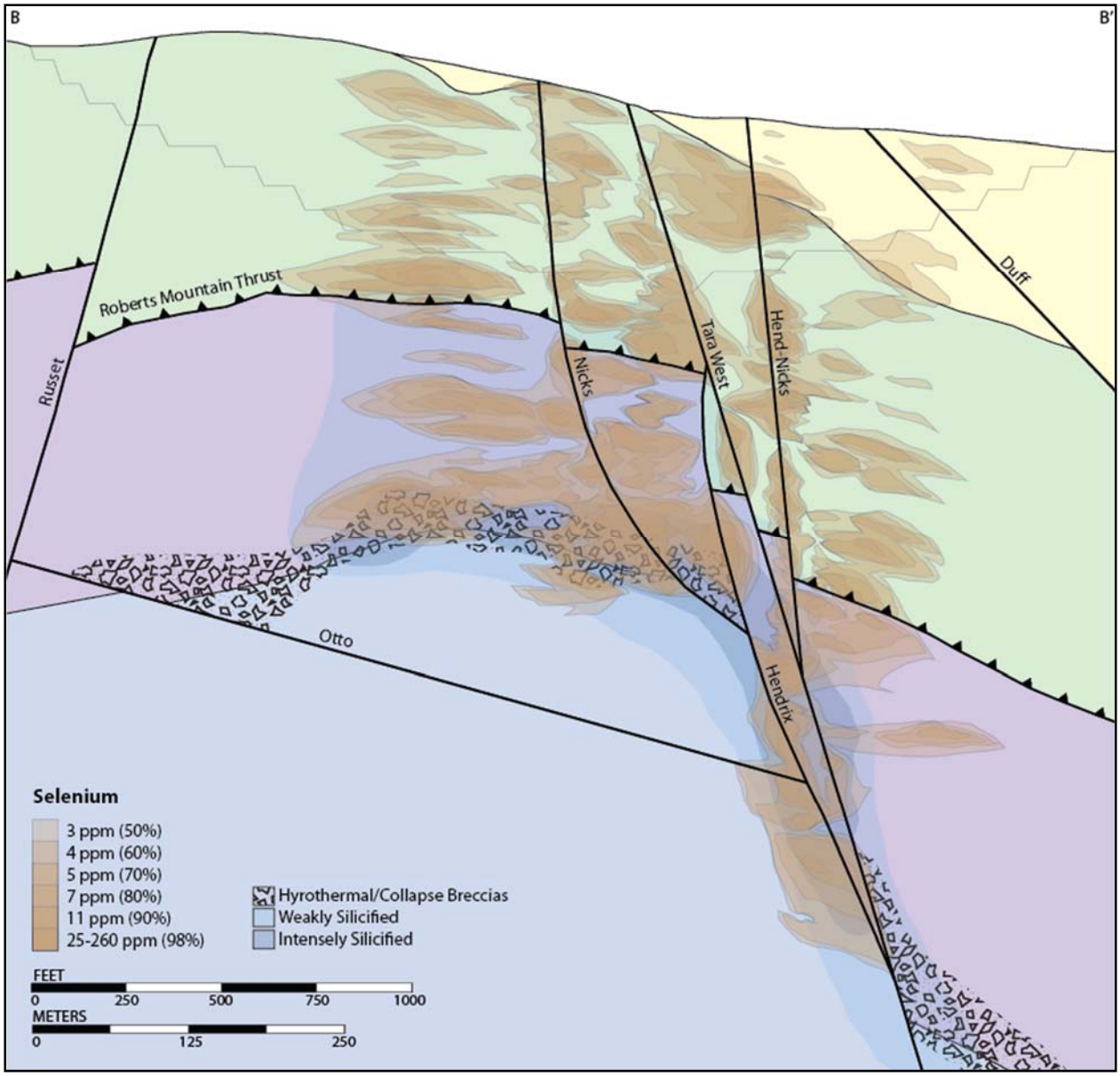

Figure 64. Cross-section through the El Niño mine with contours of selenium enrichment (3-260 ppm) relative to the major faults, four major formations, breccias, and silicification zones. See Figure 7 for unit legend and drill-hole locations.

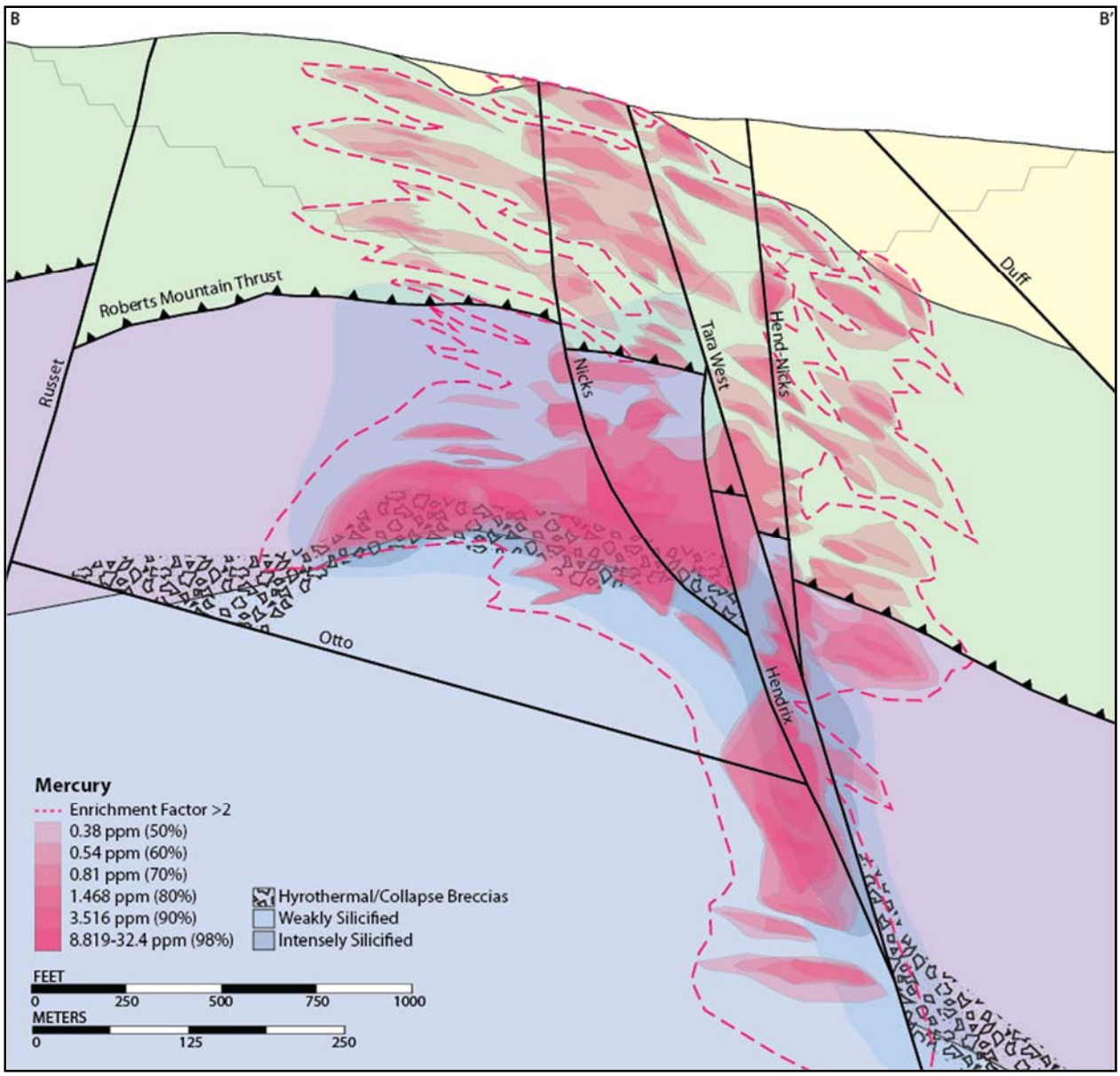

Figure 65. Cross-section through the El Niño mine with contours of mercury enrichment (0.38-32.4 ppm) and EFS >2 relative to the major faults, four major formations, breccias, and silicification zones. See Figure 7 for unit legend and drill-hole locations.

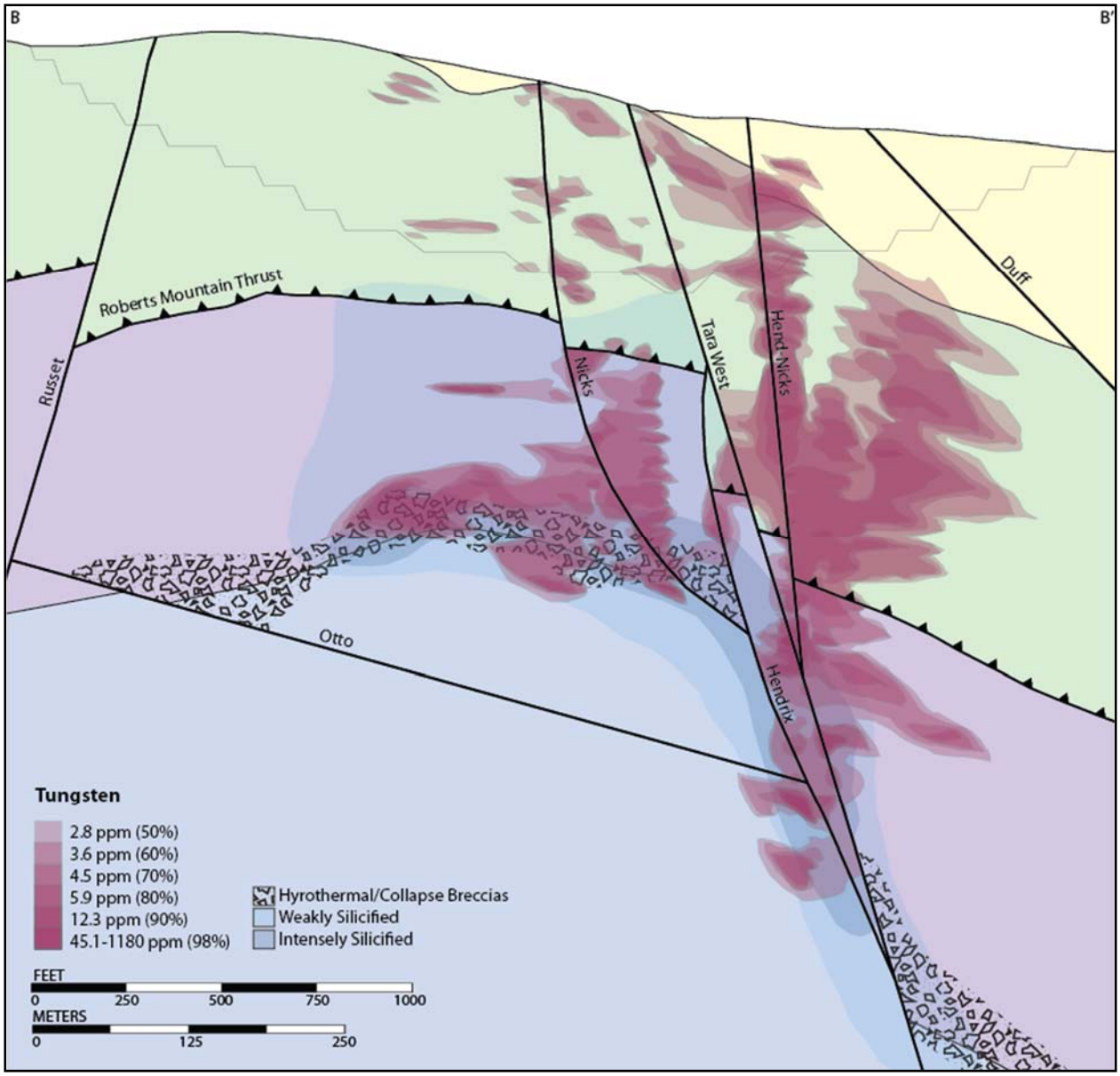

Figure 66. Cross-section through the El Niño mine with contours of tungsten enrichment (2.8-1180 ppm) relative to the major faults, four major formations, breccias, and silicification zones. See Figure 7 for unit legend and drill-hole locations.

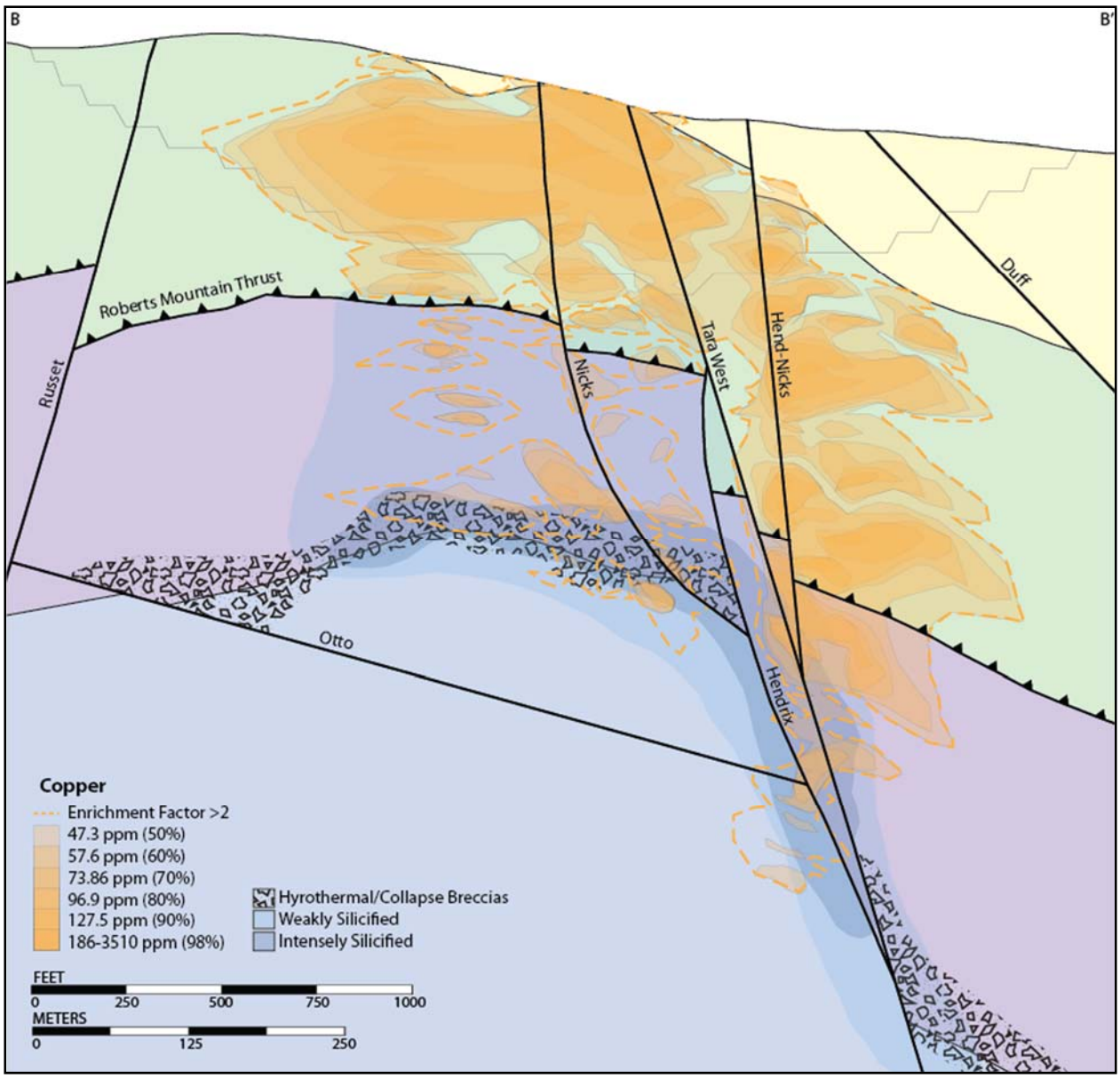

Figure 67. Cross-section through the El Niño mine with contours of copper enrichment (47.3-3510 ppm) and EFS >2 relative to the major faults, four major formations, breccias, and silicification zones. See Figure 7 for unit legend and drill-hole locations.

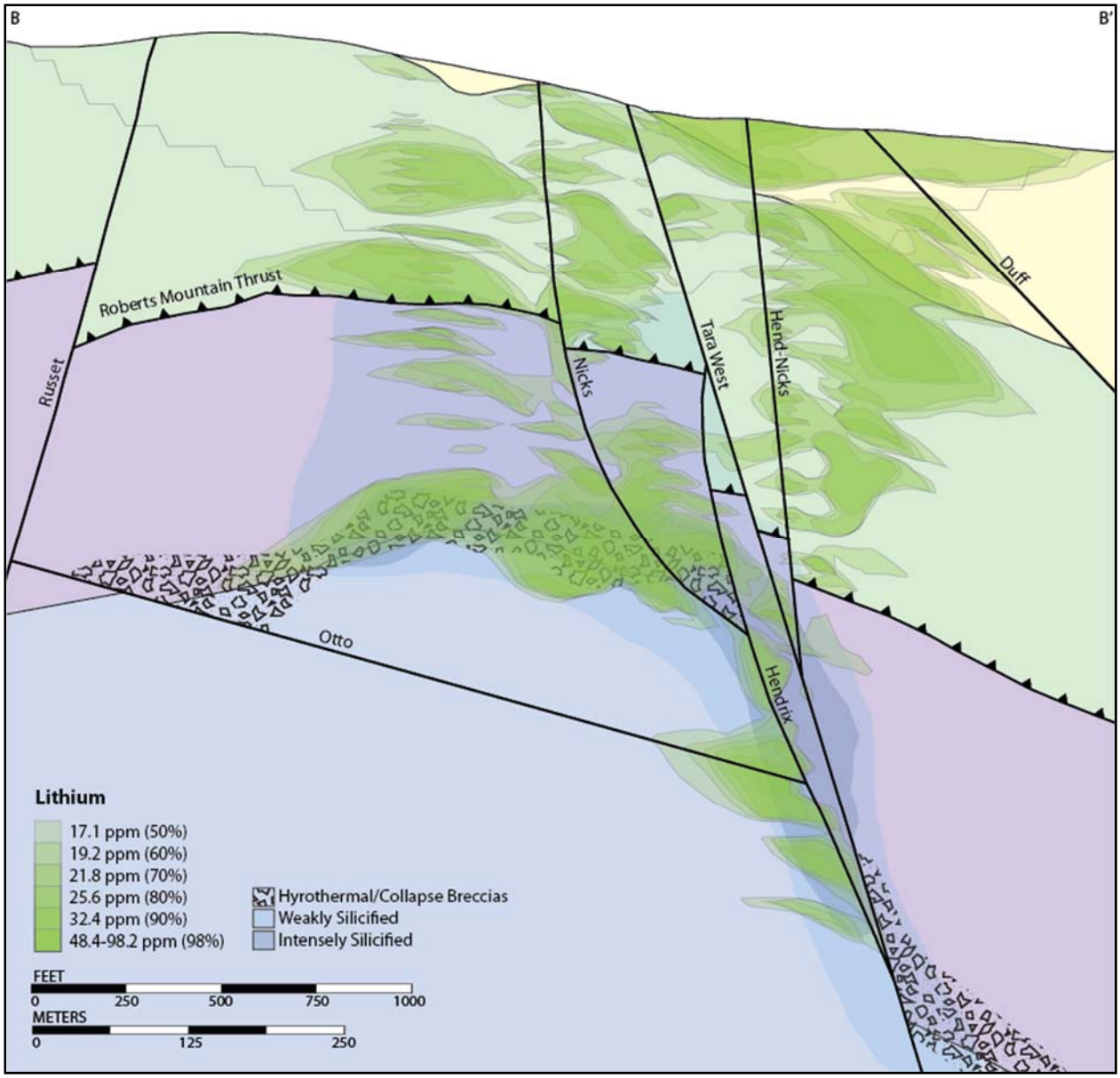

Figure 68. Cross-section through the El Niño mine with contours of lithium enrichment (17.1-98.2 ppm) and EFS >2 relative to the major faults, four major formations, breccias, and silicification zones. See Figure 7 for unit legend and drill-hole locations.

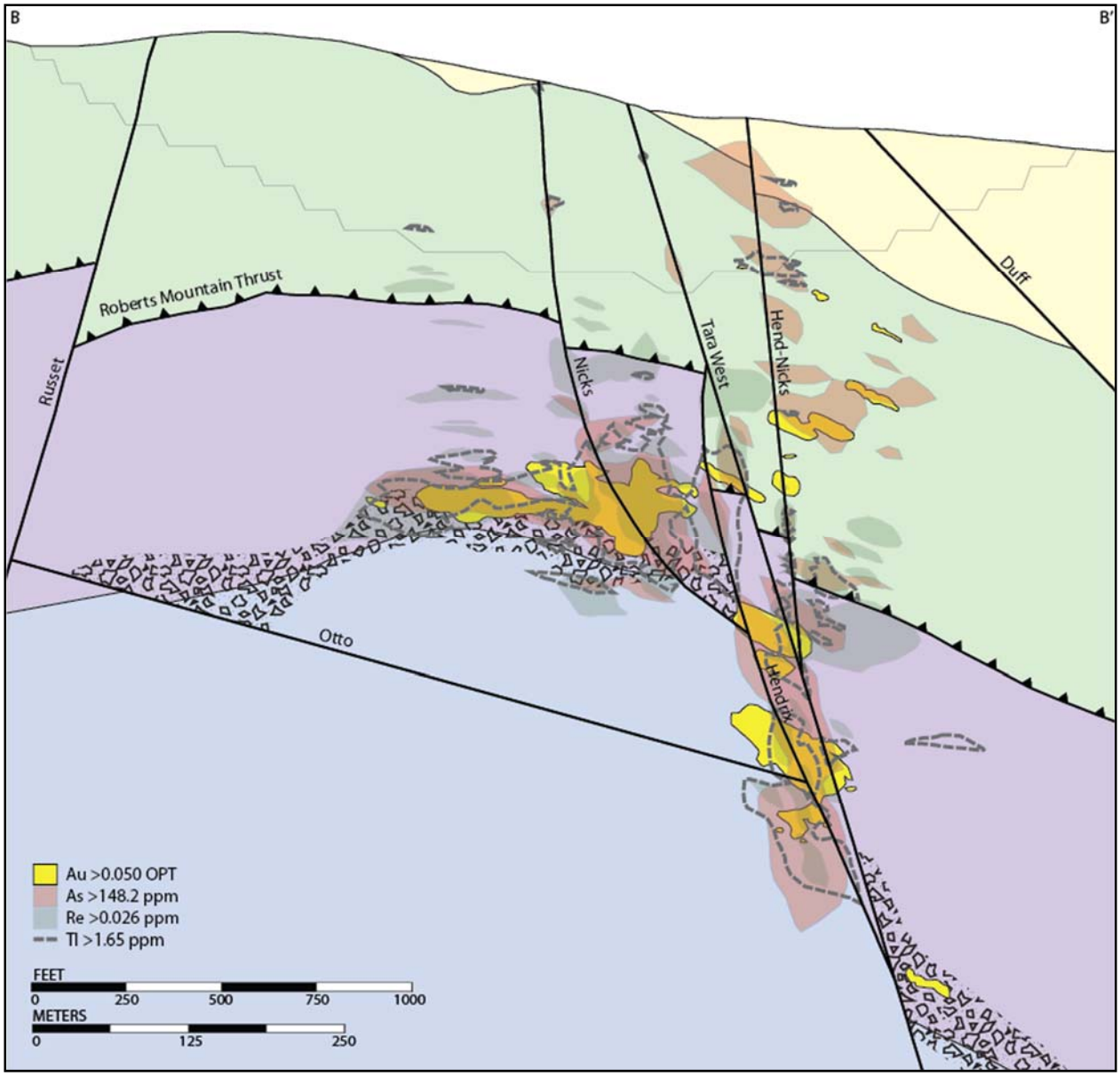

Figure 69. Cross-section through the El Niño mine with contours of gold enrichment (>0.050 opt) compared to arsenic (>148.2 ppm), rhenium (>0.026 ppm), and thallium (>1.65 ppm) relative to the major faults, four major formations, breccias, and silicification zones. See Figure 7 for unit legend and drill-hole locations.

Lithium (Figure 68) is the only element that appears to be evenly distributed between the upper and lower plates. High concentrations are found above and below the intensely silicified breccia zone, at the Otto-Hendrix intersection and near the surface in the Tertiary Carlin Formation at the Hend-Nicks fault. Lower concentrations are in the same areas but with a larger footprint, the largest of which is the surface, where it spreads out from the Hend-Nicks fault into the Carlin and Vinini Formations. High lithium values are also present throughout the breccia zone and spread out along bedding planes in the Rodeo Creek and Vinini (both SE and NW of the Tara West fault).

Figure 69 shows the first group of elements at As >148.2 ppm, Re >0.026 ppm, Tl >1.65 ppm and Au >0.050 opt. The highest concentrations are found near the upper contact of the breccias, along the Hendrix and Hend-Nicks faults and in pods of enrichment throughout the Rodeo Creek and Vinini Formations. These elements have a strong correlation in the Rodeo Creek. Au and As have the strongest correlation in the Vinini. There are high concentrations of Re with Au in the Rodeo Creek Formation; however, there are also pods of high concentration that are not associated with gold in both the upper and lower plate. As closely mimics gold in the lower plate, but extends beyond the 0.050 opt Au contour along the Hend-Nicks fault in the Vinini Formation.

Figure 70 shows the contour geometries of Ag >0.250 opt, Hg >1.47 ppm, Se >7 ppm, and Te >0.12 ppm in relation to each other. At these concentrations, there is significant spatial overlap of enrichment of the four elements, especially in the lower plate rocks. The upper plate concentrations have a lot of overlap; however, do not always align, possibly due to a difference in concentration, a lack of correlation, or subtle differences in rock type or temperatures that caused variations in precipitation.

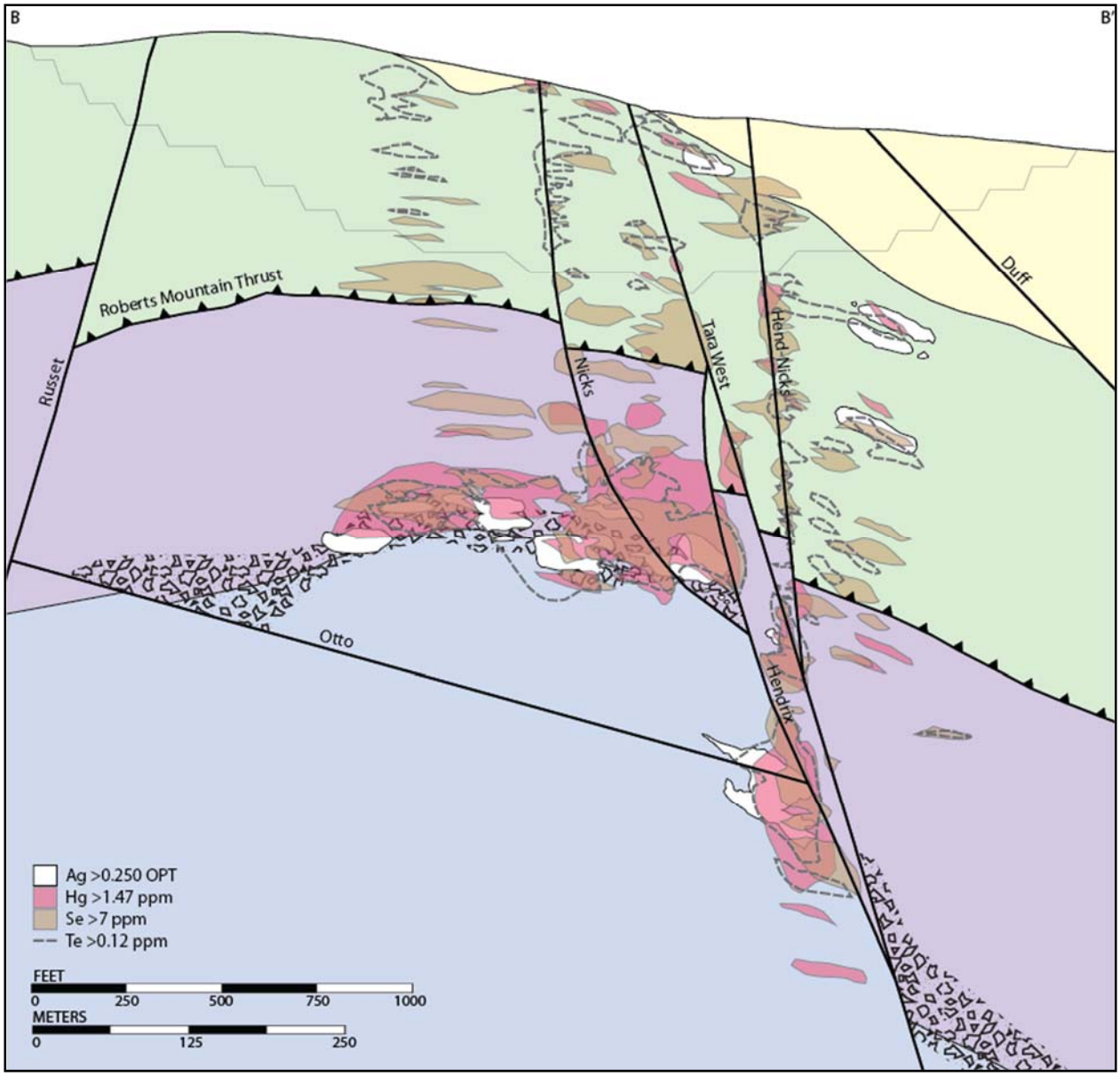

Figure 70. Cross-section through the El Niño mine with contours of silver enrichment (>0.250 opt) compared to mercury (>1.47 ppm), sellenium (>7 ppm), and tellurium (>0.12 ppm) relative to the major faults, four major formations, breccias, and silicification zones. See Figure 7 for unit legend and drill-hole locations.

4.10 Discussion and Interpretations

4.10.1 Lithogeochemical Suite of Elements

The principal component analysis (PCA) identified four suites of elements. Fe, Ce, Al, La, Ti, Nb, Zr, and Th (suite 1) were interpreted as being the group of elements that were immobile in the mineralization zone. This suite likely represents original clay geochemistry due to the correlation of this suite to Al. Scatter plots showed strong correlations of Al with suite 1, with the exceptions of Fe and Th in some rocks. Data points from the Carlin Formation also deviated from the trendlines in most cases, suggesting a difference in controls on original sedimentary geochemistry in the Tertiary units.

Downhole plots show a predictable variation of Al, Fe, Th, Ti, Zr, Nb, Ce, and La at unit contacts, making the prospect of using them for lithology identification promising. Box plots also show a somewhat predictable variation in unit-lithologies throughout Button Hill. However, the spread in the data and the variability within each identified lithology make lithology identification difficult. More data with careful correlation to lithology would likely be needed for this to be a viable method for lithology identification.

Grant isocon and EFS plots show that Fe, Ce, Al, La, Ti, Nb, Zr, and Th are often aligned along a single isocon, supporting the interpretation that they are immobile. Al, Ti, and Zr are the three elements that are consistently aligned and so have been used to make the isocon plots and to compare against for the EFS.

The EFS down-hole plot of BD15-052 shows the surprisingly consistent EFS value of 1, being neither enriched or depleted for Al, La, Ti, Zr, and Fe. Fe and La; however, deviate slightly, being marginally enriched in the mineralized zone.

4.10.2 Alteration Suite of Elements

The PCA identified Ca, Mg, S, CO_3, C and Mn as a related suite (suite 3). These elements are major components of minerals added or removed in the alteration types associated with Carlin-type mineralization. Ca, Mg, CO_3, and Mn are depleted during decalcification/decarbonatization. Organic carbon can be replaced during silicification and C as CO_3 can be depleted during decalcification. S is enriched during sulfidation. S is also shown to be associated with Au mineralization, while Ca, Mg, CO_3, C, and Mn have no correlation. The lack of correlation could suggest that removal of these elements is thorough in Au mineralized zones or that the decalcification footprint is broader than mineralization.

4.10.3 Anoxic Deposition Suite of Elements

Suite 4 of the PCA consists of P, Zn, Y, Pb, and Mo, which is consistent with anoxic to euxinic deposition in a metalliferous shale facies (Tribovillard et al., 2006). This suite was not grouped with suite 1 because this suite is often regarded as mobile, as shown by the depletion of these elements in the Grant isocon plot of average brecciated Rodeo Creek Formation. This is also consistent with the EFS down-hole plot that shows a value near 1 in the relatively unaltered Rodeo Creek rocks, enrichment in the intensely silicified zone, depletion of Zn and P in the decalcification zone, and enrichment in the mineralized zone.

4.10.4 Mineralization Suite of Elements

Of those suites identified by the PCA, Au, Ag, Cu, As, Sb, Te, Tl, and W (suite 2) was interpreted as being associated with Au-Ag mineralization because of the presence of those two precious metals and other known ore associated elements (As, Sb, Te, Tl, and W).

The scatter plots confirmed that there are correlations between As, Sb, Te, and Tl from suite 2 of the PCA. The scatter plots also suggest that there are two mineralization suites. The first mineralization suite consists of Au, Ag, As, (Cu?), Fe, Hg, Re, S, Sb, (Se?), Te, and Tl, shown by the positive correlation of Au with those elements. The correlation of Cu and Se to Au is unclear. The apparent lack of correlation of Cu to Au is demonstrated in the cross-sections that show a very different enrichment pattern for Cu, and the raw geochemical data that demonstrates Cu values that are very near average crustal abundance. S, Fe, Re, and Se were added to suite 2 after trialing scatter plots and finding a convincing trends between these elements and Au.

The second mineralization suite consists of Ag, Au, (As?), Cu, (Fe?), Hg, (Re?), S, Sb, Se, Te, and (Tl?), shown by the positive trends of Ag plotted with the other elements. Many of these elements (Au, As, Fe, Re, and Tl) appear to only have a positive correlation at low Ag concentrations, suggesting again that the highest Ag grades have a different chemical signature.

The correlation matrices of suite 2 elements for samples containing >0.05 opt Au and samples containing >0.05 opt Ag are consistent with the idea that there are two mineralization suites, though, many of the elements shown to be correlated in the lower grades are not correlated in the higher grades. Higher grade Au is shown to be associated with As, Cu, Fe, Hg, S, Te, Tl, and W, while higher grade Ag is associated with Hg, Sb, Se, and Te. At these higher grades, Au is not correlated with Ag. High Au grades are also not associated with Se, and Re and Sb have negative correlations. The cross-section of Re suggests that it is associated with silicification. Re may be remobilized in the high-grade gold samples. Sb has a very strong negative correlation which is consistent with the observations that it spikes above and below the Au ore body (Table 3, Figure 38, and Figure 45).

High grades of silver are negatively correlated with Cu which may suggest Cu was remobilized during Ag mineralization. In fact, in the high-grade Ag samples, Cu has a negative correlation to As, Hg, Re, S, Sb, Te and Tl.

The down-hole plots show that concentrations of the mineralization suite are somewhat controlled by lithology; however, contacts often have little effect on concentration. Gold in a typical mineralized zone has a broad "hump" that extends from the middle Rodeo Creek Formation to the upper contact of the Bootstrap Formation. Ag generally increases with Au; however, rarely has the same broad hump shape, but rather has a lower and thinner high grade zone, consistent with the lack of correlation in the correlation matrix of high-grade Au and Ag. Te is associated with both Au and Ag, mimicking the behavior of both, also consistent with the correlation matrixes that show a correlation of both high-grade Au and high-grade Ag to Te. As closely mimics gold; however, often has a slightly broader footprint centered on the zone of Au mineralization. Tl also mimics Au, but doesn't spike until Au reaches a threshold of around 0.5-1 ppm. Hg appears to mimic Ag the closest, but is also associated with Au. Sb often has spikes at the top and bottom of gold mineralized zones. This may explain the negative correlation of high-grade Au to Sb in the correlation matrix.

The Grant isocon plot for all of the El Niño samples identified as breccia by Barrick Goldstrike within the Rodeo Creek Formation show enrichment in suite 2 (Ag, Au, As, Cu, Sb, Tl, Te and W) together with S and Li. Li has been found to be enriched in other Carlin-trend deposits and is thought to be due to Li enrichment in evaporites at or near the surface that was scavenged by fluids that take the same paths as Au mineralizing fluids, causing it to precipitate Li in many of the same areas (Hofstra et al, 2010). The cross-section of Li enrichment shows the highest concentrations at or near the surface, consistent with the evaporite interpretation.

The patterns of enrichment of the different elements in the different breccias was investigated using enrichment factor scores (EFS) in down-hole plot to effectively reduce the noise from variable concentrations of each element. They show a very similar pattern of gold enrichment that doesn't exactly line up with Ag enrichment. The also show that W, Te, Sb, and Hg appear to mimic Ag, while As, Tl and Te mimic Au. The EFS was used to demonstrate which breccia types appear to be enriched in mineralization suite associated with Au and which appear to be associated with Ag.

Overall, the Roberts Mountain thrust tectonic breccia (Bx1) is associated with both Au and Ag mineralization suites in different parts of the deposit based on selective whole-rock geochemistry; however, Bx1 is most commonly associated with higher Au values. Bx2, the vuggy quartz veined breccia, appears to also host both types of mineralization. Bx3b, the pyrite veined breccia that is not associated with bleaching, is associated with Au mineralization in the one sample selectively sampled for whole-rock geochemistry, so it is unknown if this is the case everywhere; however, it is the only pyrite veined sample to have a low Ag/Au ratio and high concentrations of elements associated with Au mineralization. Bx3a consistently shows a high Ag/Au ratio and is often associated with notably high Se, Te, and Sb.

Although an association of Ag mineralization and Bx3a is apparent, the lack of association of Ag to Fe or S suggests that it is not associated with pyrite. It may be that the Ag is mineralogically associated with bleaching, and not necessarily pyrite. It is noted that the Bx3a bleached selvages are not everywhere accompanied by pyrite or pyrite veining. In the collapse breccia samples (Bx5) it is not possible to determine whether bleaching has occurred. The rocks are noticeably lighter, though, many of these rocks consist of limestone as a major constituent, which is naturally lighter in color and contains less organic material.

The spatial distributions and geometries of concentrations of ore-related elements in cross-section are very similar. There is a spatial association of all suite 2 elements with the modeled breccia zone and the Hend-Nicks fault, with a consistent thin "chimney" that reaches the base of the Tertiary units in the case of As, Sb, Hg and Cu, and into the Tertiary units with Tl, Re, Te, Se, and W, possibly suggesting remobilization. The difference in Au mineralization (+As, Tl and Re) and Ag mineralization (+Te, Se, and Hg) is that the former tends to have the highest concentrations above the intensely silicified zone, partly in the main breccia zone and partly in the overlying Rodeo Creek Formation, while the highest concentrations of Ag are typically below Au and within the breccias. Important to note is that Bx1 was not considered in the breccia model and that which is modeled as Rodeo Creek Formation is likely Bx1. Another difference is in the extent of Ag mineralization in the upper plate, especially NW of the Tara West fault. Sb has a similar pattern as Au, and so has been grouped with Au, despite the lack of correlation with the highest grades of Au. W has overlap with both Au and Ag; however, the highest concentrations are in the upper plate, suggesting that it may be sourced from an unrelated fluid that took similar flow paths or has been precipitated in different rock and temperature conditions. Cu and Li are also highest in the upper plate. Li, however, is highest near the surface, consistent with the idea that it was deposited from surface derived evaporites. Re is poorly correlated to both Au and Ag, and the cross-sections show that it is closely associated with the zone of weak silicification. Re may be associated with the fluids that caused this silicification.

The differences in spatial distribution and associations suggest that there are two separate deposits that make up the Au and Ag ore bodies of the Button Hill mineralization zone. Gold mineralization was likely Carlin-type in view of its geochemistry, low Ag/Au ratio, location on the Carlin-trend and the close proximity to other Carlin-type Au deposits. Carlin-type mineralization isn't clearly spatially associated with any one single brecciation event; however, is found within Bx1,

Bx2, Bx3b, and Bx5b. Based on observations from geochemical contours in cross-section, fluids carrying Au, As, (Cu?), Hg, S, Te, Tl, and (W?) rose buoyantly along the Hend-Nicks fault zone where it spread out at zones of high permeability such as the Otto fault and at fault intersections, along bedding contacts, porous lithologies and the breccia zone, precipitating gold in areas of high liberated iron and/or iron as iron sulfide, or bringing Fe in the fluids. Either source of Fe would be consistent with the relatively low EFS score of Fe in BD15-052 that increases slightly in the mineralized zone (Figure 45), and the positive Fe-Au correlation. Sb may have been associated with this fluid, or may have been later, precipitating in zones surrounding Au mineralization.

Later fluids carrying Ag, Hg, Sb, Se, and Te followed the same pathway as Au carrying fluids, and deposited in similar, but not exactly the same, areas. The Ag-bearing fluid was likely associated with low-sulfidation epithermal mineralization in the Miocene due to the following: 1) The geochemical suite is similar to that found in the epithermal Ag-Se deposit in the nearby storm mine (Trotman, 2009), 2) The close proximity to the Storm mine, 3) The close proximity to the Northern Nevada Rift that contains other epithermal deposits (Midas and Ivanhoe; Davis and Muntean, 2016), 4) In cross-section, the epithermal fluids appear to have used the Tara West fault as a conduit and, in some cases, appears to have crossed over the fault to the northwest. This is in contrast to the Au suite that appears to be cut off by the Tara West fault. Tara West is a north-south high-angle normal fault thought to be associated with Basin and Range extension. It could be that the older deposit is cut off by the Tara West (Eocene Carlin-type Au) and the younger deposit used it as a conduit (Miocene low-sulfidation epithermal Ag). The lack of apparent offset of mineralization one would expect to see if cut by a younger fault may be the result of error associated with drawing the mineralization contours. Offsets are difficult to visualize and contour within areas of sparse drill-core data.

CHAPTER 5 – SHORT-WAVE INFRARED SPECTROSCOPY

5.1 Mineralogy

Phyllosilicate, carbonate, silica, iron oxide, and sulfate mineralogy in the Button Hill deposit were determined via short-wave infrared (SWIR) spectroscopy method and mapped over visible light core photographs of approximately 181.2 m (594.6 ft.) of core. Minerals and classifications identified using SWIR include; white mica, ammonium mica, silica, kaolinite, montmorillonite, calcite, iron-rich carbonate, goethite, hematite, jarosite, an unknown iron-silicate, aspectral, and undifferentiated dark rock (see Figure 81 for example of mineral mapping results). Variations in compositions and/or crystalline structure were identified for mica, iron-carbonate, carbonates, and aspectral minerals.

Figure 72 and Figure 74 show spectral results from Corescan and TerraSpec side-by-side for comparison and to demonstrate repeatability of the spectral results.

5.1.1 Micas

White mica is the dominate phyllosilicate mineral group identified in the Button Hill deposit. The term "white mica" is used for the phyllosilicates muscovite, phengite, paragonite and illite undifferentiated. White mica spectra is characterized by an OH absorption feature at 1400nm, an H_2O absorption feature at 1900nm and absorption features at 2200nm and 2350nm (Looby, 2006).

White mica composition was determined by the position of the 2200nm (AlOH) absorption feature (Figure 71). Wavelength position of the AlOH absorption feature within 2185-2196nm is characteristic of paragonite ($NaAl_2(Si_3Al)O_{10}(OH)_2$), 2196-2212nm indicates muscovite

$(KAl_2(Si_3Al)O_{10}(OH,F)_2)$ and 2212-2225nm represents phengite $(K(AlMg)_2(OH)_2(SiAl)_4O_{10})$ (Scott and Yang, 1997).

White mica at the Button Hill deposit ranges from muscovite to phengite, with the lowest 2200nm feature position being at the muscovite-paragonite transition of 2196nm. Figure 71 shows the range of the 2200nm feature position in a transect through a typical silicified breccia. It ranges from ~2200nm to ~2210nm in this example.

Figure 73 is an example of a carbonate matrix collapse breccia that contains a variety of mica compositions. The variety of mica reflects the variation in lithology in the clasts, as well as the matrix. Spectra was taken from 3 points to show the range in 2200nm feature positions. In this example, the feature ranges from 2196nm to 2228nm (muscovite to phengite).

Ammonium bearing mica is present in the upper sections of the silicified breccia zones. It is associated with pyrite veinlets and small (1-5 cm) bleached selvages within Bx3a crackle breccia of the Rodeo Creek mudstone and tectonic breccia (Bx1). Ammonium mica spectra displays a step-like pattern between 1900 and 2200nm which consists of low amplitude absorption features at approximately 2000 and 2110nm (Looby, 2016). Figure 72 shows spectra collected from both the TerraSpec Halo and Corescan Mark III spectrometers. The spectra demonstrates how the two systems compare when analyzing an ammonium mica-rich breccia. Spot locations 1-3 from both systems demonstrate similar absorption features, including the small absorption features at 2000 and 2110nm. The Mark III, however, produced an undifferentiated spectra in spot 4, while the Halo showed ammonium mica. This is likely due to the higher spatial resolution of the Mark III spectrometer. Spectrum CS6 was collected outside of the ammonium mica alteration zone, within the white mica, and shows no absorption feature at 2000nm.

Both muscovite and phengite can be ammonium-bearing; however, muscovite is the primary ammonium-bearing mineral. Phengite is rarely seen in the hydrothermally altered rocks.

In drill-holes BD15-053, BD15-051, and BD14-04C phengite is largely associated with relatively unaltered limestone, with the exception of BD15-052, where the 2200nm absorption feature lies near the paragonite/muscovite transition at 2196nm. In the silicified zones, phengite is only locally present, often associated with breccia clasts and weakly associated with a brown-red stained silicified limestone matrix of a collapse breccia (Bx5b).

The illite spectral maturity (ISM), shown on Figure 101, is determined based on the depth ratio of the 2200nm and 1900nm absorption features for illite spectra. This is a measure of molecular water in muscovite, which is a proxy for the evolution, or maturity, of phyllosilicates with increasing temperature. Increasing sharpness and intensity of the 2200nm absorption feature coupled with a smaller and less defined 1900nm feature (H_2O) increase the ISM value and therefore the temperature of crystallization (Doublier et al., 2010). The ISM is a "scalar" value automatically generated from the TerraSpec Halo on-board computer program when illite is identified. ISM has been shown to have a correlation with the Kübler index (KI), which is an indirect measurement of crystallinity. The equation for the best fit line of ISM versus KI, $y = 2.6503e^{-1.0294x}$ (Doublier et al., 2010), was used to determine the KI value which was used to estimate the temperature of formation from experimental work by Abad (2007).

For samples identified by the TerrasSpec, the term "illite" is used to describe the phyllosilicates muscovite, phengite, paragonite and illite undifferentiated.

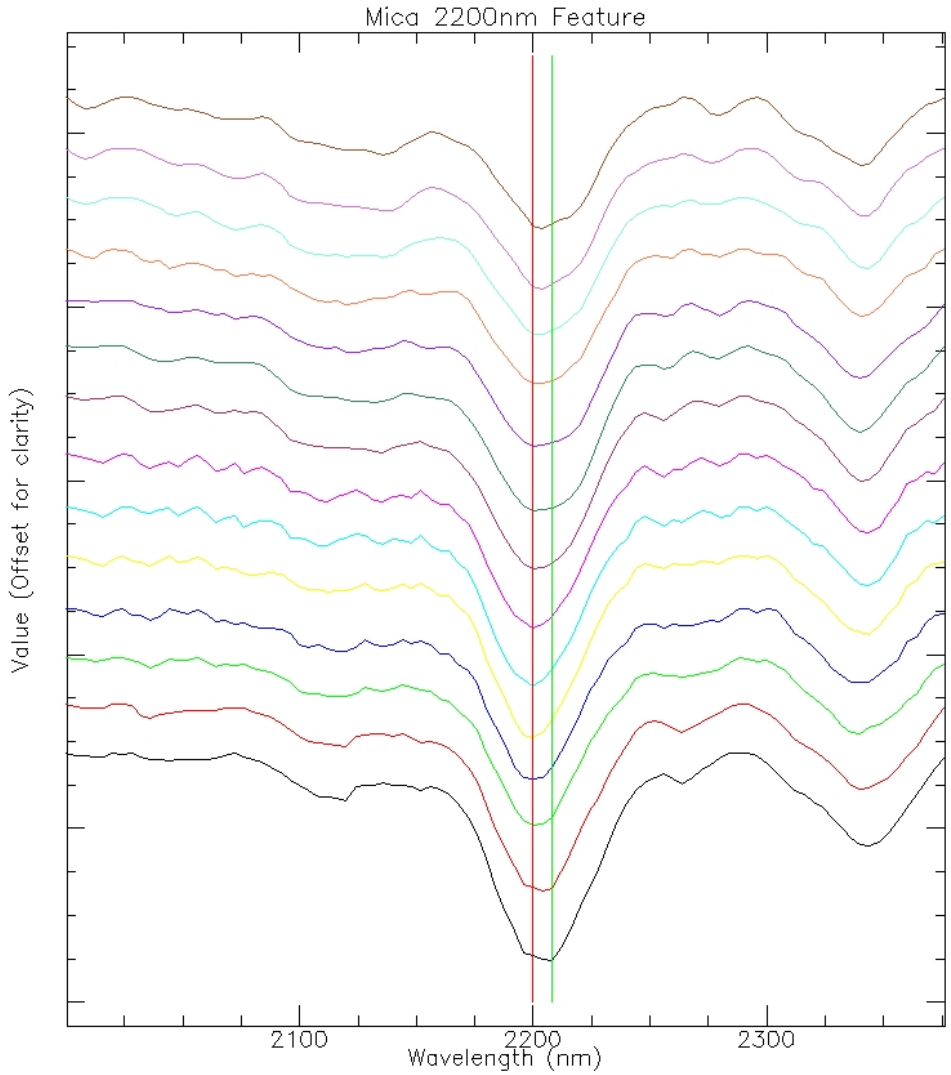

Figure 71. Spectra from a transect through sample BD15-052_795.7 (Figure 89) that demonstrates the range of the 2200nm feature position. It ranges from ~2200nm (red line) to ~2210nm (green line), within the muscovite range (Scott and Yang, 1997). The total spectral range in this figure is from 2000nm to 2375nm, shown with continuum removed.

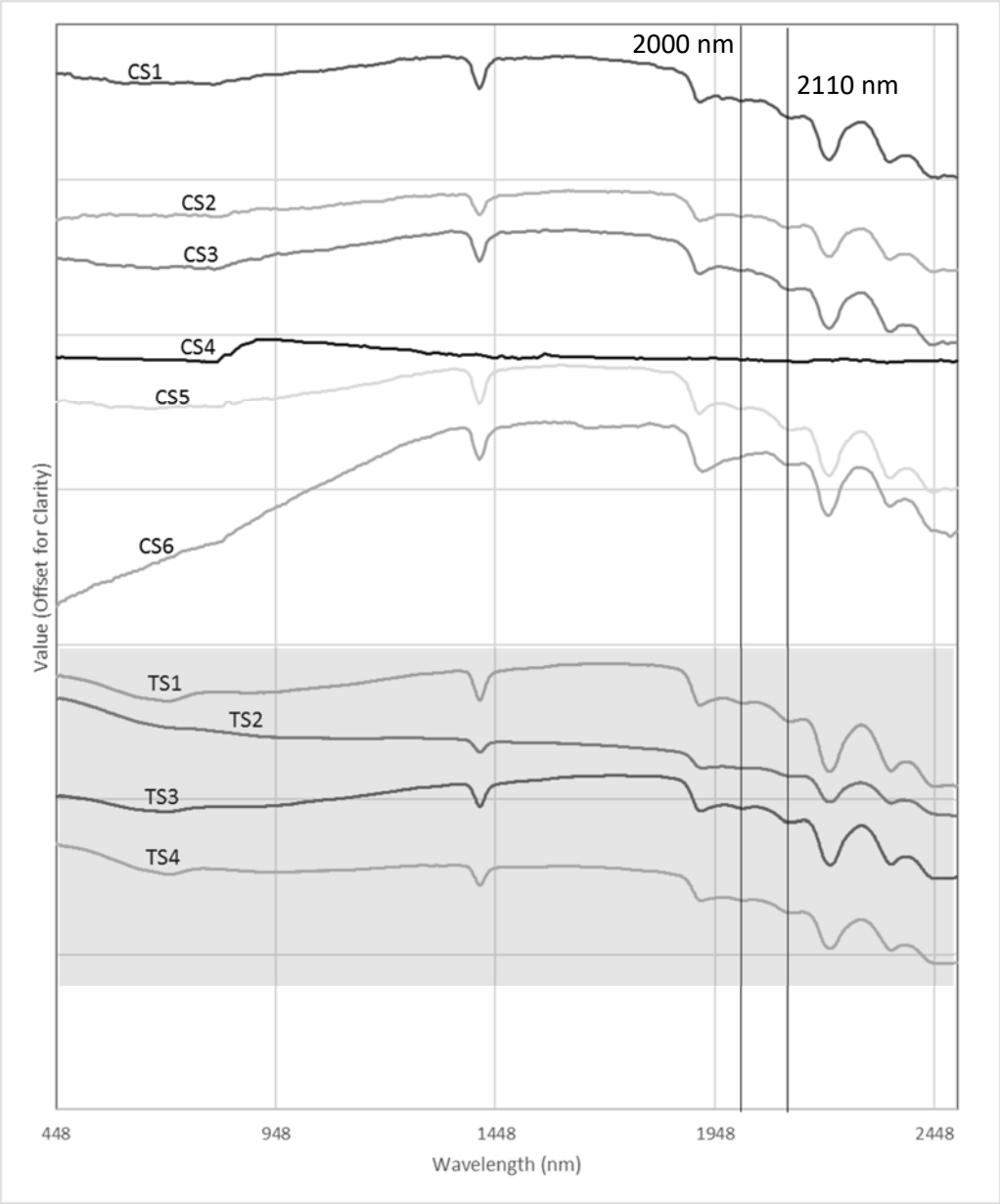

Figure 72. Spectra from sample BD15-052_795.7 (Figure 89) that shows data collected by both the TerraSpec Halo (TS, in gray) and Corescan Mark III (CS) spectrometers. The spectra demonstrates how the two systems compare when analyzing an ammonium mica-rich breccia. Spot locations 1-3 from both systems demonstrate similar absorption features at 2000 and 2110nm. The Mark III produced an undifferentiated spectra in spot 4, while the Halo identified ammonium mica, likely a result of the higher spatial resolution of the Mark III. Spot analysis CS5 is within the higher confidence zone for ammonium mica in the mineral map, likely due to the more pronounced step-like pattern in the 2000 and 2110nm features. CS6 is taken outside of the ammonium mica zone, within the white mica, and shows no absorption feature at 2000nm. Y-axis represents reflectivity, offset by 0.1 for clarity.

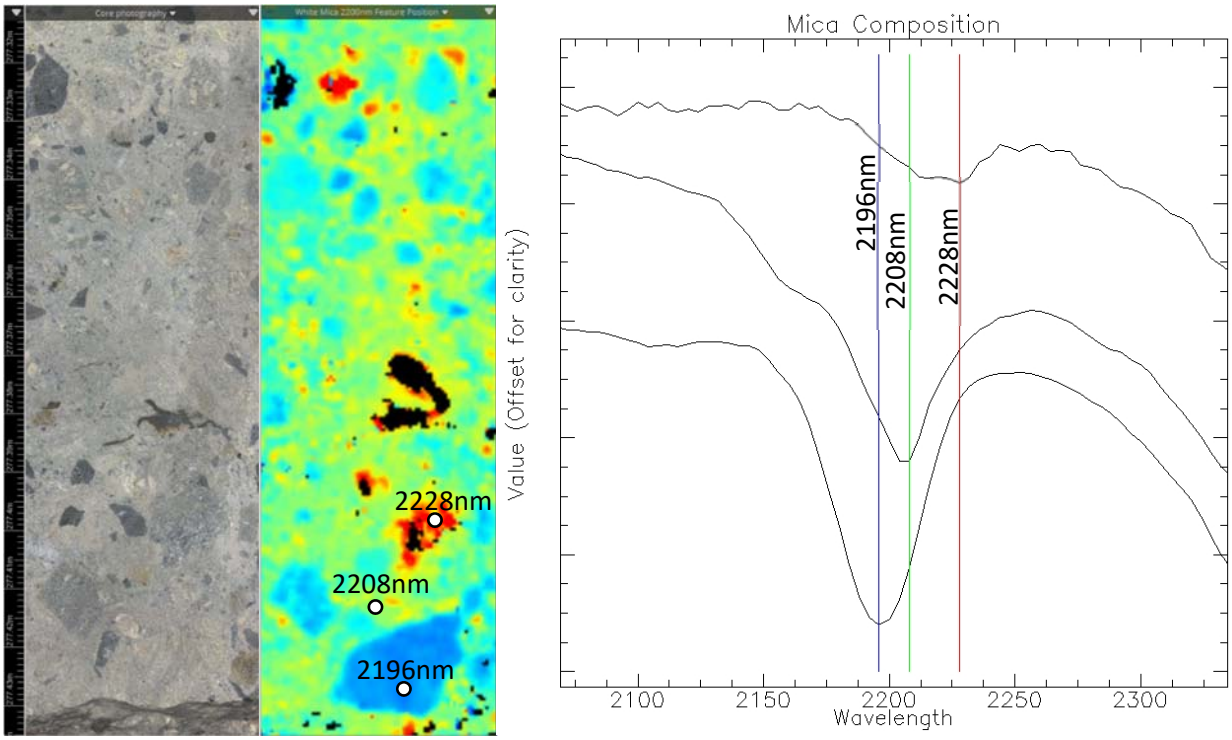

Figure 73. Sample BD14-04C_745.3-746 is an example of a carbonate matrix collapse breccia that contains a variety of mica compositions, shown by the mineral map of the 2200nm feature position. Spectra was taken from 3 points to show the range in 2200nm feature positions which ranges from 2196nm to 2228nm (muscovite to phengite). Y-axis represents reflectivity, offset for clarity with continuum removed.

5.1.2 Carbonates

Carbonate spectra is characterized by absorption features at approximately 1900nm and 2335nm. Carbonate chemistry is differentiated by the wavelength position of the 2335nm absorption feature (Looby, 2006). An absorption feature at approximately 2340nm indicates a calcite composition, an absorption feature at 2317nm represents dolomite, 2327nm is siderite and 2370nm represents rhodochrosite (Laukamp, 2011). At the Button Hill deposit, the 2335nm absorption feature is consistently located at approximately 2336nm (yellow in the color scheme used for the '2335nm Feature' false color images, Figure 95), indicating that all analyzed carbonates are calcite, and that dolomite was not identified. The mineral class "carbonate" is an undifferentiated composite of calcite, carbonate 2, and Fe-carbonate.

Carbonate 2 is the name given to calcite that has a variation in the 1900nm absorption feature. The 1900nm feature in carbonate spectra of the Button Hill deposit transitions from a single rounded feature with a minimum at 1920-1940nm, to two small, sharp absorption features at approximately 1885nm and 1985nm, which is identified as Carbonate 2 (Figure 74) (Looby, 2016). Carbonate 2 is most commonly well-formed, crystalline calcite in calcite veins and breccias (Figure 95). According to Clark et al. (2007) the "carbonate 2" spectra is consistent with pure calcite, while the rounding of the 1900nm absorption feature may be associated with a compositional difference or some mixture of spectra from other minerals (calcite and silica for example). Figure 74 shows carbonate and carbonate 2 spectra from the Mark III and Halo spectrometers. Spectra from both locations (site 1 and 2) have the same absorption features with both hyperspectral analyzers.

Another variation to the composition of carbonate at Button Hill is the iron content. A broad U-shaped doublet absorption feature at approximately 1150nm and 1450nm, and the CO_3 absorption feature at 2336nm (Figure 75), is characteristic of calcite that is Fe-rich. In the false color images (Figure 95), this is classified as "Ferroan Calcite." The slope of the 1750nm to 1360nm feature in the raw spectrum is taken as a measure of iron content within the calcite. A steep slope represents a higher iron content than a shallow slope. This may however also be affected by carbonates mixing with aspectral minerals or organic material (Looby, 2016).

The narrow range of the carbonate 2330nm absorption feature location is shown in Figure 76. Figure 76 is the spectra from the transect through sample BD15-052_948.4 (Figure 95) and it shows a range from 2335-2338nm, consistent with the spectral parameters for calcite.

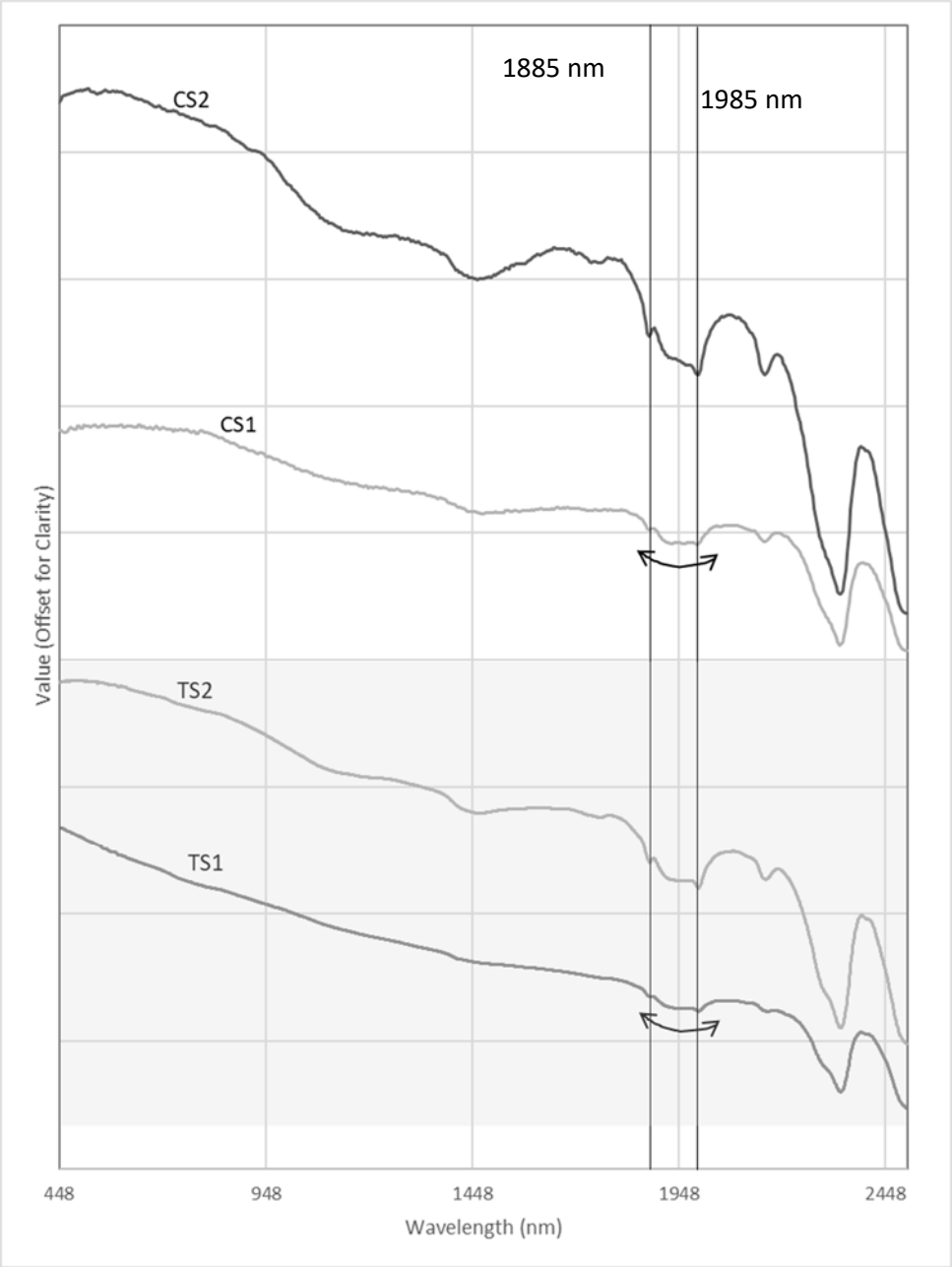

Figure 74. Spectra from sample BD15-052_948.4 (Figure 95) from Corescan (CS) and TerraSpec Halo (TS) from the same locations for comparison. Site 1, in both cases is from the mineral class "carbonate" and site 2 is from "carbonate 2." The 1900nm feature transitions from two small, sharp absorption features (CS1 and CS2) at approximately 1885nm and 1985nm to a single rounded feature with a minimum at 1920-1940nm (CS2 and TS2). These represent the differentiating characteristic for carbonate 2 and carbonate respectively. Y-axis represents reflectivity, offset by 0.1 for clarity.

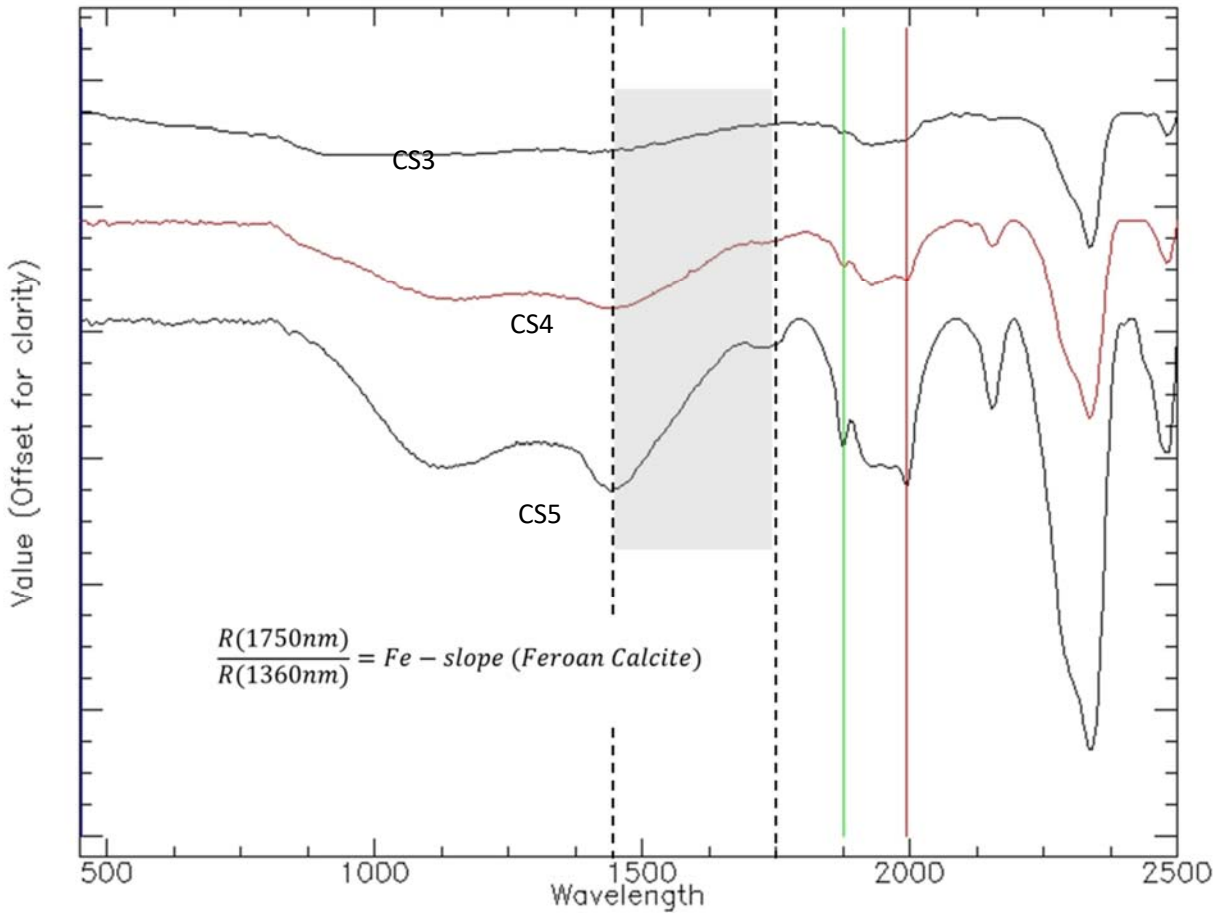

Figure 75. Spectra from sample BD15-052_948.4 (Figure 95) showing the method for determining the Fe-slope spectral parameters. The slope from 1750nm to 1360nm features (in gray, between the dashed lines) represents variation of iron content within the calcite. The steep slope of CS5 likely represents a higher iron content than the shallow slope of CS3 and CS4. Y-axis represents reflectivity, offset by 0.1 and continuum is removed for clarity (slope is however measured from the raw spectrum).

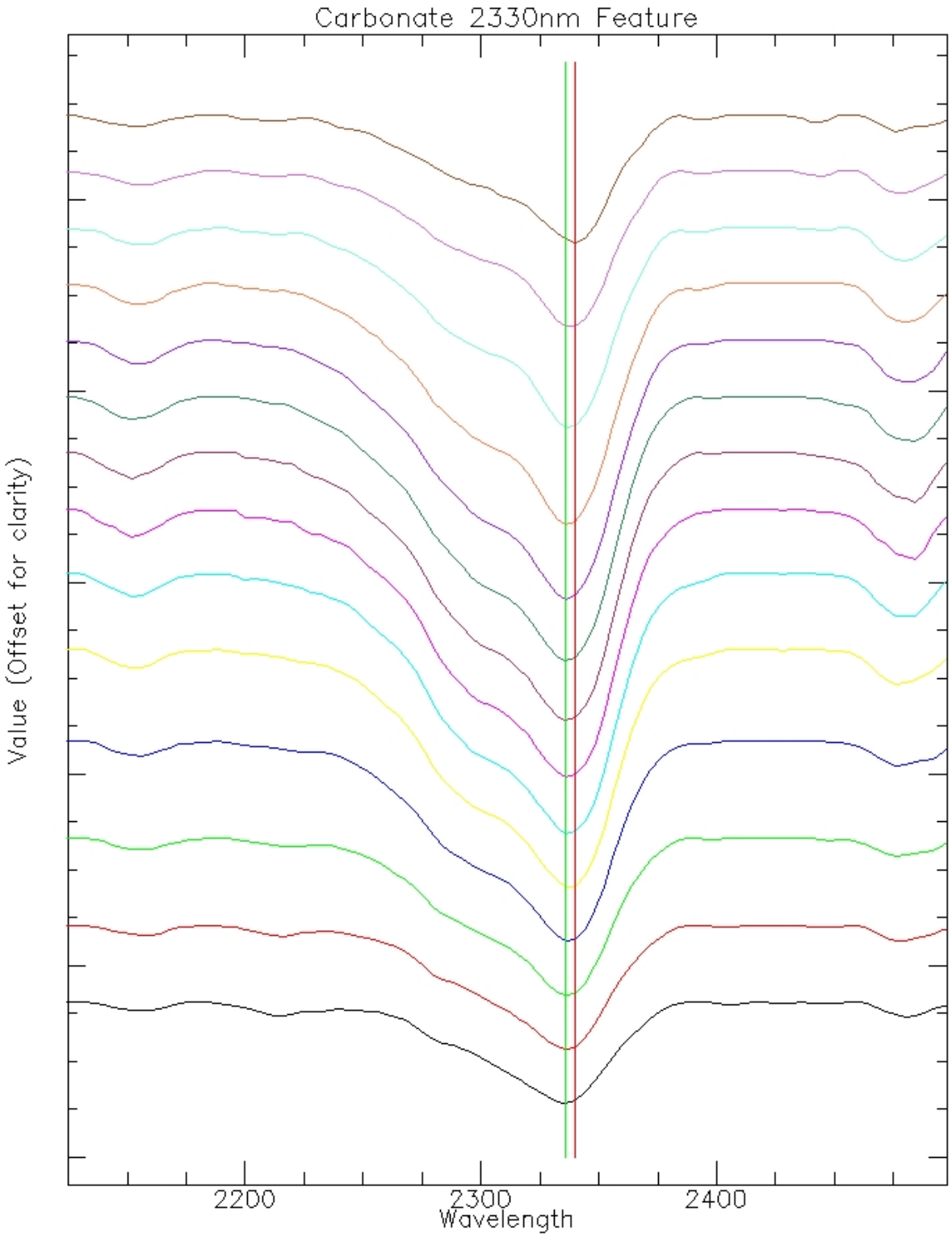

Figure 76. Spectra from a transect through sample BD15-052_948.4 (Figure 95) that demonstrates the narrow range of the carbonate 2330nm absorption feature location in the Button Hill samples. It ranges from 2335nm to 2338nm, consistent with the spectral parameters for calcite. Y-axis represents reflectivity, offset by 0.1 for clarity with continuum removed.

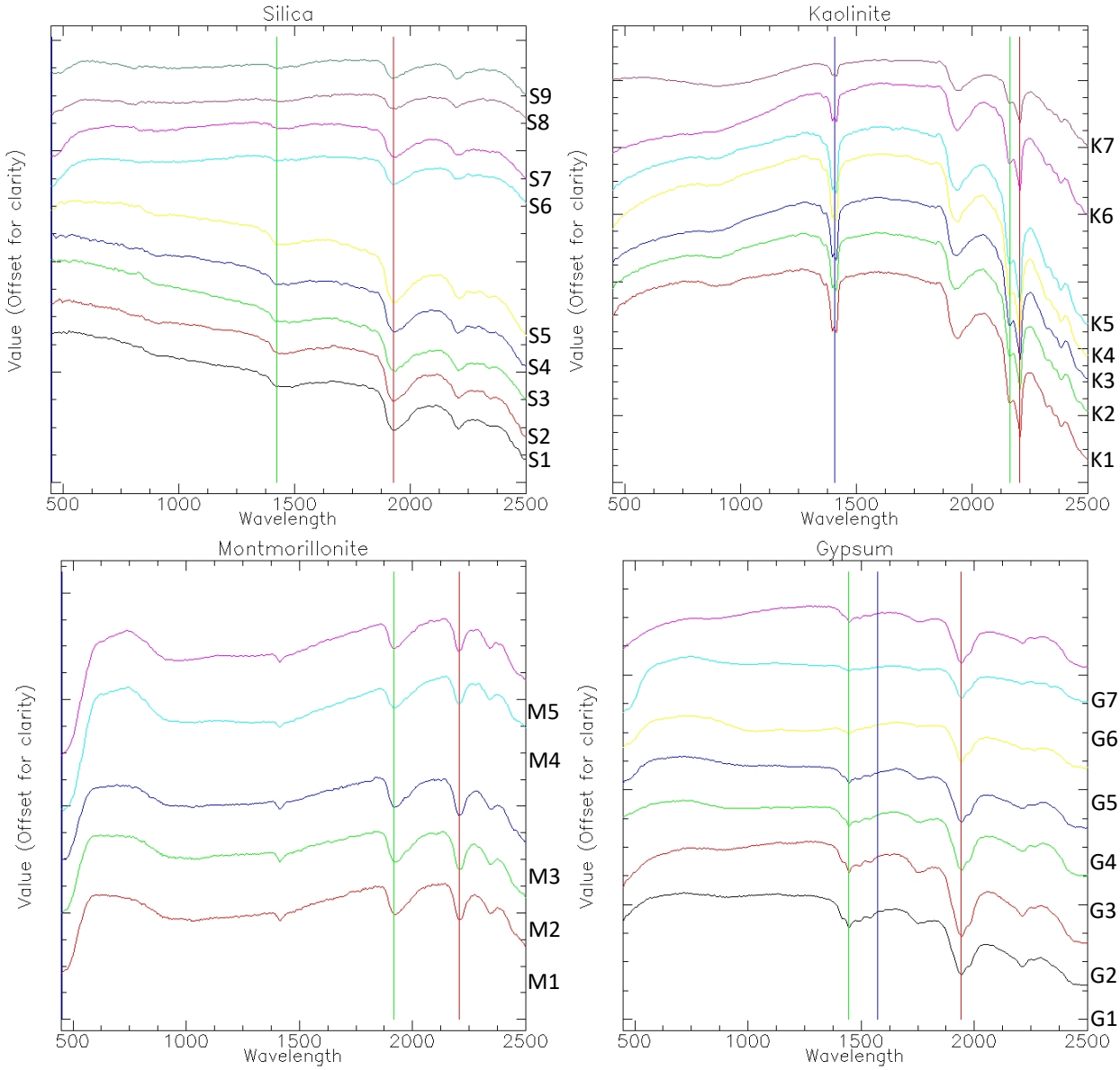

Figure 77. Spectra from sample BD15-052_948.4 (Figure 96) for silica (upper left), kaolinite (upper right), montmorillonite (lower left) and gypsum (lower right). Silica spectra is characterized by absorption features at approximately 1440nm (OH) and 1935nm (H2O). Kaolinite spectra exhibits two characteristic doublet absorption features at approximately 1395nm-1410nm (OH) and 2165nm-2205nm (AlOH). Montmorillonite spectra is distinguished by absorption features at approximately 1400nm (OH), 1900nm (H2O), and 2200nm (AlOH). Gypsum spectra has a characteristic staircase pattern between 1400nm and 1550nm with two small absorption features at approximately 1500nm and 1525nm and a long H2O absorption feature at approximately 1940nm

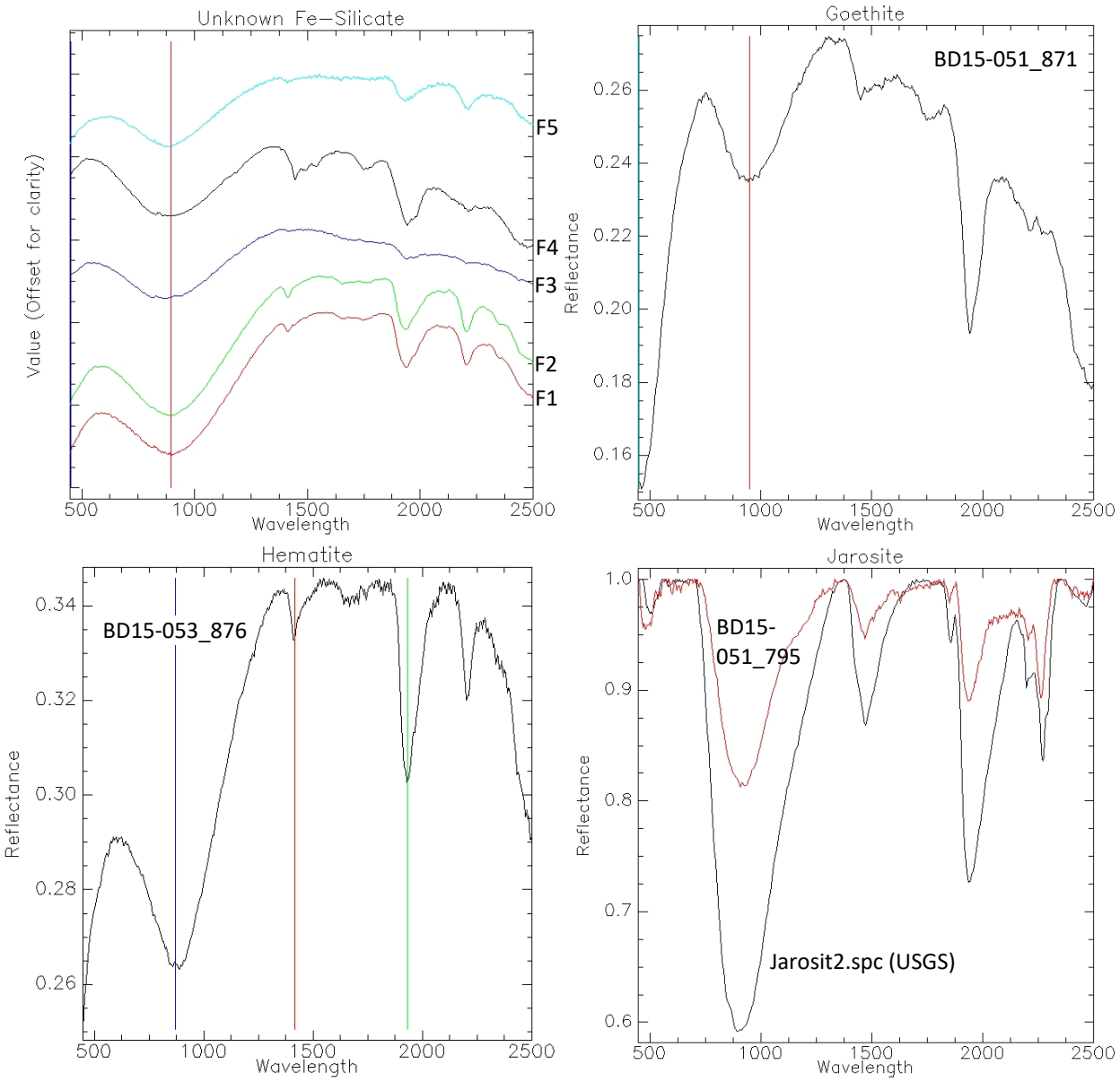

Figure 78. Spectra showing the unknown Fe-mineral from sample BD15-052_948.4 (upper left) (Figure 96) goethite from sample BD15-051_871 (upper right), hematite from BD15-053_876 (bottom left), and jarosite form sample BD15-051_795 (bottom right). The unknown Fe-mineral is characterized by a large, broad absorption feature at ~910nm, distinguished from hematite by the much shallower H2O absorption feature at ~1900nm and the slightly shifted 910nm feature in the Fe-mineral as opposed to a minimum at 840-900nm in hematite. Goethite spectra is characterized by a large, broad absorption feature with a minimum between 900-940nm and a positive slope between 900nm and 1250nm. Hematite spectra is characterized by a large broad absorption feature with a minimum between 840-900nm, and a positive slope between 840nm and 1250nm. Jarosite is distinguished from goethite and hematite by the doublet between 2200nm and 2300nm.

5.1.3 Silica

Silica spectra is characterized by a blunt absorption features at approximately 1440nm (OH) and 1935nm (H_2O) (Figure 77), which are the absorption features for free H_2O, and is distinguished from other hydrous minerals by the lack of other distinguishing characteristics such as the lack of staircase pattern in the ~1440nm feature for gypsum (Looby, 2016). For mineral identification and mineral mapping of silica (Figure 96) these features have been interpreted to be from the free H_2O in hydrous silica and/or fluid inclusions within quartz, thus, the term "silica" refers to any hydrous silica polymorph.

Si-O bond absorption feature is not within the short-wave infrared spectrum and so identification of silica using this method is not infallible. Only the areas of very strongly silicified rock and quartz veins are identified in the false color mineral maps. Areas of week silicification are typically too dark or overwhelmed with other minerals for this method to identify the silica present.

5.1.4 Kaolinite

Kaolinite spectra exhibits two characteristic doublet absorption features at approximately 1395nm-1410nm (OH) and 2165nm-2205nm (AlOH) (Figure 77) (Looby, 2016).

Kaolinite is not common within the Button Hill deposit. It is largely a weathering product found coating fractures. However, it is also prevalent in an unmineralized dissolution collapse breccia and weakly silicified limestone (Bx5b) (Figure 96).

5.1.5 Montmorillonite

Montmorillonite spectra is distinguished by absorption features at approximately 1400nm (OH), 1900nm (H_2O), and 2200nm (AlOH) (Figure 77). Montmorillonite spectra is differentiated from white mica by the deep 1900nm absorption feature relative to the 2200nm feature and the

lack of feature at 2350nm. At the Button Hill deposit, Montmorillonite spectra often has the deep 1900nm feature; however, also has a feature at 2350nm (Looby, 2016). This is likely due to the prevalence of white mica and the presence of both minerals within each of the analyzed pixels, possibly intergrown.

Montmorillonite is present as a coating mineral along fractures, within mostly unaltered limestones (Figure 96) and in the matrix of unaltered dissolution collapse breccias.

5.1.6 Sulfates

Gypsum spectra has a characteristic staircase pattern between 1400nm and 1550nm with two small absorption features at approximately 1500nm and 1525nm. There is also a relatively high amplitude H_2O absorption feature at approximately 1940nm (Figure 77) (Looby, 2016). Gypsum is a minor constituent found on some weathered surfaces and within vuggy silica veins and breccia matrix.

Jarosite is distinguished from goethite and hematite by the doublet between 2200nm and 2300nm (Looby, 2016). Jarosite (Figure 78d) is also a minor constituent at the Button Hill deposit. It is often found coating fracture surfaces.

5.1.7 Unknown Fe-Silicate

The mineral classified as "Unknown Fe-Silicate" in the false color mineral maps is characterized by a large, broad absorption feature at ~910nm (Figure 78). This is distinguished from hematite by the much shallower H_2O absorption feature at ~1900nm and the slightly shifted 910nm feature in the Fe-mineral as opposed to a minimum at 840-900nm in hematite (Looby, 2016). The classification name suggests that the unknown mineral is a silicate; however, could also

be an oxide or hydroxide. Figure 78a shows spectra collected from an area with the unknown Fe-mineral signature; however, F4 appears to have identified a signature from gypsum.

5.1.8 Iron Oxides

Goethite, and hematite (Figure 78) are minor constituents at the Button Hill deposit. They are often found coating fracture surfaces. Goethite and hematite are also found within vuggy silica veins and in some breccias spatially associated with gypsum.

Goethite spectra is characterized by a large, broad absorption feature with a minimum between 900-940nm and a positive slope between 900nm and 1250nm (Looby, 2016).

Hematite spectra is characterized by a large broad absorption feature with a minimum between 840-900nm, and a positive slope between 840nm and 1250nm (Looby, 2016).

5.1.9 Aspectral and Undifferentiated Dark Rock

"Aspectral" is the designation given to the classification of spectra that exhibits no distinguishable absorption features in the short-wave and has a generally negative slope between approximately 850nm and 2400nm (Figure 79) (Looby, 2016).

Variations in the aspectral mineral class is calculated based on the percentage of reflectance. Typically, lower reflectance correlates to finer grains, while higher reflectance correlates to coarser grains and/or lighter colored minerals. Aspectral is the dominant classification and may be attributed to silicification, due to the increase in albedo.

Aspectral reflectance is also measured and given as a mapped variation in the mineral maps (see Figure 85). This class variation is created by measuring the reflectance of the aspectral spectra between 450-900nm and ranges from -10 to 35 (unitless).

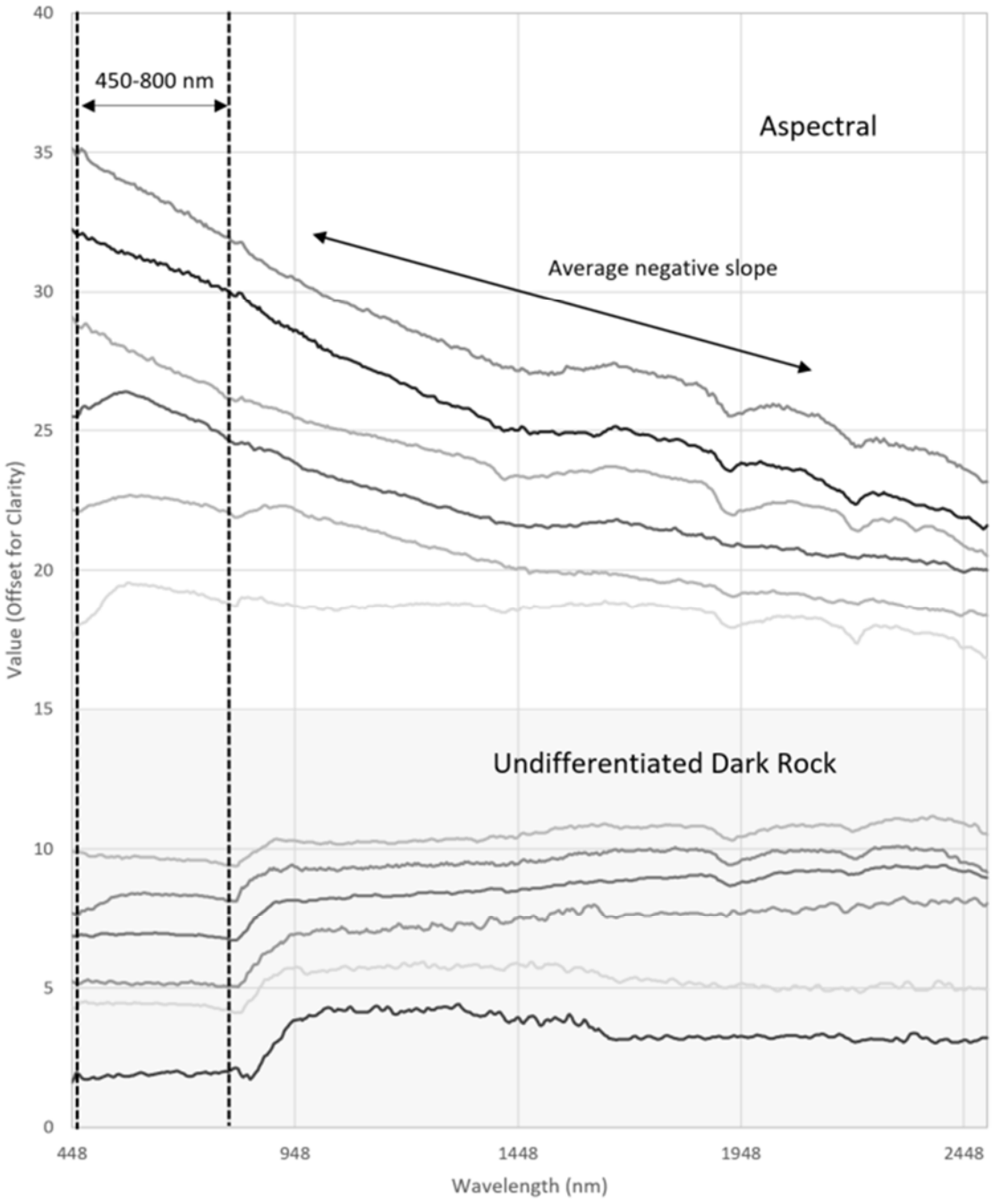

Figure 79. Spectra showing the aspectral and undifferentiated dark rock (gray box) mineral classes from sample BD15-052. Aspectral exhibits no distinguishable absorption features in the short-wave and has a generally negative slope between approximately 850nm and 2400nm. Undifferentiated dark rock has an albedo lower than 18% across the short-wave spectral range and contains no distinguishing absorption features. This is distinguished from the aspectral class by the lack of overall negative slope and lower albedo.

"Undifferentiated dark rock" is the designation for rocks that have an albedo lower than 18% throughout the short-wave range and contains no distinguishing absorption features (Figure 79) (Looby, 2016). This is the second most prevalent mineral class and is distinguished from the aspectral class by the lack of overall negative slope and lower albedo.

An intermediate classification is identified in the mineral class maps called "aspectral-undifferentiated dark rock." This is a classification for spectra that has the very low reflectivity; however, also has the general negative slope.

5.1.10 Mineral Class Map

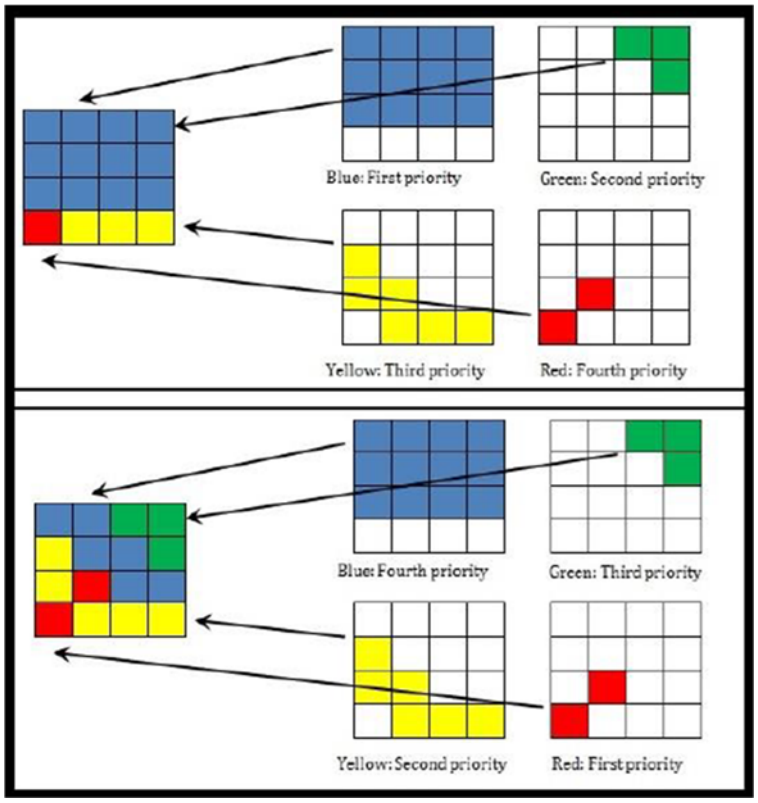

Figure 80. Examples of how the mineral class map is created given different priorities for each mineral class.

The purpose of the mineral class map is to show all the identified mineral classes in one mineral map. It is created by considering each of the mineral classes identified within each pixel

and assigning that pixel a single mineral class according to the priority it was given by Corescan spectral geologists (Figure 80) (Looby, 2016).

5.2 General SWIR Core Mineral Map Observations

Figure 81 is a profile of the scanned portion of hole BD15-052. It shows general patterns of alteration throughout the breccia system by showing mineral classes and Au content in the breccia zones. These features are compared to core logs of lithologic formations and breccia types.

The "aspectral" classification is by-far the most prevalent in the scanned core. This classification appears to be associated with the silicification zone in the Rodeo Creek Formation; however, changes very little at the mapped silicification contact within the Bootstrap limestone.

The second most abundant mineral class is the "undifferentiated dark rock." This mineral class is due to a lack of reflectivity in the rock and so is associated with the dark rock and negatively correlated with the pervasive silicification zone, which contains an abundance of white quartz, and the limestone that has a much higher albedo.

The highest grade of gold in this hole is at the very top of the weekly silicified Bx1, shown by the purple lines in the "Au concentration" column in Figure 81. The grade decreases, but remains relatively high in the weakly silicified zone of Bx3a; however, drops significantly on the lower contact of Bx3a. Silver values are not available for this section of BD15-052.

Ammonium mica has a relatively strong signature in the upper silicified breccia zone of Bx3a. It is associated with the bleached alteration in Bx3a. There are two Bx3a bodies in BD15-052. The upper body has the strongest ammonium mica signature. The lower end of the upper ammonium mica signature marks the beginning of the silicification signature; however, Bx3a is visibly silicified in hand sample and thin section. In hole BD14-04C, ammonium-mica is spatially associated with the diorite dike. A zone of bleached, ammonium-mica-altered rock (Bx3a) is above

and below the dike. Within the dike, micas are also ammonium-bearing (Figure 83), suggesting that the Bx3a alteration was after emplacement of the dike.

White mica in all drill-cores is predominately muscovite with minor phengite. The phengite is spatially associated with faults and within unsilicified and silicified collapse breccia (Bx5a and Bx5b) matrix. There appears to be a positive correlation of some phengite to gypsum, kaolinite, and montmorillonite in the faults, and a general correlation to zones of increased carbonate in the collapse breccias. Bx1a, Bx2, and Bx3a are strongly associated with muscovite. Bx1a clasts within the BD15-052 collapse breccia consist of muscovite cores and phengite rims (Figure 82), suggesting that phengite was in equilibrium with circulating fluids and that muscovite was altered to phengite after brecciation.

On a large scale, silica has a negative correlation to carbonates. Silica in BD15-052 appears within a zone that starts at a depth of approximately 245 m and goes to ~285 m. This is a zone of intense silica alteration of Bx1a, Bx2 and Bx5b; however, the texturally preserved silicification zones of Bx3a and parts of Bx2 do not have a silica signature. This may be due to the lack of reflectivity and/or interference from other mineralogy. Because the identification of silica is dependent on the presence of water and absence of other signatures, interference can occur when any other mineral is present.

Within Bx4 fault zones, gypsum, kaolinite, montmorillonite, iron oxides (jarosite, hematite, and goethite), and the unknown Fe-mineral have a positive correlation, conversely, white mica has a negative correlation.

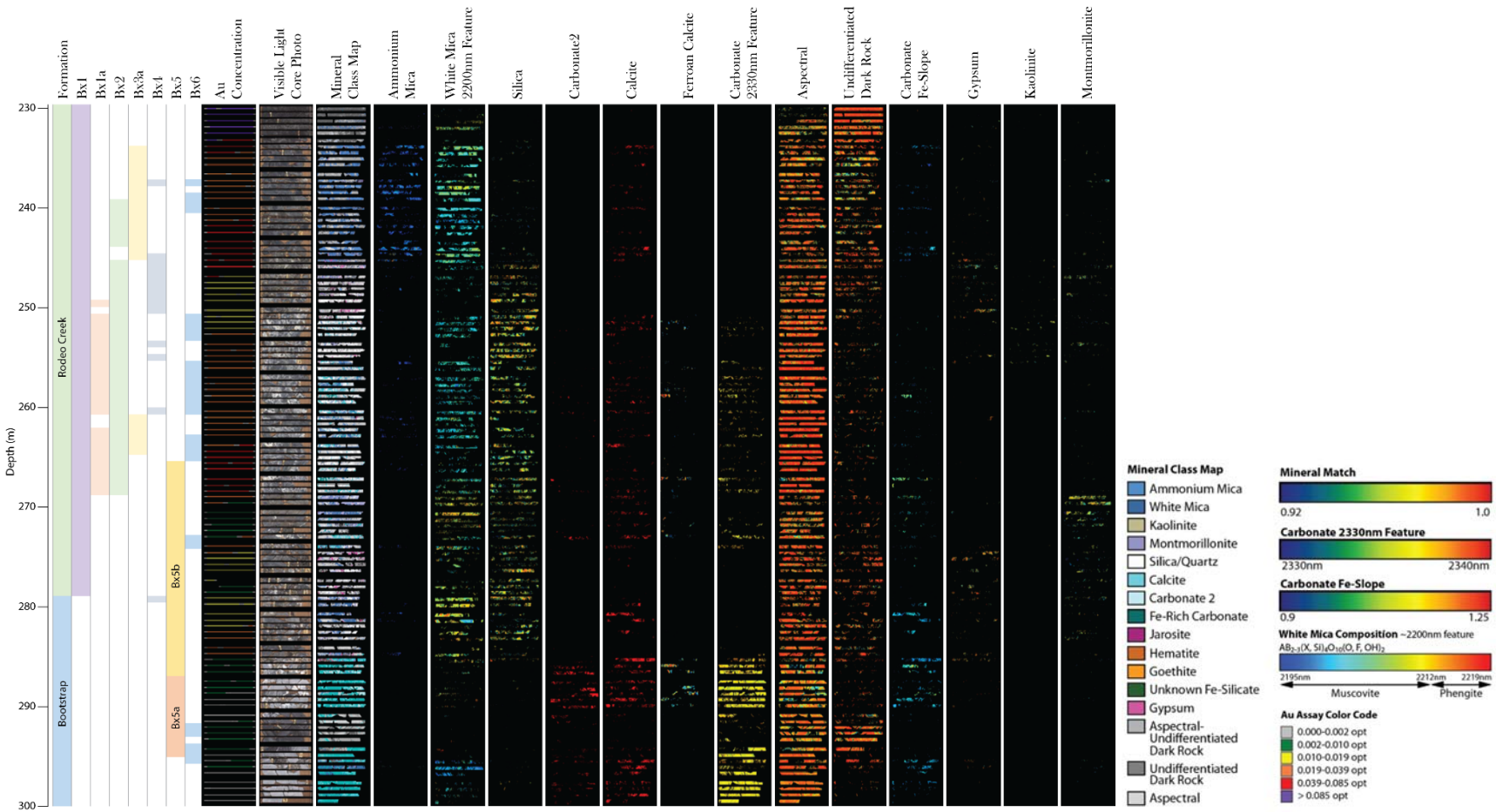

Figure 81. Profile of the scanned portion of hole BD15-052 showing general patterns of alteration throughout the breccia system by showing mineral classes, and Au content, in the breccia zone. Mineral classes include: ammonium mica, white mica (2200nm absorption feature), silica, carbonate 2, calcite, ferroanc calcite, carbonate 2330nm absorption feature, aspectral, undifferentiated dark rock, carbonate Fe-slope, gypsum, kaolinite, and montmorillonite. This is compared to core logs that show formation and breccia types versus depth. The mineral class map legend (left) is for all identified mineral classes. Au assay is from the El Niño geochemical database which was input into Coreshed for comparison. Legth of core varries from row to row. Gaps in data to the right of the core row may be due to size of the core samples.

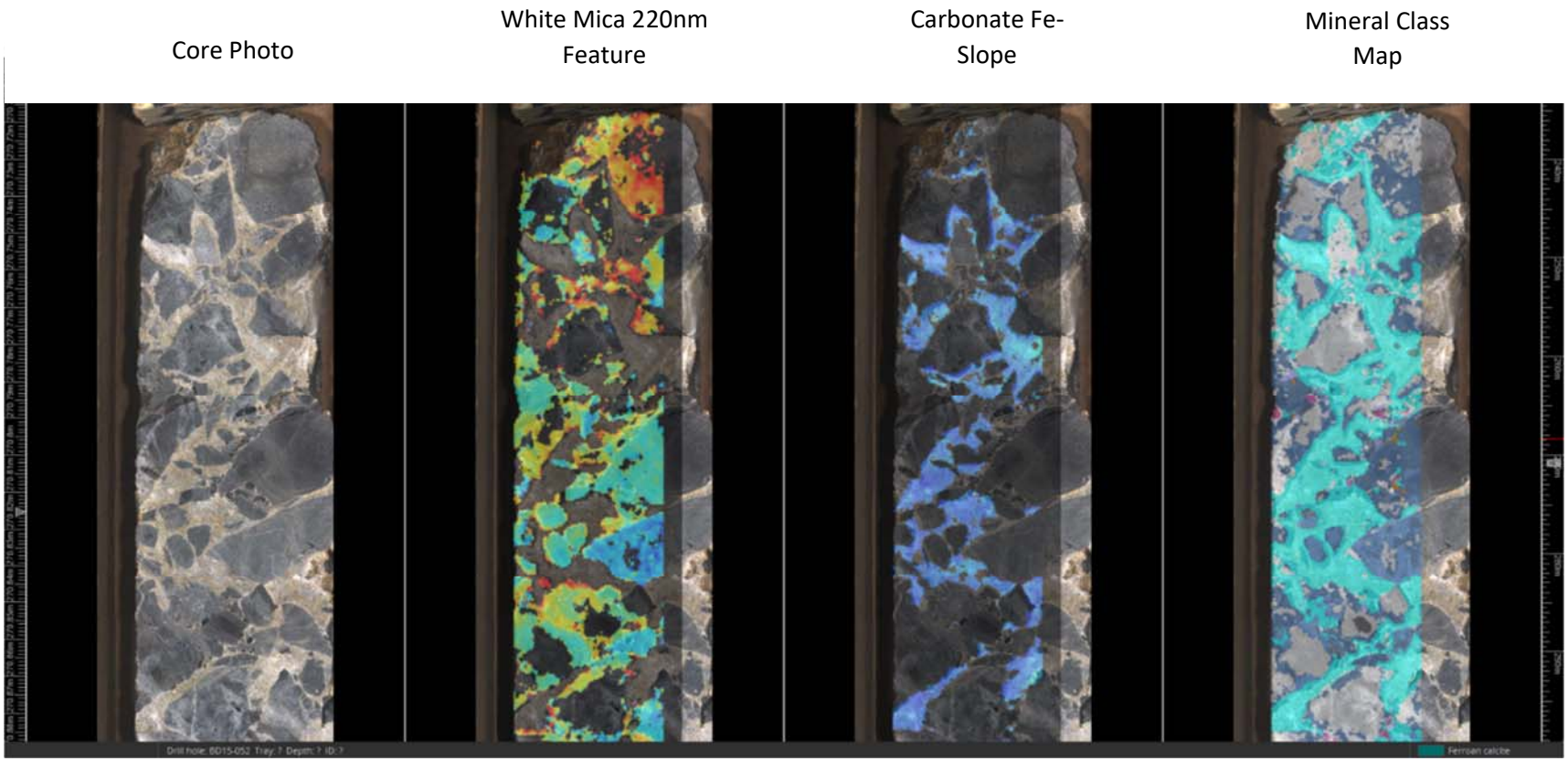

Figure 82. Bx1a clasts within the BD15-052 collapse breccia consist of muscovite cores and phengite rims that suggests muscovite was altered to phengite after brecciation.

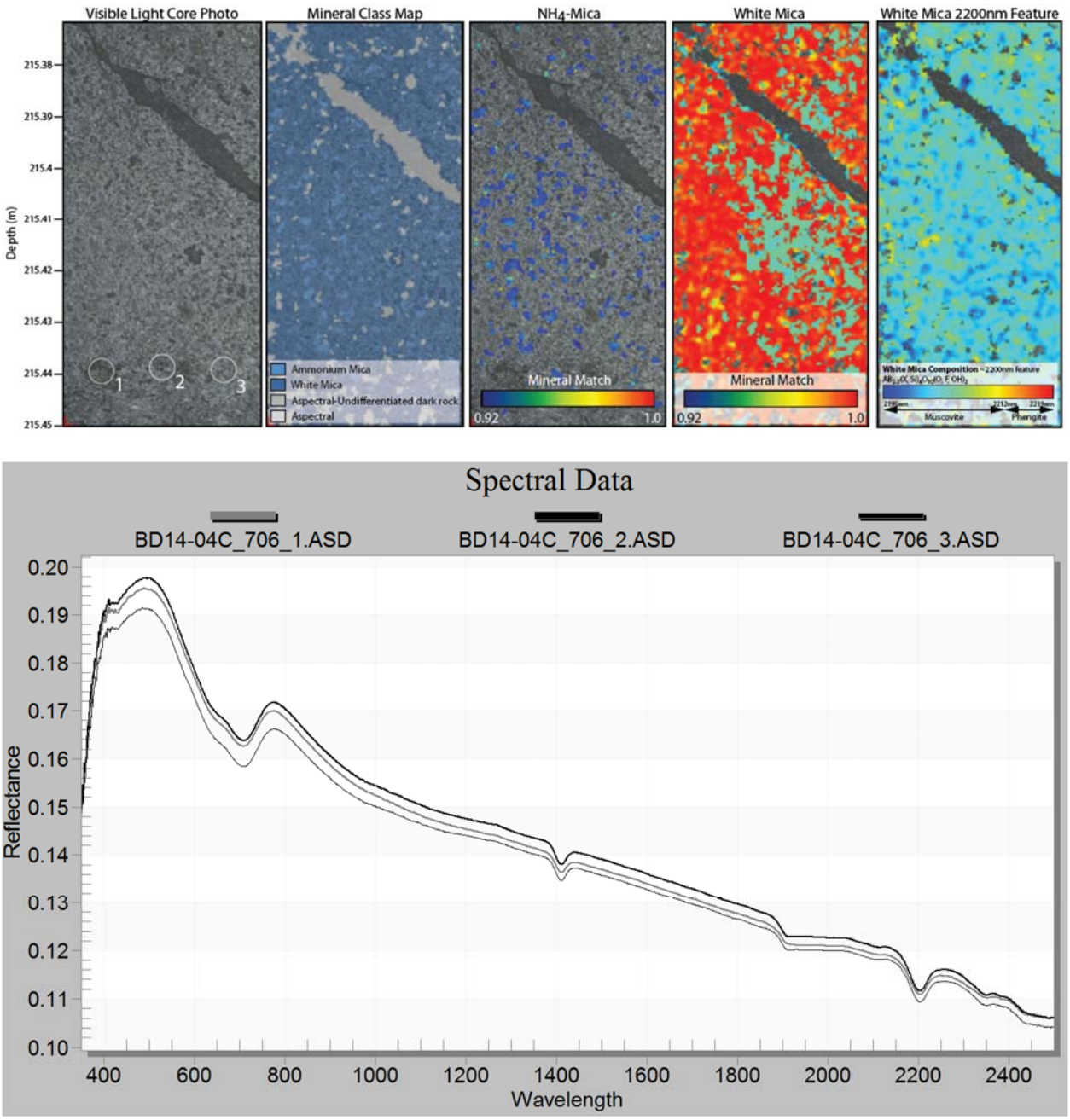

Figure 83. Mineral maps and spectra from sample BD14-04C_706, Russet diorite dike (upper). The mineral maps show the presence of ammonium mica and muscovite within the diorite. The lower image shows spectra that demonstrates the consistency of the mica spectral features and the possible presence of the step-like pattern between 1900 and 2200nm which contains small absorption features at approximately 2000 and 2110nm, characteristic of ammonium mica

5.3 SWIR of Breccias

As seen in Figure 81, many of the breccias are associated with specific mineral signatures and mineral compositions. The following is a description of the mineralogy identified by short-wave infrared based on a selection of core lengths of each identified breccia type.

5.3.1 Tectonic Breccias

5.3.1.1 Bx1: Roberts Mountain Thrust Tectonic Breccia

The Roberts Mountain thrust tectonic breccia (Bx1), where not overprinted by other breccias, is relatively simple in the SWIR mineral maps. Figure 84 shows a high-grade Au sample of Bx1. The lack of reflectivity of this rock make it difficult to determine mineralogy from SWIR absorption features. The figure shows a general signature that is a combination of aspectral and undifferentiated dark rock. The reflectance between 450nm and 900nm has values that are very near zero, which is likely due to the presence of organic matter.

5.3.1.2 Bx4: Other Fault Breccias

Figure 85 shows an example of a fault breccia (Bx4) from hole BD15-023A. This sample gives a somewhat consistent aspectral signature throughout. The mineral map shows that, despite the obvious silicification in the clasts, silica is only identified in very small patches. White mica also has a very weak signature, consistent with the identification of ~2-3% mica in thin-section.

The general negative slope and lack of significant absorption features in the spectra is consistent with the aspectral signature shown in the mineral map.

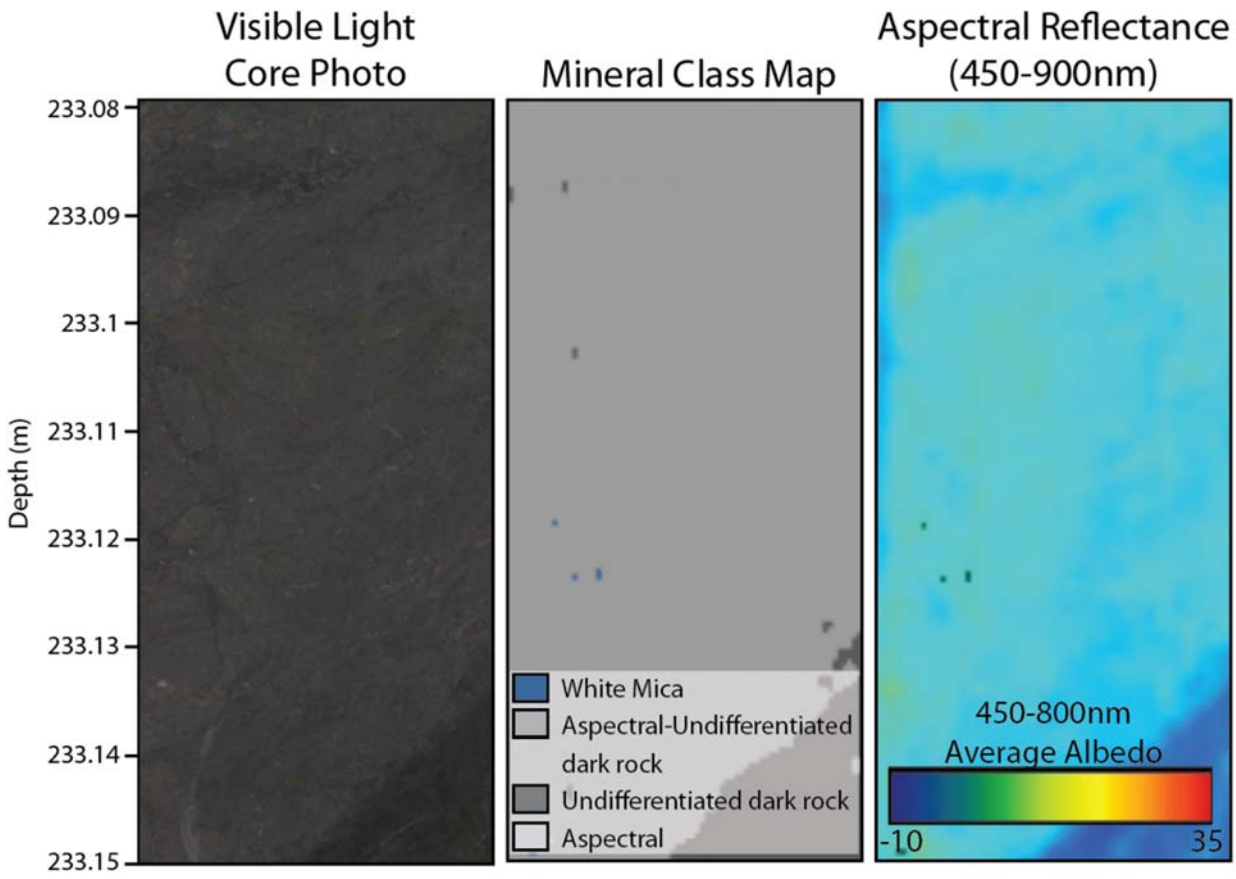

Figure 84. Sample BD15-053_233m is an example of a high-grade Au-bearing Bx1. The mineral maps show the lack of any distinguishable SWIR spectral characteristics in the dark mudstones.

Figure 86 shows a tectonic breccia with silicified mudstone and diorite clasts. This Bx4 sample contains a high percentage of ammonium mica and muscovite. This is likely due to overprinting during Bx3a alteration of minerals within the diorite clasts. The spectra includes absorption features at 2000nm and 2110 in spots 1 and 3, in addition to the white mica features at 1400, 1900 and 2200 nm (e.g. spot 1). Spot analyses 2 and 4 have a general negative trend and lack any significant absorption features, consistent with the aspectral signature identified in the mineral map.

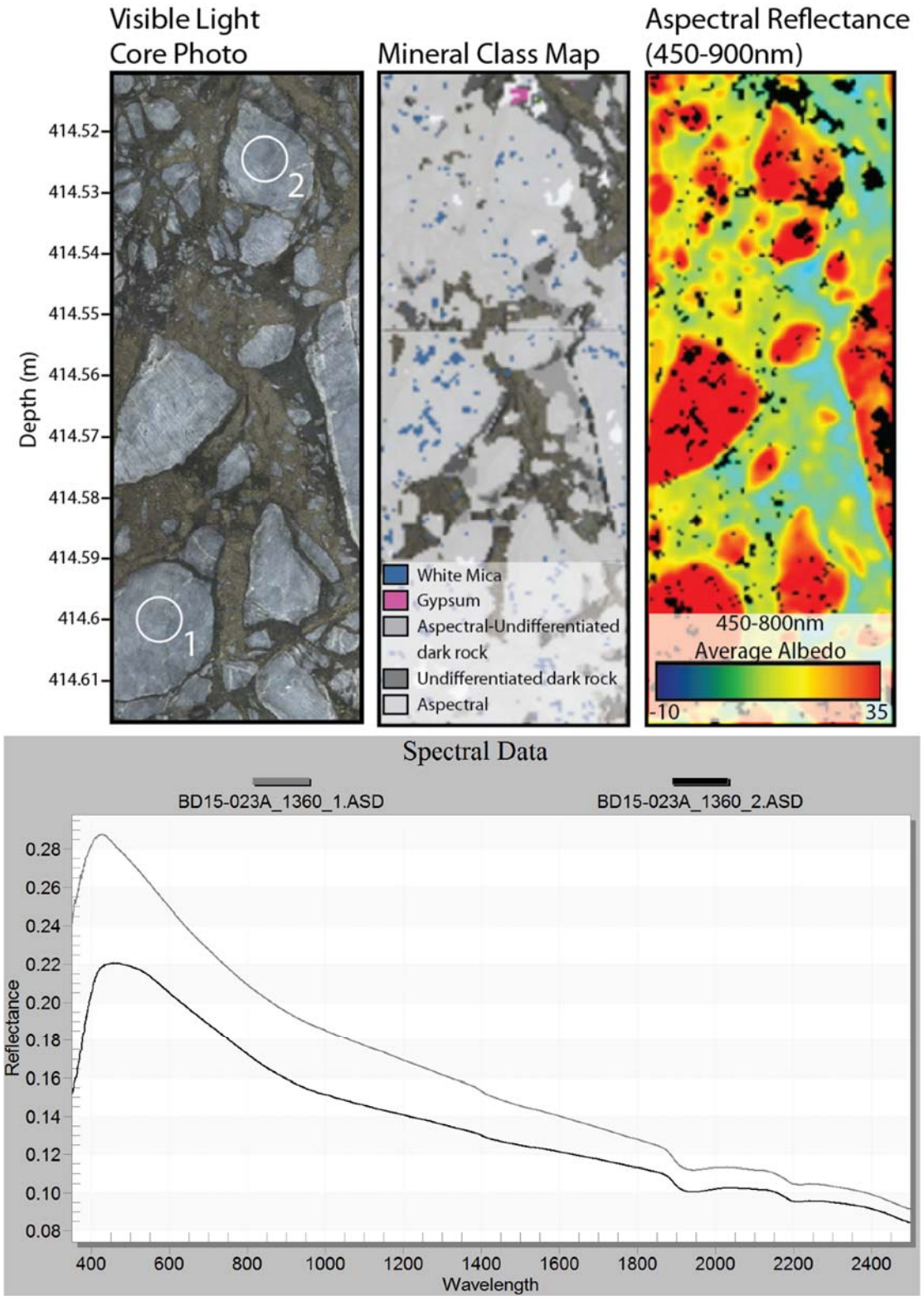

Figure 85. Sample BD15-023A_1360 is an example of a Bx4, tectonic breccia. The mineral maps show the lack of any distinguishable SWIR spectral characteristics in the dark matrix, as well as the intensely silicified clasts. The associated spectra (lower) demonstrates the lack of characteristics in the spectra.

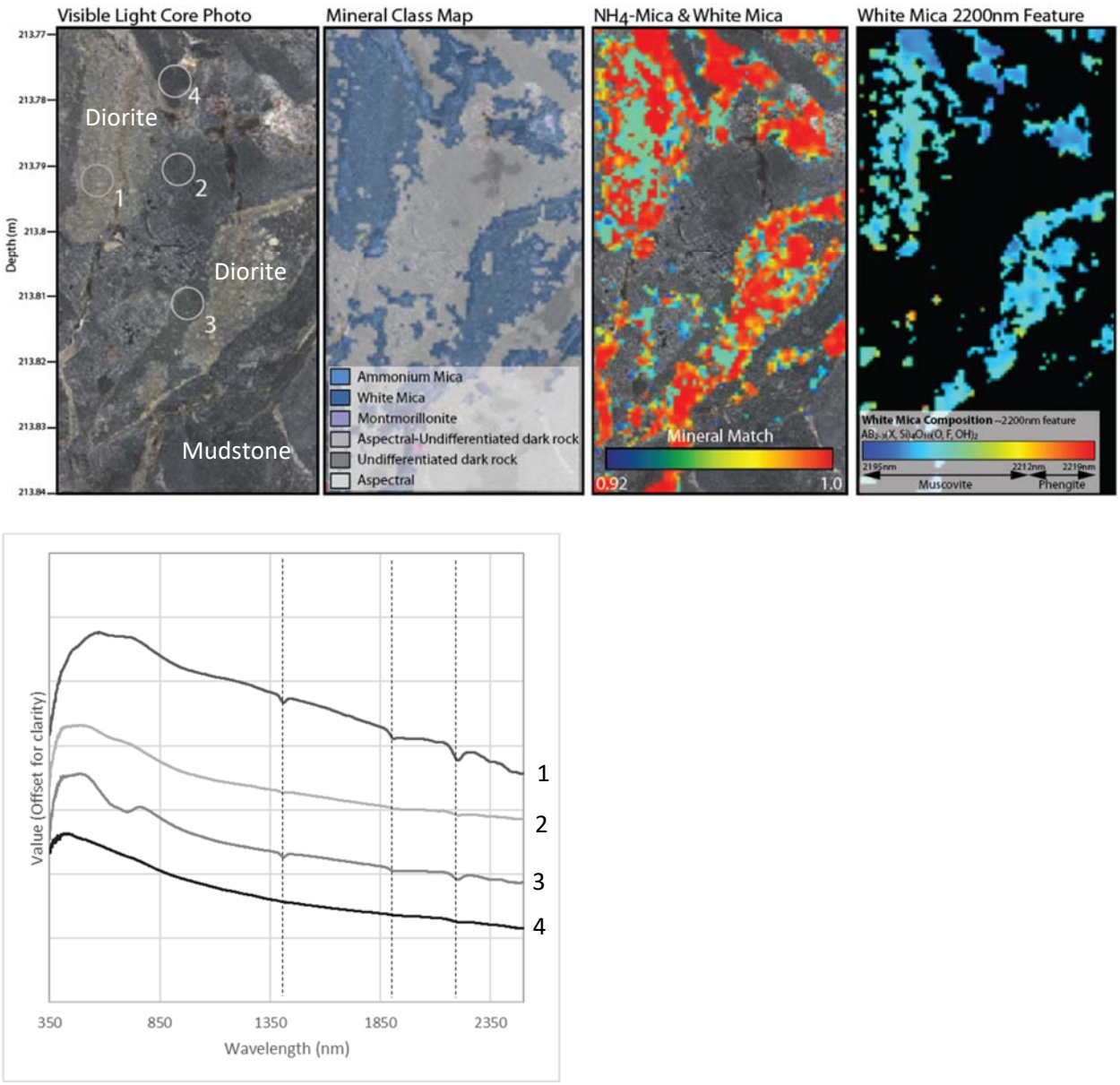

Figure 86. Mineral map of sample BD14-04C_701.2, a Bx4 with diorite and mudstone clasts. Spectra has absorption features at 2000nm and 2110 in spots 1 and 3, consistent with white mica. There may be two very small absorption features at 1900 and 2200nm in spot 1 which is consistent with the ammonium mica identified in the mineral map. Spot analyses 2 and 4 have a general negative trend and lack any significant absorption features, consistent with the aspectral signature identified in the mineral map.

5.3.2 Hydrothermal Breccias

5.3.2.1 Bx1a: Intensely Silicified Mudstone/Limestone

Bx1a is characterized by intense silicification of the host rock. In SWIR, the white silica is easily identified, as shown in Figure 87. The darker zones in this sample are not always identified

as quartz, but rather yields an aspectral signature. The opposite is true for white mica. The strongest mica signatures are in the darker, less silicified sections, which is consistent with thin-section observations. Mica in this sample has a 2200nm feature position that is usually close to 2200 (muscovite); however, varies from approximately 2195nm to 2219nm (muscovite to phengite).

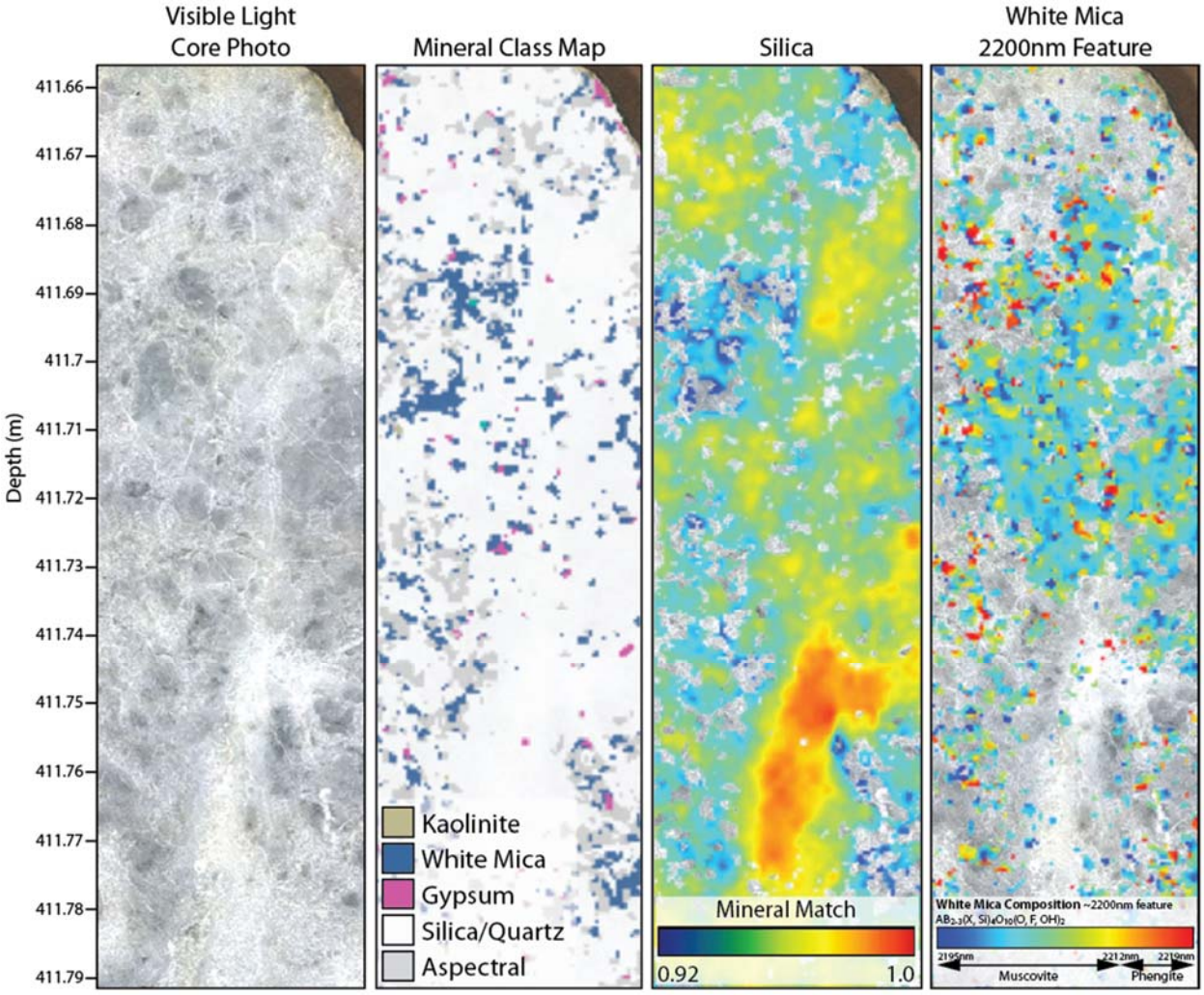

Figure 87. Mineral maps of sample BD15-023A_411m Bx1a, intensely silicified Bx1 with silica and white mica 2200nm absorption feature.

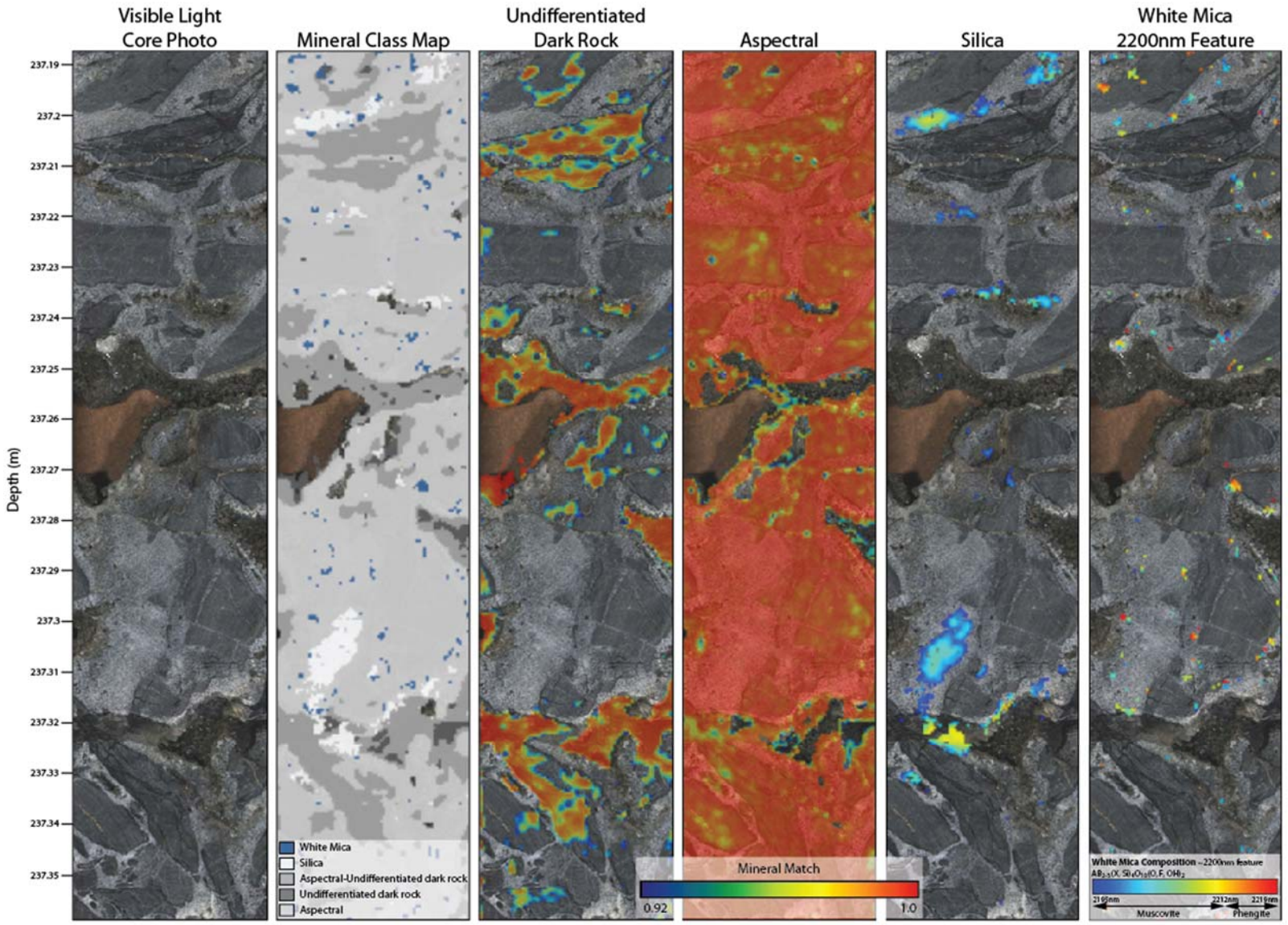

Figure 88. Mineral maps of sample BD15-053_237m, Bx2, vuggy silica cemented mudstone. Mineral maps consist of undifferentiated dark rock, aspectral, silica and white mica 2200nm absorption feature.

5.3.2.2 Bx2: Vuggy Silica Cemented/Veined Hydrothermal Breccia

Figure 88 shows the spectral mineral maps of a Bx2 sample from hole BD15-053. Because of the lack of reflectivity in the rocks, the major mineral classes are aspectral and undifferentiated dark rock; however, the vuggy silica matrix has signatures of silica and white mica. The silica is only identified in the areas of highest reflectivity, which comes to approximately 10% of the total silica matrix that is identified by SWIR in this sample. White mica is identified in spots throughout the breccia, including the matrix and clasts, mostly in close proximity to the vuggy silica matrix. Mica composition ranges from muscovite to phengite.

5.3.2.3 Bx3a: Bleached Pyrite Veined Hydrothermal Crackle to Chaotic Breccia

Hyperspectral images of Bx3a are characterized by an ammonium mica signature within the bleached selvage that zones out to muscovite. Figure 89 and Figure 90 are from BD15-052, showing different sections of the same Bx3a breccia zone. Figure 90 is slightly shallower than Figure 89 and shows narrow bleached selvages associated with pyrite veinlets. Ammonium mica alteration in Figure 90 is more pervasive and has no visible association to pyrite. Figure 23 is from hole BD15-051 and shows a more voluminous bleached zone, similar to that of Figure 90. The weak silicification of Bx3a does not produce a silica signature, likely due to the lack of reflectivity and/or interference from other mineralogy. The presence of a carbonate signature points to a less complete decalcification in Bx3a, compared to Bx1a. There is no clear relationship between carbonates and clasts, fractures or ammonium mica alteration, which may suggest that the alteration fluids that formed ammonium mica may not have been responsible for decalcification.

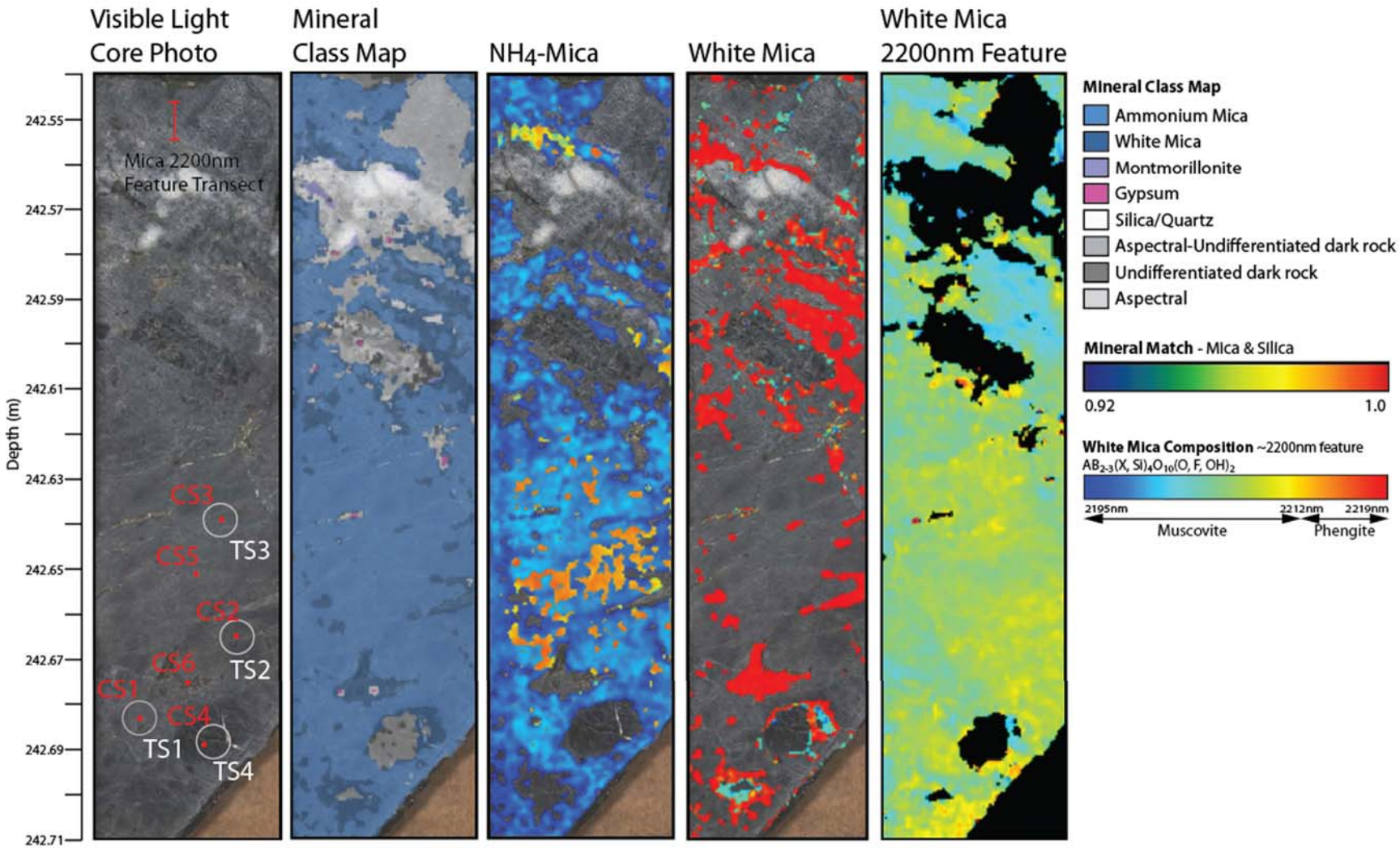

Figure 89. SWIR mineral map of Sample BD15-052_795.7 showing a mineral class map, ammonium mica, and white mica signatures with the white mica 2200nm absorption feature position. The visible light core photo shows were spectra was taken, small dots are from Corescan (CS1-CS6) and circles are from the TerraSpec Halo (TS1-TS4). The transect (shown by the red line) was taken from Corescan data and is for Figure 71. The spectra from the point analyses are shown in Figure 72.

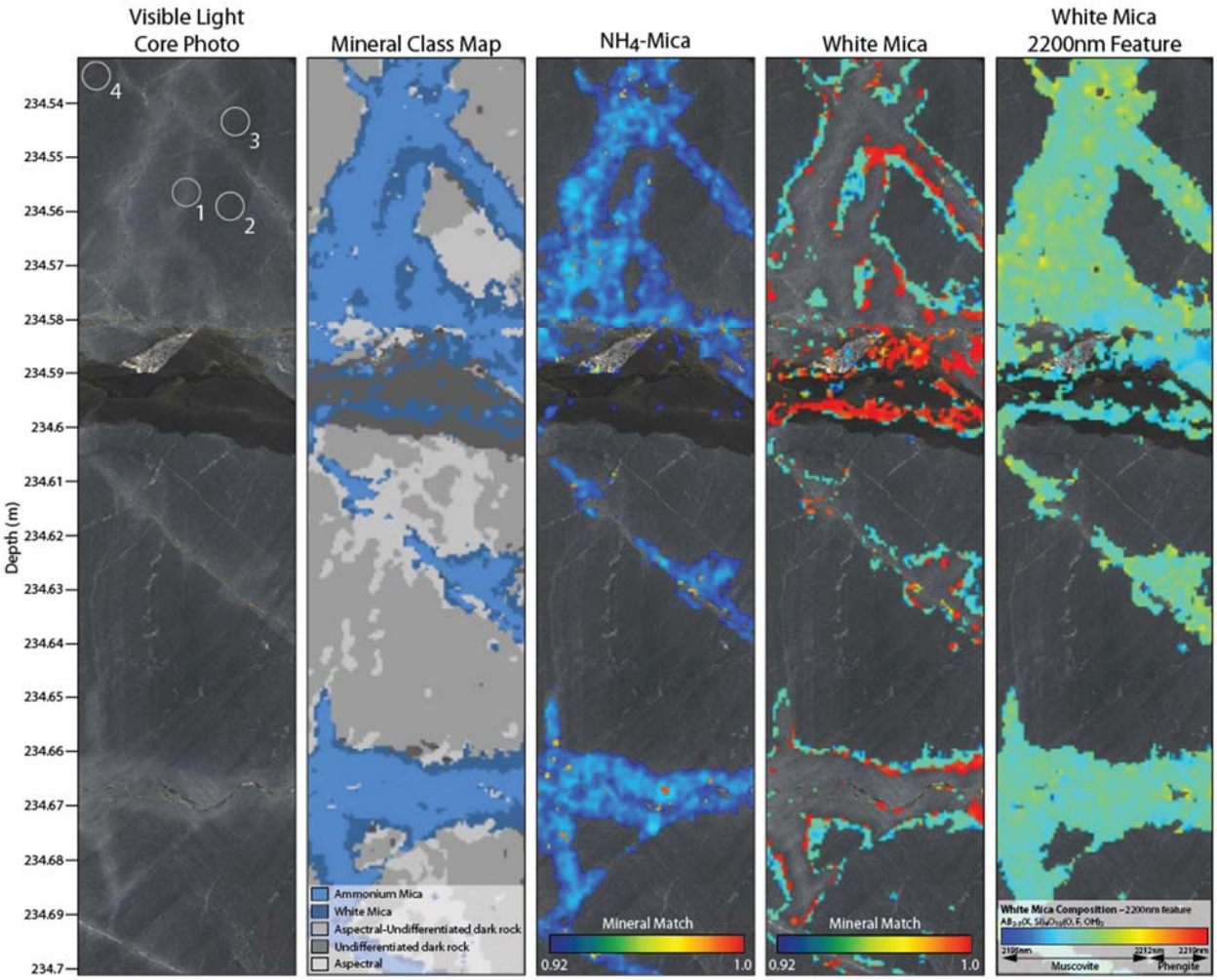

Figure 90. Mineral maps of sample BD15-052_234m, Bx3a, quartz, sericite, pyrite altered crackle breccia. Mineral maps consist of ammonium mica, white mica, and white mica 2200nm absorption feature. This figure shows the zoning of ammonium mica with white mica in the bleached zones associated with pyrite veins in the Bx3a.

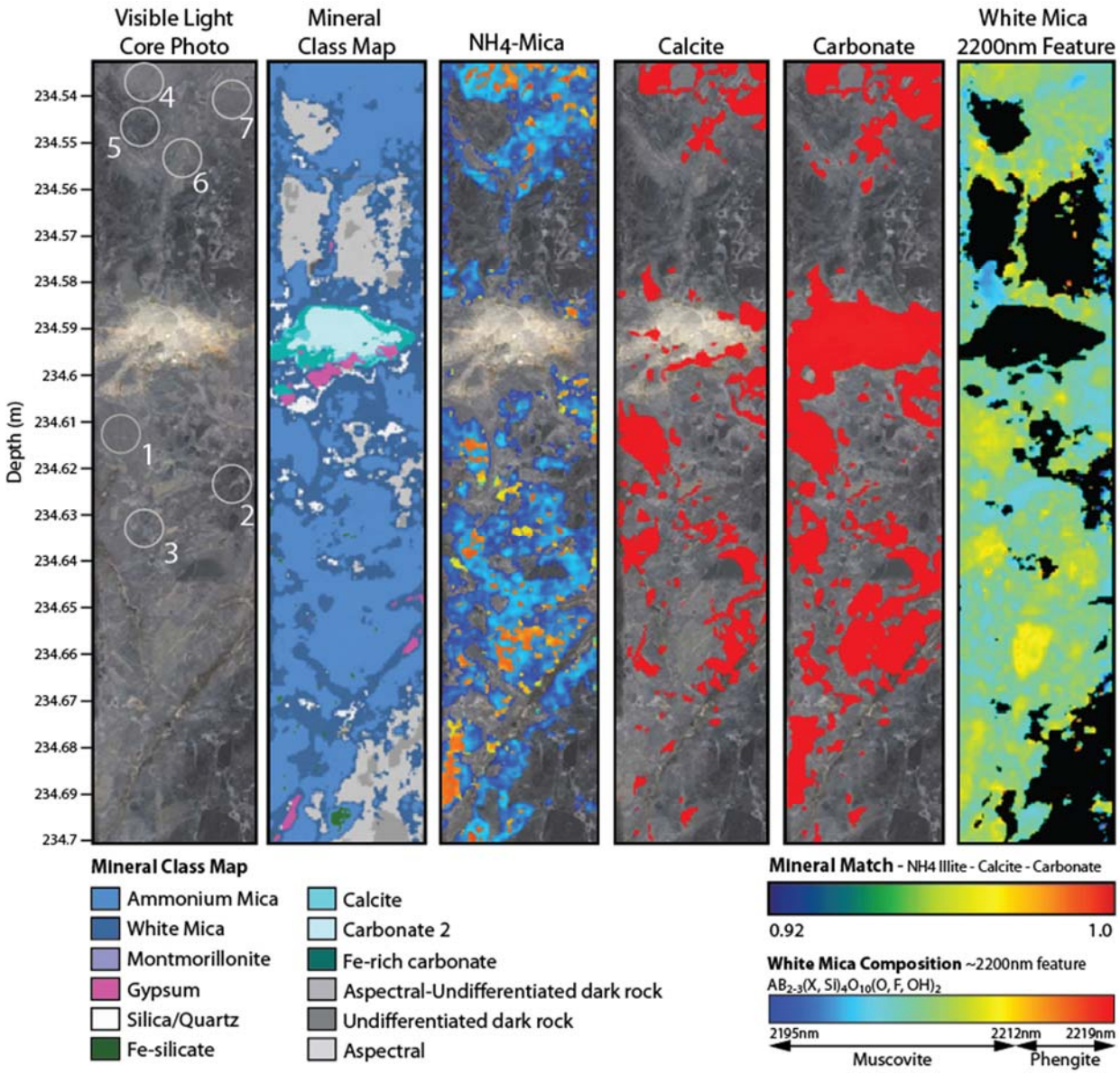

Figure 91. Mineral maps of sample BD15-051_804.5, Bx3a, quartz, sericite, pyrite altered crackle breccia with a cross-cutting calcite vein. Mineral maps consist of ammonium mica, calcite, carbonate (including calcite, carbonate 2 and Fe-rich carbonate), and white mica 2200nm absorption feature. This figure shows that decalcification is not complete in this example of Bx3a breccia.

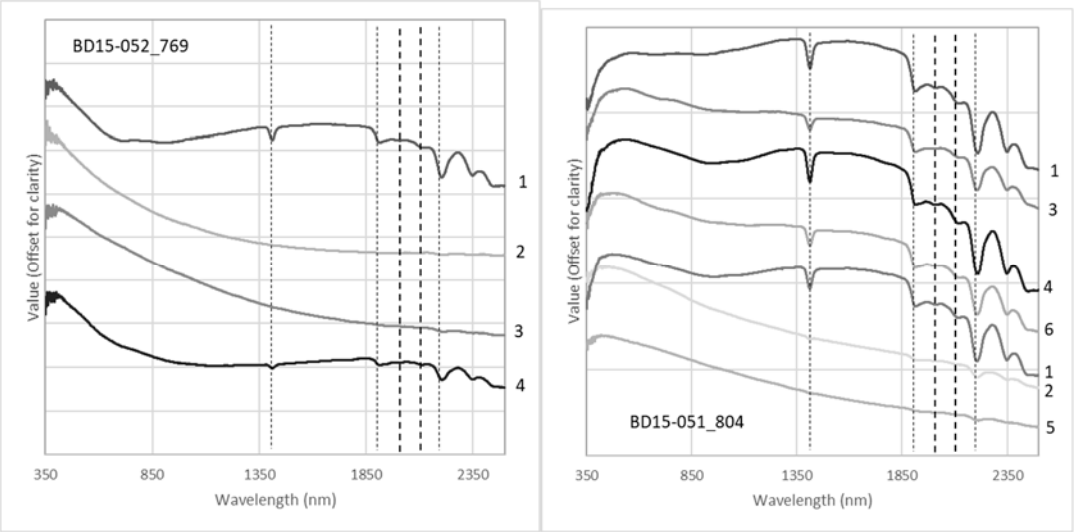

7

Figure 92. Spectra from BD15-052_769 (Figure 90) and BD15-051_804 (Figure 91). The spectra exhibits characteristics that are consistent with ammonium-bearing mica, except in the cases that an aspectral spot was analyzed, in which case an aspectral signature was recorded (spots 2 and 3 from BD15-052_769 and spots 2 and 5 from BD15-051_804).

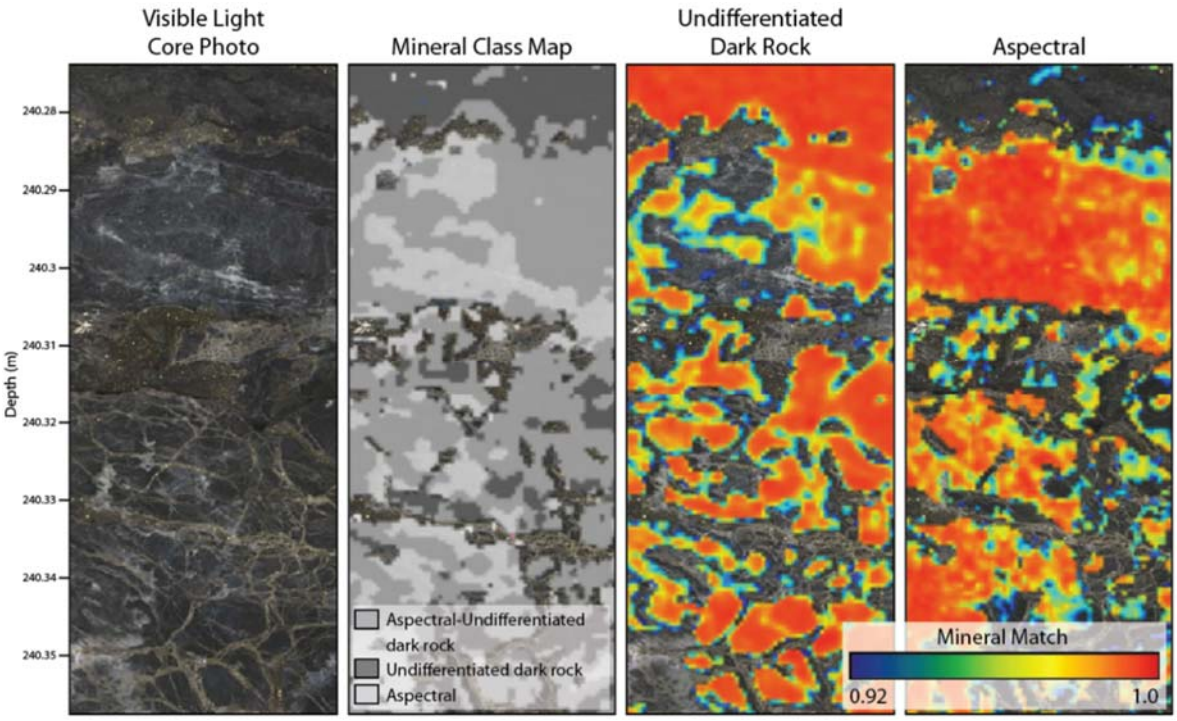

Figure 93. Mineral maps of sample BD15-053_240m, Bx3b, pyrite veined breccia. Mineral maps consist of undifferentiated dark rock and aspectral mineral classes. This shows that Bx3b is distinguished from Bx3a by the lack of ammonium mica in the SWIR and the lack of bleaching in hand sample.

5.3.2.4 Bx3b: Pyrite Veined Hydrothermal Breccia

Bx3b, like that of Bx1 and Bx4, does not produce a hyperspectral signature other than aspectral and undifferentiated dark rock due to the lack of reflectivity (Figure 93). The absence of ammonium mica in these samples suggests a difference in the hydrothermal chemistry of formation between these two pyrite-bearing breccias.

5.3.2.5 Bx6: Calcite ± barite matrix crackle to chaotic breccia

Hyperspectral images of Bx6, Calcite ± barite matrix crackle to chaotic breccia, have a strong carbonate signature. The difference, however, in the carbonate signature of Bx6 compared to limestone is the presence of ferroan calcite. The slope of the 1750nm to 1360nm absorption feature is typically greater than 1, suggesting a higher iron content than that of the limestone. Figure 94 shows the strong ferroan calcite signature in the calcite cement, as well as carbonate 2 and calcite. The 2330 nm absorption feature is approximately 2336-2340nm, a slightly wider range than that of the limestones; however, is still identified as calcite. It may be that the higher wavelength number is associated with the clasts, rather than the calcite matrix. The clasts of this Bx6 example also show signatures of silica and white mica.

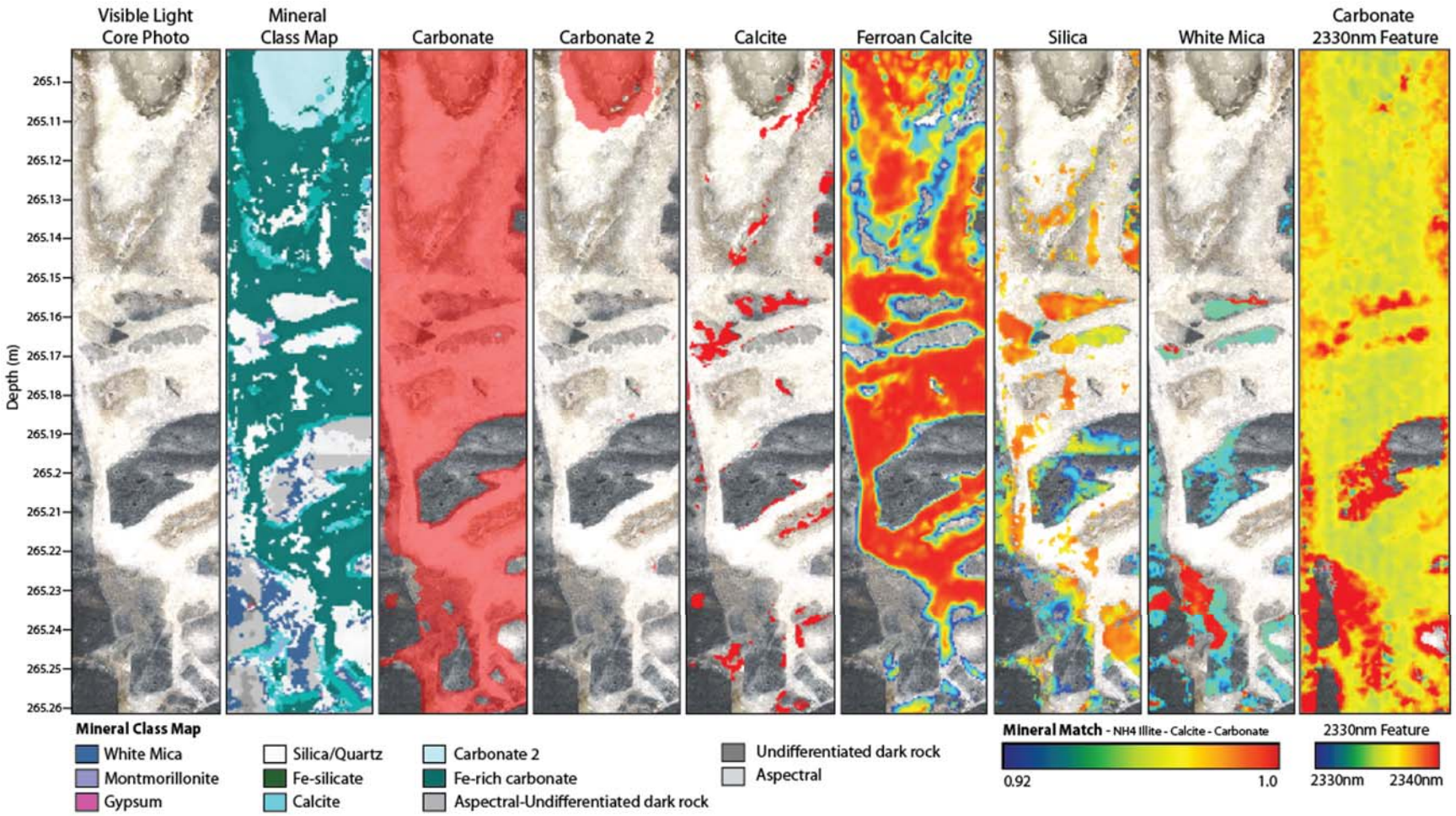

Figure 94. Mineral maps of sample BD15-052_265m, Bx6, calcite + barite cemented hydrothermal breccia. Mineral maps consist of carbonate, carbonate 2, calcite, ferroan calcite, silica, white mica and carbonate 2330 nm feature position. This shows that the carbonate signature is strong in Bx6 and that the ferroan calcite is more closely associated with the latest known calcite veining and brecciation event, as apposed to limestone.

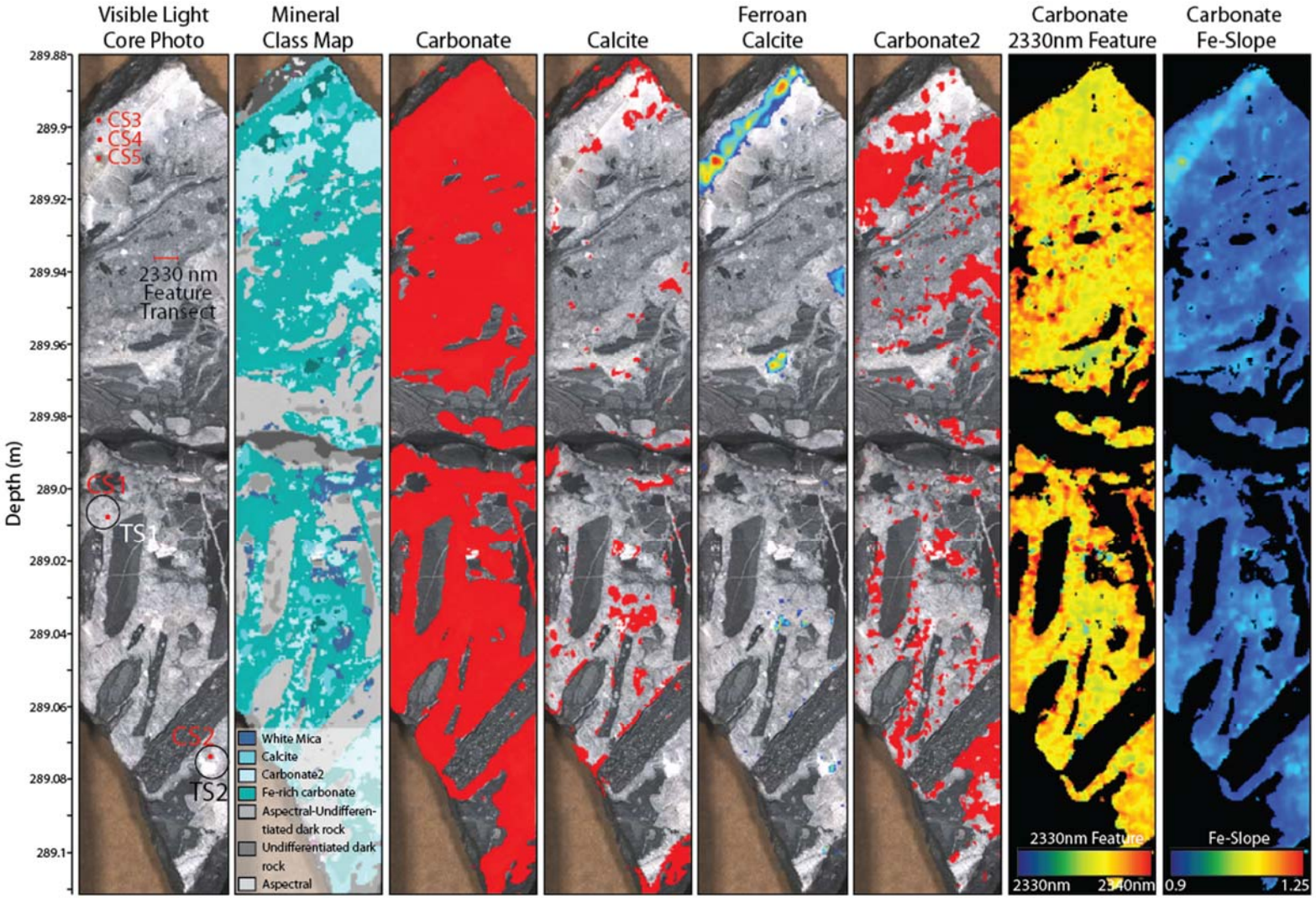

Figure 95. SWIR mineral maps of sample BD15-052_948.4 (Bx5a) showing a mineral class map, carbonate, calcite, ferroan calcite, and carbonate 2 with the carbonate 2330nm absorption feature position and carbonate Fe-slope. The visible light core photo shows were spectra was taken, small dots are from Corescan (CS1-CS6) and circles are from the TerraSpec Halo (TS1-TS4) (Figure 74 and Figure 75). The transect (shown by the red line) was taken from Corescan data and is for Figure 76.

5.3.3 Dissolution Collapse Breccias

5.3.3.1 Bx5a: Dissolution Collapse Breccias

Figure 95 is mineral maps of a Bx5a, collapse breccia with calcite cement and mudstone clasts. The matrix of the unsilicified collapse breccias is almost entirely carbonates including calcite, ferroan calcite and carbonate 2. The calcite signature is strongest with calcite that is free from impurities such as clays and organic material. Carbonate 2 appears to be coarse calcite crystals. Ferroan calcite is mostly in calcite veins; however is also within the collapse breccia matrix as latent calcite cement. The carbonate 2330nm feature has a narrow range of approximately 2330 to 2340 in the El Niño samples, with most feature locations at around 2337nm, indicating calcite, as opposed to dolomite (Laukamp, 2011). The Fe-slope is relatively consistent around 0.9-1; however, in the ferroan calcite class is up to 1.1, consistent with a higher Fe content than the carbonates in the surrounding rock. Minor amounts of white mica are identified in the matrix, consistent with thin-section observations. The dark mudstone clasts of this collapse breccia have signatures that are almost purely aspectral and undifferentiated dark rock mineral class.

Other Bx5a samples, such as BD15-053_954.2, have similar SWIR signatures that primarily consists of carbonate; however, in this example, there is also a strong mica signature in the matrix with 2200nm feature at approximately 2219nm, indicating a composition of phengite. In this example, the clasts are limestone and so also have a carbonate signature.

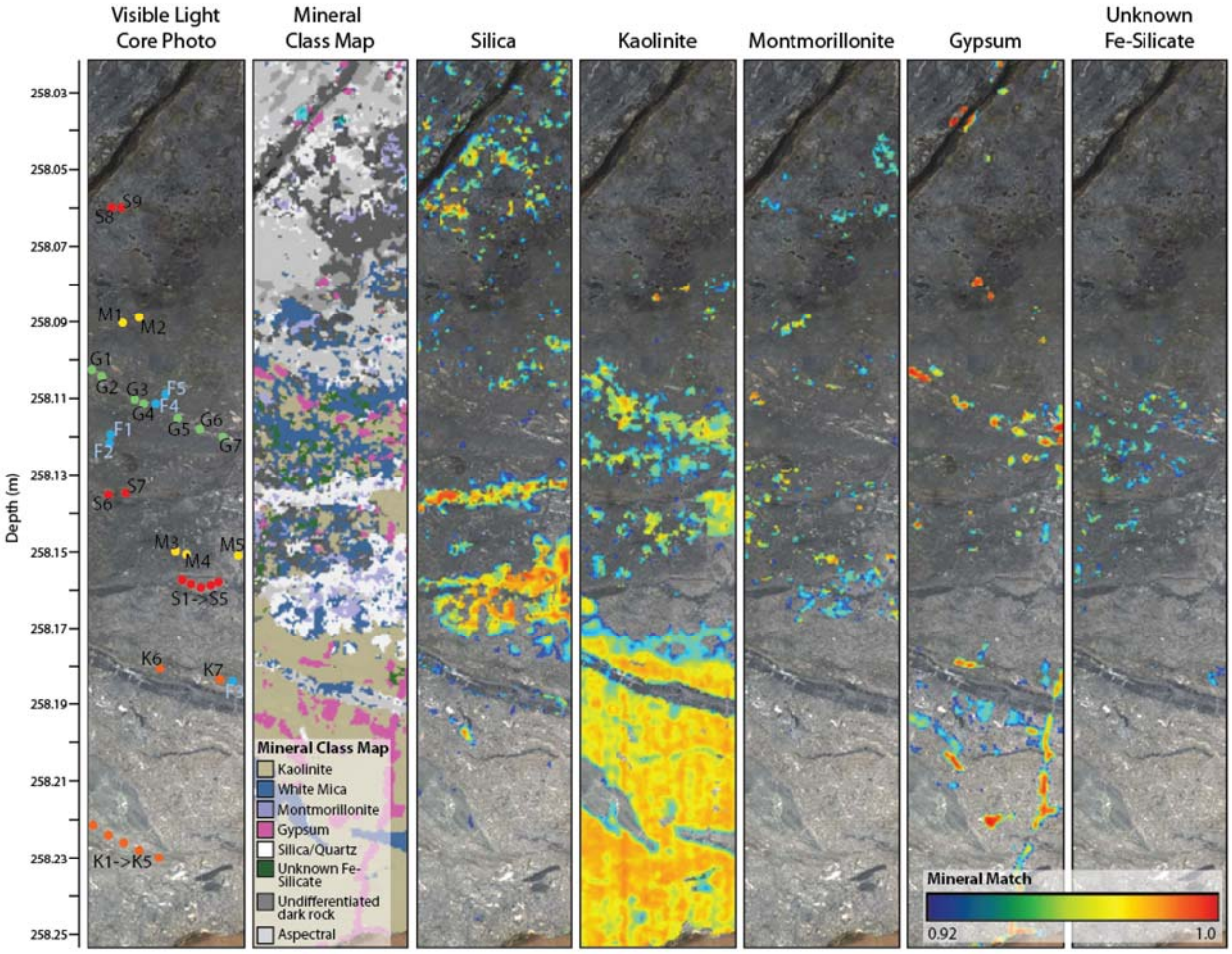

Figure 96. SWIR mineral maps of sample BD15-051_861 showing a mineral class map, silica, kaolinite, montmorillonite, gypsum and an unknown Fe-mineral. The visible light core photo shows were spectra was taken from the Corescan data-set for silica (S1-S9, red), kaolinite (K1-K7, orange), montmorillonite (M1-M5, yellow), gypsum (G1-G7, green, and unknown Fe-mineral (F1-F5, blue).

5.3.3.2 Bx5b: Silicified Dissolution Collapse Breccias

Figure 96 shows the transition zone of Bx5a (unsilicified collapse breccia, bottom of figure) to Bx5b (silicified collapse breccia, top of figure). In this example the carbonate signature is absent, even in the unsilicified zone, consistent with thin-section observations. The mineral maps show a weak silica signature in the silicified zone that grades into a zone of kaolinite + gypsum in the unsilicified zone and montmorillonite and an unknown Fe-mineral in the transition zone.

5.4 Quantitative Evaluation of SWIR Data

Quantitative data from the Corescan hyperspectral analysis is based on a pixel count of the mineral maps over approximately 1 ft. intervals of core. Each pixel is evaluated and identified as one of the mineral classes. The pixels of each mineral class are counted and given a value over the interval of core.

Quantitative data from the TerraSpec Halo is from identification of spectra from spot analyses and the corresponding scalar values, or specific properties of mineral crystallinity or composition from the Halo on-board mineral identification and evaluation software.

The following is an evaluation of the quantitative data from Corescan and the TerraSpec Halo data.

Table 7 is a correlation matrix that quantitatively shows the correlations of minerals observed in the Corescan mineral maps. Silica and white mica have a positive correlation to many of the other minerals, likely due to the prevalence of each mineral in the Button Hill deposit. However, silica has no apparent correlation with gypsum, unknown Fe-mineral or calcite. This is consistent with the observations in the mineral maps that show low calcite in silicified zones, and the high gypsum and unknown Fe-mineral at the lower silicification contact. Ammonium mica is shown to have a negative correlation to silica; however, the silica signature is weak to non-existent in the weakly silicified zone that the Bx3a and the ammonium mica are associated with. White mica is not correlated with kaolinite, Fe-carbonate or jarosite.

Montmorillonite, kaolinite, gypsum, goethite, hematite, jarosite and the unknown Fe-mineral are not common in the Button Hill deposit. They are locally present in faults and collapse breccias. Montmorillonite is associated with goethite and hematite. Gypsum is associated with goethite and the unknown Fe-mineral and strongly correlated with hematite. The unknown Fe-mineral is also strongly associated with hematite. Kaolinite is only correlated with silica in the

mineral classes listed. This is consistent with the observations in BD15-051_861 collapse breccia that shows the strongest kaolinite signature at the base of the zone with montmorillonite and unknown Fe-mineral.

Table 7. Correlation matrix of identified minerals from the SWIR quantitative data. Blue represents 1 to 1 correlation, dark green represents 0.50-0.99 correlation, light green represents 0.10-0.49 correlation. Orange represents negative correlation (light orange: -0.10 to -0.49, dark orange: -0.50 to -0.99).

Correlation	Silica	Montmorillonite	Kaolinite	Gypsum	White Mica	Calcite	Fe-Carbonate	NH4 Mica	Goethite	Hematite	Jarosite	UNK Fe-Silicate
Silica	1.00	0.28	0.27	0.05	0.26	0.01	0.34	-0.13	0.14	0.12	-0.03	0.01
Montmorillonite	0.28	1.00	0.03	-0.01	0.35	0.06	0.06	-0.06	0.28	0.13	0.09	0.06
Kaolinite	0.27	0.03	1.00	0.00	0.10	-0.03	0.10	-0.04	0.02	0.06	-0.06	0.06
Gypsum	0.05	-0.01	0.00	1.00	0.10	0.09	-0.08	-0.05	0.38	0.60	0.09	0.27
White Mica	0.26	0.35	0.10	0.10	1.00	0.26	-0.05	0.31	0.40	0.23	-0.10	0.22
Calcite	0.01	0.06	-0.03	0.09	0.26	1.00	0.38	0.01	0.60	-0.01	-0.05	0.04
Fe-Carbonate	0.34	0.06	0.10	-0.08	-0.05	0.38	1.00	-0.22	0.12	-0.16	-0.04	-0.13
NH4 Mica	-0.13	-0.06	-0.04	-0.05	0.31	0.01	-0.22	1.00	-0.01	0.01	0.09	0.02
Goethite	0.14	0.28	0.02	0.38	0.40	0.60	0.12	-0.01	1.00	0.32	0.22	0.17
Hematite	0.12	0.13	0.06	0.60	0.23	-0.01	-0.16	0.01	0.32	1.00	0.22	0.78
Jarosite	-0.03	0.09	-0.06	0.09	-0.10	-0.05	-0.04	0.09	0.22	0.22	1.00	-0.07
UNK Fe-Silicate	0.01	0.06	0.06	0.27	0.22	0.04	-0.13	0.02	0.17	0.78	-0.07	1.00

Figure 97 shows that the white mica 2200nm absorption feature position is largely within the muscovite range, with minor amounts of phengite.

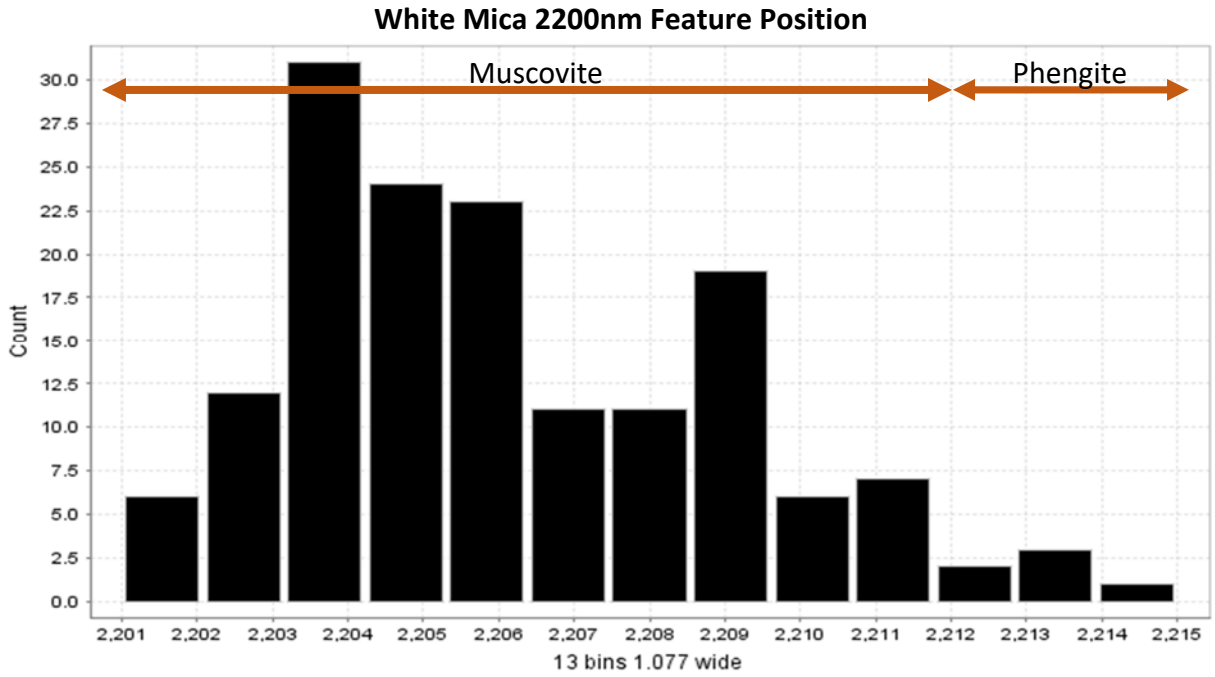

Figure 97. Histogram of white mica 2200nm absorption feature position that demonstrates that the white mica composition is largely muscovite with minor phengite.

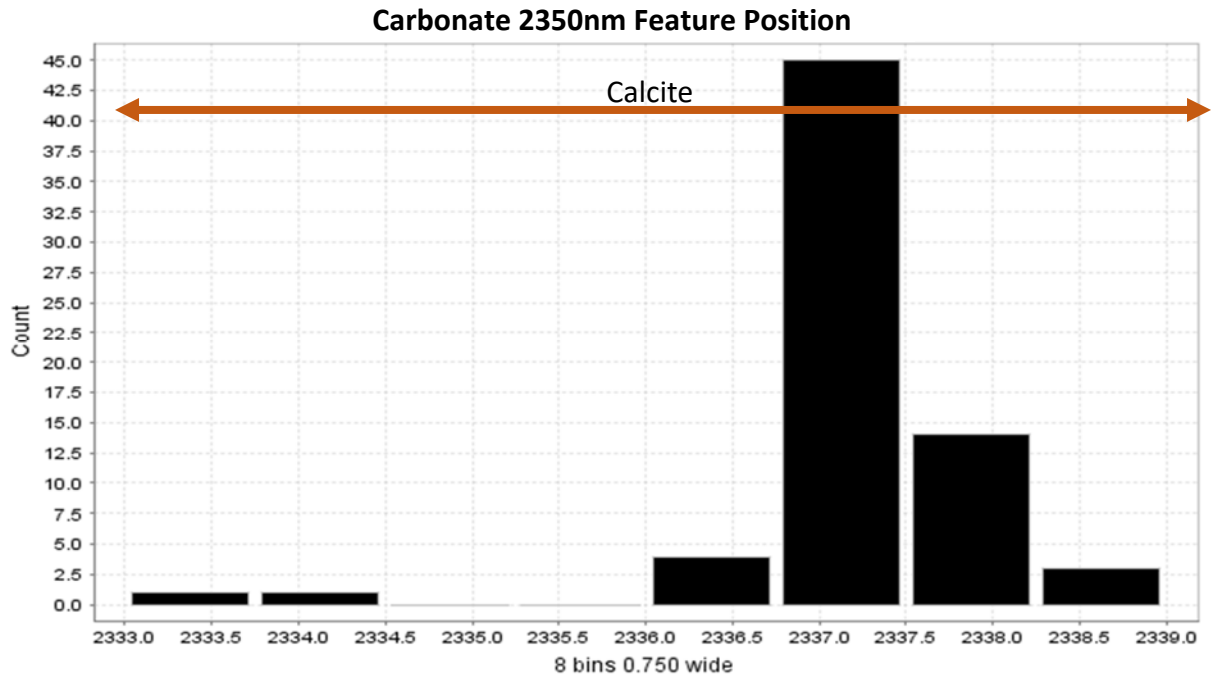

Figure 98. Histogram of the carbonate 2350nm absorption feature position that shows the narrow compositional range of carbonates within the Button Hill deposit. The identified carbonates are calcite, as opposed to dolomite.

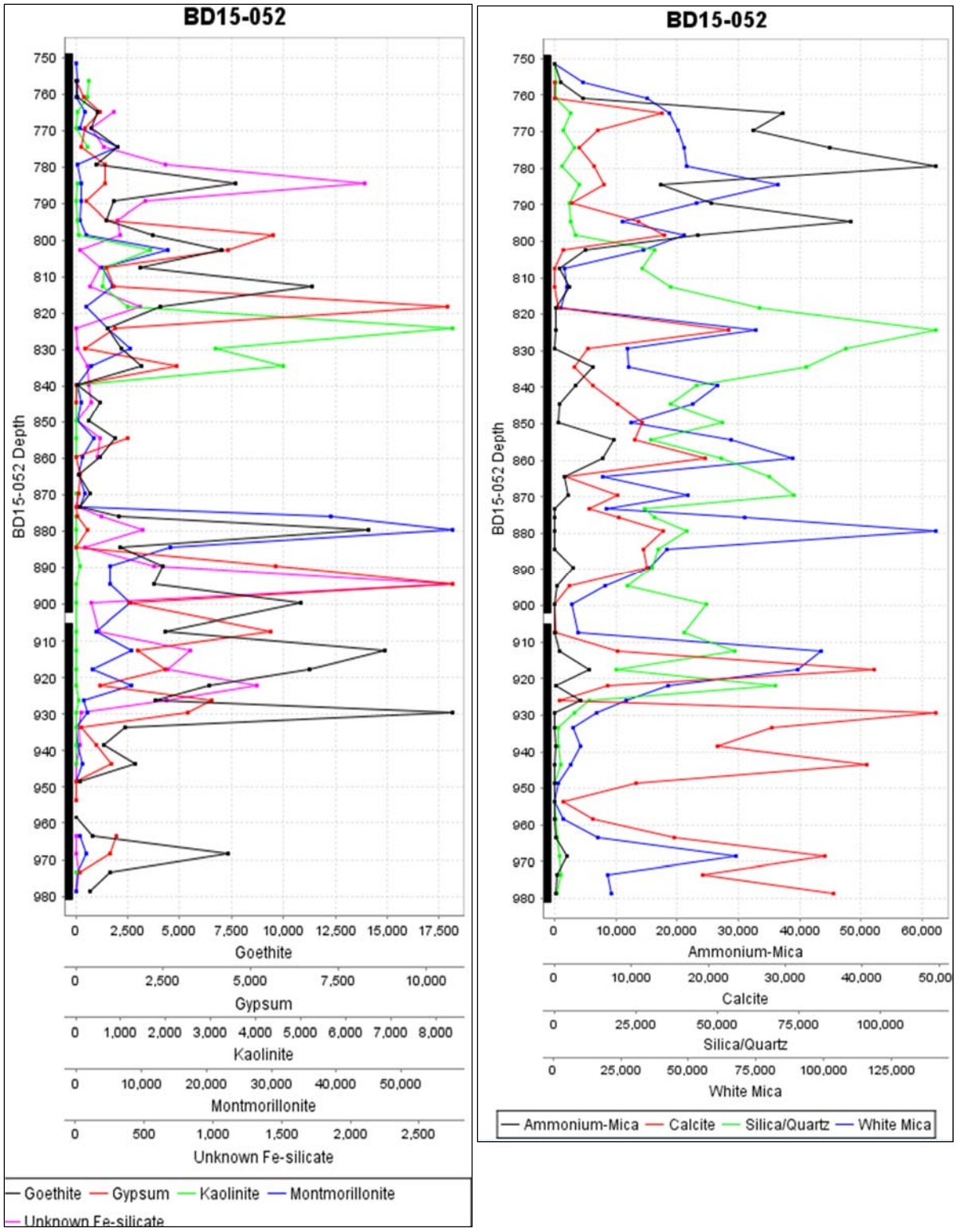

Figure 99. A (left): downhole plot of quantitative SWIR data for goethite gypsum, kaolinite, montmorillonite, and unknown Fe-mineral. B (right): downhole plot of quantitative SWIR data for ammonium mica, calcite, silica, and white mica. Depth (y-axis) is in feet and mineral count (x-axis) is in count per unit area (usually 1' x 2" (width of core)). For geology, Au values and mineral maps for this interval of core see Figure 81.

Figure 98 shows the narrow range of the carbonate 2330nm absorption feature in the Button Hill samples. Most of the 2330nm features are located at approximately 2337nm. This shows that all the identified carbonates in these samples are calcite and that dolomite is not present.

The downhole plots of the BD15-052 breccia zone (Figure 99) demonstrate the spatial correlation of ammonium mica, calcite, silica and white mica (Figure 99a), and between goethite, gypsum, kaolinite, montmorillonite and the unknown Fe-mineral (Figure 99b). Ammonium mica is everywhere recorded with relatively high abundance of white mica. It is much less abundant than other white micas; however, is more abundant near the top of the weakly silicified zone, associated with Bx3a hydrothermal breccia. Carbonate and silica are also associated with increase white mica abundance. Silica spikes below ammonium mica and drops off at approximately 930 ft. depth where calcite abundance increases.

Figure 99b shows the increase abundance of goethite, gypsum, montmorillonite, and unknown Fe-mineral in two zones. The upper enrichment zone is spatially associated with faults and the lower is associated with collapse breccias. Both are zones of significant permeability in the rocks. Kaolinite is high in the upper zone faults but not in the collapse breccias.

The relationship between white mica, silica, and calcite can be shown on ternary plots. White mica appears to be associated with silicification and calcite. Figure 100 shows this relationship. The highest point density is between white mica and silica, but there is another population along the white mica to calcite line. Very few rocks contain both silica and calcite signatures, consistent with the observations of silica and calcite being negatively correlated.

The TerraSpec Halo spot analyses and scalar identification by the Halo on-board software show that there is a relationship between illite composition, the Al-OH (2200nm) absorption feature position and the illite spectral maturity (ISM). The ammonium-bearing illites consistently

have a higher ISM value, suggesting that they may be precipitated from a higher temperature fluid than that which the Halo identified as "K-illite" and "Mg-illite." It also has a narrow range of 2200nm feature position from approximately 2204.75nm to 2208.5nm.

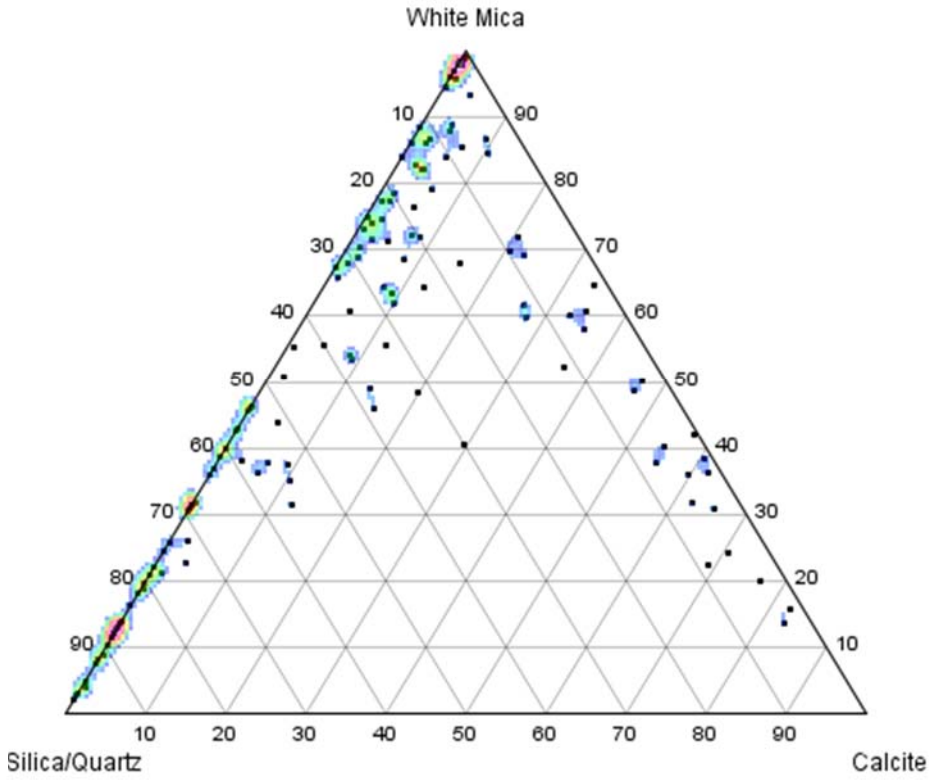

Figure 100. Ternary plot of white mica, silica and calcite that shows a relationship with white mica to silica and calcite but not with silica and calcite.

The average ISM value for ammonium-illite is approximately 2.229 which equates to a Kübler index (KI) value of approximately 0.169, based on experimental work by Doublier et al. (2010). According to Abad (2007), illites from metapelites with KI values this low are in the "epizone" metapelitic zone which corresponds to a temperature of ≥300°C. Compared to the average KI value of 0.852 for non-ammonium-bearing illite that corresponds to the deep diagenetic zone and approximate 100°C - 200°C temperature of formation.

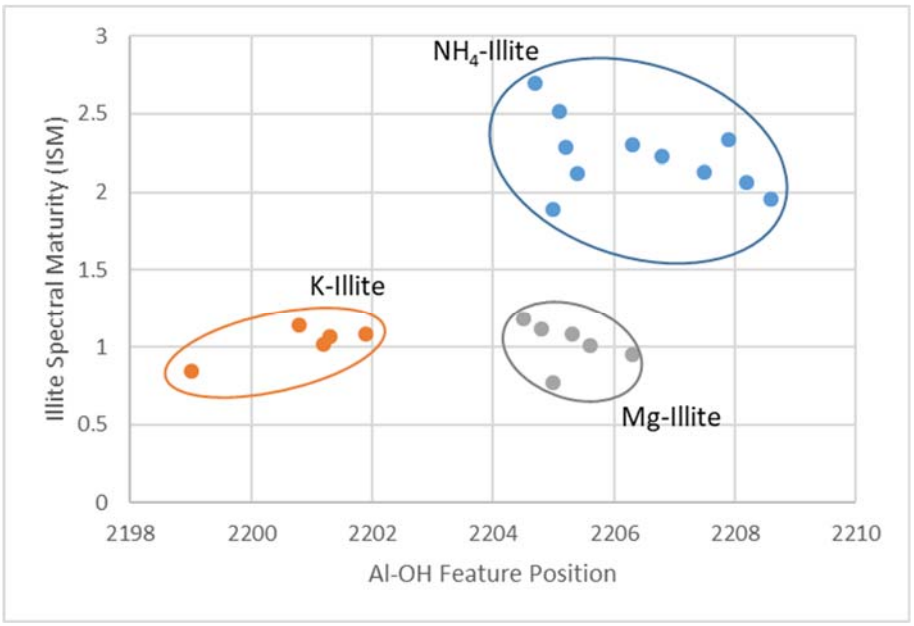

Figure 101. Scatter plot of illite spectral maturity (ISM) versus Al-OH feature position that demonstrates the higher fluid temperature associated with ammonium mica compared to what the TerraSpec Halo on-board software identified as K-illite and Mg-illite. The ISM value is based on work from Doublier et al. (2010).

5.5 Discussion and Interpretations

Short-wave infrared spectroscopy been successfully applied here to identify phyllosilicates, carbonate, silica, iron oxide and sulfate mineralogy. At the Button Hill Au deposit, SWIR spectroscopy has identified 16 mineral classes and 3 mineral compositions. Mapping of these mineral classes can contribute to the delineation of hydrothermal alteration footprints, identifying overprinted alterations and describing their relationship to one another, and describing the mineralogy and mineral composition of each alteration type.

Muscovite is the major mica in the altered rocks. This is shown by the mineral maps and histogram of the mica 2200nm absorption feature position. Phengite is a minor mica that appears to be associated with weathering and some unaltered limestone. It is likely that most phengite is altered from muscovite in areas of fractures and porous rock associated with oxidation from groundwater flow. This is consistent with the presence of phengite rims and muscovite cores in

collapse breccia clasts that are also associated with a large amount of porosity and iron oxides. Montmorillonite, gypsum, goethite, hematite, jarosite and the unknown Fe-mineral are also associated with weathered zones in faults and porous collapse breccias. Montmorillonite is associated with goethite and hematite in the correlation matrix and visibly in the mineral maps. Gypsum is associated with goethite and the unknown Fe-mineral and strongly correlated with hematite. The unknown Fe-mineral is also strongly correlated with hematite. Kaolinite is found coating some faults and fractures; however, the majority is within a specific collapse breccia at the lower contact of silicification. Kaolinite is not found to be correlated to any other identified mineral except silica in the correlation plots and ternary plot. It may be that most the kaolinite is part of the original minerology of this specific Bx5 breccia and not associated with alteration.

Ammonium mica has a relatively strong signature in the upper silicified breccia zone, especially in BD15-052, but also in BD14-04C and BD15-051. The presence of ammonium mica in the bleached rock is likely a direct result of the replacement of organic material by silica. During replacement of organic material, ammonia (NH_3) would have been liberated. After interaction with hydrogen ions it forms ammonium (NH_4^+) which replaces K^+ ions in the muscovite to produce ammonium mica (Browning, 2014).

Thin section observations of cross-cutting relationships suggest that Bx3a was formed much later than Bx1a. The position of Bx3a over Bx1a could suggest that the lack of permeability in the intensely silicified rock caused it to act as an aquitard for the bleaching fluids, as well as the Carlin Au-bearing fluids that deposited Au in the mudstones just above Bx3a.

Additional evidence for ammonium mica being associated with alteration unrelated to Carlin Au introduction is the illite spectral maturity. Previous work on ISM by Doublier et al. (2010) was on the alteration of metamorphic rocks up to approximately 350°C. If this is applicable to the illites of Carlin-type and low-sulfidation epithermal deposits, it suggests that the higher ISM

values associated with ammonium illite are indicative of a higher temperature fluid of alteration (≥300°C) compared to non-ammonium-bearing micas that had an approximate temperature range of 100-200°C, consistent with Carlin-type gold deposit formation temperatures of 180-245°C (Teal and Jackson, 2002; Cline et al., 2005). The higher temperature of crystallization for ammonium illite could potentially be from epithermal fluids. At the very least, the ISM may show that the fluid responsible for this alteration is different than that associated with the non-ammonium bearing illite alteration. An alternative is that the presence of ammonium in the illite affected the ISM value, causing an apparent increase in temperature.

Carbonates in the breccia zone are negatively correlated with silica. The carbonate signature is spotty throughout both the intensely silicified and weakly silicified zones and is highest below the silicification zone. In fact, the carbonate signature is even weaker in the weakly silicified zone above and below Bx1a. This suggests that the fluids which caused silicification may also have been responsible for decalcification, and the fluids that caused the weak silicification may have had a larger effect on decalcification, or the combined effects of both siliceous fluids caused more decalcification on the periphery of the Bx1a body. This is consistent with the observations of Volk et al. (1995) that pre-ore silica replacement is associated with decarbonatization, but in contrast to the Betze and Lower Post deposits of the Goldstrike mine in which the extensive decalcification has no obvious association to mineralization or silicification (Leonardson and Rahn, 1995).

The absence of dolomite in the SWIR samples is in contrast to other deposits. Kuehn and Rose (1992) described the alteration of major Carlin-type deposits as having 4 steps, 3 of which include dolomite as a mineral within the alteration assemblage.

The Fe-carbonate class appears to be strongly related to the late calcite ± barite veins and breccias (Bx6). According to the Fe-slope of the 1750nm to 1360nm feature, calcite in these veins

and breccia matrix have a higher Fe content than does the sedimentary carbonates in the Rodeo Creek mudstones, Bootstrap limestone and carbonate cements of the Bx5 collapse breccias.

The aspectral classification appears to be associated with silicification. The presence of anhydrous silica/quartz likely increased reflectivity that caused the undifferentiated dark rock to be identified as aspectral. The classification in BD15-052 extends from the weakly silicified zone and into the unaltered limestone.

The problems with SWIR spectroscopy, in the case of silica, is that silica is non-diagnostic in this part of the spectrum and so the presence of free H_2O is a proxy for silica identification. If there are other minerals present that contain H_2O, the silica is not identified. Silica identification is also affected by the albedo of the sample. In the weakly silicified zone, silica is rarely identified. However, this may also be an effect of interference from other minerals: the silica signature in Bx1a is much more intense because it is not masked by features of other minerals.

The second major problem with SWIR in these samples is that low reflectivity in many samples causes a bias in mineral identification. As demonstrated in thin section, micas, silica and carbonate are present within Bx1 and Rodeo Creek mudstones; however, the SWIR spectra is devoid of any of these signatures, causing it to appear as though the mineral classes mentioned are not present. This may have even caused an error the interpretation that muscovite is associated with hydrothermal alteration. The evidence for muscovite being an alteration product is that it is spatially associated with other alteration minerals such as silica. The lack of mica identified in Bx1 may be a consequence of the SWIR spectrometer's inability to identify it in such dark rocks.

Like many other Carlin-type gold deposits, much of the gold is hosted in organic carbon-rich, dark mudstones that are not easily characterized using SWIR because of the lack of reflectivity and so mineralogical correlations to Au in the dark mudstones is not possible using this method. SWIR; however, has been effective at characterizing the silicified breccias associated with

Au mineralization. Hole BD15-052 (Figure 81) is an example which illustrates that Au is typically found mostly within the relatively unsilicified Bx1 breccia, but also within the weakly silicified Bx1 and in Bx3a, which is often found near the upper contact of the Bootstrap limestone. The higher-grade gold above the Bx1a breccia, within Bx3a, could suggest that the lack of permeability in the intensely silicified rock caused it to act as an aquitard for the Carlin Au-bearing fluids that deposited Au in the mudstones just above Bx3a. The Au assay values in Figure 81 show that Au is highest above the Bx3a with slightly lower values in the Bx3a, zoned out from the center from lowest to highest values. This could be the result of remobilization or dilution of Au if Bx3a brecciation did indeed occur after Carlin-Au mineralization.

CHAPTER 6 – CONCLUSIONS

A principle component analysis (PCA) has identified 4 distinct chemical suites within the El Niño Au-Ag deposit. Suite 1 (Al, Ce, Fe, La, Nb, Th, Ti, and Zr) is interpreted to represent lithogeochemistry, or immobile elements within original clay mineralogy. Suite 2 (Au, Ag, As, Cu, Sb, Te, Tl and W) is the mineralization suite. Suite 3 (C, CO3, Ca, Mg, Mn, and S) is an alteration suite of elements, or elements lost and gained during decarbonatization, carbon replacement and sulfidation. Suite 4 (Mo, P, Pb, Y, and Zn) is interpreted to be associated with layers of primary organic-rich, metalliferous deposition in an anoxic to euxinic marine environment.

Suite 1 elements were shown by scatter plots to have a strong correlation to Al, strengthening the argument that this represents clay chemistry. Downhole plots and box-plots showed that this suite of elements varies predictably with changing lithologies; however, the Grant isocon and EFS plots show that Al, Ti, and Zr are the only three elements that are consistently immobile, the others of which show some minor enrichment or depletion in areas of hydrothermal alteration.

Suite 3 consists of major components of minerals added or removed in alteration associated with Carlin-type mineralization. The PCA identified Ca, Mg, S, CO_3, C and Mn. Sr is included in this suite as Grant isocon and EFS plots show a correlation with Ca.

The PCA identified Mo, P, Pb, Y and Zn as a distinct suite (suite 4) that is interpreted as being related to anoxic to euxinic deposition. Cr, Th, U, V, W, Mn, Mg, and Fe are additional elements deposited in euxinic facies, as scatter plots show that these elements also have correlations to the suite 4 elements. These elements also represent an aspect of original geochemistry; however, as some are generally considered mobile, demonstrated by EFS down-hole plots, they are not grouped with suite 1.

The mineralization suite of elements (suite 2) as identified by the PCA, consisted of Au, Ag, Cu, As, Sb, Te, Tl, and W. Scatter plots aided to identify other elements which correlate with suite 2 including; Fe, Hg, Re, S, and Se. It further demonstrates that there are likely two separate suites associated with mineralization. The first suite consists of Au, Ag, As, (Cu?), Fe, Hg, Re, S, Sb, (Se?), Te, and Tl. The second suite consists of Ag, Au, (As?), Cu, (Fe?), Hg, (Re?), S, Sb, Se, Te, and (Tl?). The correlation matrix for higher grade Au (>0.05 opt) samples and higher grade Ag (>0.05 opt) samples reduced these suites to 1) Au, As, Cu, Fe, Hg, S, Te, Tl, and W, and 2) Ag, Hg, Sb, Se, and Te. At these higher grades Au does not correlate with Ag. High Au grades are also not associated with Re, and Se, and Sb has a strong negative correlation. In high grade Ag samples there is a negative correlation of Cu to Ag, As, Hg, Re, S, Sb, Te and Tl which may suggest Cu was remobilized during Ag mineralization. However, the very low overall concentrations of Cu at El Niño calls to question any apparent correlations of Cu to other mineralization suite elements.

The differences in spatial distribution and associations of the two mineralization element suites suggest that there are two separate deposits that make up the Au and Ag ore bodies of Button Hill. Gold mineralization was likely Carlin-type because of the geochemical signature that is consistent with other Carlin-type deposits. This includes low Ag/Au ratio (Table 6) and an associated of Au to As, Hg, Tl, Te, and Cu, consistent with trace elements identified in Carlin-type Au-bearing pyrite rims (Cline et al., 2005). Fluids carrying Au, As, (Cu?), Hg, S, Te, Tl, and (W?) are interpreted to have rose buoyantly along the Hend-Nicks fault zone where it spread out at areas of high permeability such as the Otto fault and other fault intersections (Bx4), bedding contacts, porous lithologies and the Bx1, Bx2 breccia zone, precipitating gold and other suite 2 elements.

Later fluids carrying Ag, Hg, Sb, Se, and Te followed the same pathway as Au-bearing fluids, and deposited in similar but not exactly the same areas. The Ag-bearing fluid is interpreted

to be associated with low-sulfidation epithermal mineralization from the Miocene demonstrated by a geochemical suite similar to that found in the epithermal Ag-Se deposit in the nearby storm mine (Trotman, 2009). Based on the distribution of this element suite in cross-section, the epithermal fluids appear to have used the Tara West fault as a conduit and, in some cases, are enriched along the fault. The Au mineralization suite; however, is not enriched along the Tara West fault, which may have offset the Au-ore body. Tara West is a north-south high-angle normal fault thought to be associated with Basin and Range extension. If the Tara West fault was not present during Carlin mineralization it may have offset the Carlin-Au deposit and later the Miocene low-sulfidation epithermal Ag deposit used it as a conduit. The interpretation that Ag mineralization is separate from Au is further strengthened by short-wave infrared spectroscopy that has identified a distinct ammonium mica alteration that appears to be associated with high Ag/Au ratios and an enrichment of Hg, Sb, Se, and Te, and the high illite spectral maturity of the ammonium mica that suggests a higher temperature of formation than other Button Hill micas.

6.1 Breccia Descriptions, Geochemistry, and Hyperspectral Signatures

The major hosts of Au and Ag at the El Niño mine are tectonic (Bx1 and Bx4) and hydrothermal (Bx2 and Bx3) breccias, and to a lesser degree, collapse breccias (Bx5b) of the Rodeo Creek and Bootstrap Formations. Bx1a is rarely mineralized and Bx6 is not associated with mineralization. Following is a description of the lithology, mineralogy and geochemistry of the identified breccias associated with the El Niño deposit.

6.1.1 Tectonic Breccias

6.1.1.1 Bx1: Roberts Mountain Thrust Shear Zone Tectonic Breccia

The thickest (up to 65m) and most continuous breccia is the Roberts Mountain thrust tectonic breccia (Bx1). Bx1 is a deformed mélange of carbonaceous and metalliferous limey mudstone clasts and matrix primarily derived from the Rodeo Creek Formation. The general high original porosity and presence of diagenetic pyrite in Bx1 makes it a favorable host to Carlin-type Au. Bx1 is most commonly associated with Au mineralization; however, Bx1 does host high grades of Ag near Bx3a, the pyrite veined breccia associated with bleached selvages. The low albedo in unsilicified Bx1 makes it difficult for mineral identification using short-wave infrared (SWIR). Samples typically only have signatures of aspectral and undifferentiated dark rock.

6.1.1.2 Bx4: Other Fault Breccias

Bx4 is the name for all tectonic breccias along faults that are not the Roberts Mountain thrust (Bx1). It is characterized by angular clasts and rock-flour matrix with slip-surface contacts between clasts and between clasts and matrix. Bx4 is distinguished from Bx1 by the presence of; 1) Bx1 clasts in the breccia, 2) pure limestones clasts from the Bootstrap Formation, 3) vertical or near vertical orientation of faults, and/or 4) presence of any clast that is younger than Antler shortening (i.e. Jurassic diorite), or a younger alteration type (silicification, quartz veining, and pyrite veining). The distribution of suite 2 elements shows that fault zones, especially fault intersections, are a major host to Au and Ag mineralization; however, the selective sample for whole rock geochemistry from BD15-023A exhibited high As and Sb with minor enrichment of Au, Ag, W, Cu, Re, Se and Te but no significant Au or Ag concentrations. Unsilicified Bx4 breccias have SWIR signatures of aspectral and undifferentiated dark rock due to the low albedo in the samples that were selected.

6.1.2 Hydrothermal Breccias

There are four types of hydrothermal breccias in the Button Hill Au-Ag deposit. They are: 1) Bx1a: the strongly silicified tectonic breccia (Bx1), which consists of two subtypes, a white quartz flooded breccia, and a dark vuggy silica flooded breccia, 2) Bx2: vuggy silica cemented hydrothermal breccia that is often composed of Bx1, 3) Bx3: pyrite matrix hydrothermal breccia. Of the Bx3 breccias, there appears to be at least two subtypes. The first is a crackle to chaotic breccia associated with thin bleached selvages (Bx3a) around the pyrite veinlets. Bx3b contains pyrite veining with no bleached selvage. 4) Bx6: the youngest of the hydrothermal breccias, a late calcite ± barite matrix crackle to chaotic breccia.

6.1.2.1 Bx1a: Intensely Silicified Mudstone/Limestone

Bx1a is a texturally destructive intensely silicified (white quartz) mudstone/limestone hydrothermal breccia. It is often found within the Bx1 breccia body; however, is also found at the upper contact of the Bootstrap limestone. The geochemical cross-sections show that both Au and Ag can be hosted within the intensely silicified zone; however, it appears to have acted as a partial barrier to mineralizing fluid flow because of the limited penetration of ore into this silica zone, compared to the upper weakly silicified zone and Bx1 breccia. A white silica Bx1a sample (BD15-052 815.1-815.3) is enriched in the mineralization suite (Ag, Au, Sb, Te, Li, Re, Se, Tl, As, W, and Cu) and depleted in Ca and Mg (suite 3, decalcified), with a high Ag/Au ratio of 25.09. It is unknown if the bleaching fluids have affected this rock because of the inability to observe bleaching, due to the light color and lack of organic material of Bx1a. In SWIR, the white silica is easily identified; however, the darker zones are not always identified as silica, but rather yields an aspectral signature. The opposite is true for white mica. The strongest mica signatures are in the darker, less silicified sections, which is consistent with thin-section observations. The lack of SWIR

identified quartz in the darker sections may also be a result of spectral interference from white mica.

6.1.2.2 Bx2: Vuggy Silica Cemented/Veined Hydrothermal Breccia

Bx2 is the most widespread hydrothermal breccia in the Arturo pit. It is a vuggy silica cemented chaotic hydrothermal breccia within the larger tectonic breccia body (Bx1). Bx2 can be a host to gold and silver mineralization, and the vugs associated with the quartz veins often host pyrite, stibnite, calcite and barite. Because of the lack of reflectivity in the Bx2 clasts, the major mineral classes identified with SWIR are aspectral and undifferentiated dark rock; however, the vuggy silica matrix has signatures of silica and white mica.

6.1.2.3 Bx3a: Quartz-Ammonium mica- Pyrite Altered Mudstone Crackle Breccia

Bx3a is a quartz-ammonium mica- pyrite altered mudstone crackle breccia. It is characterized by pyrite veinlets and bleached selvages that cross-cut Bx1, Bx1a, and Bx2. The selected samples of Bx3a have Ag greater than Au (2.22-120.83 Ag/Au ratios), are depleted in Mg and Ca, and are enriched in As, Sb, Se, Te, and Tl. The bleaching associated with Bx3a is due to dissolution of organic material. Hyperspectral images of Bx3a are characterized by an ammonium mica signature within the bleached selvage which zones out to muscovite. The presence of ammonium mica in the bleached rock is likely a direct result of the replacement of organic matter by silica. During replacement of organic matter, ammonia (NH_3) would have been liberated. After interaction with hydrogen ions it forms ammonium (NH_4^+) which replaces K^+ ions in the muscovite to produce ammonium mica. Bx3a breccia is relatively easily identified in the hyperspectral images due to the ammonium mica signatures. Ammonium mica has a relatively strong signature in the upper silicified breccia zone.

The illite spectral maturity (ISM) for ammonium mica is consistently higher than other mica samples, suggesting a separate, hotter (≥300°C) alteration fluid that caused the bleaching and precipitated ammonium mica.

6.1.2.4 Bx3b Pyrite Matrix Crackle to Chaotic Hydrothermal Breccia

Bx3b is a pyrite matrix crackle to chaotic hydrothermal breccia, similar to Bx3a. It is distinguished from Bx3a by the lack of apparent relationship to silicification, and lack of white mica alteration and leaching/replacement of organic material. The pyrite of Bx3b is primarily in high density clusters of veinlets that crisscross and fill open void space in Bx1 and Bx2 breccias. Samples of Bx3b are typically enriched in suite 2 elements and have a low Ag/Au ratio. Bx3b does not produce a hyperspectral signature other than aspectral and undifferentiated dark rock due to the low reflectivity. The absence of ammonium mica in these samples suggests a difference in the timing and environment of formation of the two pyrite-bearing breccias.

6.1.2.5 Bx6: Calcite ± barite matrix crackle to chaotic breccia

The youngest observed hydrothermal breccia is a coarse-grained calcite ± barite matrix crackle to chaotic breccia that is localized along fractures, faults and void space in bodies that ranges from sub-millimeter to 10's of centimeters thick. It occurs throughout the entire mineralized system and cross-cuts all other breccia types. It has no obvious relationship to mineralization and so no samples were collected for whole rock geochemistry. Hyperspectral images of Bx6 have a strong carbonate signature. The slope of the 1750nm to 1360nm absorption feature is typically greater than 1, suggesting a higher iron content (ferroan calcite) than that of the unmineralized Bootstrap limestone.

6.1.3 Collapse Breccias

The second most prevalent breccia in the Button Hill deposit are the collapse breccias (Bx5). There are several varieties of Bx5 breccias; however, they all form from the dissolution of Bootstrap limestone and collapse of stratigraphically higher material, either on the upper contact of the Bootstrap Formation, or along faults and fractures that cut the Bootstrap limestone. Of the collapse breccias, there are two major subtypes characterized by the presence of silicification (Bx5b), or lack of silicification (Bx5a). The unsilicified collapse breccias (Bx5a) have a strong signature of carbonates that includes calcite, ferroan calcite and carbonate 2, as well as white mica. Bx5b has a very different SWIR signature that includes silica, white mica, gypsum and the weathering minerals, montmorillonite, kaolinite, unknown iron silicate and iron oxides. Bx5b is often weakly enriched in the mineralization suite elements with relatively low Ag/Au ratios.

6.2 Timing of Mineralization, Alteration, and Brecciation

Deposition of miogeoclinal sediments occurred in the Paleozoic. The Vinini Formation was first deposited in the Ordovician. This was followed by the Bootstrap Formation in the Silurian and Devonian, and the Rodeo Creek Formation in the Devonian.

The first brecciation event was the Roberts Mountain thrust (Bx1), shown by the presence of Bx1 clasts within all other breccia types. This event thrust the Ordovician Vinini Formation over the Devonian Rodeo Creek Formation. Early calcite and barite veins occur in many of the Bx1 samples, and in these settings, appear to be after and coincident with Roberts Mountain thrust-related deformation.

A relatively small portion of Bx1 was intensely silicified (Bx1a) at the lower contact with the Bootstrap limestone. It is likely that collapse breccias played a role in controlling the flow of this silica-bearing fluid by increasing porosity for silica-bearing fluids to flow and precipitate.

The diorite intrusion (Russet Dike) in the North wall of the Arturo pit intruded into the Russet fault and cross-cuts Bx1 and Bx1a.

Bx2 hydrothermal breccia occurred after the intense silicification of Bx1a but before the local fault brecciation of BD15-023A (Bx4), shown by the presence of Bx2 clasts in the fault breccia. Bx4 fault brecciation in this sample developed after Bx2 but before Bx3b pyrite, shown by the later sulfidation of Bx2, but lack of bleaching and mica alteration. There was likely silicification associated with Bx3b.

Carlin-type Au mineralization may have occurred during or just after the Bx3b pyrite breccia, based on the presence of sulfidation, silicification and stibnite combined with the relatively undeformed state of the pyrite veins in this breccia.

Bx3a quartz-sericite-pyrite alteration may have happened after Bx3b; however this is uncertain. Pyrite of Bx3b, in almost all cases, has been broken by small fractures. This is not the case for Bx3a. Bx3a pyrite has always been observed completely intact. If this breccia is indeed younger than Carlin-type Au mineralization, it may be associated with Miocene low-sulfidation epithermal Au-Ag mineralization, like that seen in the neighboring Storm mine (Trotman, 2009).

Bx5 dissolution collapse brecciation likely occurred at different stages throughout the development of the Button Hill system.

The coarse-grained calcite ± barite veins and breccia matrix (Bx6) cross-cuts all other features at the Button Hill deposit and thus is the youngest. This event is not related to Au-Ag mineralization and is likely from circulating groundwater precipitating calcite and barite in void space created by dissolution and faulting.

6.3 Controls on Mineralization

Deposition of Au and Ag is interpreted to have been in two phases. The first was Eocene Carlin-type Au mineralization that involved fluids carrying Au, As, (Cu?), Hg, S, Te, Tl, and (W?) that rose buoyantly along the Hend-Nicks fault zone where it spread out at areas of high permeability such as the Otto fault, Hendrix fault and Nicks fault, as well as bedding contacts, porous lithologies and breccia zones. The largest Au-ore body is hosted in Bx1 and Bx2 at the upper contact of the intensely silicified Bx1a breccia. The fluids appear to have preferentially precipitated Au in the rocks above the Bx1a breccia, likely due to its lack of permeability.

The distribution of Carlin-Au-related elements shows that mineralization above the Roberts Mountain thrust was local and generally low grade; however, many of the elements such as As, Sb and Te are enriched within a much larger volume of rock than Au, reaching as high as the unconformity surface. Even Tl and Re appear to have remobilized and precipitated anomalous values where faults breach the surface. Anomalous values of these elements at the present surface is potentially valuable as pathfinders for future exploration efforts.

The second phase is interpreted to be a Miocene low-sulfidation epithermal Ag deposit that enriched the ore-system in Ag, Hg, Sb, Se, and Te. These fluids followed the same pathways as Carlin-Au-bearing fluids; however, precipitated in slightly different areas. The main breccia-hosted Ag-ore body is slightly lower than the Au-ore body. It penetrates the Bx1a breccia to slightly lower depths; however, also appears to have been controlled by the lack of permeability associated with the intense silicification. Ag, Hg, Se, and Te also have a much more widespread distribution in the upper plate and appear to have also precipitated along the Tara West fault, suggesting that it was used as a conduit for these fluids.

SWIR signatures of ammonium mica are associated with the bleaching alteration of Bx3a hydrothermal breccia. Geochemistry of Bx3a shows that they are enriched in the Ag mineralization

suite and have high Ag/Au ratios. The ISM for ammonium micas is higher than that of other identified micas, suggesting that the alteration fluids that formed ammonium micas were a higher temperature. These lines of evidence also suggest that the Bx3a breccia is associated with Ag mineralization. The easily identified ammonium mica in SWIR then has the potential of being another pathfinder if IR is applied to other core samples and/or the surface.

6.4 Recommendations for Future Studies

More data over a broader scope is always helpful but not always possible. In regards to this project, further investigation into several aspects regarding geochemistry and IR spectroscopy could potentially be beneficial to the understanding of, not only this Au-Ag deposit, but also some techniques that could be used in other deposits and future studies.

In this study, the Grant isocon method was used to estimate the change in mass of altered Rodeo Creek Formation rocks. A positive change in mass was assumed to be due to silicification and thus the positive change in mass was used as a proxy for silica due to silicification. More work investigating the link between the change in mass measured using the Grant isocon method and alteration silica may be beneficial to quantifying silica on a large scale. In the case of El Niño, silica is not geochemically analyzed due to the difficulty and expense; however, having silica values would be beneficial to predicting silica encapsulation and to assist in adjusting milling procedures.

The potential for using ammonium mica as a pathfinder in remote sensing exploration is not a new idea (Browning, 2014); however, it continues to be underutilized, perhaps due to the lack of understanding of how ammonium mica relates to mineralization. Further research linking ammonium mica to Au-Ag mineralization would be beneficial to this cause.

REFERENCES

ALS, 2009, ME-MS61m: Ultra-trace level method using ICP-MS and ICP-AES, ALS Geochemical Procedures, In-house report.

Arehart, G., Foland, K., Neaser, C., and Kesler, S, 1993, 40Ar/39Ar K-Ar and fission track geochronology of sediment-hosted disseminated gold deposits at Post-Betze, Carlin trend northeastern Nevada: Economic Geology, v. 88, p. 622–646.

Armstrong, A. K., Theodore, T. G., Kotlyar, B. B., Lauha, E. G., Griffin, G. L., Lorge, D. L., and Abbott, E. W., 1997, Preliminary facies analysis of Devonian autochthonous rocks that host gold along the Carlin Trend, Nevada: Guidebook Series, vol. 28, p. 53-73.

Ashley, R. P., Cunningham, C. G., Bostick, N. H., Dean, W. E., and Chou, I. M., 1991, Geology and geochemistry of three sedimentary-rock-hosted disseminated gold deposits in Guizhou Province, People's Republic of China, Ore Geology Reviews 6, p. 133-151

Bakken B.M., 1990, Gold mineralization, wall-rock alteration and the geochemical evolution of the hydrothermal system in the main ore body, Carlin Mine, Nevada: Unpublished Ph.D. thesis, Stanford, CA, Stanford University, 236 p.

Barbalace, K., 2017, Periodic Table of Elements. EnvironmentalChemistry.com

Berger, V. I., Mosier, D. L., Bliss, J. D., Morning, B. C., 2014, Sediment-hosted gold deposits of the world-Database and grade and tonnage models, USGS Open-File Report 2014-1074, v. 1.1.

Bettles, K., 2002, Exploration and geology, 1962 to 2002 at the Goldstrike property, Carlin Trend, Nevada, Global Exploration in the Twenty-First Century, Society of Economic Geologists Special Publication, v. 9, p. 275-298.

Browning, D. A., 2014, Hyperspectral remote sensing in mineral exploration: ammonium-illite as a pathfinder for gold, Masters Thesis, University of Idaho, Moscow, ID, 102 p.

Clark, R. N., 1999. Spectroscopy of Rocks and Minerals, and Principles of Spectroscopy, Manual of Remote Sensing, Remote Sensing for the Earth Sciences, v. 3, p 3- 58.

Clark, R. N., Swayze, G. A., Wise, R., Livo, E., Hoefen, T., Kokaly, R. F., and Sutley, S. J., 2007, USGS digital spectral library splib06a. US geological survey, digital data series 231.

Cline, J. S., Hofstra, A. H., Muntean, J. L., Tosdal, R. M., Hickley, K. A., 2005, Carlin-type gold deposits in Nevada: critical geologic characteristics and viable models, Economic Geology 100th Anniversary Volume, p. 451-484.

Cook, D., Crackel, D., Jensen, M., 2002, The Dee North mine, Elko County, Nevada, The Mineralogical Record, v. 33, p. 225-234.

Cope, E., Hipsley, R., Dobak, P., Arbonies, D., Brower, S., 2008, South Arturo: a recent gold discovery on the Carlin Trend, Mining Engineering, v. 39448, p. 19-25.

Davies, A.G.S, 2002, Geology and genesis of the Kelian gold deposit, east Kalimantan, Indonesia; Doctoral dissertation, University of Tasmania, Hobart, Tasmania, Australia, 389 p.

Davis, D. A., Muntean, J. L., 2016, Metals. The Nevada mineral industry 2014, Nevada Bureau of Mines and Geology Special Publication MI-2014, p. 3-12.

Davis, D. A., Tingley, J. V., 2005, Precious metals deposits of Nevada, Geological Society of Nevada Symposium, p. 179-186.

Dobak, P. J., Arbonies, D., Hipsley, R., Visher, M., 2002, Geology of the Storm gold deposit, Gold deposits of the Carlin trend: Nevada Bureau of Mines and Geology Bulletin, v. 111, p. 46-53.

Doublier, M. P. , Roache, M. P. , Potel, S. , 2010, Application of SWIR spectroscopy in very low-gade metamorphic environments: a comparison with XRD methods, Geological Survey of Western Australia, Record 2010/7, 61 p.

Ellis, R., 1986, The Dee gold mine, The Mining Magazine, v. 154, 2, p. 112-115.

Emsbo, P., Hofstra, A. H., 2003, Origin and significance of postore dissolution collapse breccias cemented with calcite and barite at the Meikle gold deposit, Northern Carlin Trend, Nevada, Economic Geology, v. 98, p. 1243-1252.

Evans, J. G., Mullens, T. E., 1976, Bootstrap window, Elko and Eureke Counties, Nevada, Journal of Research, U.S. Geologic Survey, v. 4, 1, p. 119-125.

Evans, D. C., 2000, Carbonate-hosted breccias in the Meikle mine, Nevada and their relationship with gold mineralization: Masters Thesis, Colorado School of Mines, Golden, CO, 266 p.

Fleck, R. J., Theodore, T. G., Sarna-Wojcicki, A.M., and Meyer, C.E., 1998, Age and possible source of air-fall tuffs of the Miocene Carlin Formation, Northern Nevada: U.S. Geological Survey Open-File Report: OF 98-0338-B, p. 176-192.

Furley, R. A., 2001, Sequence stratigraphic framework for the Silurian-Devonian Bootstrap Limestone, Roberts Mountains, and Devonian Popovich Formations, Northern Carlin Trend, Elko and Eureka Counties, Nevada, Masters Thesis, Colorado School of Mines, 131 p.

Garwin, S. L., Hendri, D., and Lauricella, P. F., 1995, The geology of the Mesel deposit, North Sulawesi, Indonesia, Proceedings of the PACRIM 1995 Conference, p. 221-226.

Grant, J. A., 1986, The isocon diagram - A simple solution to Gresens' equation for metasomatic alteration, Economic Geology, v. 81, p. 1976-1982.

Grant, J. A., 2005, Isocon analysis: A brief review of the method and applications, Physics and Chemistry of the Earth, v. 30, p. 997-1004.

Gresens, R. L., 1967, Composition-volume relationships of metasomatism, Chemical Geology, v. 2, p. 47-65.

Greybeck, J. D. , 1985, Geology of the Dee Mine area, Elko County, Nevada, Masters Thesis, University of Idaho, Moscow, 96 p.

Hausen, D.M., and Kerr, P.F., 1968, Fine gold occurrence at Carlin, Nevada, in Ridge, J.D., ed., Ore deposits of the United States, 1933–1967: New York, American Institute of Mining Engineers, v. 1, p. 908–940.

Henry, C. D., and Faulds, J. E., 1999, Preliminary geologic map of the Emigrant Pass Quadrangle, Nevada: Nevada Bureau of Mines and Geology Open-File Report 99-9, scale 1:24,000, 20 p. text.

Henry, C., McGrew, A., Colgan, J., Snoke, A., and Bruseke, M., 2011: Timing, distribution and causes of Cenozoic extension in the northern Great Basin: Geological Society of America, Field Guide 21.

Hipsley, R., Dobak, P., Arbonies, D., 2006, South Arturo, Nevada, Barrick Gold Corp., In-house Report, p. 1-7.

Hofstra, A. H., Christiansen, W. D., Zohar, P. B., Tousignant, G., 2010, Lithogeochemistry of the Devonian Popovich Formation in the Northern Carlin Trend, Nevada, Geologic Society of Nevada Symposium, p. 63-96.

Humphreys, E., 1995, Post-Laramide removal of the Farallon slab, western United States: Geology, v. 23, p. 987–990.

Jackson, M. L., 2008, Evolution of the northeast zone breccia body, Mount Polley mine, British Columbia, Masters Thesis, v. The University of British Columbia, 244 p.

Kuehn, C.A., 1989, Studies of disseminated gold deposits near Carlin, Nevada: Evidence for a deep geologic setting of ore formation: Unpublished Ph.D. thesis, University Park, Pennsylvania State University, 396 p.

Laukamp, C., 2011, Short Wave Infrared Functional Groups of Rock-forming Minerals. CSIRO Earth Science and Resource Engineering Report Number EP115222, 20 p.

Looby, E., 2016, Button Hill: Corescan Technical Report JA0246. 31 p.

Mehrabi, B., Yardley, B. W. D., and Cann, J. R., 1999, Sediment-hosted disseminated gold mineralisation of Zashuran, NW Iran, Mineralium Deposita, v. 34, p. 673-696.

Morgan, C. E., 2007, Alteration of the Bootstrap limestone, Northern Carlin Trend, Elko County, Nevada, Masters Thesis, Colorado School of Mines, 149 p.

Mortensen, J., Thompson, J., and Tosdal, R., 2000, U-Pb age constraints on magmatism and mineralization in the northern Great Basin, Nevada. Cleur, J.K., Price, J.G, Struhsaker, E,M., Handyman, R,F., and Morris, C.L., eds., Geology and Ore Deposits 2000: The Great

Basin and Beyond. Geological Society of Nevada Symposium, Proceedings, May 2000, p. 419–438.

Muntean, J. L., 2016, Overview. The Nevada mineral industry 2014, Nevada Bureau of Mines and Geology Special Publication MI-2014, p. 3-12.

Nuckolls, H. M., 1985, Geology of the Bootstrap mine, Nevada; A sediment-hosted disseminated gold deposit: Masters Thesis, Stanford University, Stanford, CA, 62 p.

Peters, S. G., Leonardson, R. W., Ferdock, G. C., Lauha, E. A., 1997, Breccia types in the Betze orebody, Goldstrike Mine, Eureka County, Nevada, Carlin-type deposits field conference. SEG Guidebook Series, v. 28, p. 87-100.

Pettijohn, F. J., 1975, Sedimentary rocks: 3rd Ed. Harper and Row, 718 p.

Radtke, A.S., 1985, Geology of the Carlin gold deposit, Nevada: U.S. Geological Survey Professional Paper 1267, 124 p.

Rhys, D., Valli, F., Burgess, R., Heitt, D. G., Griesel, G., Hart, K., 2015, Controls of Fault and Fold Geometry on the Distribution of Gold Mineralization on the Carlin Trend, Geological Society of Nevada Symposium, p. 333-389.

Scott, K. M., Yang, K. , 1997, Spectral reflectance studies of white micas, Australian Mineral Industries Research Association Ltd. report 439 , v. 35.

Stewart, J.H., 1980, Geology of Nevada: Nevada Bureau of Mines and Geology Special Publication 4, p. 136

Stewart, J.H., 1997, Triassic and Jurassic stratigraphy and paleogeography of west-central Nevada and eastern California. U.S. Geological Survey Open-File Report 97–495, p. 57

Teal, L., Jackson, M., 2002, Geologic overview of the Carlin Trend gold deposits, Gold deposits of the Carlin trend: Nevada Bureau of Mines and Geology Bulletin, v. 111, p. 9-19.

Tosdal, R., Wooden, J., and Kistler, R., 2000, Geometry of the Neoproterozoic continental break-up, and implications for location of Nevadan mineral belts, in Cluer, J.K., Struhsacker, E.M., Hardyman, J.F., and Morris, C.L., eds., Geology and Ore Deposits 2000: The Great Basin and Beyond: Geological Society of Nevada Symposium Proceedings, May 15-18, 2000, p. 451–466.

Tribovillard, N. , Algeo, T. J., Lyons, T. , Ribulleau, A. , 2006, Trace metals as paleoredox and paleoproductivity proxies: An update, Chemical Geology, v. 232, p. 12-32.

Trotman, R. B., 2009, Geology of the Storm Gold-Silver Deposit Elko County, Nevada, Masters Thesis, University of Nevada, Reno, 163 p.

Valliant, W. W., Collins, S. E., Scholey, B. J. Y., 2015, Technical report on the South Arturo mine, Elko County, State of Nevada, U.S.A., RPA NI 43-101 Report for Premier Gold Mines Limited, 147 p.

Wallace, A. R. , John, D. A., 1998, New studies of Tertiary volcanic rocks and mineral deposits, northern Nevada rift. Contributions to the gold metallogeny of northern Nevada, USGS Open-File Report 1998, p. 98-338.

Wijns, C., Hall, G., Groves, D., and Muntean, J., 2004, Compressional tectonics of the Carlin gold trend: Proceedings, Predictive mineral discovery conference, Barossa Valley, p. 292–295.

Williams, C. L., 1992, Breccia boddies in the Carlin Trend, Nevada; Classification, interpretation and role in ore formation, Masters Thesis, Colorado State University, Fort Collins, 213 p.

Williams, C., 1993, Handout for the symposium on Northeast Nevada breccia bodies, GSN Special Reports, 19.

Wyld, S.J., 2000, Triassic evolution of the arc and backarc of northwestern Nevada and evidence for extensional tectonism, in Soreghan, M.J., and Gehrels, G.E., eds., Paleozoic and Triassic Paleogeography and Tectonics of Western Nevada and Northern California: Geological Society of America Special Paper 347, p. 185–207.

Zoback, M.L., McKee, E.H., Blakely, R. J., and Thompson, G.A., 1994, The northern Nevada rift: Regional tectono-magmatic relations and middle Miocene stress direction: Geological Society of America Bulletin, v. 106, p. 371-382.

APPENDIX

Table 8. List of drill-holes used in this study. RC indicates that the sample are "chips" from a reverse circulation drill. Core indicates that the samples collected from the drill-hole are core.

1	BD-001		21	BD-459	RC	41	BD-490	RC	61	BD-518	RC	81	BD-574	RC	101	BD13-09	RC	121	BD15-032	RC
2	BD-005C	Core	22	BD-460	RC	42	BD-491	RC	62	BD-521	RC	82	BD-575	RC	102	BD13-10	RC	122	BD15-050A	
3	BD-012C	Core	23	BD-461	RC	43	BD-492	RC	63	BD-522	RC	83	BD-577	RC	103	BD13-11C	Core	123	BD15-051	Core
4	BD-014C	Core	24	BD-462	RC	44	BD-493	RC	64	BD-525	RC	84	BD-579	RC	104	BD13-12	RC	124	BD15-052	Core
5	BD-015		25	BD-463	RC	45	BD-494	RC	65	BD-526	RC	85	BD-580	RC	105	BD13-13C	Core	125	BD15-053	Core
6	BD-030		26	BD-464C	Core	46	BD-495C	RC	66	BD-534	RC	86	BD-581	RC	106	BD13-15	RC	126	BD15-054	Core
7	BD-227	RC	27	BD-465	RC	47	BD-504	RC	67	BD-535	RC	87	BD-583	RC	107	BD13-16C	Core	127	BD15-055	
8	BD-234C	Core	28	BD-471	RC	48	BD-505	RC	68	BD-536	RC	88	BD-596	RC	108	BD13-17C	Core	128	BO295	UNK
9	BD-264	RC	29	BD-473	RC	49	BD-506	RC	69	BD-538	RC	89	BD-597	RC	109	BD13-18C	Core	129	RM13-WB02	Core
10	BD-265	RC	30	BD-475	RC	50	BD-507	RC	70	BD-539	RC	90	BD-598	RC	110	BD13-21	RC	130	RM13-WB03	Core
11	BD-278C	Core	31	BD-476	RC	51	BD-508C	Core	71	BD-545	RC	91	BD-600		111	BD13-22C	Core	131	RM15-WB01	Core
12	BD-280	RC	32	BD-477	RC	52	BD-509C	Core	72	BD-546	RC	92	BD-607		112	BDE13-02C		132	RM15-WB02	Core
13	BD-321	RC	33	BD-478	RC	53	BD-510	RC	73	BD-547	RC	93	BD13-01	RC	113	BDE13-03C		133	RM15-WB10	Core
14	BD-327	RC	34	BD-481	RC	54	BD-511C	Core	74	BD-548	RC	94	BD13-02	RC	114	BD14-04C	Core	134	WBD15-05	
15	BD-336C	Core	35	BD-482	RC	55	BD-512	RC	75	BD-549	RC	95	BD13-03	RC	115	BD14-06C	Core	135	WBM15-03	
16	BD-360	RC	36	BD-483	RC	56	BD-513	RC	76	BD-550	RC	96	BD13-04	RC	116	BD15-023	RC			
17	BD-373	RC	37	BD-486	RC	57	BD-514	RC	77	BD-551	RC	97	BD13-05	RC	117	BD15-023A	Core			
18	BD-374	RC	38	BD-487	RC	58	BD-515	RC	78	BD-552	RC	98	BD13-06	RC	118	BD15-024	RC			
19	BD-375	RC	39	BD-488	RC	59	BD-516	RC	79	BD-553	RC	99	BD13-07C	RC?	119	BD15-027A	Core			
20	BD-376	RC	40	BD-489	RC	60	BD-517	RC	80	BD-572C	Core	100	BD13-08	RC	120	BD15-031	RC			

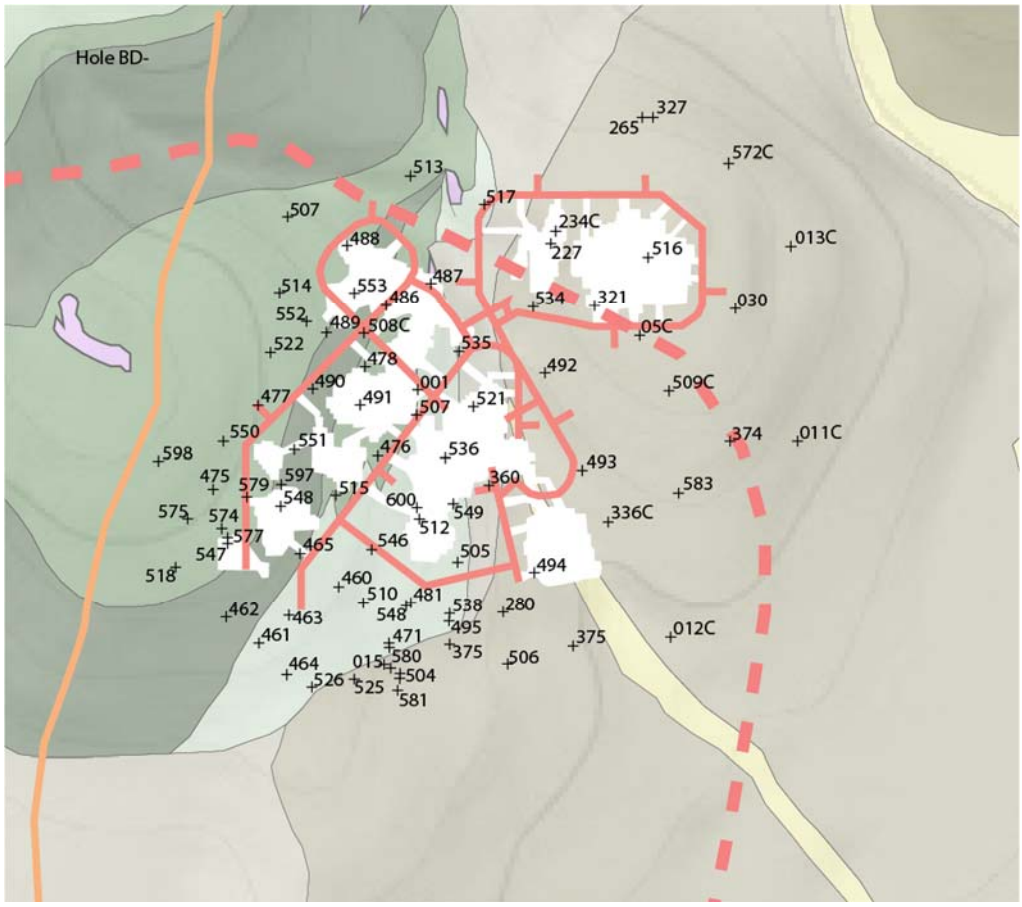

Figure 102. Drill-hole collar locations for BD holes. Hole numbers are denoted by BD- and the corresponding number.

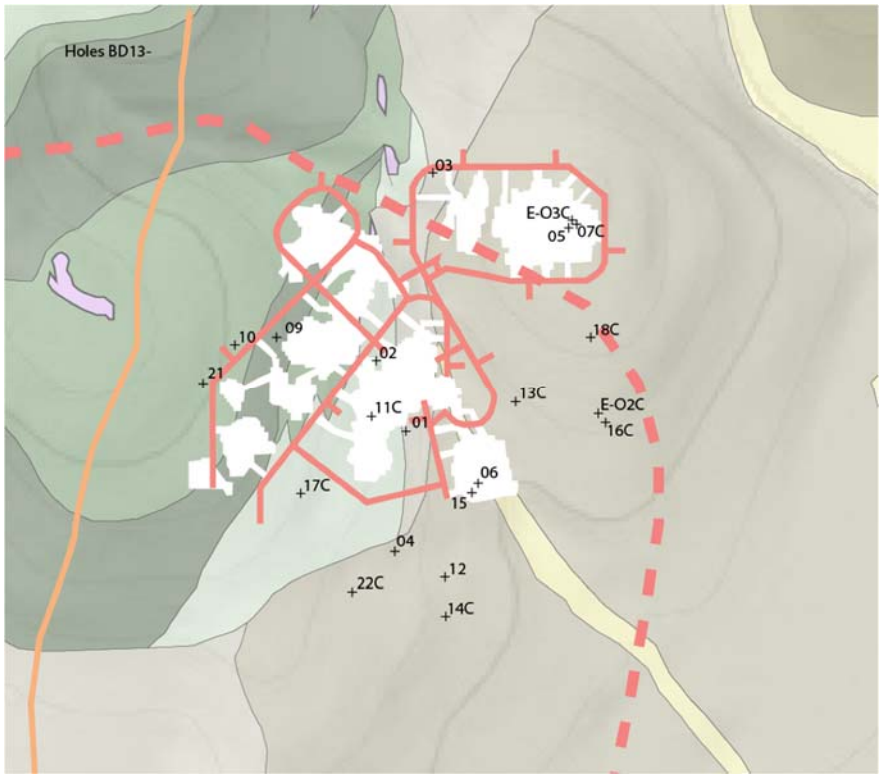

Figure 103. Drill-hole collar locations for BD13 holes. Hole numbers are denoted by BD13- and the corresponding number.

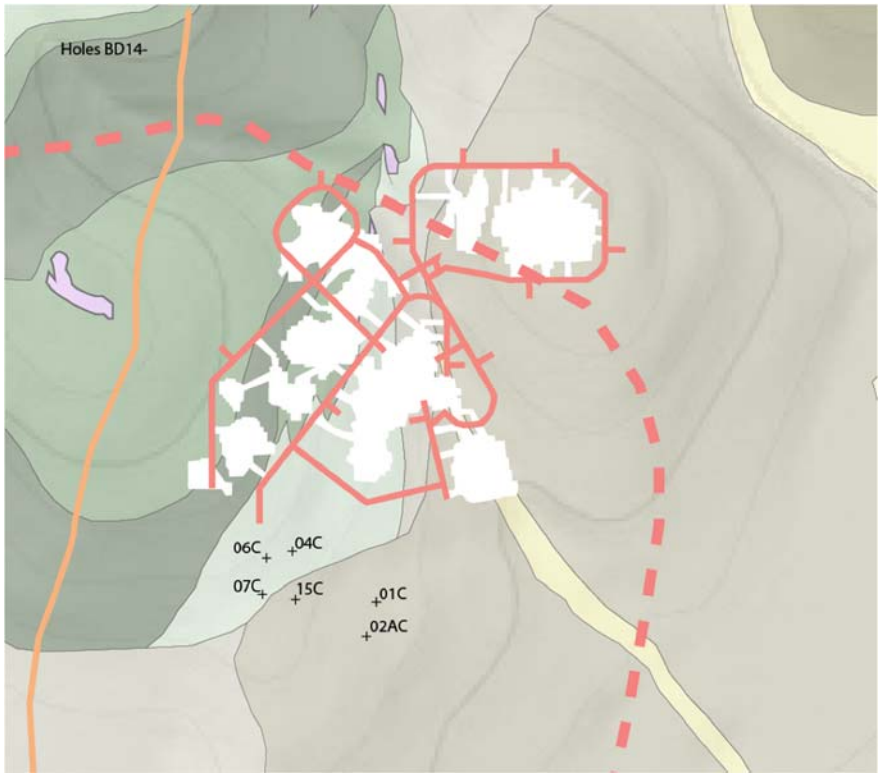

Figure 104. Drill-hole collar locations for BD14 holes. Hole numbers are denoted by BD14- and the corresponding number.

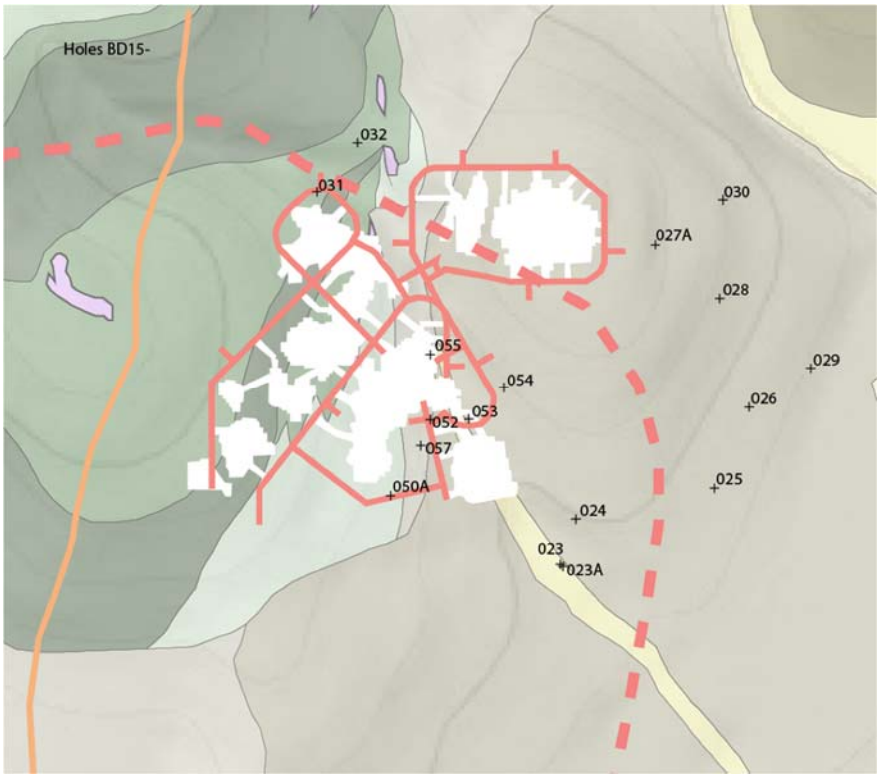

Figure 105. Drill-hole collar locations for BD15 holes. Hole numbers are denoted by BD15- and the corresponding number.

Table 9. Drill-hole number and depth for samples analyzed by Corescan.

BD15-051		BD15-052		Hand Samples	BD14-04C		BD15-050A		BD15-023A		BD15-053		
From	To	From	To		From	To	From	To	From	To	From	To	
795	881	753.5	762.5	BD14-01C-694	700	735	722.7	724.5	1339.5	1340.3	764.5	787	
		762.5	771	BD14-02AC-748	735	742			1342	1343.5	787	801.2	
		771	781.5	BD14-05C-591	742	747.5			1346.3	1379	801.2	811.2	
		781.5	792	BD14-06C-656					1410.6	1415.1	811.2	876.4	
		792	804	BD14-06C-683					1420	1421	876.4	955.8	
		804	819	BD14-07C-647									
		819	828.8	BD14-08C-551									
		828.8	839	BD14-08C-571									
		839	852	BD14-15C-655									
		852	860.9	BD14-16C-529									
		860.9	869.6	BD14-16C-558									
		869.6	878	BD14-16C-567									
		878	887.6	BD14-16C-590									
		887.6	901.3	BD15-04C-655									
		901.3	915.8										
		915.8	923.3										
		923.3	934.5										
		934.5	947.7										
		947.7	958										
		958	974.2										
		974.2	981										
													Grand total
Total Footage	86		227.5			47.5		1.8		40.5		191.3	594.6

Table 10. Terraspec Halo point data, minerals identified, and scalars.

				Mineral ID by Halo with confidence																										
				VNIR - Minerals			SWIR - Minerals																	Scalars						
Hole	Depth	#	Halo Sample#	Goethite	Ferrihydrite	No Match	Phengite	NH3_I/S	Mg-illite	K-illite	Muscovite	Illite/Smec	Kaolinite	Kaolinite W	Aragonite	Calcite	Chabazite	Brucite	Gypsum	Halloysite	Vermiculite	Al-OH	Kx	ISM	Mg-OH	Fe3t	Fe3i	Al-Fe-Mg		
BD14-04C	701.2	1	30079-0029			3			2	3												2200.8		1.142	2346.2			2200.8		
BD14-04C	701.2	3	30079-0031			3			3	3												2199		0.844	2340.7			2199		
BD14-04C	706.7	1	30079-0033			3				3	2											2201.2		1.02	2343.2			2201.2		
BD14-04C	706.7	2	30079-0034	2						3												2201.3		1.066	2347	998.9	0.85	2201.3		
BD14-04C	706.7	3	30079-0035	2						3												2201.9		1.083	2341.7	INV	0.849	2201.9		
BD15-023A	1360	1	30079-0043			3			1			3							2			2198.8		0.549	INV			2198.8		
BD15-023A	1360	2	30079-0044			3			1			2							1			2198.9		0.496	INV			2198.9		
BD15-051	804.5	1	30079-0036			3				3												2208.6		1.955	2346.2			2208.6		
BD15-051	804.5	3	30079-0038			3				3	3											2205		1.887	2345.6			2205		
BD15-051	804.5	4	30079-0039			3				3												2207.9		2.333	2346.2			2207.9		
BD15-051	804.5	5	30079-0040			3				3	2											2204.5		1.224	2347.7			2204.5		
BD15-051	804.5	6	30079-0041			3				3	3											2205.4		2.124	2346.7			2205.4		
BD15-051	804.5	7	30079-0042			3	3	3														2205.2		2.283						
BD15-051	861.3	1	30079-0053			3				2									1		1	2207.7		0.838	2349.6			2207.7		
BD15-051	861.3	5	30079-0057			3			2						1					3		2207.2	1.007	2.34	2347.9			2207.2		
BD15-051	861.3	6	30079-0058			3	1		2						1				1	3		2207.5	1.014	1.991	2350.6			2207.5		
BD15-051	861.3	7	30079-0059			3			2				3						3			2207.2	0.997	1.815	2382.4			2207.2		
BD15-051	861.3	10	30079-0062			3			2					3					3			2207.4	0.985	1.996	2383.4			2207.4		
BD15-051	861.3	11	30079-0063			3			2					3					3			2207.3	0.979	2.192	2382.8			2207.3		
BD15-051	861.3	12	30079-0064			3			3					3					2	1		2207.4	0.979	2.861	2381.8			2207.4		
BD15-051	861.3	13	30079-0065			3				3				3					2			2207.4	0.99	2.647	2352.8			2207.4		
BD15-051	861.3	14	30079-0066			3			2					3					3			2207.3	0.974	2.599	2382.2			2207.3		
BD15-052	769.2		30079-0015			3	3	3														2205.1		2.517						
BD15-052	769.2	1	30079-0019			3	3	3														2204.7		2.7						
BD15-052	769.2	4	30079-0022			3	3		2													2204.9		1.644	2345.7			2204.9		
BD15-052	795.7		30079-0016			3	3	3														2206.8		2.23						
BD15-052	795.7	1	30079-0023			3	3	3							1							2206.3		2.302						
BD15-052	795.7	2	30079-0024			3	3	3														2208.2		2.064						
BD15-052	795.7	3	30079-0025			3	3	3														2207.5		2.126						
BD15-052	795.7	4	30079-0026			3	3		2									1	1			2203.9		1.031	2343			2203.9		
BD15-052	874.5	1	30079-0007			3			3		2				1							2205.3		1.085	2343.4			2205.3		
BD15-052	874.5	2	30079-0008		2				3													2206.3		0.953	2344			2206.3		
BD15-052	880.4	1	30079-0017		3				3													2205		0.767	2341.2			2205		
BD15-052	893.2		30079-0013			3	2											2	1			2210.1		0.512						
BD15-052	907.1	1	30079-0004		2				3	3												2204.5		1.185	2345.8			2204.5		
BD15-052	907.1	2	30079-0005		2				2	3												2204.8		1.118	2343.4			2204.8		
BD15-052	907.1	3	30079-0006			3			3		3											2205.6		1.005	2345.8			2205.6		
BD15-053	954.2	1	30079-0047			3			2							3						2223.4		1.682	2339.5			2339.5		
BD15-053	954.2	3	30079-0049			3			3							3						2225.9		0.69	2337.1			2337.1		
BD15-053	954.2	6	30079-0052			3				3						3						2219.2		2.029	2340.1			2219.2		

Table 11. Drill-hole and depth for thin section samples.

Hole ID	Footage	Column2
BD14-01C	701.5	
BD14-01C	746	
BD14-01C	746	
BD14-17C	615	
BD15-051	716.5	716.8
BD15-051(0	826.5	826.6
BD15-051	840.5	841.8
BD15-051	868	867.8
BD15-053	781.8	
BD14-17C	597.5	
BD14-01C	746	
BD14-17C	597.5	
BD14-17C	597.5	
BD14-17C	561	
BD14-01C	773	
BD14-01C	727	
BD14-01C	702.5	
BD14-01C	692	
BD14-01C	692	
BD14-01C	692	
BD14-17C	596.5	
BD14-01C	692	
BD14-01C	657	
BD14-01C	657	
BD14-01C	657	
BD14-01C	657	
BD14-01C	657	
BD14-01C	577	
BD14-01C	695.6	
BD14-01C	645.6	
BD14-17C	541	

Hole ID	Footage	Column2
BR-1		
BR-2		
SKARN HILL		
BD14-01C	647.5	
BD14-01C	647.5	
BD14-01C	738	
BD14-17C	586	586.5
BD15-04C	655	655.5
BD14-04C	700.8	701
BD14-04C	701.2	701.4
BD14-04C	706	706.4
BD14-04C	706.7	707
BD14-04C	713.3	713.7
BD14-04C	745.3	746
BD15-053	781.5	781.8
BD15-053	783	783.3
BD15-053	786.2	786.6
BD15-053	789.4	789.6
BD15-053	790.9	791.1
BD15-053	801.3	801.8
BD15-053	881.8	882.1
BD15-053	954.2	954.8
BD14-16C	519-519.4	
BD14-16C	558	558.5
BD14-16C	567	567.5
BD14-16C	590	590.4
BD15-052	739.6	
BD15-052	746.2	
BD15-052	847	848.3
BD15-052	847	848.3
BD15-052	847	848.3

Hole ID	Footage	Column2
BD15-052	914.9	915.5
BD15-052	923.6	924
BD15-052	959.1	959.4
BD15-052	769.2	769.5
BD15-052	795.7	796.3
BD15-052	814.6	815.1
BD15-052	841.2	842
BD15-052	841.2	842
BD15-052	871.3	872
BD15-052	871.3	872
BD15-052	874.5	875
BD15-052	880.4	881
BD15-052	893.2	893.5
BD15-052	907.1	907.6
BD15-052	948.4	948.8
Dior-1		
Dior-1		
BD14-02AC	748	748.4
BD15-050A	722.7	723.5
BD15-050A	722.7	723.5
BD15-050A	722.7	723.5
BD15-050A	723.8	724.5
BD15-050A	723.8	724.5
BD15-051	793.9	
BD15-051	804.5	805.3
BD15-051	804.5	805.3
BD15-051	860.8	861.3
BD15-051	861.3	868
BD15-051	861.3	868
BD15-051	861.3	868
BD15-051	878	878.7

Hole ID	Footage	Column2
BD15-051	880.3	880.9
BD15-023A	1312.4	1312.6
BD15-023A	1320.9	1321.2
BD15-023A	1347.1	1347.5
BD15-023A	1351.9	1352.3
BD15-023A	1360	1360.5
BD15-023A	1362.1	1362.5
BD15-023A	1363.8	1364.5
BD15-023A	1363.8	1364.5
BD15-023A	1377	1377.8
BD15-023A	1410.6	1411
BD15-023A	1414.1	1414.9
BD15-023A	1531.1	1531.9
BD14-16C	529	529.4
BD14-15C	655	655.4
BD14-08C	571	571.4
BD14-08C	551	551.3
BD14-07C	647	647.2
BD14-06C	683	683.3
BD14-06C	656	656.4
BD14-05C	591	591.3
BD14-01C	694	694.4

Figure 106. Drill hole BD15-052, 736.5-745 ft. depth. Image of weakly silicified and decalcified, carbonaceous mudstone, clast supported tectonic breccia (Bx1).

Figure 107. Drill hole BD15-052, 771-781.5 ft. depth. Image of quartz-(ammonium) sericite- pyrite altered mudstone crackle breccia (Bx3a).

Figure 108. Drill hole BD15-052, 808.5-819 ft. depth. Image of Bx1a, intensely silicified (clast and matrix) mudstone/limestone hydrothermal breccia which rebrecciated Bx1 and Bx2 vuggy silica cemented hydrothermal breccia that rebrecciated Bx1 tectonic breccia.

Figure 109. BD15-052, 828-837 ft. depth. Image of Bx1a, intensely silicified (clast and matrix) mudstone hydrothermal breccia which rebrecciated Bx1

Figure 110. BD15-052, 929.5-38.5 ft. depth. Image of decalcified, silicified, chaotic limestone clasts, matrix supported, calcite cemented collapse breccia (Bx5b).

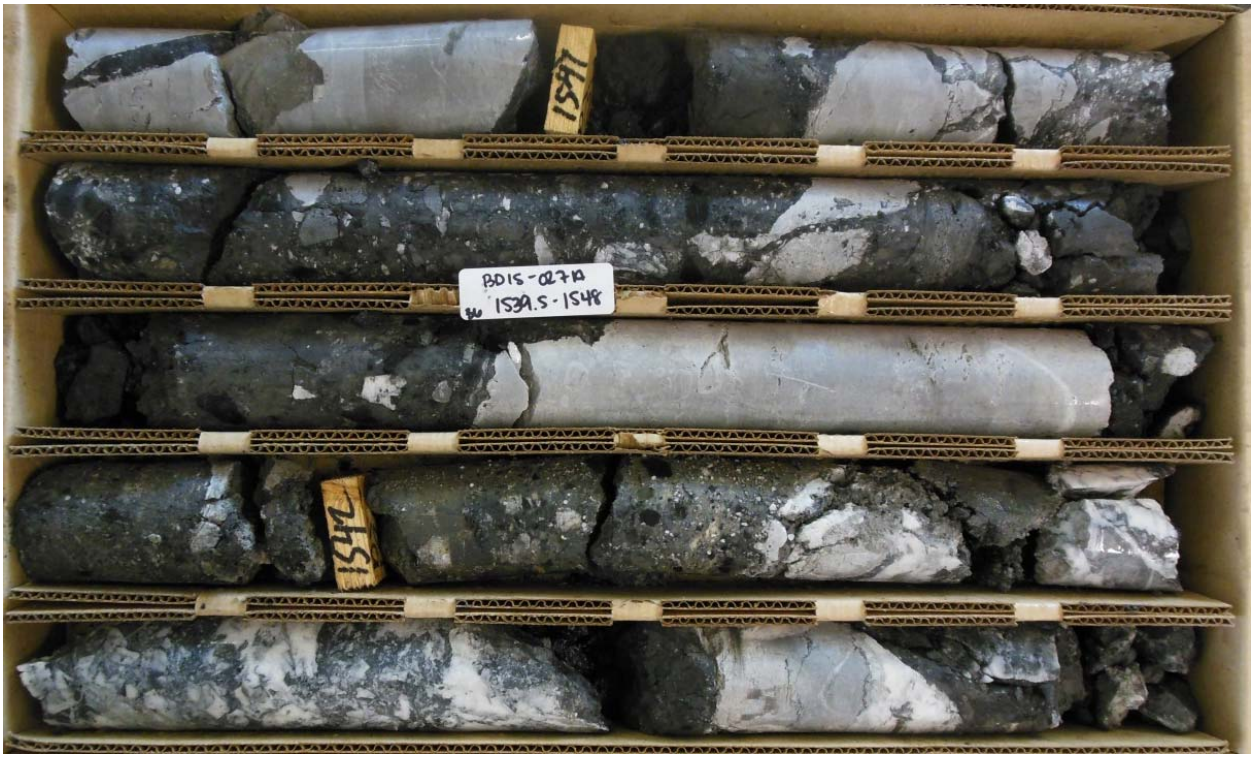

Figure 111. BD15-027A, 1539.5-1548 ft. depth. Image of Bx5a unsilicified dissolution collapse breccia.

Figure 112. BD15-052, 874.5-884 ft. depth. Bx5b, decalcified, silicified, chaotic limestone clasts, matrix supported, calcite cemented collapse breccia.

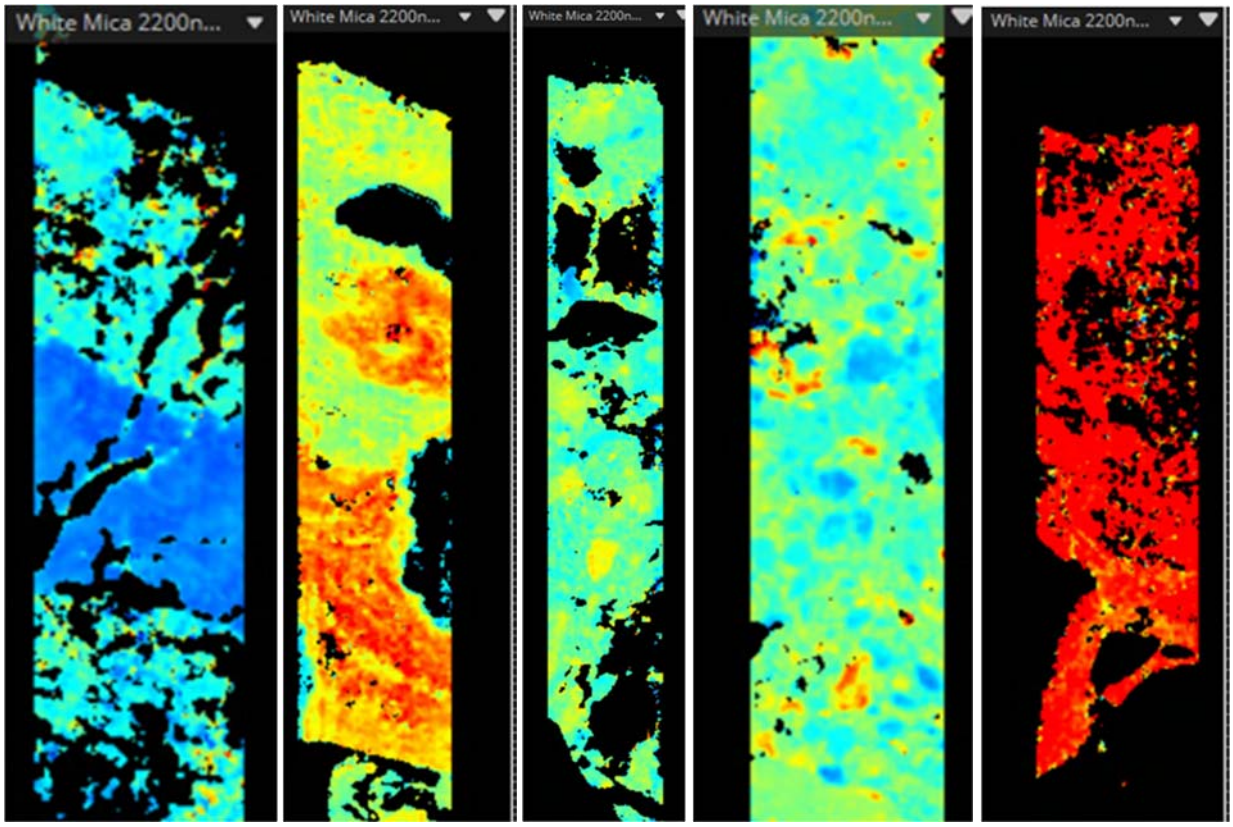

Figure 113. From left to right, BD15-052 841.2 842, BD15-052 914.9 915.5, BD15-051 804.5 805.3, BD15-053 881.8 882.1, and BD15-053 954.2 954.8 showing the variability in the white mica species. Blue to yellow represents muscovite, orange to red represents phengite.

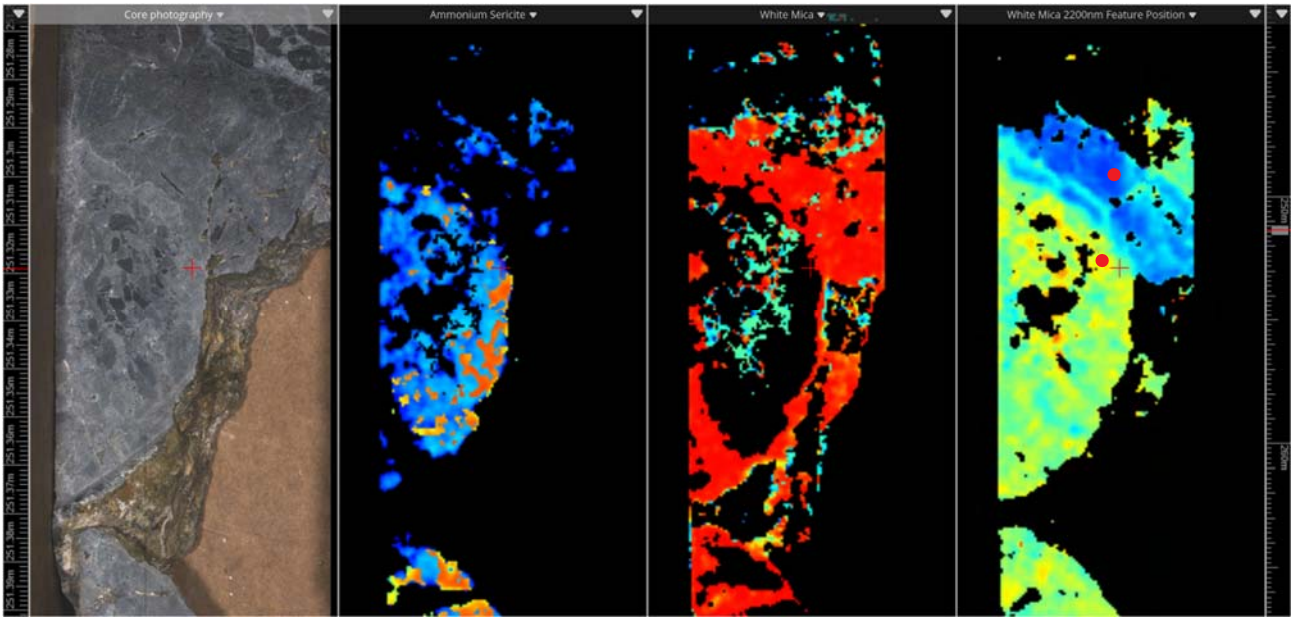

Figure 114. Hyperspectral images of BD15-052 Bx3a bleached alteration. Ammonium mica is strongest in the bleached areas, zones out to white mica. Two points of spectra taken from an area above the ammonium mica (blue) and within the ammonium mica (yellow).

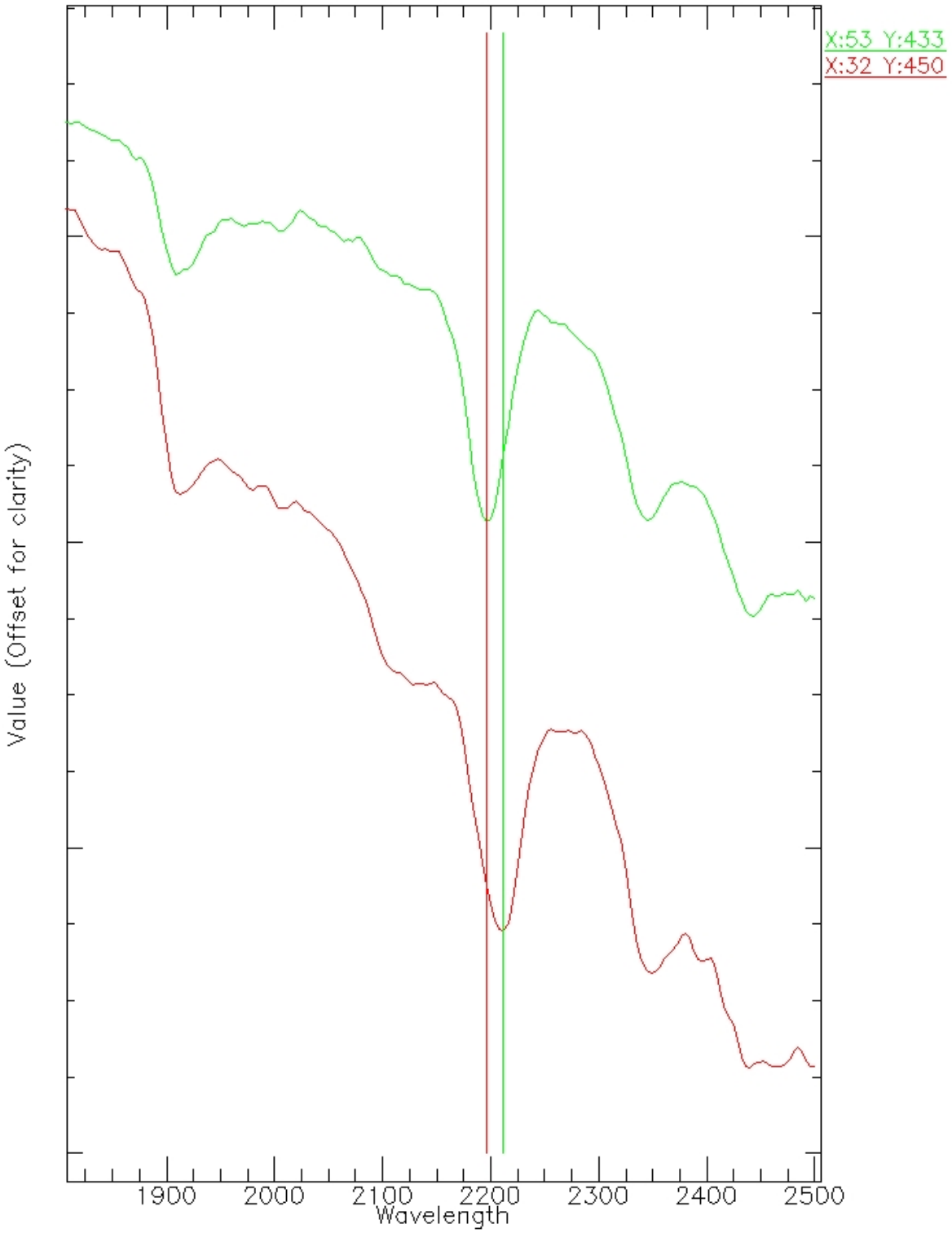

Figure 115. Two points from hyperspectral image (Figure) showing white mica (green) and an increase in Mg, approaching phengite (red).

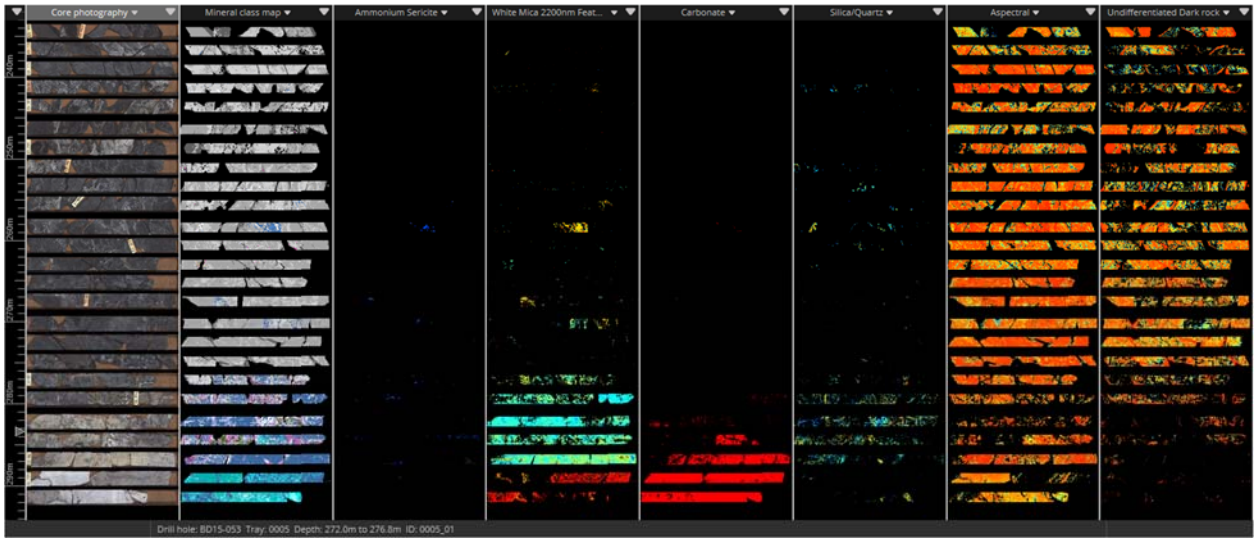

Figure 116. Drill hole BD15-053 hyperspectral images.

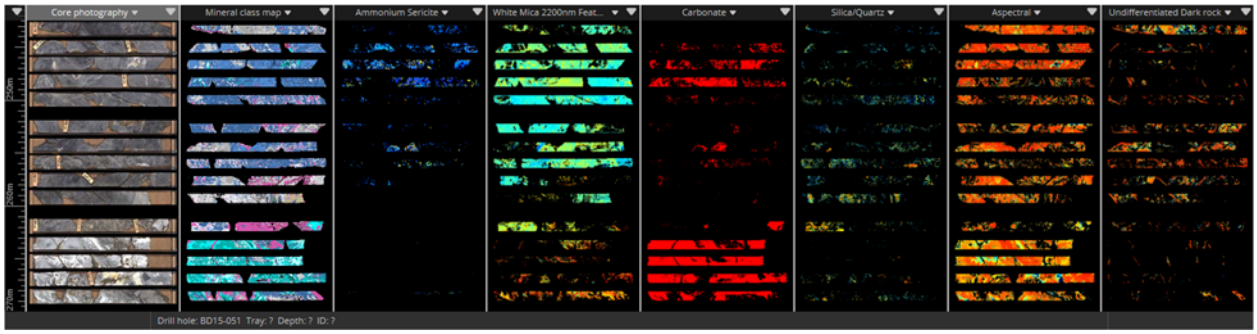

Figure 117. Drill hole BD15-051 hyperspectral images.

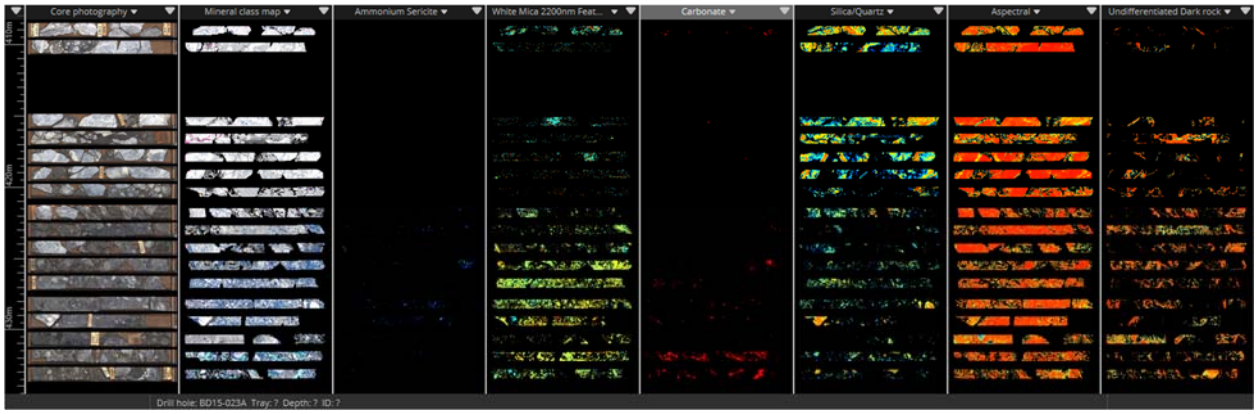

Figure 118. Drill hole BD15-023A hyperspectral images.

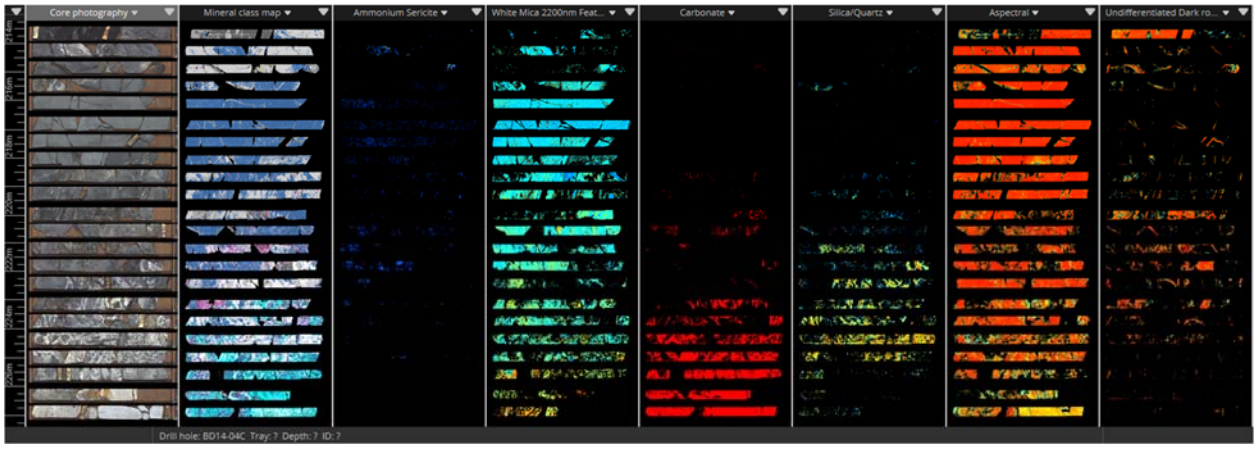

Figure 119. Drill hole BD14-04C hyperspectral images.

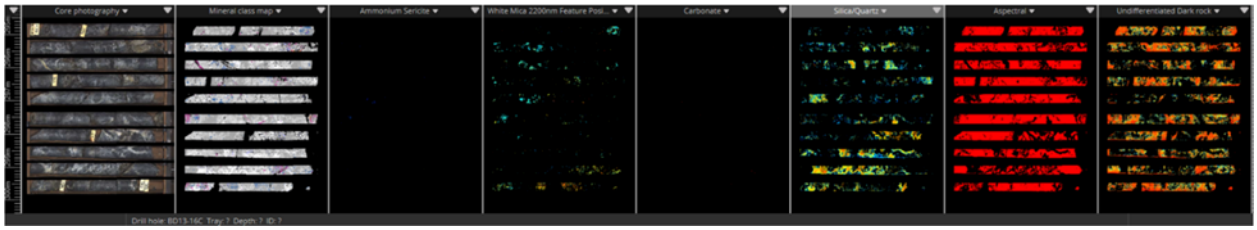

Figure 120. Drill hole BD13-16C hyperspectral images.

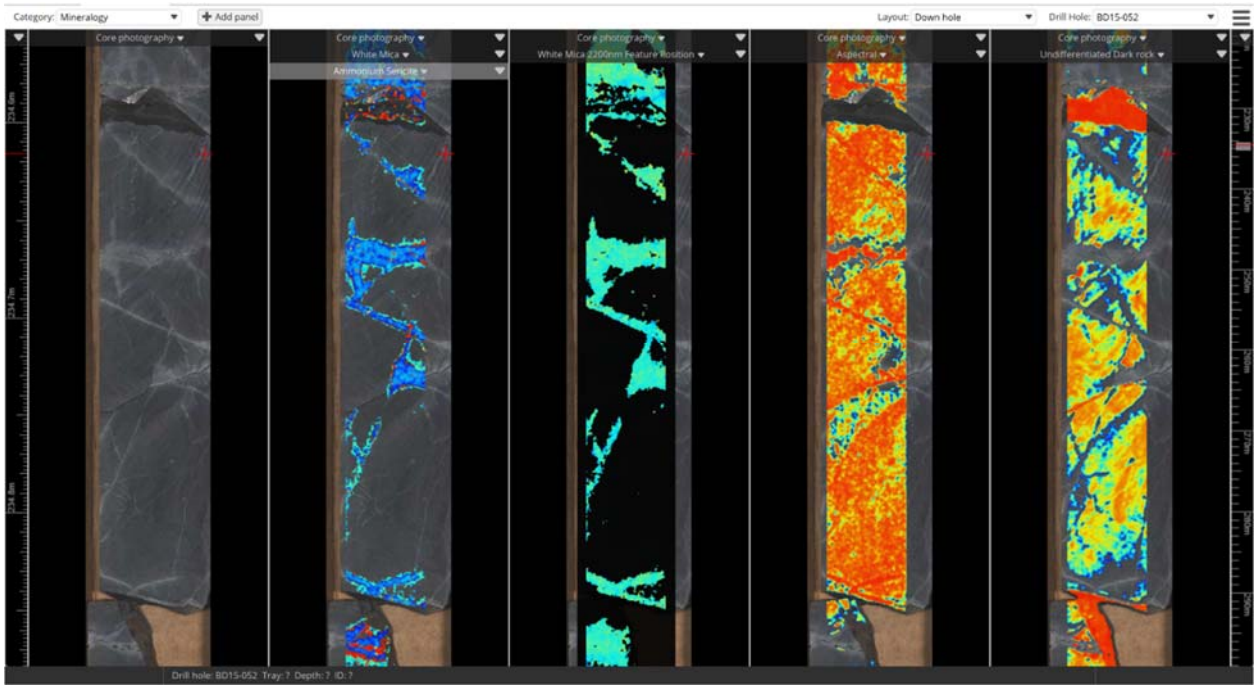

Figure 121. Bx3a sample from hole BD15-052 showing ammonium mica in bleached selvages.

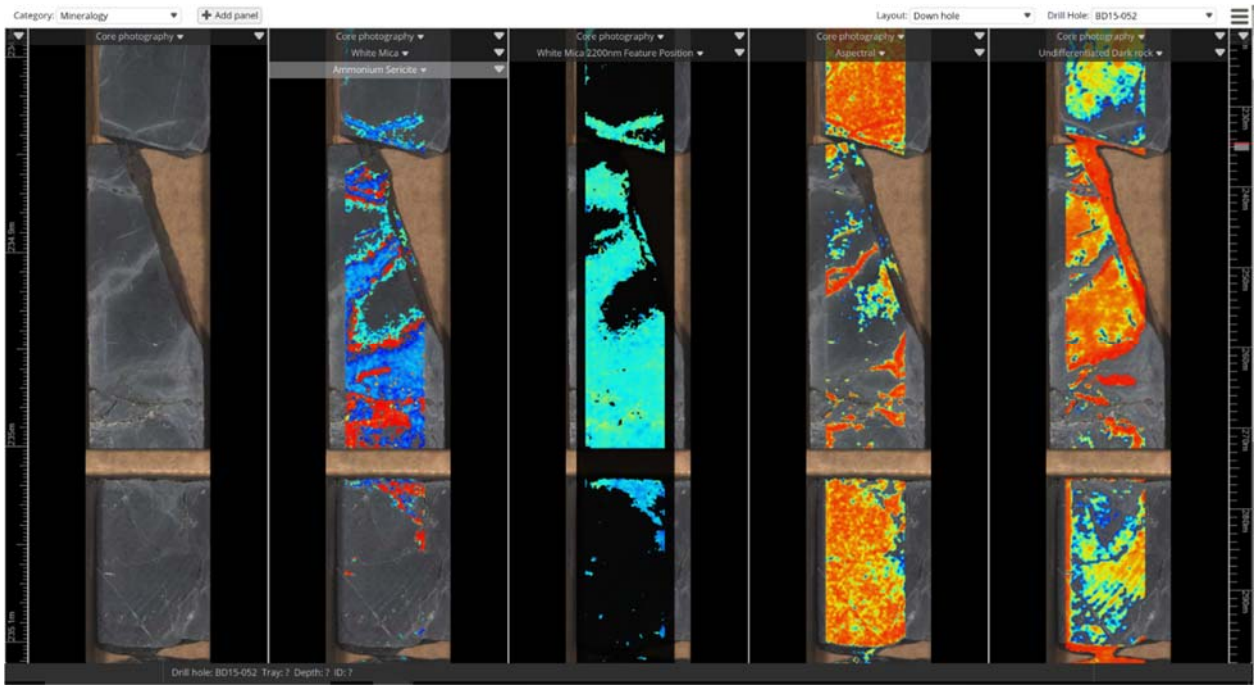

Figure 122. Bx3a sample from hole BD15-052 showing ammonium mica in bleached selvages.

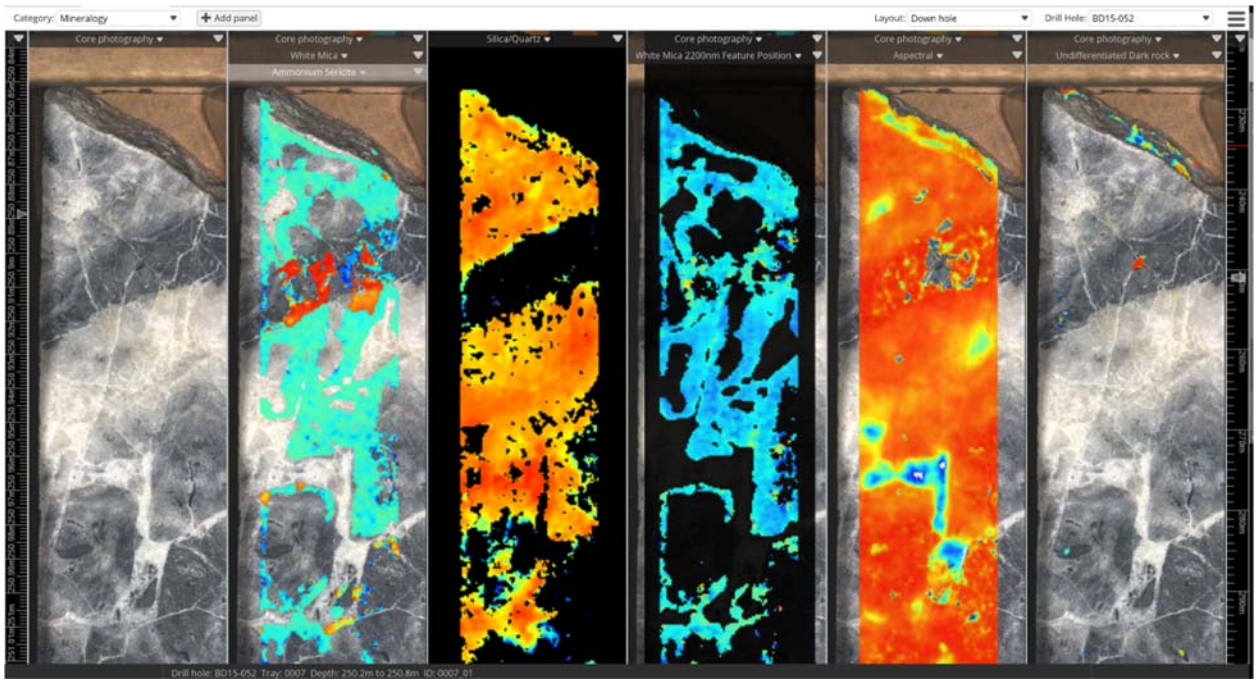

Figure 123. BD15-052. Bx3a ammonium mica/ bleaching overprinting Bx1a intensely silicified tectonic breccia. Ammonium mica is not present in rock that did not have organic material present before alteration.

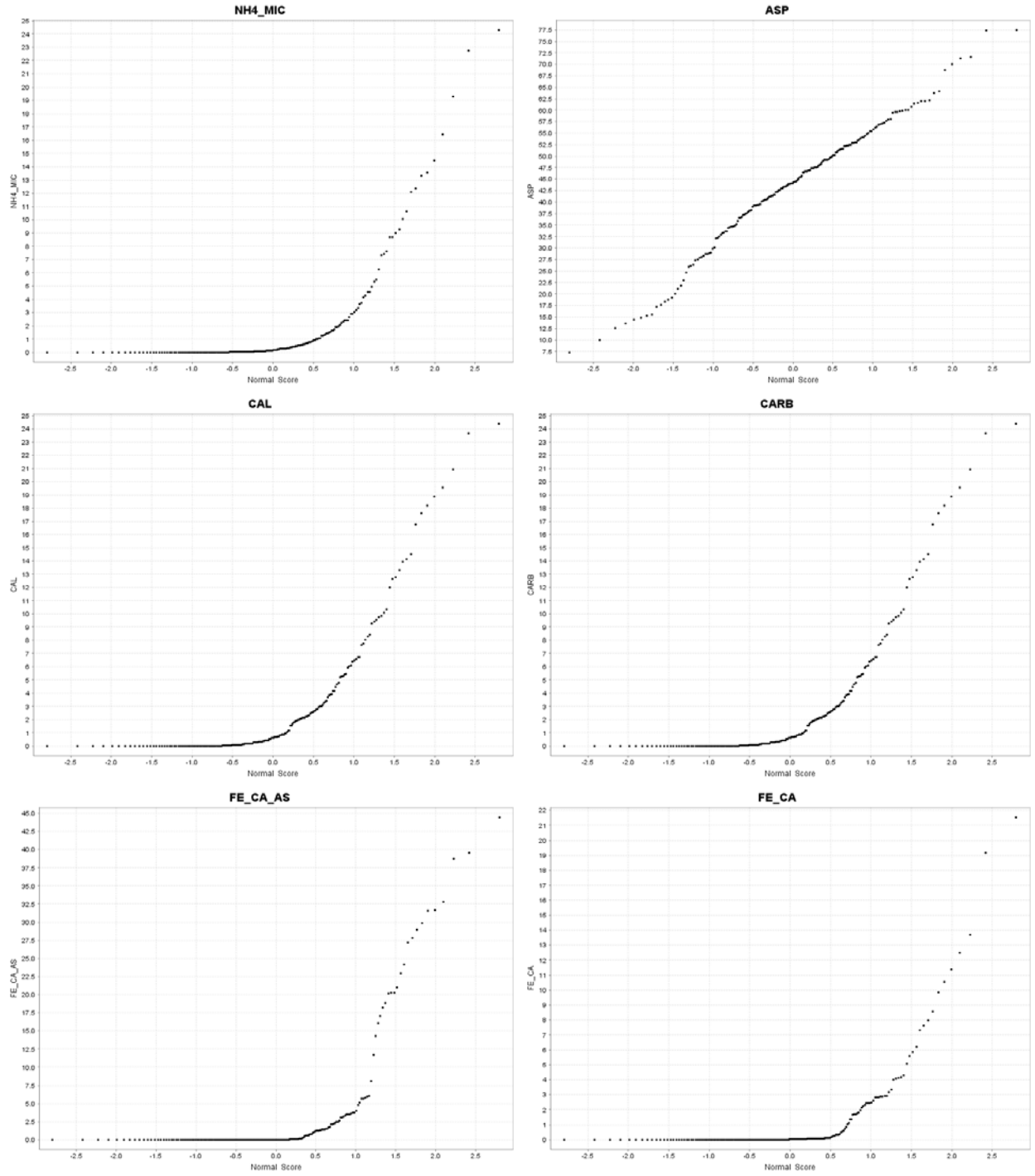

Figure 124. Normal probability plots for hyperspectral identified mineral counts.

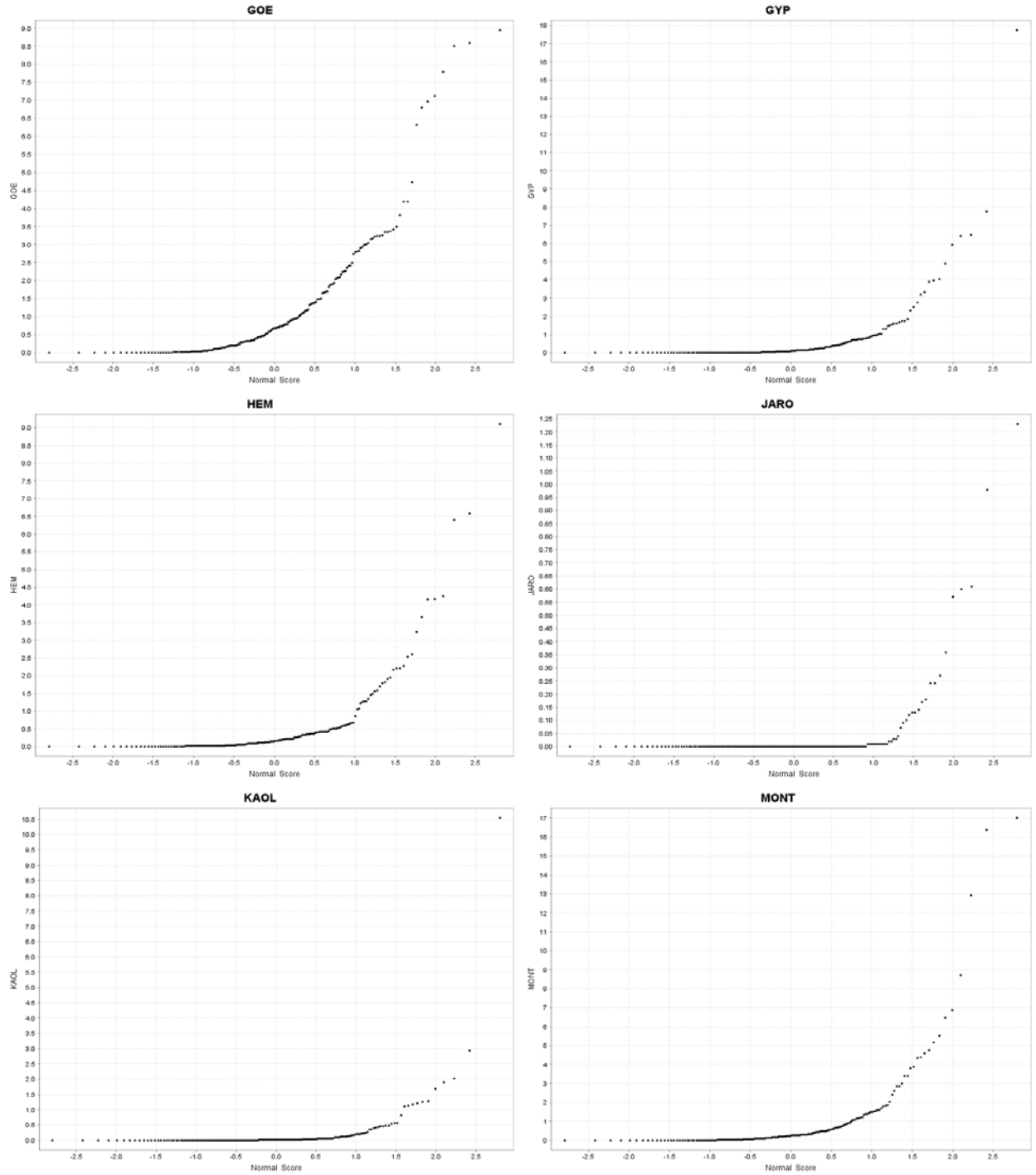

Figure 125. Normal probability plots for hyperspectral identified mineral counts.

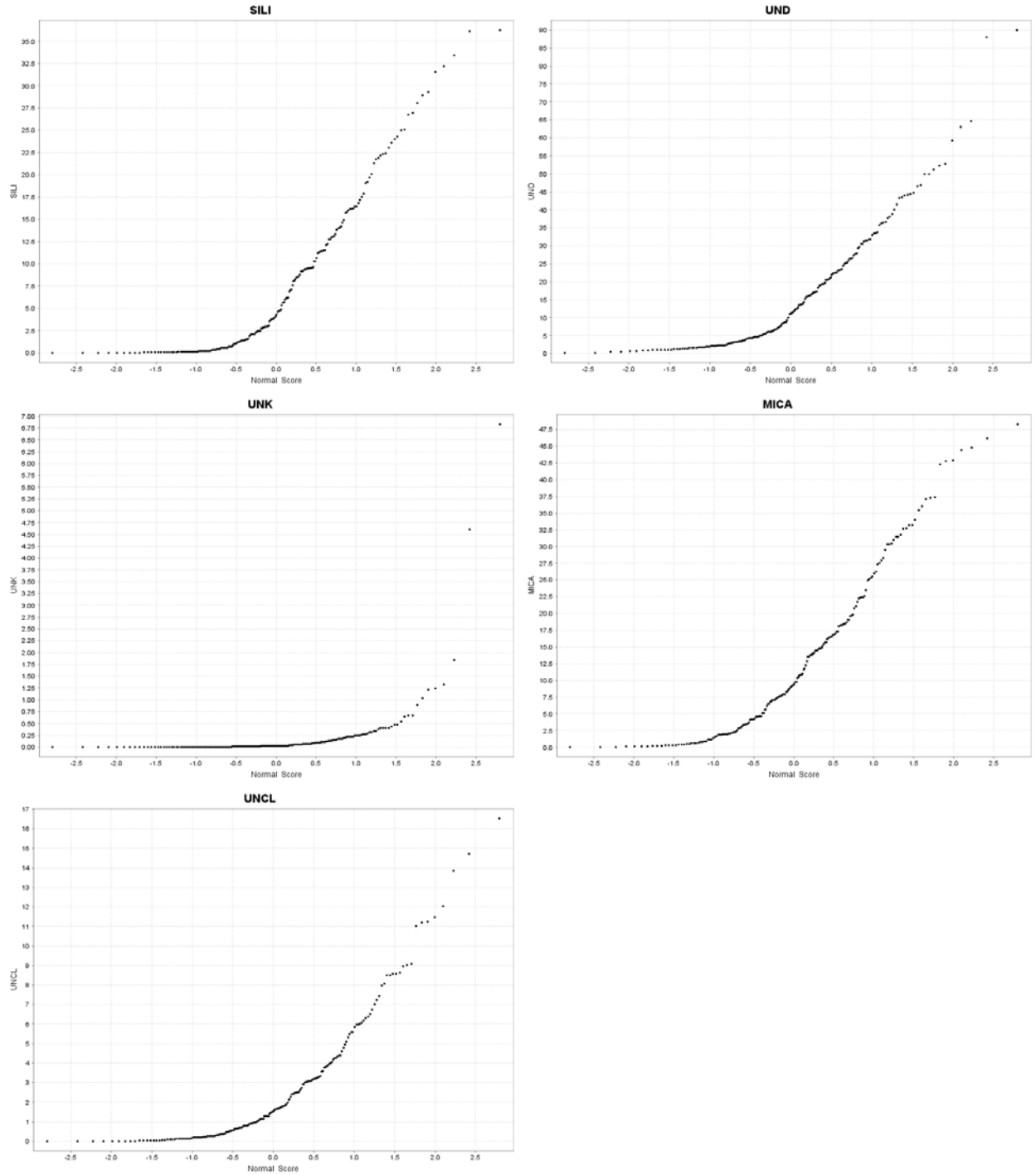

Figure 126. Normal probability plots for hyperspectral identified mineral counts.

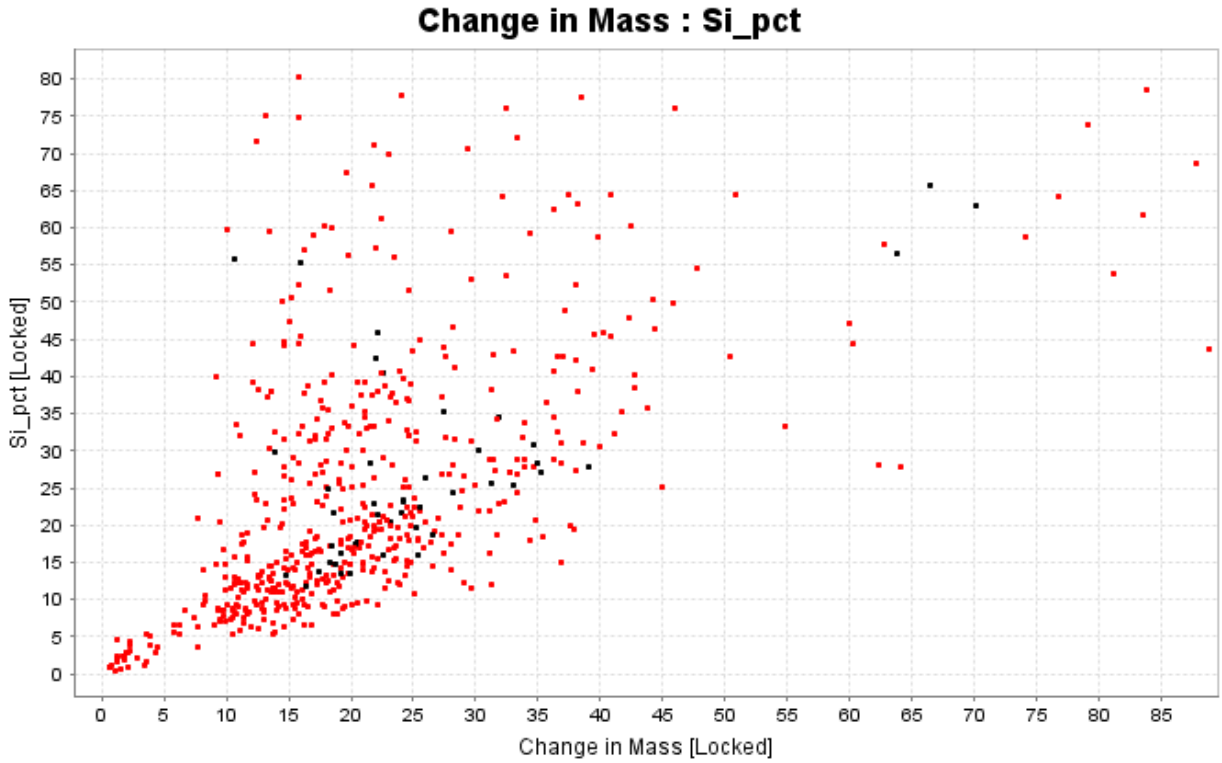

Figure 127. Change in mass versus silica showing the correlation between an increase of mass and silica (silicification?).

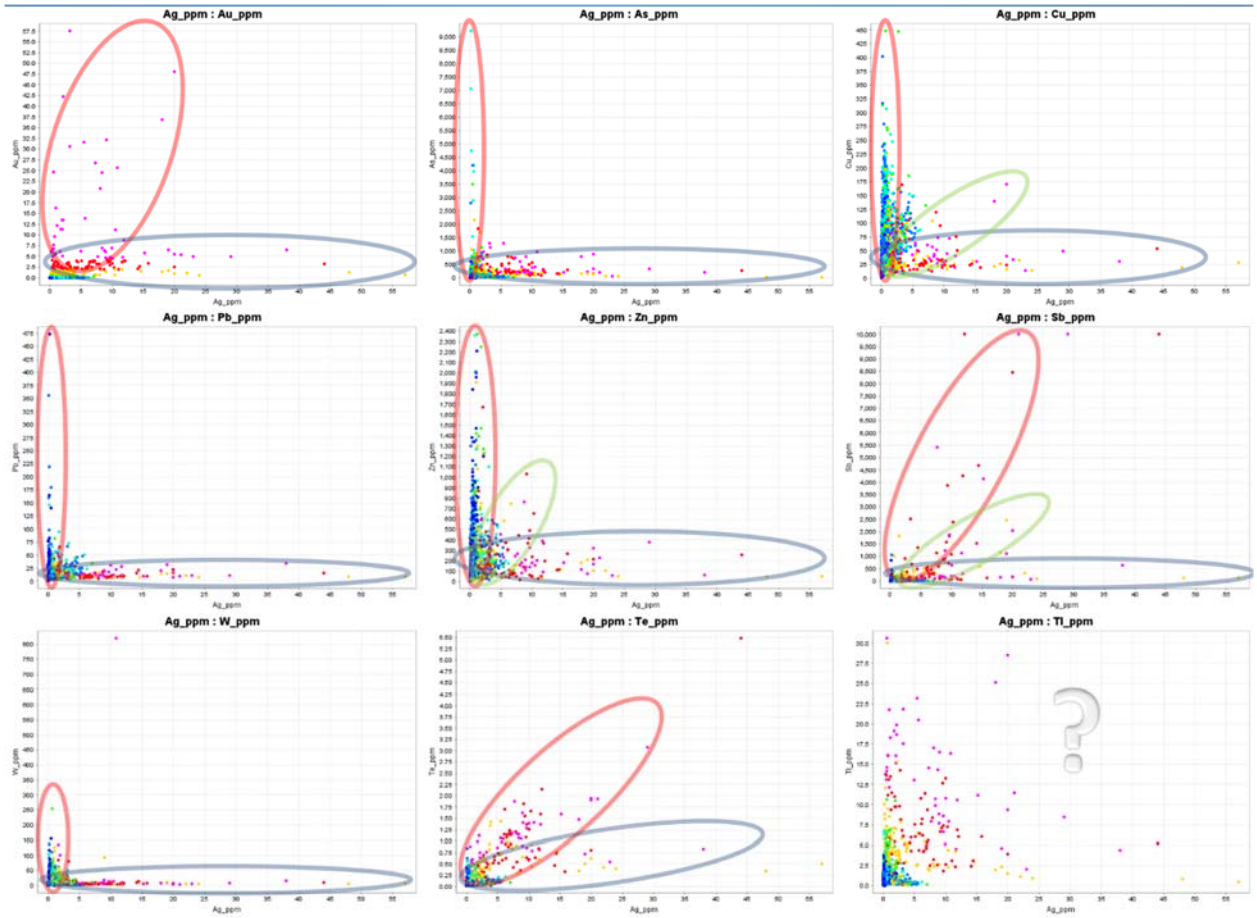

Figure 128. Ag compared to other mineralization suite elements from the Button Hill deposit for comparison to Storm geochemistry.

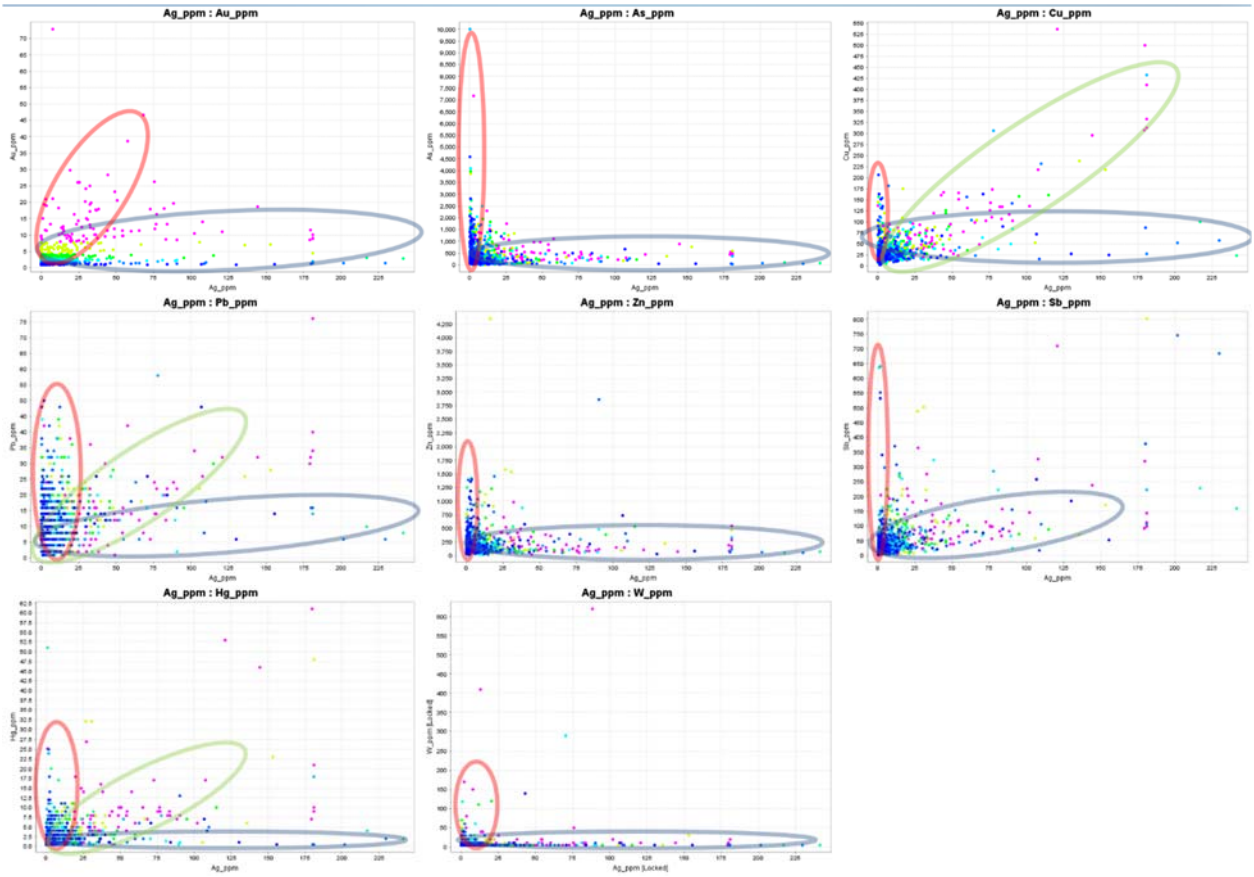

Figure 129. Ag compared to other mineralization suite elements from the Storm deposit for comparison to Button Hill geochemistry.